UNIVERSIDADE DA CORUÑA

DOCTORAL THESIS

Phase-field modeling and isogeometric analysis of cell crawling

Adrian MOURE ROSENDE

Supervisor:

Dr. Héctor GÓMEZ DÍAZ

Programa de doctorado en Ingeniería Civil
2017

Acknowledgments

I would like to express my gratitude to all the people who, one way or another, made this thesis possible. These years have been an extraordinary period of my life that has meant to me much more than this thesis. I would like to express special thanks to the following individuals,

To my advisor Héctor Gómez. I can only say thanks. Thanks for trusting me and the opportunity you gave me, thanks for your advise, your time, your effort, thanks for everything. It has been a great pleasure sharing with you this experience.

To my lab colleagues: Carles, Jesús, Hugo, Guillermo Lorenzo, Guillermo Vilanova, Jiangping, Pablo Domínguez, and Pablo Orosa. Also Nati and Alba, you are part of the group. Not a group, a family. I would like to say a word about each one of you, share a memory that would make you smile, but I would need another 100 pages.

To my colleagues and friends at UDC: Iván, Luis, Raquel, and the other members and professors of the GMNI. Also to the people of the GME, especially Antonio, Fran, Miguel Costas, and Rubén. And finally, Pablo Vázquez and Miriam. I really appreciate your efforts to make me feel at home. I do not feel like a stranger at the School anymore.

To my colleagues at Purdue University, especially Daihui and Ali, who welcomed me with open arms and supported me in those endless days when I wrote this thesis. And again, thanks to Pablo Domínguez, and foremost, to Miriam. I hope these months are the beginning of a fruitful period of our lives.

To my friends at UPM: Andrea, Dani, Gabriel, Javi, Juan Pablo, Juan Morales, Manuel, María Dolores, Marta, Patricia, Ricardo, Víctor, and, finally, Juan Gómez, who gave me good advice. To all the people and professors with whom I shared those years in Madrid, with a special mention to professors Carlos Gordo, Vicente

Negro, and Celso Iglesias.

To my dearest friends: Álex, David Galante, Diego, Fernán, Fernando, Luis Teira, Santiago, Sergio Gómez, and Sergio Varela. You mean a lot to me. Without those weekends I do not know what I would have done. Special thanks to Pablo Sende, our paths may join and separate, but you have been always there for me.

E finalmente, grazas a toda a miña familia. Sen dúbida teño unha familia extraordinaria, e non só polo número de membros. Quero dar as grazas especialmente aos meus pais, José Luis e María del Carmen. Aínda que nunca o diga, sabedes que estou incriblemente agradecido. Grazas ás miñas queridísimas irmás, sabedes como son, e sabedes que vos quero. Non podo rematar sen dar as grazas á miña avoa María. Avoa, grazas por tódolos teus consellos.

Abstract

A fascinating feature of eukaryotic cells is their ability to move. Cellular motility controls crucial biological processes such as, e.g., cellular nourishment, wound healing, tissue growth, pathogen removal, or metastatic disease. Cell migration through biological tissues is an exceedingly complex process, which is usually understood as a continuous cycle of five interdependent steps, namely: protrusion and elongation of the leading edge driven by actin polymerization; cell-matrix interaction and formation of focal contacts via transmembrane adhesion proteins; extracellular matrix degradation by cell surface proteases; actomyosin contraction generated by active myosin II bound to actin filaments; and detachment of the trailing edge and slow glide forward. Cell migration may be directed by different external stimuli perceived through the cell's membrane via membrane proteins. Those stimuli, which may take the form of chemical cues or changes in the physical properties of the environment, produce a cellular response that modifies the motile behavior of the cell. Moreover, motile cells may exhibit a number of morphological variants, called modes of migration, as a function of endogenous and exogenous factors such as, e.g., cell-cell and cell-extracellular matrix adhesion, extracellular matrix degradation, orientation of the extracellular matrix fibers, or the predominant cytoskeleton structure. The prominent modes of individual cell migration are mesenchymal, amoeboid, and blebbing motion. Cells can compensate the loss of a particular motile ability by developing migratory strategies, which include the transition between different modes of cell migration.

In this thesis we develop three mathematical models of individual cell migration. The models account for the interactions between the cytosolic, membrane, and extracellular compounds involved in cell motility. The motion of the cell is driven by the actin filament network, which is assumed to be a Newtonian fluid subject to forces caused by the cell motion machinery. Those forces are the surface tension of the membrane, cell-substrate adhesion, actin-driven protrusion, and myosin

contraction. Also, a repulsive force acting on the cell's membrane accounts for the interaction with obstacles, which may represent fibers or walls. The models are grounded on the phase-field method, which permits to solve the partial-differential equations posed on the different domains (i.e., the cytosol, the membrane, and the extracellular medium) by using a fixed mesh only. The solution of the higher-order equations derived from the phase-field theory entails a number of challenges. To overcome those challenges, we develop a numerical methodology based on isogeometric analysis, a generalization of the finite element method. For the spatial discretization we employ B-splines as basis functions, which possess higher-order continuity. We propose a time integration algorithm based on the generalized-α method.

The first model focuses on mesenchymal motion. The model proposes a novel description of the actin phase transformations based on a free-energy functional. The results show that the model effectively reproduces the behavior of actin in keratocytes. The simpler case of cell migration in flat surfaces produces stationary states of motion that are in good agreement with experiments. Also, by considering obstacles, we are able to reproduce complex modes of motion observed in microchannels, such as, e.g., oscillatory and bipedal motion.

The second model is used to analyze the spontaneous migration of amoeboid cells. The model accounts for a membrane-bound species that interacts with the cytosolic compounds. The model results show quantitative agreement with experiments of free and confined migration. These results suggest that coupling membrane and intracellular dynamics is crucial to understand amoeboid motion. We also show simulations of a cell moving in a three-dimensional fibrous environment, which we interpret as an initial step toward the computational study of cell migration in the extracellular matrix.

The third model focuses on chemotaxis of amoeboid cells. The model captures the interactions between the extracellular chemoattractant, the membrane-bound proteins, and the cytosolic components involved in the signaling pathway that originates cell motility. The two-dimensional results reproduce the main features of chemotactic motion. The simulations unveil a complicated interplay between the geometry of the cell's environment and the chemoattractant dynamics that tightly regulates cell motility. We also show three-dimensional simulations of chemotactic cells moving on planar substrates and fibrous networks. These examples may constitute a first approach to simulate cell migration through biological tissues.

Contents

List of Figures

List of Tables

List of Symbols

Abbreviations

CAD Computer aided design

DNA Deoxyribonucleic acid

ECM Extracellular matrix

EMT Epithelial-mesenchymal transition

FEA Finite element analysis

IGA Isogeometric analysis

LEGI Local excitation global inhibition

MAT Mesenchymal-amoeboid transition

MET Mesenchymal-epithelial transition

MMPs Matrix metalloproteases

MSD Mean squared displacement

NURBS Non-uniform B-splines

PDEs Partial differential equations

PIs Phosphoinositides

RNA Ribonucleic acid

Main variables of the mathematical models

δ_m Membrane marker

$\mathbf{u}$ F-actin network velocity

ϕ Phase field (cell marker)

ψ Extracellular marker

ρ_f F-actin

ρ_g G-actin

ρ_m Myosin

a Activator

q Chemoattractant

Main constants of the mathematical models

$\beta_{\overline{\nabla q}}$ Bias induced by chemoattractant gradient

$\beta_{\overline{q}}$ Bias induced by chemoattractant average concentration

$\beta_{\mathrm{R/L}}$ Pseudopod right/left bias

$\Delta\tau_i$ Pseudopod interval time

ΔT_i Pseudopod growth time

η_{rep} Strength of repulsive forces

γ Membrane surface tension

$\mathcal{N}$ Total actin

μ Dynamic viscosity

$\overline{\eta}_f$ Strength of protrusive forces

$\overline{\eta}_m$	Strength of contractile forces
$\overline{\nabla q}$	Chemoattractant gradient (signaling parameter)
$\overline{\rho}_f$	Density for lamellipodium/pseudopod tracking
$\overline{q}$	Chemoattractant average concentration (signaling parameter)
ρ_f^{pa}	F-actin passive concentration
ρ_f^{pr}	F-actin protrusive concentration
ρ_g^{eq}	G-actin equilibrium concentration
ε	Phase-field interfacial length scale
P_{PE}	Pseudopod extension probability

Chapter 1

Introduction

1.1 Motivation and research objective

Motivation

This thesis is part of the research developed by the Group of Numerical Methods in Engineering (GMNI) at *Universidade da Coruña* in the field of computational mechanics. The thesis expands the work done by other members of the group in the sub-field of computational biomechanics, under the project *Modeling and Simulation of Cancer Growth* (MuSIC). The project MuSIC aims at introducing predictive models for cancer growth that take the form of mathematical theories developed from first principles. The project also aims at proposing new numerical algorithms that permit to obtain fast and accurate simulations. In the following paragraphs, we illustrate the importance of cancer in the present days and reveal the relation between cancer growth and cell motility, in particular, cell crawling, which motivates the development of this thesis.

Cancer hallmarks Cancer is a group of diseases that share common characteristics: The uncontrolled proliferation of cells and their ability to invade other tissues and continue there with their abnormal proliferation (Alberts *et al.*, 2007). The origin of cancer is a cell that undergoes mutations, i.e., changes in its DNA. This process, called *carcinogenesis*, causes the cells become potentially malignant. Carcinogenesis is a complex multi-step process (Hanahan and Weinberg, 2000,

2011) that usually takes a long time, even decades, to be fully completed and needs more than one mutation to achieve its malignant phenotype (Loeb *et al.*, 2003). The reason for all those mutations is not fully understood. Therefore, we usually refer to factors rather than mutations themselves when speaking about cancer causes. These factors may be divided into exogenous factors (physical, chemical, or biological) and endogenous factors (produced by hereditary alterations in the DNA sequence). Once a cell has acquired certain capacities due to the mutations, it starts to proliferate. The daughter cells inherit those capacities and continue spreading, forming an avascular tumor or neoplasm and recruiting other cells in the nearby microenvironment —the stroma— using them to their own purposes. The avascular tumor grows until it reaches a stable limit above which it can not grow longer without an extra nutrient supply. Up to this point, if the tumor does not have the ability to invade the surrounding tissues, it is a benign, i.e., non-mortal, tumor.

Cancer cells can acquire the ability to induce the growth of new blood vessels and lymph capillaries from the existing vasculature (i.e., *angiogenesis*), thus destabilizing the tumor, allowing it to grow further, and providing it with routes to migrate to other tissues through the blood stream or the lymph, in a process known as *metastasis*. This avascular to vascular shift plays a critical role in cancer. The human body, as a multicellular organism, exerts a control to maintain a viable number of cells. However, cancer cells multiply ignoring the signals that the own body sends. They divide and proliferate into a mass that becomes denser while pushing all the neighbor host tissue cells and elements of the extracellular matrix (ECM), generating mechanical pressure. This pressure may be increased, reaching values that can lead to the loss of function of the organ in which the tumor is located, and eventually, causing death. Nowadays, the importance of cancer can be understood by the following facts (Torre *et al.*, 2015): Worldwide, one in seven deaths is caused by cancer. When countries are grouped according to economic development, cancer is the second leading cause of death in developed countries (following heart diseases) and the third leading cause in low- and middle-income countries. By 2030, the number of cancer cases and the number of cancer deaths are expected to increase $\sim$55%, simply due to the growth and aging of the population.

Cancer metastasis The term metastasis is defined as the transfer of disease from one organ or part to another not directly connected to it. Tumor metastasis is a multistage process during which malignant cells spread from the primary tumor to discontinuous organs. Malignant tumors rarely encapsulate, grow rapidly, and experience morphologic abnormalities that make the host tissue become unrecognizable. Malignant tumors also invade regional tissues and metastasize.

Metastasis involves a series of steps, dependent on both the intrinsic properties of the tumor cells and the host response. This process consists of sequential and interrelated steps, each of which can be rate limiting because a failure at any step may halt the process. In principle, the steps or events required for metastasis are the same for all tumors. The steps in the metastatic process (Talmadge and Fidler, 2010), which have been plotted in figure 1.1, are the following:

1. A slow and progressive growth of the neoplastic cells.
2. Angiogenesis: New vasculature is required to exceed a tumor of 1 to 2 mm. The synthesis and secretion of angiogenesis factors has a critical role in establishing a vascular network within the surrounding host tissue.
3. Local invasion of the host stroma by tumor cells.
4. Penetration into small blood and lymph vessels.
5. Formation of tumor cell aggregates: Tumor cells interact with cells in the circulatory system giving rise to emboli (small clumps of tumor cells that travel through the vascular system).
6. Circulation of these emboli within the vascular system.
7. Survival of tumor cells that trafficked through the circulatory system and arrest in a capillary bed.
8. Extravasation[1] of the tumor embolus by mechanisms similar to those involved in the initial tissue invasion.
9. Proliferation of the tumor cells within the organ parenchyma[2] resulting in a metastatic focus.
10. Establish new vasculature and defenses against host immune responses.
11. Restart the process for the development of metastases from metastases.

Therefore, the outgrowth of a metastatic lesion requires that it develops a vascular network, evades the host's immune response, and responds to organ-specific factors that influence growth. Thereafter, the tumor cells can again invade the host stroma, penetrate blood vessels, and enter the circulation to produce secondary metastases. Each step of the metastatic cascade is potentially rate limiting. The failure of a tumor cell to complete any step effectively impedes the attainment of the process. Thus, only a few cells in a primary tumor are believed to be able to give rise to a metastasis. Note that the presence of tumor cells distant from the primary tumor does not prove that metastasis has occurred. The arrest of circulating emboli in a

[1] Extravasation refers to the cells exiting the capillaries and entering the organs.
[2] Functional tissue of an organ.

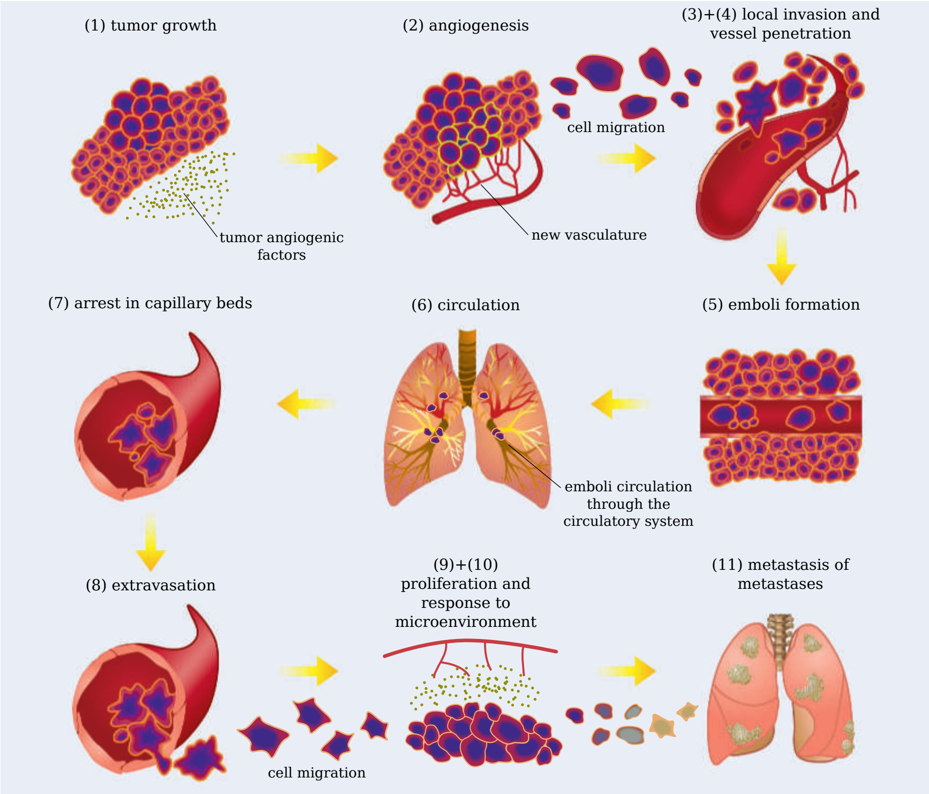

Figure 1.1. Sequential process of metastasis. *Cell migration occurs in steps* 3 *and* 8*. Each step of the metastatic cascade is potentially rate limiting. (Adapted from Talmadge and Fidler, 2010)*

capillary bed frequently results in cellular apoptosis or dormancy, rarely produces a clinically detectable metastasis.

Role of cell migration in cancer According to the metastatic cascade plotted in figure 1.1, cell motility has an outstanding role in two steps of the metastatic process. First, the invasion and infiltration of cancer cells into the surrounding normal host tissue. This step, achieved by the crawling motion of the cells, concludes with the penetration into small vascular or lymphatic channels; see steps 3 and 4 in figure 1.1. Second, the extravasation of tumor emboli and arrest in distant organs (step 8 in figure 1.1), which involves the migration of the tumor cells towards the location of the future metastatic focus.

More than 80% of human cancers are carcinomas, i.e., epithelial in origin (see subsection 1.2.1). A loss of normal epithelial tissue cohesion, which depends on cell-cell adhesion, is a prerequisite of cancer cell spread. Cell-cell adhesion of normal epithelial cells is mediated via members of the cadherin superfamily (to be introduced in subsection 1.2.2). In particular, E-cadherin is responsible for changes in cell shape and migratory activity. The loss of this protein is a common finding in the most aggressive and advanced carcinomas. The process of tumor invasion has been defined as a derangement in the proper sorting of cell populations, causing a violation of normal tissue boundaries. The three general mechanisms of tumor cell invasion (Hart, 2005) are:

- Mechanical pressure. This process may be analogous to the way plants force their roots through the soil. Cell invasion is simply a direct consequence of uncontrolled growth causing pressure from the growing tumor mass.
- Release of lytic enzymes[3]. Malignant tumors produce and secrete lytic enzymes capable of degrading normal tissue. These enzymes are capable of digesting proteins and components of the extracellular matrix. ECM degradation causes tissue damage and promotes tumor cell invasion.
- Increased motility of tumor cells. Tumor cells exhibit the same mechanisms of cellular migration used by healthy cells. However, the motile abilities of cancer cells are enhanced with respect to healthy cells. Cancer cells are able to move through normal tissues displaying a great number of migratory and invasive strategies. In addition, tumor cells can select and change to the most appropriate invasive strategy depending on the surrounding conditions.

All these ideas may be summed up in the concept of epithelial-mesenchymal transition (EMT). EMT results in the loss of epithelial properties, including cell-cell adhesion, and the gain of motile properties that increase the ability to migrate through different tissues and the extracellular matrix. The bases of cell motility and the different migratory mechanisms will be treated in detail in section 1.2.

Objectives

The main goal of the thesis is to model and simulate the crawling motion of cells. Under this general objective, a number of particular research objectives can be summarized in the following points:

- **Modeling:** The goal is to develop models that account for the dynamics of the cytosolic compounds that drive cell motion. The cytosolic compounds are controlled by a set of signaling proteins whose reactions are triggered

[3] Enzymes are substances that accelerate chemical reactions.

by membrane molecules. Thus, the coupling between the cytosol and the membrane must be addressed. We also aim at modeling the movement of the cells in three-dimensional fibrous environments that mimic the extracellular matrix. The first step to reach this goal is the incorporation of rigid obstacles to the model using a continuum approach. Cells not only interact with the ECM, but also with extracellular substances that may direct the movement of the cells. Coupling the dynamics of the extracellular substances to the cell's membrane, and also to the extracellular fibers, constitutes another goal of this thesis.

- **Developing numerical algorithms:** The tracking of moving domains poses a number of computational challenges. We resort to an emerging technology (the phase-field or diffuse domain method; see Gomez and van der Zee, 2017) that permits to reformulate problems with interfaces as partial-differential equations on fixed domains. Phase-field models usually include high-order partial differential equations. To overcome this limitation, we make use of isogeometric analysis (IGA) (Hughes *et al.*, 2005). IGA is a finite element method that uses B-splines or non-uniform B-splines (NURBS), which have controllable global continuity, as basis functions. The objective is to develop a robust numerical algorithm that solves the proposed phase-field models efficiently. In addition, the description of the phase field (it takes the value 0 outside the cell) produces ill-conditioned systems. Thus, we also aim at proposing efficient methodologies that lead to well-conditioned systems. To reach this objective, we build a code on top of PetIGA (Dalcin *et al.*, 2016), which adds NURBS discretization capabilities and integration of forms to the scientific library PETSc (Balay *et al.*, 2016) and allows for parallel implementation.

- **Application:** The first objective here is to test the proposed models and computational methods by comparing two-dimensional results of mesenchymal and amoeboid migration with experiments. We also aim at unveiling the complex interplay between the membrane and the cytosolic compounds. In particular, two-dimensional simulations of cells in microchannels and environments with obstacles may provide insight into the cytosol-membrane interactions. Another goal is to simulate chemotaxis and study the influence of the environment (i.e., the ECM geometry) and the cell itself on the dynamics of the chemoattractant, and vice versa. The final objective is to perform three-dimensional simulations of cells moving on planar substrates and within fibrous environments. Cell motion on a planar substrate is usually analyzed using two-dimensional models, but the three-dimensional approach may enable a better understanding of the dynamics of the substrate-cell adhesions. In case of the fibrous environment, the three-dimensional simulations may constitute the first approach to study cell migration in the ECM.

1.2 Cell crawling: unraveling the biomechanical process

Cell motion is a prerequisite for life. Motion manifests itself at different scales, e.g., subcellular, cellular, and tissue scales. There are cells that swim using cilia or flagella, but most eukaryotic cells move across solid media, such as, e.g., the extracellular matrix or epithelial tissue. The latter kind of cell migration is known as cell crawling, the subject of this thesis. Hereinafter in this thesis, by cell migration we refer to the crawling movement of cells in solid environments.

Cellular motion is a tightly regulated action that plays a crucial role in several biological processes such as tissue formation, wound healing, and immune response. Thus, it is not surprising that an abnormal behavior of motile cells may lead to serious conditions, including vascular disease and cancer metastasis. The mechanisms that drive cancer cell migration are analogous to those of healthy cells (Friedl and Wolf, 2003). In this section, we study the mechanisms that produce cell motion and highlight the special features for the case of tumor cells. Beforehand, we provide a biological background of the cell and the environment where cell migration occurs.

1.2.1 The eukaryotic cell

Eukaryotic cells (see figure 1.2) may be distinguished from other type of cells by their nucleus, a membrane-enclosed intracellular compartment where DNA is kept. Eukaryotic cells also have a cytoskeleton that provides support and drives movement, as well as intracellular compartments that carry out diverse metabolic functions. The metabolism of this kind of cells depends on the oxidation of organic molecules. Most of the dry mass of a cell consists of macromolecules that have been produced as linear polymers of amino acids (proteins) or nucleotides (DNA and RNA).

Proteins Proteins are the principal catalysts for most of the chemical reactions occurring in the cell. Proteins also accomplish the selective transport of small molecules across the cell membrane. The main features of proteins (Alberts *et al.*, 2007) can be summarized as follows:

- Shape and structure: Proteins are composed of modular units, called domains, which display a globular shape. The domains usually contain from 40 to 350 amino acids. Small proteins typically consist of a single domain only, while large proteins are composed of several domains connected together.

- Regulation of cell processes: Proteins reversibly change their shape when a ligand binds to their surface. The changes in protein conformation produced by one ligand may affect the binding of a second ligand. This relation between the two ligand-binding sites provides a crucial mechanism for regulating many cell processes. For example, many metabolic pathways are controlled by feedback regulation: some molecules inhibit, while others activate, certain enzymes early in a pathway. This mechanism permits the enzymes to create a steep response.

- Worker and messenger: Chemical energy can drive changes in the shape of the protein, which allow proteins to do useful work. For example, some proteins can generate a mechanical force and also move long distances (e.g., the myosin family; see subsection 1.2.2). Other proteins can work as input-output devices that transport information (e.g., membrane receptors or pro-nucleation factors; see subsection 1.2.2).

Genetic information The genetic information is stored in the DNA. The genetic information contains the instructions for all the proteins the organism will ever synthesize.

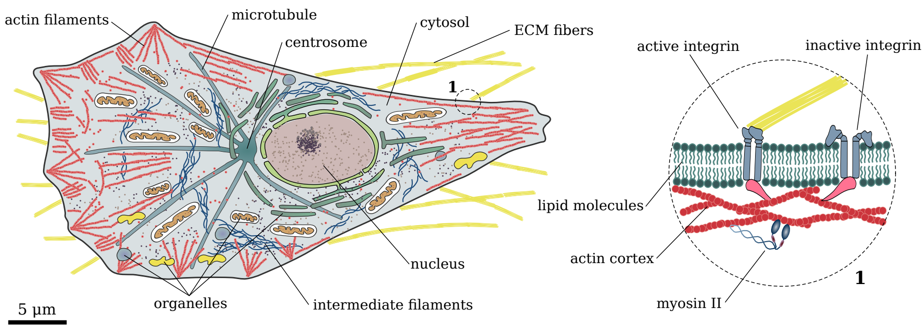

Figure 1.2. The eukaryotic cell. *Schematic representation of an eukaryotic cell. Inset* 1 *shows a detailed view of the cell membrane. (Adapted from Alberts* et al.*, 2007)*

The cell membrane The membrane of the cell consists of a continuous double layer of lipid molecules in which the membrane proteins are embedded (see inset 1 in figure 1.2). In the in-plane direction, the lipid bilayer may be treated as a fluid, where the individual lipid molecules are able to diffuse rapidly within their own monolayer. The lipid molecules are amphiphilic[4]. They assemble into bilayers, which form closed compartments. The compositions of the inner and outer monolayers are different, reflecting the different functions of the two faces of the cell membrane (Alberts *et al.*, 2007). Whereas the lipid bilayer determines the basic structure of the biological membrane, the membrane proteins are responsible for most of the membrane functions (e.g., transduction of extracellular signals or cell-cell and cell-ECM adhesion). Many membrane proteins are able to diffuse rapidly in the plane of the membrane. However, cells can immobilize specific membrane proteins, and also confine other proteins to certain regions of the lipid bilayer, causing the polarization of the cell (the concept of polarization will be introduced in subsection 1.2.3).

Cytoplasm, cytosol, and organelles The cytoplasm comprises the cytosol and the organelles (see figure 1.2). The cytosol, or intracellular fluid, is a complex mixture of substances dissolved in water located in the cell's interior. The cytosol consists mostly of water, dissolved ions, small molecules, and large water-soluble molecules such as proteins. The compounds of the cytosol are not necessarily mixed randomly inside the cell. There are several levels of organization that may cause the location of certain components in specific regions within the cytosol (Alberts *et al.*, 2007). The eukaryotic cell is subdivided into functionally distinct membrane-enclosed compartments. Each compartment, or organelle, contains its own characteristic set of enzymes and other specialized molecules. Thus, each organelle displays a different structural organization. On average, the membrane-enclosed compartments together occupy nearly half the volume of the cell. The cytosol constitutes the other half. The cytoskeleton is a cellular scaffolding or skeleton that plays important roles in both intracellular transport, cellular division, and cell motility. The membrane-enclosed organelles often have characteristic positions in the cytosol, which depend on the interactions between the organelles and the cytoskeleton. We will study in detail the properties of the cytoskeleton in subsection 1.2.2, since it is one of the main elements involved in cell motility.

Cellular organization, body tissues Tissue is a cellular organizational level intermediate between cells and organs. A tissue is an aggregate of similar cells

[4]The lipid molecules possess one end with hydrophilic properties and the other end with hydrophobic properties.

that have the same origin and together carry out a specific function. Animal tissues can be grouped into four basic types:

- Connective tissue supports, connects, and separates different types of tissues and organs of the body. The ECM, which is comprised by a collection of extracellular molecules secreted by cells, belongs to this kind of tissue.
- Nervous tissue is the main component of the nervous system.
- Muscle tissue is a soft tissue that composes muscles and provides the ability to contract. It may be divided in skeletal, smooth, and cardiac muscle.
- Epithelial tissue lines the cavities and surfaces of the structures throughout the body. The main functions of epithelial tissue include secretion of substances, selective absorption, protection, and transcellular transport. Epithelial layers are avascular. They must receive nourishment via diffusion of substances from the underlying connective tissue.

1.2.2 Constituents of cell motility

In this section, we introduce the main elements that take part in cell motion. As we will see in subsection 1.2.3, cell migration arises as a result of complex interactions between these elements.

Cytoskeleton

The cytoplasm of the cell is spatially organized by a network of protein filaments known as the cytoskeleton (Alberts *et al.*, 2007). Other functions performed by the cytoskeleton are cell division, cell polarity, cell motility, and providing a stable shape to the cell. The cytoskeleton is composed of three types of filaments (see figures 1.2 and 1.3):

- **Actin filaments:** Two-stranded helical polymers comprised by the protein actin. They are flexible structures with a diameter of 7 to 9 nm. Actin

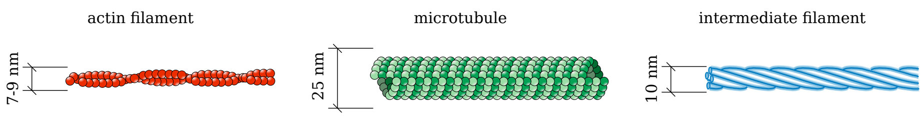

Figure 1.3. The cytoskeleton filaments. *Actin filaments, microtubules, and intermediate filaments. (Adapted from Alberts* et al.*, 2007)*

filaments are organized into a variety of linear bundles, two-dimensional networks, and three-dimensional gels.

- **Microtubules:** Long and hollow cylinders with an external diameter of 25 nm made of the protein tubulin. They are usually organized with one end attached to a single microtubule-organizing center, called centrosome (see figure 1.2).
- **Intermediate filaments:** Ropelike fibers with a diameter of 10 nm. They are made of intermediate filament proteins, which constitute a large and heterogeneous family of proteins. Each member of the intermediate filament family is in charge of different functions, such as, e.g., provide mechanical strength or span the cell junctions.

Henceforth, we focus on actin filaments and microtubules, since intermediate filaments play a secondary role in cell motility. Microtubules and actin filaments are made up of smaller subunits that are compact and globular. The small subunits are called actin subunits (G-actin) for actin filaments (F-actin), and tubulin subunits for the case of microtubules. The subunits can diffuse rapidly within the cytosol. However, the assembled filaments belong to a network that is attached at some point of the cell. Cells are able to undergo rapid structural reorganizations by disassembling filaments at certain regions of the cell and reassembling new filaments in other regions. The filaments are stable and resistant because they are built out of multiple protofilaments (long and linear strings of joint subunits). The protofilaments are associated laterally and twisted around in a helical lattice, as shown in figure 1.3.

Polymerization is the process where small molecules assemble into filaments. We can distinguish three stages in the process of polymerization: (1) Nucleation. The process begins with the assembly of few subunits creating a short oligomer[5]. (2) Elongation. The subunits rapidly assemble to the ends of the nucleated filaments. (3) Steady state. The rate of addition of new subunits to the end of the filament balances the rate of dissociation. The filament subunits can be found in two different states depending on the binding of nucleotides[6]. Each subunit state assembles to one end of the filament. Thus, the behavior of each end of the filament is different, i.e., the filaments are polar. In particular, the rate constants for association and dissociation are greater in one end (the plus end) than in the other (the minus end).

Note that, as we show in subsection 1.2.3, compared to microtubules, actin filaments play the principal role in the modes of cell migration studied in this thesis.

[5] An oligomer is a molecular complex comprised of few monomer units. In contrast, the term polymer considers an unlimited number of monomers.

[6] In this context, nucleotides are organic molecules that carry packages of chemical energy.

Hence, most of the elements related to cell motion explained in the following paragraphs are related to actin filaments.

Accessory proteins

By accessory proteins we refer to hundreds of proteins that regulate the spatial organization and the dynamic behavior of the filaments. The response of these cytoskeleton-associated proteins is dictated by extracellular and intracellular signals. The accessory proteins modify the behavior of filaments and subunits by binding to them. The proteins are able to determine the location of assembly of new filaments and regulate the division of the filaments. They also can change the kinetics of filament assembly and disassembly, and link filaments to other filaments or other cell structures. Below, we list the main accessory proteins that control the behavior of actin filaments. Note that similar proteins control microtubules dynamics and organization.

- Arp2/3 complex: Serves as nucleation sites for new actin filaments. The complex binds to an existing filament and initiates the growth of a new filament that forms $\sim 70°$ with the existing filament.
- Formin: Nucleates the growth of straight and unbranched filaments. These filaments can be cross-linked by other proteins to form parallel bundles.
- Thymosin: Binds to G-actin, impeding the assembly of those G-actin monomers. Thus, thymosin impedes polymerization.
- Profilin: Binds to the face of the actin monomer that associates with the filament minus end. Therefore, G-actin can only assemble to the plus end of the filaments.
- Trompomyosin: Binds simultaneously to seven adjacent actin subunits in one protofilament. Thus, trompomyosin stabilizes the filament by preventing the interaction with other proteins.
- Cofilin: Desestabilizes actin filaments and accelerates disassembly.
- Capping proteins: Prevent assembly and disassembly at the plus end.
- Bundling proteins: Cross-link actin filaments into a parallel array. Some examples of this group of proteins are fimbrin and α-actinin.
- Gel-forming proteins: Hold two actin filaments together. The filaments form a large angle. The networks created by these proteins are loose. Some examples of this kind of proteins are filamin and spectrin.
- ERM proteins: Cross-link actin filaments with the plasma membrane.

Molecular motors

Some kinds of proteins are able to bind to a cytoskeleton filament and move steadily along it. These proteins are called motor proteins, or molecular motors, and achieve movement from the energy derived from repeated cycles of ATP hydrolysis[7]. The functions of the molecular motors are the displacement of organelles within the cell and the movement of the cell. Molecular motors can be classified according to the filament they bind to. Thus, we distinguish three families of molecular motors: myosin (moves on F-actin), kinesin, and dynein (both move on microtubules).

Let us focus on the myosin family, in particular, on myosin II, the molecular motor that generates all the contractile activity in motile cells. The myosin II molecule is composed of two heavy chains (see inset 1 in figure 1.2). Each chain has a globular head domain followed by a very long amino acid sequence. The myosin head, which moves along the actin filament, contains the force-generating machinery. On the other hand, the tail forms a long coiled-coil that may bundle with the tails of other myosin molecules. Myosin II achieves movement through the following mechanochemical cycle (Alberts *et al.*, 2007):

1. The myosin head is tightly attached to the actin filament.

2. A molecule of ATP binds to the myosin head and reduces the head-actin affinity.

3. The hydrolysis of ATP occurs. The inorganic phosphate produced in the reaction remains bound to the head. The reaction triggers a large shape change that produces the displacement ($\sim 5\,\text{nm}$) of the head along the filament.

4. The inorganic phosphate is released producing the tight binding of the head to the actin filament in a new site. The head recovers its original shape right after the release of the phosphate.

5. The cycle begins again with the myosin head moved to a new position in the filament.

The head remains bound to the actin filament around 5% of the cycle time. Thus, a group of linked myosins can work together in a single actin filament increasing the rate of displacement (up to 20 times with respect to a single myosin).

[7] ATP hydrolysis is a molecular reaction that produces mechanical energy from chemical energy.

Basal lamina and extracellular matrix

The basal lamina is a layer of the ECM secreted by epithelial cells. The basal lamina separates the epithelium from the underlying connective tissue, and also constitutes the mechanical connection between them; see figure 1.4. The basal lamina works as a selective filter, establishes cell polarity, and may influence the metabolism of the cells. The basal lamina also promotes cell survival, proliferation, or differentiation, and it is the substrate where cells migrate. The basal lamina is mostly composed of fibrous proteins (glycoproteins), which may be divided in: (1) Laminin: a large and flexible protein that is the main component of the basal lamina. (2) Collagen IV: molecules that assemble into a flexible and felt-like network that provides tensile strength. (3) Nidogen and perlecan: secondary proteins that connect the networks of laminin and collagen IV.

The ECM is an intricate network of macromolecules assembled into an organized mesh. The network is tightly connected to the cells that produce the macromolecules. The main component of the ECM is the polysaccharide chain named glycosaminoglycn (GAG). GAGs usually create a highly hydrated gel-like substance where the fibrous proteins are embedded. The gel provides resistance to compressive forces and also permits the rapid diffusion of nutrients through the network. The main fibrous proteins that comprise the ECM and their functions are: (1) Collagen: gives tensile strength and organizes the matrix. (2) Elastin: provides elasticity and resilience. (3) Fibronectin: has multiple binding sites for the molecules responsible of cell adhesion. Cells migrating through the ECM are totally embedded in it. The ECM not only serves as a medium for migration, but also has direct consequences on the shape, polarity, and mode of migration of the cells, as we show in subsection 1.2.3.

Cell adhesion

Cell-cell and cell-ECM junctions are diverse, but can be classified according to the function they perform in four groups: (1) The anchoring junctions transmit stresses and are connected to the cytoskeleton filaments inside the cell. (2) The occluding junctions seal the gaps between cells in epithelia. (3) The channel-forming junctions create passegeways connecting the cytosol of adjacent cells. (4) The signal-relaying junctions allow signal transduction across the cell membrane. If we focus our study on cell migration, two superfamilies of transmembrane proteins play a prominent role in adhesion and signaling transduction: the cadherin and the integrin superfamilies (represented schematically in figure 1.4).

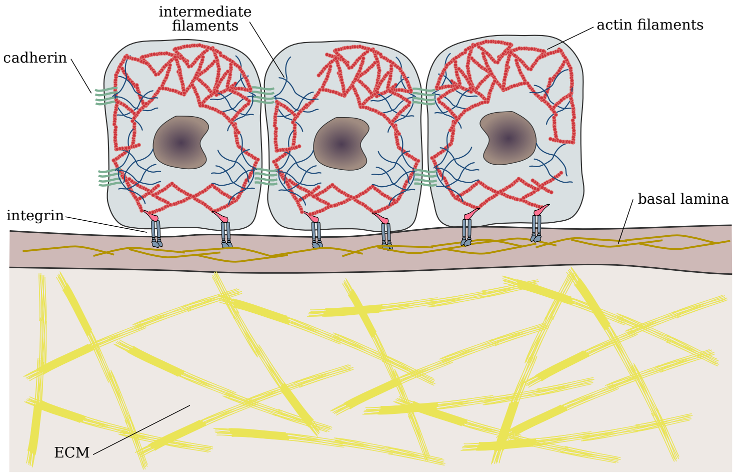

Figure 1.4. Basal lamina and extracellular matrix. *The basal lamina separates the epithelium from the underlying connective tissue. Cadherins mediate cell-cell adhesion. Integrins mediate cell-ECM adhesion.*

Cadherin and cell-cell adhesion The cadherin family mediates homophilic adhesions, that is, symmetric junctions. Cadherin usually binds to other members of its family with relatively low affinity. Strong attachments are achieved by the formation of many individual bonds in parallel. This behavior also applies to integrin in cell-ECM adhesion. The homophilic property of cadherins plays an outstanding role in tissue segregation and tissue sorting. Cadherins are also involved in processes such as contact guidance, chemotaxis, and tissue assembly. The connection between cadherins and the cytoskeleton filaments is not direct, but mediated by a cluster of accessory proteins. The proteins of the cluster are located inside the cell and connect the tail of the cadherin to the filament.

Integrin and cell-ECM adhesion Integrin is the main family of cellular receptors. Integrins are able to bind to most ECM proteins. Besides the anchoring function, integrins can also transmit signals in both directions across the cell membrane. An integrin molecule is composed of two associated glycoprotein subunits, called α and β. Both subunits span the cell membrane. Outside the cell, integrin binds to specific amino acid sequences such as laminin of fibronectin. Inside the cell, integrin binds to a complex of proteins (similar to the cluster of accessory proteins of cadherins) that is connected to the cytoskeleton. In case of integrin-actin filament binding, the main compounds of the cluster are talin and vinculin. Integrin molecules may be found in an active or an inactive state (see inset 1 in figure 1.2). Integrins are prepared for attachment only when active. The activation of integrins can be done by two modes: (1) Outside-in activation: caused by an extracellular ligand that binds to integrin. In this case, talin is exposed and allows the connection to the actin filament. (2) Inside-out activation: triggered by intracellular regulatory molecules that activate talin, and consequently, integrin. The extracellular ligands and the intracellular regulatory molecules are produced in response to signals generated by other cells or by the cell itself. The crosstalk between these signaling pathways permits complex interactions between the cell and its physical and chemical environment. Thus, cell growth, proliferation, and survival depend on the presence of a substrate (the basal lamina or the ECM) and are mediated by integrins.

Actin cortex

The actin cortex is a thin network composed of actin filaments, myosin motors, and actin-binding proteins that lies directly beneath the plasma membrane (Chugh *et al.*, 2017); see figure 1.2. The actomyosin cortex is attached to the cell membrane via ERM proteins. The stresses generated in the cortex by the myosin activity produce contractile tension that modifies the properties of the cell membrane, specially, the surface tension of the cell. Changes in the mechanical properties of the cortex are involved in cellular processes such as, e.g., cell division, tissue morphogenesis, and cell migration.

Membrane receptors

Membrane receptors are transmembrane proteins that mediate the communication between cells and their environment. They also undergo complex interactions within the plasma membrane, including other membrane proteins such as integrin or cadherin. Receptors detect extracellular signals and trigger intracellular signal transduction pathways that control the cellular response to those signals. The signal transduction process is initiated by an extracellular molecule, known as ligand, that binds to the extracellular domain of the receptor. The receptor can undergo morphological changes or chemical reactions that produce the activation of intracellular proteins, which modifies the cell's behavior. Receptors are key elements in the migration of cells directed by external signals.

Proteases

By proteases we refer to any kind of enzyme that is able to perform proteolysis, that is, the breakdown of proteins in smaller amino acids. The main proteases involved in ECM degradation are metalloproteases-desintegrin and matrix metalloproteases (MMPs). As we show in subsection 1.2.3, MMPs have an outstanding role in cell migration and tumor invasion (Chang and Werb, 2001). They modulate the extracellular microenvironment providing new escape routes for the cells.

1.2.3 Cell migration

Cell migration is a complex multistep process where cells can utilize different strategies to accomplish movement. In this section, we aim at unveiling the biomechanical processes that orchestrate cell motion, and also, the diverse strategies developed by the motile cells.

Molecular mechanisms

Cell crawling is a multistep process that involves the integration and coordination of complex biochemomechanical signals. Cell motion can be initiated by chemical and physical factors in the cell environment, but some cells also can undergo spontaneous migration. Individual cell migration is explained by the five-step model (Friedl and Wolf, 2003) plotted in figure 1.5. The closely coordinated steps of the model are the following:

1. **Protrusion of the leading edge.** Actin filaments assemble and push the cell membrane outwards. Different kinds of protrusive structures may be generated: filopodia (one-dimensional protrusions), lamellipodia (sheet-like structures), or pseudopodia (three-dimensional protrusions). Cell protrusion involves the polymerization of F-actin underneath the membrane. The plus ends face forward, whereas the minus ends are usually attached to the sides of other F-actin by Arp2/3 complex. By assembling, the filaments push the membrane and generate a protrusive force.

2. **Cell-matrix interaction and formation of focal contacts.** Integrins mediate cell-ECM adhesion. Integrins bind to ECM ligands at the leading edge of the cell, followed by the clustering of integrins and the recruitment of signaling proteins. This process leads to the formation of focal adhesions, which are multiprotein structures that cover more than $1\,\mu m^2$ and regulate the cell response depending on the adhesion to the ECM. The focal adhesions

serve as anchoring points for force transmission and also coordinate cell motility through multiple signaling pathways.

3. **ECM degradation.** Proteolysis of the ECM by recruitment of surface proteases. Proteases degrade ECM components to create active soluble MMPs. ECM degradation is likely to provide the space required for cell expansion and migration.

4. **Cell contraction by actomyosin.** Myosin II binds to actin filaments forming a network known as actomyosin network. Myosin causes the contraction of the actomyosin network. Actomyosin contraction is located at the rear and central part of the cell. The contraction generates the forces necessary for cell motion. These forces are transmitted to the cell substrate through the actin cytoskeleton and the adhesion points.

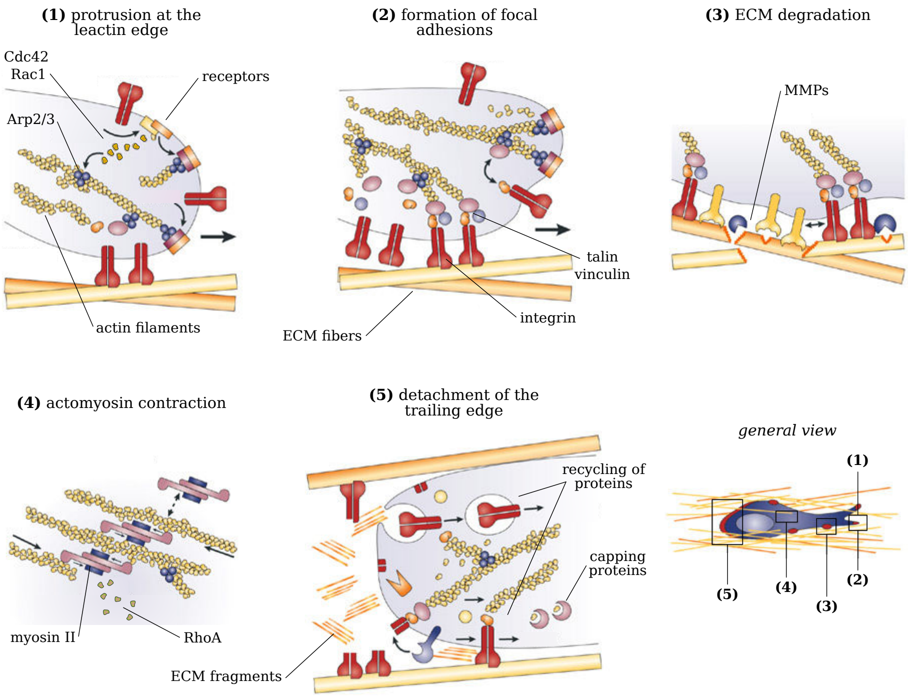

Figure 1.5. Five-step model of cell migration. *The steps are closely coordinated and correspond to cell motion through the ECM. In case of migration on a planar surface (e.g., the basal lamina) the steps are analogous with the exception of ECM degration, which does not occur. (Adapted from Friedl and Wolf, 2003)*

5. **Detachment of the trailing edge.** Focal contacts disassemble at the trailing edge. Since the front adhesion points are tightly attached, the actomyosin contraction produces the displacement of the cell body towards the leading edge.

The process can be summed up as the extension of F-actin structures that touch the ECM and initiate binding via integrin molecules. Integrins cluster and develop a small focal complex. The small focal complex can grow, stabilize, and form focal adhesions, which also regulate cell motility. Focal adhesions lead to the recruitment of proteases that degrade the ECM compounds located in the vicinity of the cell surface. ECM degradation facilitates the extension of protrusions at the front of the cell. At the same time, the actomyosin network undergoes contraction at the back of the cell. The extension of protrusions at the cell's front and the retraction of the cell's back cause the motion of the cell.

The multistep model of cell migration presented above applies to tumor cells (Clark *et al.*, 2000; Flanagan *et al.*, 2001; Koblinski *et al.*, 2000). Cancer cell motility involves integrin signaling, focal adhesion formation, and actomyosin-dependent contraction. ECM-degrading enzymes, such as MMPs, are frequently upregulated in tumor cells. Thus, the basic migration machinery of normal cells is retained in tumor cells.

Regulation of cell motion

The cellular response to temporal and spatial gradients of extracellular signals causes specific molecular events in different regions of the cell. The spatially distinctive molecular accumulation inside the cells, usually a front-back distinction, is known as *cell polarity* (Otsuji *et al.*, 2007). Significant progress (Dawes and Edelstein-Keshet, 2007; Swaney *et al.*, 2010; Van Haastert and Devreotes, 2004) has been made to uncover the interactions between the different signaling pathways, also known as modules. The modules can be classified according to their main compound, namely, phosphoinositides (PIs), their phosphatases, and the Rho GTPases. A detailed study of the reactions and interplays between the different modules is beyond the scope of this thesis. However, a brief description of one of these modules may be enough to illustrate the mechanisms of regulation of cell motility. Let us focus on the Rho GTPases, a family of small signaling G proteins and key regulators of cell motility (Mori *et al.*, 2008). The main members of the Rho GTPases family involved in cell motility are the Cdc42, Rac1, and RhoA proteins. Rho proteins are evenly distributed in a resting and unpolarized cell. When the cell receives a signal that induces motion, Rho proteins reorganize spatially, such that Cdc42 and Rac1 are located at the cell's front and RhoA at the cell's back. These proteins can exchange between a membrane-bound state and a cytosolic state, which permits a rapid diffusion throughout the cell. Cdc42 and Rac1 promote actin polymerization. In particular, activate the Arp2/3 complex, underregulate cofilin, and inhibit the contractile ability of myosin. The activation of Cdc42 and Rac1 is done by members of the PIs module, which are initially activated by membrane receptors (including integrins) or other intracellular compounds. An example of the complex interconnections between the different modules is the local activation of Rac1, which is maintained and amplified by several feedback loops between compounds of the PIs and Rho modules. RhoA, located at the back of the cell, promotes both the bundling of F-actin via formin and the clustering of integrins and their associated proteins to create focal adhesions. Note that also feedback loops between members of the same signaling pathway may control cell polarity. For example, Cdc42-Rac1 activation, as well as Rac1-RhoA and Cdc42-RhoA inhibition are observed in motile cells (Dawes and Edelstein-Keshet, 2007). The mechanisms of cell regulation vary depending on the cell type and the mode of migration displayed by the cell.

Directed motion An outstanding feature of motile cells is their ability to perceive external stimuli that can direct their motion. The external stimuli are usually sensed by membrane proteins that process the signals and trigger a set of reactions in the cytosol. Some examples of directed cellular motion are:

- **Chemotaxis:** The movement of cells guided by chemical cues. The extracellular ligand binds to the membrane receptors. Variations in the number of bound receptors produce the reactions between the different signaling pathways that generate a chemotactic response (Van Haastert and Devreotes, 2004).

- **Haptotaxis:** Cell migration driven by a gradient of cellular adhesion sites in the ECM or the substrate where migration takes place. The maximum speed is attained at intermediate levels of adhesiveness (Barnhart *et al.*, 2011). Therefore, cells move towards regions of optimal density of adhesion sites.

- **Durotaxis:** The velocity and direction of the moving cell depends on the rigidity of the substrate. Cells usually tend to migrate to stiffer substrates because stronger forces can be transmitted through the focal adhesions. Like in haptotaxis, there may be an optimal substrate rigidity that maximizes cell speed (Discher *et al.*, 2005).

- **Mechanotaxis:** The directed movement of cells via mechanical cues. The mechanical strain can be sensed by cell adhesion receptors, i.e., integrins and cadherins. Apart from the integrin- and cadherin-mediated signaling, the surface tension on the cell membrane and the stress on the cytoskeleton may also regulate cell motility.

- **Others:** electrotaxis (Cortese *et al.*, 2014), tensotaxis (Bueno *et al.*, 2017), etc.

Diversity in cell migration

Friedl and Wolf (2009) classify the types of cell migration in individual and collective migration. Each type of cell migration displays different morphological variants based, among other factors, on the cell type, the level of integrin engagement, the predominant cytoskeleton structure, and the production of proteases. The morphological variants are denoted as *modes of cell migration* (see figure 1.6), and are the following:

- **Mesenchymal migration.** Individual cell migration that presents high levels of cell-ECM adhesion and cytoskeleton contractility. These cells also present focalized cell-ECM interaction, including ECM degradation, and a fibroblast-like shape. The movement of mesenchymal cells follows the five-step model explained above.

- **Amoeboid migration.** Individual migration of elongated cells that translocate via rapid extensions and retractions of the membrane. The extensions are caused by dynamic actin-rich structures that get entangled in the ECM. These cells usually lack stress fibers, focalized proteolytic activity, and mature focal adhesions (i.e., they display low adhesion to the substrate).

- **Blebbing migration.** Individual cell migration similar to amoeboid motion. Blebbing cells acquire a more rounded shape and the extensions are caused by blebs. Blebs (Charras and Paluch, 2008) are rounded protrusions of the cell membrane produced by the increase of the intracellular cytosolic pressure along with the disruption of the membrane-actin cortex connection. Contrary to the previous modes of migration, membrane protrusions are not driven by cytoskeleton structures.

- **Chain migration.** Cells stream one after another in a strand-like fashion. It is not considered a collective, but a multicellular mode of migration. The strand is generated by the first invading cell that remodels the ECM. The rest of the cells transiently form and disrupt cell-cell contacts while moving along the track.

- **Collective migration.** The cytoskeletons of different cells can be connected via cell-cell adhesion. The formation of these anchoring junctions leads to a

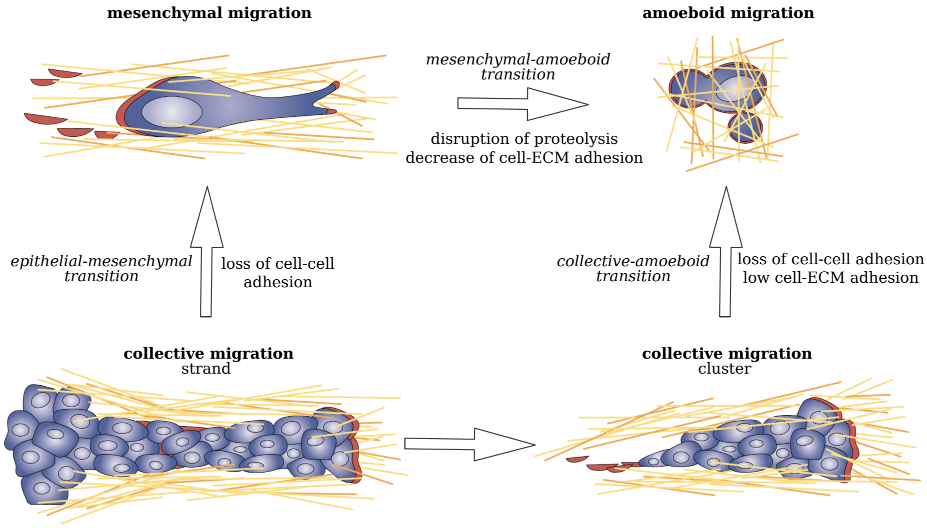

Figure 1.6. Modes of cell migration. *Different modes of individual and collective cell migration. Cells can undergo transitions between different modes of migration. A transition implies an adaptive response to changes in the factors that control the modes of migration. We have indicated the main transitions observed in cell motility. Note that transitions are bidirectional processes (not indicated in the figure). (Adapted from Friedl and Wolf, 2003)*

large and multicellular body that moves as a functional unit. In the body, highly motile cells located at the front produce the migratory traction. In contrast, the inner and trailing cells are passively dragged behind. We can observe two kinds of collective migration:

1. **Strand.** The protruding body maintains contact with the original location while invading the surrounding tissue.

2. **Cluster.** The group of cells detaches from the original tissue.

Individual tumor cells have been identified as the main cause for dissemination and metastasis. However, collective invasion predominates in highly differentiated tumors. Moreover, tumor cells can compensate the loss of a particular motile ability by developing migratory escape strategies, which include the transition between different modes of cell migration. This adaptive response, known as *plasticity*, is analyzed in the next section.

Plasticity of cell migration

Each type of cell displays a particular *default* mode of migration. If any of the factors that determine the mode of migration is altered, the cell could stop. However, cells may modify the mode of migration showing an adaptive response. The adaptive response is known as plasticity (Te Boekhorst *et al.*, 2016) and applies to healthy and cancer cells, though the response is enhanced in case of tumor cells. There are several factors that control the mode of cell migration. The list of factors presented in the previous section is expanded with the following factors (Friedl and Wolf, 2009): The type of extracellular environment, the density and orientation of the ECM fibers, the ECM stiffness, the cell-cell and cell-ECM adhesion, and the mode of force generation. The cells may alter the mode of migration as an escape strategy in a process known as *transition*. The main transitions involved in cell invasion (some of them are shown in figure 1.6) are the following:

Epithelial-Mesenchymal Transition (EMT) EMT is a biological process where a polarized epithelial cell undergoes multiple biochemical changes that make the cell acquire a mesenchymal phenotype (Thiery, 2002). The molecular processes that initiate the EMT are triggered by EMT-inducing signals. In the case of tumors, these signals are usually released by the tumor stroma. The EMT involves the loss of the epithelial cell polarity and the detachment from the basal lamina. The loss of cell-cell adhesion, which is regulated by E-cadherins, plays a crucial role not only in the EMT but also in the metastatic process. The composition of the basal lamina is modified. The changes in the basal lamina readjust the interactions between the cell and the ECM and activate different signaling pathways. The emerging proteolytic activity produces interstitial forms in the basal lamina, which enable the penetration of the cells. Finally, the cell assumes a mesenchymal phenotype and starts its migration, as shown in figure 1.7.

Mesenchymal-Amoeboid Transition (MAT) Cells can experience the transition from a mesenchymal to an amoeboid phenotype. This transition produces a change in the cell's morphology, the distribution of integrins, and the organization of the actin cytoskeleton. The main factors that cause MAT are the following:

1. Disruption of proteolysis. MAT may be a compensatory mechanism after the inhibition of the ECM proteolysis. Cells acquire the ability to undergo non-proteolytic amoeboid migration.

2. Decrease of cell-ECM adhesion. The disruption of integrin-mediated adhesion makes cells to acquire a spherical morphology which, in most cases, is

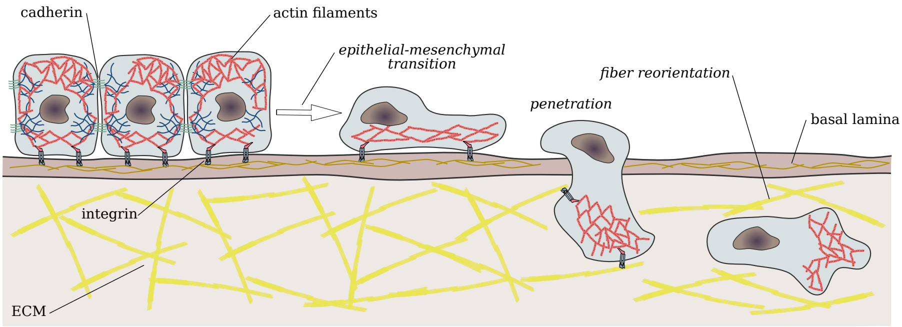

Figure 1.7. Ephitelial-mesenchymal transition. *Epithelial cells lose cell-cell adhesion and undergo the epithelial-mesenchymal transition. Mesenchymal migration in the ECM causes fiber degradation and reorientation.*

unable to achieve motion. The gain of amoeboid morphodynamics permits an integrin-independent migration.

3. Inhibition of RhoA activity. The lack of stress fiber formation, which is regulated by the RhoA protein, is related to the transition to the amoeboid mode of migration.

Collective-Amoeboid Transition (CAT) CAT displays many similarities to EMT. In this case, after the rupture of the cell-cell adhesions, the cell detaches from the epithelium or the multicellular body and moves according to the integrin-independent amoeboid migration.

Mesenchymal-Epithelial Transition (MET) Plasticity of motile cells may occur in a bidirectional path. Transitions from amoeboid to collective phenotype have been observed. Also transitions from amoeboid to mesenchymal migration. In the case of tumor cells, the most common transition when extravasation occurs is the MET. The molecular processes involved in MET are the same that we have mentioned for EMT, but in the opposite direction: gain of E-cadherin expression, downregulation of proteases, and attachment to the host tissue. In conclusion, the loss of the motile characteristics. MET also plays a crucial role in cancer metastasis. Therefore, targeting EMT and MET may provide a strategy to inhibit the progression of tumor metastasis.

Role of proteolytic activity

MMPs are the main class of proteases that cause ECM cleavage and remodeling. The behavior of MMPs depends on the mode of migration displayed by the cells and the characteristics of the ECM (Friedl and Wolf, 2008). The proteolytic activity can be distinguished in:

1. Individual mesenchymal migration through poorly organized networks. The proteolytic activity takes place in the cell membrane around 10 µm behind the leading edge. Thus, the protrusive forces produced at the leading edge can be tightly transmitted to the substrate. Instead of a complete breakdown, the fibers of the ECM are reoriented parallel to the direction of the cell's motion; see figure 1.7. This kind of proteolytic activity is related to EMT and results in ECM micropatterning and microtracks of low resistance.

2. The inhibition of proteolysis leads to MAT, where cell movement is achieved by squeezing through the gaps between the ECM fibers. Cells can undergo amoeboid migration while the fiber density, the gap size, and the resistance of the ECM are in a suitable range of values.

3. The transition from individual to collective migration leads to ECM macropatterning mediated by proteolysis. The microtrack created by the leading cell (or cells) of the multicellular body is subsequently filled by the following cells. The cell-ECM interface along the body shows proteolytic activity that causes macrotrack formation.

1.3 Background on computational modeling

An introduction to computational modeling of cell motility is necessary to put in context the work developed in the following chapters. In this section, we first review the state of the art of mathematical modeling of cell migration. Then, we introduce the methodology employed to track the cell, that is, the phase-field method. Finally, we explain the basis of isogeometric analysis, which is the numerical method used to solve the models proposed in this thesis.

1.3.1 Mathematical models of cell crawling

This section reviews the mathematical models that are setting the basis for modeling cell motility. Since the literature related to models of cell migration is extensive, we will focus on what we perceive as the most prominent models. Detailed reviews can be found in Camley and Rappel (2017); Danuser *et al.* (2013); Holmes and Edelstein-Keshet (2012); Jilkine and Edelstein-Keshet (2011); Te Boekhorst *et al.* (2016); Ziebert and Aranson (2016).

Mathematical models of cell motility are based on experimental and theoretical evidences. For instance, early experimental works analyzed cell-motion patterns (Gail and Boone, 1970; Potel and Mackay, 1979) describing walk models through velocity, persistence time, or contact distributions. New experimental techniques (Chen *et al.*, 2014; Rugar and Hansma, 1990) have led to more detailed studies, where the modes of cell motion (Discher *et al.*, 2005; Driscoll and Danuser, 2015; Friedl and Wolf, 2003, 2009; Lämmermann and Sixt, 2009; Te Boekhorst *et al.*, 2016) and the cytosol dynamics (Bergert *et al.*, 2012; Choi *et al.*, 2008; Del Alamo *et al.*, 2007; Li *et al.*, 2005; Vicente-Manzanares *et al.*, 2011) are explained, as well as the regulatory systems involved in the membrane signaling pathways (Elosegui-Artola *et al.*, 2016; Lecuit and Lenne, 2007; Mak *et al.*, 2016; Roussos *et al.*, 2011). Those experimental works have allowed to understand the main mechanisms of cell motility, though there is still a great lack of knowledge. For example, the interplay between the different signaling pathways, the regulation of cellular transitions (e.g., epithelial-mensenchymal transition), or the cell-extracellular matrix interaction are complex processes that continue to be investigated. Computational modeling has been recently proposed as an effective way to test conceptual models of cell motility.

Classification of the models

We can not refer to a unique classification of the computational models of cell motility. Different classifications may arise according to the factors selected to carry out the sorting. The number of spatial dimensions (one, two, and three dimensions) or the numerical method employed to solve the model (e.g., spectral methods, Lattice–Boltzmann, finite differences, or finite volume methods) are examples of those factors. Here, we propose three levels of sorting:

1. **Scale.** Mathematical models may be classified according to their scale:
    - Subcellular models explain particular processes occurring at some regions of the cell, such as actin polymerization (Cardamone *et al.*, 2011; Kim *et al.*, 2009a), bleb formation (Strychalski and Guy, 2012), actomyosin networks (Borau *et al.*, 2012; Kim, 2015; Kim *et al.*, 2009b), or cell-substrate adhesion (Chan and Odde, 2008; Elosegui-Artola *et al.*, 2016; Walcott and Sun, 2010).
    - Cellular-scale models simulate the entire cell. This kind of models may focus either on the membrane molecules dynamics (Levchenko and

Iglesias, 2002; Meinhardt, 1999), on the laws governing the cytosolic components (Allena and Aubry, 2012; Aubry *et al.*, 2015; Löber *et al.*, 2014; Shao *et al.*, 2012, 2010), or couple both compartments including the interaction between the cytosolic and membrane compounds (Marth and Voigt, 2014; Moure and Gomez, 2016).

- Tissue-level models represent collective cell motion (Allena *et al.*, 2013; Allena and Maini, 2014). Some of them consider each cell as an individual behaving under certain rules (Marée and Hogeweg, 2001; Rey and Garcia-Aznar, 2013), while others treat the cell population under the assumptions of continuum mechanics (Valero *et al.*, 2013; Xu *et al.*, 2017).

2. **Cell deformation.** Modeling the deformation of the cell's membrane in a motile cell entails a number of difficulties. Thus, cellular-scale models can be classified as:

    - Fixed-geometry models. Some studies assume that the geometry of the cell remains constant during motion (Barnhart *et al.*, 2011; Kockelkoren *et al.*, 2003; Meinhardt, 1999; Subramanian and Narang, 2004).

    - Moving-boundary models. Significant progress in recent years has allowed that most models consider deformable cells (Casquero *et al.*, 2017; Hecht *et al.*, 2011b; Liu *et al.*, 2006; MacDonald *et al.*, 2016; Novak *et al.*, 2007; Strychalski *et al.*, 2010).

3. **Moving boundary formulation.** Depending on the methodology employed to track the cell in the moving-boundary models, some authors have classified them as:

    - Tracking-interface approach. In this method the boundary (i.e., the cell's membrane) is explicitly tracked. Models where the membrane is defined by a set of Lagrangian marker points (Hecht *et al.*, 2011b; Vermolen and Gefen, 2013), models based on the immersed boundary method (Casquero *et al.*, 2017; Strychalski *et al.*, 2015), or models that use moving bulk and surface meshes (Elliott *et al.*, 2012; MacDonald *et al.*, 2016) are some examples of this group.

    - Level set method. This method avoids the algorithmic complexity of the use of moving meshes. A distance map is placed on a fixed domain and evolves in time according to a given velocity. The distance function defines the location of the cell membrane. Some examples are Neilson *et al.* (2011b); Shi *et al.* (2013); Wolgemuth and Zajac (2010).

    - Phase-field method. This method also avoids the use of moving meshes.

> The phase-field method resorts to an auxiliary field that identifies the region occupied by the cell. Besides tracking the cell, the phase-field method permits the localization of the evolution laws of different compounds to the region where they take place; namely, the cytosol, the membrane, or the extracellular medium. The phase-field method has emerged as a powerful methodology for problems of cell migration (Biben *et al.*, 2005; Camley *et al.*, 2014, 2017; Dreher *et al.*, 2014; Löber *et al.*, 2014; Moure and Gomez, 2016).

The former classification may be extended in several ways. For example, cellular-scale models that study cell polarization can be classified according to *classes* of dynamic behavior (Jilkine and Edelstein-Keshet, 2011) in: Turing-type pattern formation models (Meinhardt, 1999), gradient-sensing models that incorporate adaptation (Levine *et al.*, 2006), wave-based models (Arai *et al.*, 2010), stochastic models (Van Haastert, 2010), and models representing a detailed biochemistry (Causin and Facchetti, 2009). We cannot conclude this section without distinguishing the models according to the mathematical abstraction of the biology, into continuous, discrete, and hybrid models. Continuous models use averaged fields governed by equations that usually take the form of partial differential equations (PDEs). Discrete models are composed of single agents, or units, which interact under certain rules (see, e.g., Scianna *et al.*, 2013). Finally, hybrid models couple the continuous and discrete description of the two previous model types.

Review of the literature

Cell motility has been (and continues to be) modeled as a Brownian motion (Gail and Boone, 1970; Jin *et al.*, 2017; Novikova *et al.*, 2017). We initiate this brief review with a prominent model that reproduces the Brownian motion of cellular populations subject to chemotaxis: the continuum model proposed in Keller and Segel (1971), which accounts for the cell density and the concentration of the chemical signal. This model has become the prevailing method for representing chemotactic behavior in biological systems on the population level (a review with the models derived from Keller and Segel, 1971 can be found in Hillen and Painter, 2009). Besides the continuum approach, collective migration has been also modeled by using a discrete approach. Notable discrete models for cell migration are the cellular automaton (Hatzikirou and Deutsch, 2008; Lee *et al.*, 1995; Mallet and De Pillis, 2006) and the cellular Potts models (Marée *et al.*, 2012; Scianna *et al.*, 2013). Cellular automaton models consider different states for the discrete cells and a set of rules that control the state of each cell, whereas cellular Potts models incorporate a Hamiltonian to determine the shift between states.

Regarding the cellular-scale models, the complexity of the mathematical models has increased over the years. Models of cell motility have evolved from one- (Grimm *et al.*, 2003) to three-dimensional (Tjhung *et al.*, 2015) models, also from moving cells with fixed geometry to cells that exhibit high deformations of the membrane. Henceforth, we propose an analysis of the cellular-scale models from two points of view: First, we analyze the rheology considered for the cell's interior, i.e., the cytoskeleton. Second, we study the different types of models proposed to account for the signaling events that drive cell motility. At the end of the section we mention some works that address cell-cell and cell-ECM interaction.

The forces produced during the motion of the cell are transmitted by the cytoskeleton. As seen in subsection 1.2.3, most modes of cell migration are caused by the deformation of the F-actin network. Thus, models of cell motility have usually focused on the rheology of the F-actin network. First works considered the F-actin network as a viscoelastic gel. Bottino *et al.* (2002) proposed a crawling model for nematode sperm, where the gel is represented by a Lagrangian mesh of individual nodes connected by viscoelastic springs; see figure 1.8c. There, the forces acting on the lamellipodium (protrusion, adhesion, and retraction) are applied on the nodes. Continuous models for the viscoelastic gel have been proposed in Carlsson (2011); Gracheva and Othmer (2004); Larripa and Mogilner (2006). For instance, Carlsson (2011) applies the concept of active stress to a one-dimensional model of cell crawling; see figure 1.8a. Active stresses (Joanny and Prost, 2009) are produced internally in the cell, even in the absence of external forces, and account for the contraction and protrusion of the F-actin network. Carlsson (2011), which also includes the adhesion to the substrate, is able to reproduce the dynamics of the actin filaments. Expanding the concept of active stresses, the actomyosin network can be modeled as a Newtonian (Barnhart *et al.*, 2011; Biben *et al.*, 2005; Shao *et al.*, 2012) or non-Newtonian (Rubinstein *et al.*, 2009) fluid. The phase-field method is applied in Biben *et al.* (2005) to track the cell and derive the surface tension and bending forces of the membrane. In Biben *et al.* (2005), the cytosolic fluid is assumed to be incompressible. However, Barnhart *et al.* (2011) and Shao *et al.* (2012) consider a compressible fluid to model the F-actin dynamics inside keratocytes. In Barnhart *et al.* (2011), besides the momentum conservation equation for the fluid, evolution equations for myosin, F-actin, and adhesive complex densities are posed on a fixed domain. Barnhart *et al.* (2011) show a detailed study about the dynamics of the actin filaments in function of the adhesiveness of the substrate, though the geometry of the cell is fixed; see figure 1.8b. In contrast, Shao *et al.* (2012) propose a similar model based on the phase-field theory that permits to simulate deformable cells. Rubinstein *et al.* (2009), which also consider a compressible fluid for the lamellipodium dynamics, provide a rationale to disregard the pressure term in the Stokes-type equation that governs the flow. Some works have proposed a more detailed description of the cytosol: They assume that the cytosol is a two-phase fluid with one phase accounting for the F-actin network

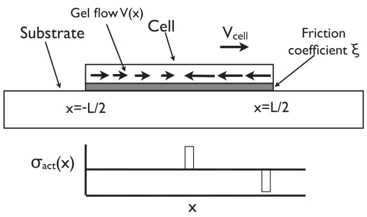

(a) *Conceptual description of the model proposed in Carlsson (2011).*

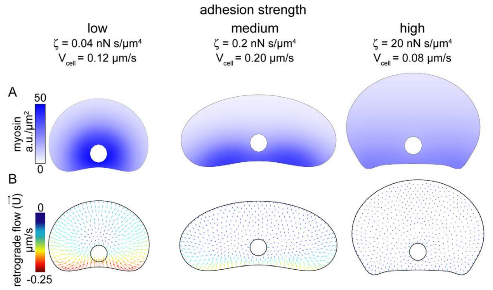

(b) *Barnhart et al. (2011) results showing myosin density and F-actin velocity on a fixed geometry, as a function of the substrate adhesiveness.*

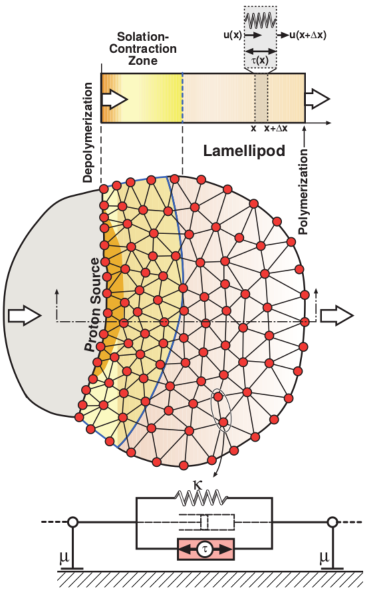

(c) *Conceptual description of the model proposed in Bottino et al. (2002).*

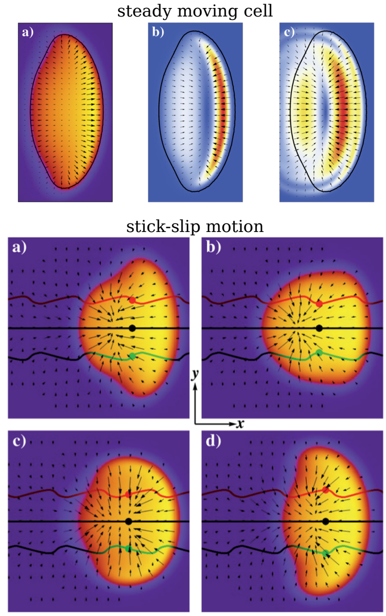

(d) *Löber et al. (2014) results. Steady motion (top): (a) Polarization field. (b) Traction force. (c) Substrate displacement. Stick-slip motion (bottom): substrate displacement at different times.*

Figure 1.8. Models of cytosol dynamics.

and the other (the solvent phase) representing the cytosolic fluid. Mesenchymal and amoeboid cells have been modeled with multiphase fluids in works such as, e.g., Alt and Dembo (1999); Kuusela and Alt (2009); Strychalski *et al.* (2015). The model proposed in Strychalski *et al.* (2015), where the phases represent a fluid and a poroelastic material under the assumptions of incompressibility, is solved by using an immersed boundary method. A review about multiphase flows applied to cell motion may be found in Cogan and Guy (2010). Finally, a different approach models the F-actin dynamics by using a vector field (named polarization) that describes the polar orientation of the filaments (Doubrovinski and Kruse, 2010). The deformation of the cell is controlled by the polarization vector; see, for instance, Dreher *et al.* (2014); Löber *et al.* (2014); Ziebert *et al.* (2011), where the phase-field method is used to track the cell. The evolution equation of the polarization may be coupled to myosin, pro-nucleation factors, or adhesions dynamics to enhance the capabilities of the models. In figure 1.8d we have plotted some results of Löber *et al.* (2014), where the two-dimensional model accounts for an elastic substrate. Löber *et al.* (2014) show interesting results of cells displaying stick-slip and bipedal motion.

Cell motility is controlled by a group of proteins that activate the cytosolic machinery; see subsection 1.2.3. A number of mathematical models have studied the interactions of these proteins along the signaling pathway. Most of these reactions occur in the vicinity of the membrane. Some models have successfully reproduced the overall behavior of these proteins by using a set of activators and inhibitors located in the membrane. Meinhardt (1999) and Levchenko and Iglesias (2002) are two remarkable works. Meinhardt (1999) proposed a model with three membrane species: an activator that submits the signal to the cytosol, a global inhibitor, and a local inhibitor that acts in the activator peaks. Pseudopod dynamics of amoeboid cells is effectively reproduced by the activator, whose behavior may be biased by extracellular signals. The concept of local excitation, global inhibition (LEGI) model was utilized in Levchenko and Iglesias (2002). The model assumes that the cellular response depends on the ratio of activator to inhibitor, where both components are linked to the extracellular signal. The activator and inhibitor are associated to members of the PIs family. The model results exhibit the main features of amoeboid motion. These two models have inspired a number of studies; see, e.g., Devreotes *et al.* (2017); Iglesias and Devreotes (2008, 2012). The previous models may be extended by adding other modules that account for cell polarization, the cytoskeleton, or biased excitable networks (BEN). For instance, the model proposed in Iglesias and Devreotes (2012) couples the LEGI and BEN modules; see figure 1.9a. A different kind of models have studied in more detail the interactions that the signaling molecules experience. These models have proposed evolution equations for the molecules that participate in the signaling cascade. Gamba *et al.* (2005); Marée *et al.* (2012); Subramanian and Narang (2004) are examples of this kind of models, whose main drawback is the great number of unknowns. In figure 1.9d we have plotted some results of Marée *et al.* (2012) that show the distribution of members of the Rho GTPases and PIs families. The signaling dynamics and the polarization of the cell may be modeled following different approaches; see Jilkine and Edelstein-Keshet (2011) for a detailed review. Stochastic models (Bosgraaf and Van Haastert, 2009b; Van Haastert, 2010) or wave-pinning models (Mori *et al.*, 2008; Otsuji *et al.*, 2007) have also had a strong impact on the field. The models that focus on the signaling pathway have been frequently analyzed on fixed geometries. To further gain insight into these models, many authors have devoted their efforts to solve them on deformable geometries. For instance, Elliott *et al.* (2012); Neilson *et al.* (2011b) solved the equations proposed by Meinhardt (1999) on a deformable membrane; see, e.g., figure 1.9b that corresponds to Elliott *et al.* (2012) and shows the activator concentration on the cell's membrane. Elliott *et al.* (2012) posed the equations on a three-dimensional moving surface mesh. The mesh moves according to a force balance equation that includes an activator-dependent protrusion, the surface tension of the membrane, a Lagrange multiplier for volume conservation, viscosity, and other external forces. Neilson *et al.* (2011b) use the hybrid method proposed in Neilson *et al.* (2011a) to move the membrane according to a velocity proportional to the activator; see figure 1.9c. Neilson *et al.* (2011a) proposed an arbitrary Lagrangian Eulerian (ALE) surface finite element method for solving the PDEs on evolving surfaces. The ALE method is coupled with a level set method to drive the movement of the domain boundary (i.e., the membrane). Shi *et al.* (2013) solved an extension of the LEGI model on a deformable membrane by using a finite difference method. Finally, Hecht *et al.* (2011b) solved their own activator-inhibitor system for amoeboid motion on a deformable two-dimensional cell. The membrane is modeled as a set of nodes (Lagrangian marker points) that move according to a force balance equation. The forces considered are similar to those of Elliott *et al.* (2012), i.e., protrusion, membrane bending, volume conservation, and a drag force.

A number of models have studied cell-ECM interaction. For instance, Ribeiro *et al.* (2017) proposed a 3D model of mesenchymal motion that couples the dynamics of the PIs with the extension of filopodia in the ECM. The ECM is assumed to be an infinite elastic body. Ribeiro *et al.* (2017) analyze the influence of the ECM and the motion of cells in compliant and tight networks. Tozluoglu *et al.* (2013) studied amoeboid migration in confined matrix environments. The hybrid agent-based/finite-element model proposed in Tozluoglu *et al.* (2013) is able to reproduce blebbing motion in different matrix geometries. The nucleus, the membrane, the actin cortex, and the ECM fibers are represented by sets of discrete nodes. The ECM fibers are flexible and a no-slip condition between the membrane and the surface of the fibers is imposed. In Heck *et al.* (2017) the ECM is modeled as a viscoelastic solid. They proposed a viscoelastic smoothed particle hydrodynamics to model the ECM in contact with a migrating cell. The method is able to capture ECM degradation and large deformations of the ECM. Others models

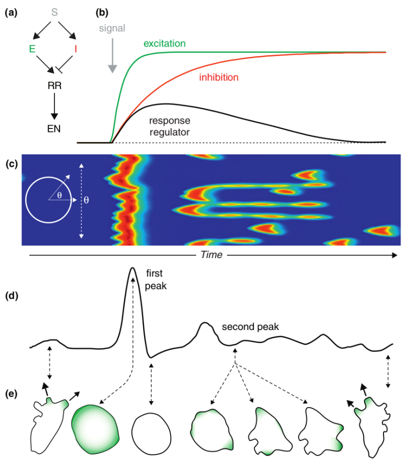

(a) *Behavior of the LEGI-BEN model proposed in* Iglesias and Devreotes *(2012) when the cell is uniformly stimulated.*

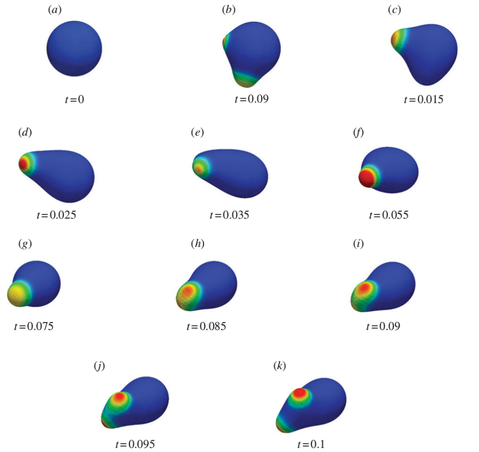

(b) Elliott et al. *(2012) results displaying 3D migration in the absence of chemoattractant. Activator concentration on the membrane.*

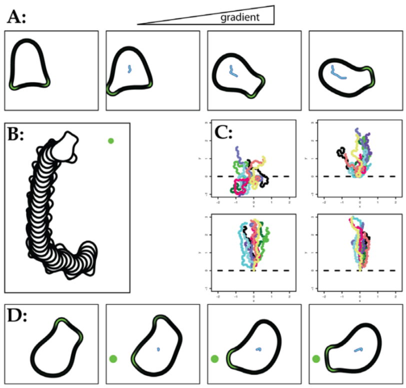

(c) Neilson et al. *(2011b) results for chemotaxis motion. The membrane activator is plotted in green.*

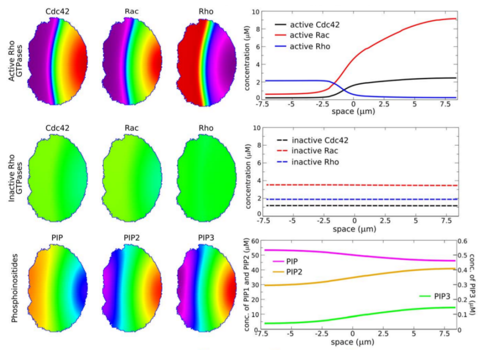

(d) *The model proposed in* Marée et al. *(2012) accounts for the dynamics of the Rho GTPases and PIs members inside the cell. The plot shows the concentrations of the Rho GTPases and PIs for steady motion.*

Figure 1.9. Models of signaling compounds dynamics.

have focused on cell-cell interaction (Camley *et al.*, 2014; Lee and Wolgemuth, 2016; Vermolen and Gefen, 2013). The model proposed in Camley *et al.* (2014) is entirely based on the phase-field theory and accounts for cell polarity, cell-cell contact, and the interaction with the nucleus. Cell-cell and cell-nucleus interactions are modeled with a Hamiltonian. The results are able to reproduce persistent rotational motion for groups of two and three cells. Finally, Lee and Wolgemuth (2016) developed an interesting work that simulates the epithelial-mesenchymal transition (EMT). They model cell monolayers that undergo cell polarization, contractile and propulsive forces, and cell-cell and cell-substrate adhesion. They propose a continuum model to study the influence of the different factors that regulate EMT, and also the particular case of tumor cells.

1.3.2 Phase-field method

A motile cell is an outstanding example of a problem with moving interfaces. Cell migration can be thought of as a moving boundary problem where the cell membrane accounts for the boundary. The classic approach to solve this kind of problems involves the solution of partial-differential equations (PDEs) posed on moving domains. These equations are coupled to other PDEs by means of boundary conditions that are posed on the moving interface, whose location is *a priori* unknown. The numerical treatment of these problems is complex. The phase-field method (Anderson *et al.*, 1998; Chen, 2002; Emmerich, 2003; Gomez and van der Zee, 2017; Lowengrub *et al.*, 2009; Provatas and Elder, 2011) (also known as *diffuse-interface* and *diffuse domain* method) has emerged as a mathematical theory that reformulates the moving boundary problem as PDEs posed on a known and fixed computational domain. The phase-field method introduces a new field, called the phase field, which is defined on the entire domain and serves as a marker of the location of the different phases[8]. The phase-field methodology assumes that the interface is actually represented by a rapid but smooth transition of the phase field (see figure 1.10), contrary to the moving boundary problems that consider a sharp transition[9]. The phase field is governed by an evolution equation, posed on the entire domain, that encodes the dynamics of the interfaces at the original moving boundary problem. The width of the interface in the phase-field problems is controlled by a length scale (or regularization) parameter (ε in figure 1.10b). In many cases, it can be proven that the phase-field problem converges to the sharp-interface problem as the regularization parameter tends to zero. This can be done by using the theory of matched asymptotic expansions (Caginalp, 1989; Fife, 1988). However, phase-field problems do not necessarily possess an associated sharp-interface problem. In general, phase-field models are derived from an energy-free functional that controls the dynamics of the phases considered in the problem. The evolution equations of the phase-field problem can be derived directly from the free-energy functional by using the classical theory

[8]The term *phase* may refer to a variety of entities depending on the problem, such as, e.g., states of matter, stable densities of a compound, or simply markers of spatial domains.

[9]The moving boundary problems are also known as *sharp-interface* problems, while the phase-field problems are referred to as diffuse-interface problems.

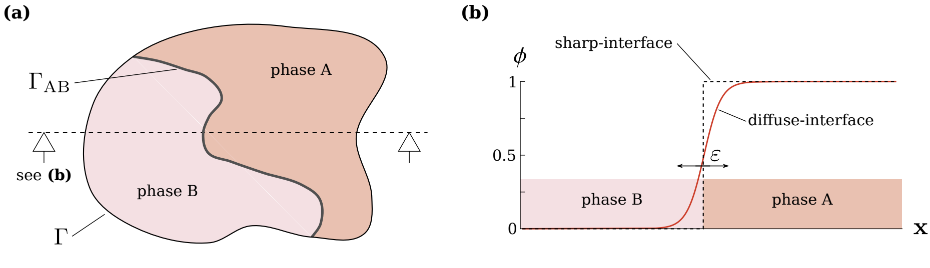

Figure 1.10. Description of the phase-field method. *(a) Phase A and phase B coexist in the domain Ω, whose boundary is Γ. The interface that separates both phases is denoted by Γ_{AB}. (b) The phase-field (or diffuse-interface) theory introduces a continuous field ϕ that identifies the phases. The interface is represented by a smooth transition of ϕ, whose width is controlled by the regularization parameter ε.*

of thermomechanics and Coleman-Noll-type approaches (Coleman and Noll, 1963; Truesdell and Noll, 2004). A different and simpler approach involves the concept of diffusifying[10] the sharp-interface problem, which for some cases can lead to the equivalent diffuse-interface problem.

The complex numerical treatment associated to the existence of moving boundaries is bypassed by the use of the phase-field method. However, different computational issues arise with phase-field problems. First, the diffuse interfaces that move along the computational domain originate large gradients of the phase field. The solution of the phase-field problem will be more accurate as the regularization parameter tends to zero, which implies larger gradients. Thus, the use of fine computational meshes or special refinement methods (e.g., Lorenzo *et al.*, 2017) is adequate. Moreover, phase-field theories are usually governed by higher-order PDEs, as we show below. The solution of phase-field problems with classical finite element methods entails a number of challenges. In subsection 1.3.3 we review a novel method, named isogeometric analysis, which bypasses the main limitations derived from the use of classic finite element analysis to solve higher-order equations. The time integration of the phase-field problems entails the last computational challenge: the kinetics of the phases, which may include the emergence and vanishing of interfaces, can lead the solution to evolve at different time scales.

In recent years, the use of the phase-field theories has experienced a great growth. On the one hand, advances in the field of the computational methods have permitted faster and more efficient numerics (Dedè *et al.*, 2012; Gómez *et al.*, 2008;

[10] Term coined in Gomez and van der Zee (2017).

Gomez and Hughes, 2011; Gomez *et al.*, 2014). On the other hand, a great number of phase-field models have successfully targeted a variety of problems such as, e.g., solidification dynamics (Caginalp, 1989; Kobayashi, 1994; Penrose and Fife, 1990), air-water flows (Ceniceros *et al.*, 2010), liquid-vapor transitions (Liu *et al.*, 2013), fracture dynamics (Borden *et al.*, 2012; Kiendl *et al.*, 2016), dendritic growth (Jeong *et al.*, 2001; Kim *et al.*, 1999), vesicle dynamics (Biben *et al.*, 2005), cancer growth (Lorenzo *et al.*, 2016; Vilanova *et al.*, 2013; Wu *et al.*, 2014; Xu *et al.*, 2016, 2017), and cell migration (Löber *et al.*, 2014; Moure and Gomez, 2016; Shao *et al.*, 2012). The following paragraphs are devoted to present the classical Allen–Cahn and Cahn–Hilliard models, which are prime examples of phase-field models. Then, we apply the diffuse domain method to the case of a moving cell, where the dynamics of intracellular, membrane, and extracellular generic compounds are posed on a single and fixed domain.

Prime examples: Allen–Cahn and Cahn–Hilliard equations

First, we define the phase field $\phi(\mathbf{x}, t)$, where $\mathbf{x} \in \mathbb{R}^{d_s}$ is a point in a space of d_s dimensions and t denotes time. The field ϕ localizes the generic phases A and B, as shown in figure 1.10. ϕ is defined in the entire domain $\Omega \subset \mathbb{R}^{d_s}$ such that $\phi(\mathbf{x}, t) = f\left(\frac{d_t(\mathbf{x})}{\sqrt{2}\varepsilon}\right)$, where $d_t(\mathbf{x})$ denotes the signed distance from $\mathbf{x}$ to the time dependent interface Γ_{AB} that separates phases A and B (see figure 1.10a). ε is the regularization parameter related to the thickness of the interface. Note that the function f usually takes the form of a hyperbolic tangent profile. Let us assume that ϕ takes approximately the value 1 in phase A and 0 in phase B, as plotted in figure 1.10b. Here, A and B represent the two components of a binary fluid.

We apply the thermomechanical framework of the phase-field theory to obtain the *canonical* Allen–Cahn (Allen and Cahn, 1979) and Cahn–Hilliard (Cahn and Hilliard, 1958) equations. The thermomechanical framework assumes that all processes are energy dissipative, which permits to impose restrictions to their constitutive relations and, thus, derive the evolution phase-field equations. The phase-field thermomechanics is based on the function of state, which is selected in function of the considered problem (examples of different functions of state are the entropy or the Gibbs free energy). Here, we consider the Helmholtz free energy Ψ, that depends on values and gradients of the phase field. The free energy for the canonical examples may be expressed as

$$\Psi = G(\phi) + \frac{\varepsilon^2}{2}|\nabla\phi|^2, \tag{1.1}$$

where the function $G(\phi)$ usually takes the form of a double well potential with minima in the two components of the binary fluid, i.e., $\phi = 1$ and $\phi = 0$. The corresponding energy functional is known as the Ginzburg–Landau functional

$$\mathcal{F}^{\varepsilon}[\phi] = \int_{\Omega} \Psi \mathrm{d}\Omega = \int_{\Omega} \left(G(\phi) + \frac{\varepsilon^2}{2} |\nabla \phi|^2 \right) \mathrm{d}\Omega. \tag{1.2}$$

The variational derivative of the functional $\mathcal{F}^{\varepsilon}$ with respect to ϕ is

$$\frac{\delta \mathcal{F}^{\varepsilon}}{\delta \phi} = G'(\phi) - \varepsilon^2 \nabla^2 \phi, \tag{1.3}$$

which is also referred to as the *chemical potential* $\mu_\phi = G'(\phi) - \varepsilon^2 \nabla^2 \phi$. Note that the constitutive relations in the phase-field models can depend on μ_ϕ and/or $\nabla \mu_\phi$.

The Allen–Cahn and Cahn–Hilliard equations are derived from the stability principle that the Helmholtz free energy is time decreasing. The Cahn–Hilliard equation imposes the mass conservation of the components. In contrast, the Allen–Cahn equation allows for non-conservative dynamics. The definition of the *constitutive class* for Ψ is the first step in the thermomechanical derivation of the canonical equations. The constitutive class is expressed as

$$\Psi = \widehat{\Psi}(\phi, \nabla \phi). \tag{1.4}$$

The notion of constitutive class implies that, according to equation (1.4), the functional Ψ is allowed to depend upon ϕ and $\nabla \phi$. The postulated energy-dissipation property can be expressed as

$$\frac{\mathrm{d}}{\mathrm{d}t} \left(\int_{\Omega_a} \widehat{\Psi}(\phi, \nabla \phi) \, \mathrm{d}\Omega_a \right) = \mathcal{W}(\Omega_a) - \mathcal{D}(\Omega_a), \tag{1.5}$$

where $\Omega_a \subset \Omega$ denotes an arbitrary region of the spatial domain Ω. The *working* term $\mathcal{W}(\Omega_a)$ is associated to energy supplies or external forces coming through the boundary. The *dissipation* term must be $\mathcal{D}(\Omega_a) \geq 0$ for all conceivable processes.

Allen–Cahn equation In the case of non-conservative dynamics, we first postulate the mass balance

$$\frac{\partial \phi}{\partial t} = -R, \tag{1.6}$$

where the function R will be defined to achieve free-energy dissipation. We assume the constitutive class for R:

$$R = \widehat{R}(\phi, \nabla \phi, \mu_\phi). \tag{1.7}$$

Now, we manipulate equation (1.5). After integrating by parts and flipping the time and space derivatives, from equation (1.5) we obtain the expression

$$\frac{\mathrm{d}}{\mathrm{d}t}\int_{\Omega_a} \Psi \,\mathrm{d}\Omega_a = \int_{\Omega_a} -\mu_\phi R \,\mathrm{d}\Omega_a + \int_{\Gamma_a} \frac{\partial \widehat{\Psi}}{\partial \nabla \phi} \cdot \mathbf{n}_{\Gamma_a} \frac{\partial \phi}{\partial t} \,\mathrm{d}\Gamma_a, \tag{1.8}$$

where we have introduced the identity of equation (1.6). In equation (1.8), Γ_a denotes the boundary of Ω_a and $\mathbf{n}_{\Gamma_a}$ is its unit outward normal. We can identify the terms $\mathcal{W}(\Omega_a)$ and $\mathcal{D}(\Omega_a)$ in equation (1.8). In particular, $\mathcal{D}(\Omega_a) = \int_{\Omega_a} \mu_\phi R \,\mathrm{d}\Omega_a$. If we force the constitutive class of R to take the form $\widehat{R}(\phi, \nabla\phi, \mu_\phi) = m(\phi)\mu_\phi$ with $m(\phi) \geq 0$, the required property of free-energy dissipation is achieved. Thus, from equation (1.6), we obtain the canonical Allen–Cahn equation

$$\frac{\partial \phi}{\partial t} = -m(\phi)\left(G'(\phi) - \varepsilon^2 \nabla^2 \phi\right). \tag{1.9}$$

Cahn–Hilliard equation The Cahn–Hilliard equation can be derived from the mass conservation equation

$$\frac{\partial \phi}{\partial t} + \nabla \cdot \mathbf{h} = 0, \tag{1.10}$$

augmented by the boundary condition $\mathbf{h} \cdot \mathbf{n}_\Gamma = 0$ on $\Gamma = \partial\Omega$, where $\mathbf{n}_\Gamma$ is the unit outward normal to Γ. The constitutive class of $\mathbf{h}$ can be expressed as

$$\mathbf{h} = \widehat{\mathbf{h}}(\phi, \nabla\phi, \mu_\phi, \nabla\mu_\phi). \tag{1.11}$$

As done in equation (1.8), basic manipulations of equations (1.5) and (1.10) lead to the expression

$$\frac{\mathrm{d}}{\mathrm{d}t}\int_{\Omega_a} \Psi \,\mathrm{d}\Omega_a = \int_{\Omega_a} \mathbf{h} \cdot \nabla\mu_\phi \,\mathrm{d}\Omega_a + \int_{\Gamma_a} \left(-\mu_\phi \mathbf{h} + \frac{\partial \widehat{\Psi}}{\partial \nabla\phi}\frac{\partial \phi}{\partial t}\right) \cdot \mathbf{n}_{\Gamma_a} \,\mathrm{d}\Gamma_a. \tag{1.12}$$

The first term of the right-hand side of equation (1.12) is identified as the dissipation, i.e., $\mathcal{D}(\Omega_a) = \int_{\Omega_a} -\mathbf{h} \cdot \nabla\mu_\phi \mathrm{d}\Omega_a$. The constitutive choice $\widehat{\mathbf{h}}(\phi, \nabla\phi, \mu_\phi, \nabla\mu_\phi) = -m(\phi)\nabla\mu_\phi$, with $m(\phi) \geq 0$, guarantees free-energy dissipation. The Cahn–Hilliard equation can be written as

$$\frac{\partial \phi}{\partial t} = \nabla \cdot \left[m(\phi)\nabla\left(G'(\phi) - \varepsilon^2\nabla^2\phi\right)\right]. \tag{1.13}$$

Remark:

1. It can be shown, by using the properties of the phase-field theory (see, e.g., Fried, 2006; Gomez and van der Zee, 2017), that the Ginzburg-Landau function of equation (1.2)

$$\mathcal{F}^{\varepsilon}[\phi] = \int_{\Omega} \left(G(\phi) + \frac{\varepsilon^2}{2} |\nabla \phi|^2 \right) \mathrm{d}\Omega \longrightarrow \mathcal{F}[\Gamma_{\mathrm{AB}}] = \psi_{\Gamma} \int_{\Gamma_{\mathrm{AB}}} \mathrm{d}\Gamma_{\mathrm{AB}} \quad (1.14)$$

as $\varepsilon \to 0$, where Γ_{AB} accounts for the interface and ψ_{Γ} is a surface-energy coefficient that can be calculated. Thus, the free energy of the Allen–Cahn and Cahn–Hilliard problems is proportional to the surface (length in 2D) of the interface, i.e., $\int_{\Gamma_{\mathrm{AB}}} \mathrm{d}\Gamma_{\mathrm{AB}}$. Since both problems model energy dissipation processes, they produce solutions that minimize the surface energy of the interface. In the Allen–Cahn problem, the solution evolves to states that minimize the surface (length in 2D) of the interface. The solution of the Cahn–Hilliard equation, which imposes mass conservation, evolves to a state of minimum surface energy for a given volume (surface in 2D).

Diffuse domain approach for the motile cell problem

We apply the phase-field method to a generic problem of cell migration to show the potential of the method. In this example, we consider a generic compound living in the cytosol and another generic compound living in the membrane. The compounds can experience interactions between them. Those interactions may represent the biochemical reactions of section 1.2.

The classic approach to solve the dynamics of a generic compound $\rho_c(\mathbf{x}, t)$ inside the cell is to pose the governing equation on a moving domain $\Omega_c(t)$, where $\Omega_c(t)$ denotes the spatial region occupied by the cell; see figure 1.11a. Let us consider the convection-diffusion-reaction problem

$$\frac{\partial \rho_c}{\partial t} + \nabla \cdot (\rho_c \mathbf{u}_c) = \nabla \cdot (D_c \nabla \rho_c) + r_c \rho_c \quad \text{in } \Omega_c(t), \quad (1.15)$$

$$D_c \nabla \rho_c \cdot \mathbf{n}_{\Gamma_c} + \rho_c (\mathbf{u}_{\Gamma_c} \cdot \mathbf{n}_{\Gamma_c} - \mathbf{u}_c \cdot \mathbf{n}_{\Gamma_c}) = -j \quad \text{on } \Gamma_c(t), \quad (1.16)$$

where D_c and r_c are the diffusion and reactive coefficients, respectively, and $\mathbf{u}_c$ is the bulk velocity of ρ_c. We define the cell membrane as $\Gamma_c(t) = \partial\Omega_c(t)$. We call $\mathbf{n}_{\Gamma_c}$ the unit outward normal to $\Gamma_c(t)$ and $\mathbf{u}_{\Gamma_c}$ the velocity of $\Gamma_c(t)$. Note that $\mathbf{u}_c$ and $\mathbf{u}_{\Gamma_c}$ do not necessarily have to coincide. The boundary condition in equation (1.16) equates the convective-diffusive flux across the membrane to the prescribed value j.

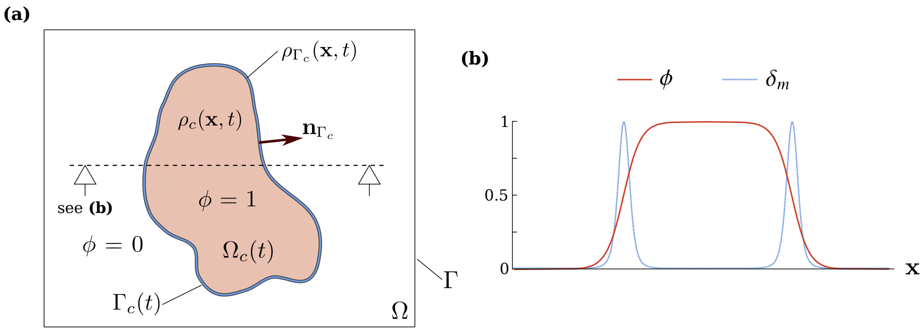

Figure 1.11. Diffuse domain approach for the motile cell problem. *(a) The cell is represented by the moving domain $\Omega_c(t)$, while the membrane is $\Gamma_c(t) = \partial\Omega_c(t)$. We consider the cytosolic compound ρ_c and the membrane compound ρ_{Γ_c}. The phase-field problem is posed on the fixed domain Ω. (b) Profiles of the phase field ϕ and the membrane marker δ_m. The markers are defined such that $\phi = 1$ inside and $\phi = 0$ outside the cell, and $\delta_m = 1$ in the membrane and $\delta_m = 0$ elsewhere.*

Let us also consider a compound $\rho_{\Gamma_c}(\mathbf{x},t)$ living in the membrane $\Gamma_c(t)$. The surface PDE that governs the dynamics of ρ_{Γ_c} is

$$\frac{\partial \rho_{\Gamma_c}}{\partial t} + \nabla_\Gamma \cdot (\rho_{\Gamma_c} \mathbf{u}_{\Gamma_c}) = \nabla_\Gamma \cdot (D_\Gamma \nabla_\Gamma \rho_{\Gamma_c}) + r_\Gamma \rho_{\Gamma_c} + j \quad \text{in } \Gamma_c(t), \tag{1.17}$$

where ∇_Γ denotes the operator ∇ on the surface Γ_c. D_Γ and r_Γ are the diffusion and reactive parameters, respectively. Note that the unknowns ρ_c and ρ_{Γ_c} are coupled through the mass flux term j. Equations (1.15) and (1.17) define the so-called sharp-interface problem. The numerical solution of the sharp-interface problem requires the use of volumetric and surface moving meshes and an algorithm to transfer information between the two meshes.

The diffuse domain approach allows a simpler treatment of the former problem. We consider a larger and fixed domain Ω such that $\Omega_c(t) \subset \Omega$ and we resort to the spatial markers ϕ and δ_m that locate the cell and the membrane, respectively. At this point, we assume that an evolution equation, similar to equation (1.9) or equation (1.13), provides the phase field ϕ that takes the value $\phi = 1$ inside the cell and $\phi = 0$ outside the cell; see figure 1.11. We can define the function δ_m in terms of ϕ as a marker of the cell membrane[11]; see figure 1.11b. We assume now that ρ_c and ρ_{Γ_c} are defined on Ω. Assuming (momentarily) that ρ_{Γ_c} is extended

[11]Common expressions for the membrane marker, but not the only, are $\delta_m(\phi) = \phi^2(1-\phi^2)$ and $\delta_m(\phi) = \varepsilon^2 |\nabla\phi|^2$.

off Γ_c constant in the normal direction[12], i.e., $\nabla\rho_{\Gamma_c} \cdot \mathbf{n}_{\Gamma_c} = 0$, we can state the equivalent diffuse-interface problem as

$$\frac{\partial(\phi\rho_c)}{\partial t} + \nabla\cdot(\phi\rho_c\mathbf{u}_c) = \nabla\cdot(\phi D_c\nabla\rho_c) + \phi r_c\rho_c - \delta_m j \quad \text{in } \Omega, \tag{1.18}$$

$$\frac{\partial(\delta_m\rho_{\Gamma_c})}{\partial t} + \nabla\cdot(\delta_m\rho_{\Gamma_c}\mathbf{u}_{\Gamma_c}) = \nabla\cdot(\delta_m D_\Gamma\nabla\rho_{\Gamma_c}) + \delta_m r_\Gamma\rho_{\Gamma_c} + \delta_m j \quad \text{in } \Omega. \tag{1.19}$$

It has been proven (Li *et al.*, 2009; Teigen *et al.*, 2009) that equations (1.18) and (1.19) converge to equations (1.15) and (1.17) as the regularization parameter ε tends to 0. The governing laws for the cytosol dynamics in the models proposed in this thesis are based on equation (1.18), while the membrane equations are based on equation (1.19). The equations that govern the extracellular dynamics are based on equation (1.18), but replacing ϕ by the spatial marker of the extracellular medium[13]. In this example, the extracellular marker would take the expression $1-\phi$.

1.3.3 Isogeometric analysis

The numerical approximation of the higher-order partial differential equations that describe the dynamics of the cell and its compounds entails several difficulties. The resolution of diffuse interfaces that evolve dynamically and the discretization of higher-order differential operators pose significant challenges for classical finite element methods. Previous works of cell motility based on phase-field models have used finite differences (Shao *et al.*, 2010), hybrid Lattice Boltzmann (Tjhung *et al.*, 2015), or spectral methods (Löber *et al.*, 2014). Isogeometric analysis (IGA) constitutes the main tool used for the spatial discretization of the models presented in this thesis.

IGA is a finite element method originally proposed by Hughes *et al.* (2005) and further explained in Bazilevs *et al.* (2010a,b); Cottrell *et al.* (2007); Schillinger *et al.* (2012); Schmidt *et al.* (2012); Scott *et al.* (2014). IGA has popularized the use of Non-uniform Rational B-spline (NURBS) (Piegl and Tiller, 2012) basis in the isoparametric Galerkin finite element method. A key feature of IGA is the use of the same basis functions to represent both the geometry and the unknowns of the problem. Isogeometric methods aim at using the Computer Aided Design (CAD) representations directly in the analysis, potentially circumventing the need to generate an intermediate geometrical description. This is achieved by the

[12] It can be shown using equation (1.19) that, to leading order, this assumption holds true.

[13] Although we have referred to Ω_c as the cell, the rationale applies also to the extracellular environment which is internally bounded by Γ_c. When we use equation (1.18) for any extracellular component, Ω_c does, indeed, represent the extracellular space.

use of NURBS basis functions. Thus, in contrast with classical Finite Element Analysis (FEA), the numerical simulations may be performed on exact geometries in many cases of engineering interest. The term isogeometric emphasizes that as the finite element space is refined, the geometric degrees of freedom can be determined such that the geometry does not change. Classical finite element spaces use basis functions that are $\mathcal{C}^0$-continuous across element boundaries, making them unsuitable for higher-order problems using a simple Galerkin formulation. NURBS-based spaces can be constructed to possess arbitrary degrees of inter-element continuity for any spatial dimension. Other properties of IGA are the higher-order accuracy, the robustness, and the ability to be refined through knot insertion, degree elevation, and k-refinement (increasing the order and the smoothness of the NURBS basis functions simultaneously).

IGA has been successfully applied to many different types of problems such as, e.g., structural vibrations (Cottrell *et al.*, 2006), fluid-structure interaction (Bazilevs *et al.*, 2008; Bueno *et al.*, 2015; Casquero *et al.*, 2015), turbulence (Bazilevs *et al.*, 2007), phase-field models (Bueno *et al.*, 2016; Gómez *et al.*, 2008), and biomedical applications (Lorenzo *et al.*, 2017; Xu *et al.*, 2017). In addition, several groups have developed software for IGA, such as PetIGA (Collier *et al.*, 2013a), igatools (Pauletti *et al.*, 2015), or GeoPDEs (de Falco *et al.*, 2011).

B-splines

NURBS are obtained from B-splines. B-splines are built on the concept of *knot vector*. In one dimension, a knot vector is a non-decreasing set of coordinates in the parameter space[14], i.e., $\Xi = \{\xi_1, \xi_2, ..., \xi_{n+p+1}\}$, where $\xi_i \in \mathbb{R}$ is the i-th knot, i is the knot index, p is the polynomial order, and n is the number of basis functions used to construct the B-spline curve. Knot vectors are uniform if the knots are evenly spaced in the parameter space. If they are unevenly spaced, the knot vector is non-uniform. The knot values may be repeated, i.e., more than one knot can take the same value. The number of times a knot value is repeated is named *multiplicity* and has important implications for the properties of the basis, as we show below. A knot vector is said to be open if its first and last knot values appear $p+1$ times. Open knot vectors are standard in the CAD literature because the basis functions created from them are interpolatory at the ends of the parameter space interval.

For a given knot vector, the B-spline basis functions are defined recursively in the parameter space starting with the piecewise constants ($p = 0$) plotted in

[14] Space where knot vectors are defined. As shown in the following paragraphs, the parametric space is different from the physical space.

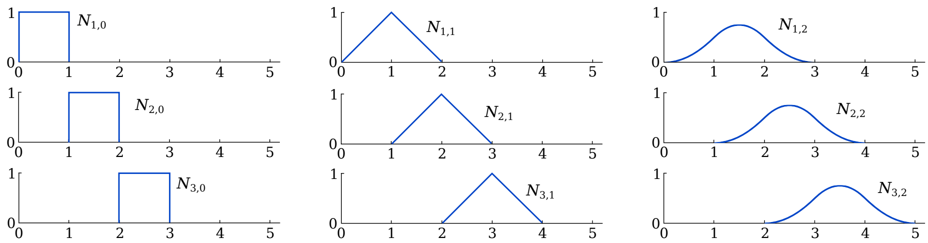

Figure 1.12. B-splines created by the Cox-de Boor recursion formula. *Basis functions of order $p = 0$ (left), $p = 1$ (middle), and $p = 2$ (right) for the uniform knot vector $\Xi = \{0, 1, 2, 3, 4, ...\}$. (Reproduced from Cottrell* et al.*, 2009)*

figure 1.12 (left), i.e.,

$$N_{i,0}(\xi) = \begin{cases} 1 & \text{if } \xi_i \geq \xi \geq \xi_{i+1}, \\ 0 & \text{otherwise} , \end{cases} \tag{1.20}$$

for $i = 1, ..., n$. The basis functions of higher degrees ($p = 1, 2, 3, ...$) are defined by

$$N_{i,p}(\xi) = \frac{\xi - \xi_i}{\xi_{i+p} - \xi_i} N_{i,p-1}(\xi) + \frac{\xi_{i+p+1} - \xi}{\xi_{i+p+1} - \xi_{i+1}} N_{i+1,p-1}(\xi), \tag{1.21}$$

for $i = 1, ..., n$. This is referred to as the *Cox-de Boor recursion formula* (Cox, 1972). Note that for $p = 0$ and $p = 1$ the resulting basis functions are the same as for standard constant and linear finite element functions; see figure 1.12. The main properties of the basis functions created from non-uniform open knot vectors (see figure 1.13) are the following:

- They constitute a partition of unity, i.e., $\sum_{i=1}^{n} N_{i,p}(\xi) = 1 \quad \forall \xi$.
- They are pointwise nonnegative over the entire domain, i.e., $N_{i,p}(\xi) \geq 0 \quad \forall \xi$.
- Functions of order p have $p - m_i$ continuous derivatives across the knot ξ_i, where m_i is the multiplicity of the value of ξ_i in the knot vector. If the multiplicity of a knot value is exactly p (see figure 1.13b), the basis function is interpolatory at that knot, i.e., $\mathcal{C}^0$. If the multiplicity is $p + 1$, the basis function becomes discontinuous.
- The support of B-spline functions of order p is always $p + 1$ knot spans. In the case that some of the knots it spans have multiplicity $p > 1$, the rule still applies taking into account that some knot spans will have zero length due to the repetition of the knot values. Thereby, the function $N_{i,p}$ begins at the knot ξ_i and ends at ξ_{i+p+1}.

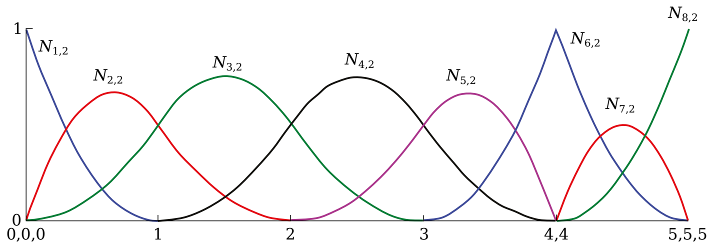

(a) *Quadratic ($p = 2$) basis functions for the open knot vector $\Xi = \{0, 0, 0, 1, 2, 3, 4, 4, 5, 5, 5\}$. The multiplicity of the knot $\xi = 4$ is 2, so that the basis functions in that knot are $\mathcal{C}^0$.*

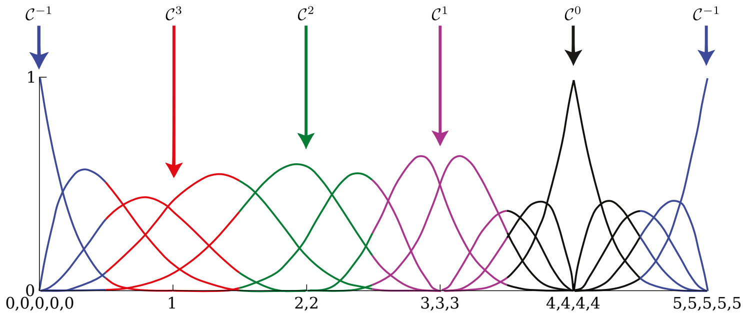

(b) *Quartic ($p = 4$) basis functions for the open knot vector $\Xi = \{0, 0, 0, 0, 0, 1, 2, 2, 3, 3, 3, 4, 4, 4, 4, 5, 5, 5, 5, 5\}$. The continuity across the element boundaries is a direct result of the polynomial order and the multiplicity of the corresponding knot value.*

Figure 1.13. B-splines basis functions and continuity. *Examples of basis functions constructed from open knot vectors. (Adapted from Cottrell et al., 2009)*

The derivatives of the B-spline basis functions are given by

$$\frac{d}{d\xi}N_{i,p}(\xi) = \frac{p}{\xi_{i+p} - \xi_i}N_{i,p-1}(\xi) - \frac{p}{\xi_{i+p+1} - \xi_{i+1}}N_{i+1,p-1}(\xi). \tag{1.22}$$

We can generalize to higher derivatives by simply differentiating each side of equation (1.22).

B-spline curves in $\mathbb{R}^{d_s}$ are constructed by taking a linear combination of B-splines basis functions, as done in classical FEA:

$$\mathbf{C}(\xi) = \sum_{i=1}^{n} \mathbf{B}_i N_{i,p}(\xi), \tag{1.23}$$

where $N_{i,p}(\xi)$ are the B-spline basis functions and $\mathbf{B}_i \in \mathbb{R}^{d_s}$ are the vector-valued

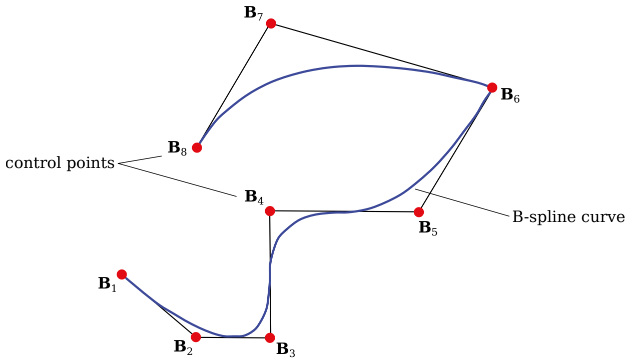

Figure 1.14. B-spline quadratic curve. *B-spline curve (blue line) created with the basis functions and knot vector used in figure 1.13a. Red circles represent the control points* ($\mathbf{B}_i$)*, which are non-interpolatory. (Adapted from Cottrell et al., 2009)*

coefficients of the basis functions, known as *control points*. The index i identifies the control point and the corresponding B-spline function. In figure 1.14 we show an example of a curve created with the B-spline functions plotted in figure 1.13a. Note that the control points are points in the space with a similar role to that of nodal points in FEA. However, in IGA the basis functions are usually non-interpolatory, as shown in figure 1.14. Using the notion of tensor products, a B-spline surface can be defined by

$$\mathbf{S}(\xi,\eta) = \sum_{i=1}^{n}\sum_{j=1}^{m} \mathbf{B}_{i,j} N_{i,p}(\xi) M_{j,q}(\eta), \tag{1.24}$$

where $N_{i,p}(\xi)$ and $M_{j,q}(\eta)$ are univariate B-spline basis functions of order p and q, respectively, corresponding to the knot vectors $\Xi = \{\xi_1, \xi_2, ..., \xi_{n+p+1}\}$ and $\Lambda = \{\eta_1, \eta_2, ..., \eta_{m+q+1}\}$. The surface is defined by the control net $\{\mathbf{B}_{i,j}\}$, with $i = 1, 2, ..., n$ and $j = 1, 2, ..., m$. The procedure to obtain B-spline solids is analogous. The properties of the B-spline geometries are derived by the properties of the tensor product: The basis functions are pointwise nonnegative, constitute a partition of unity, and their support is given by the support of the univariate functions. Also, the number of partial derivatives in a parametric direction is determined by the associated one-dimensional knot vector.

NURBS

A NURBS entity in $\mathbb{R}^{d_s}$ is obtained by the projective transformation of a B-spline entity in $\mathbb{R}^{d_s+1}$. For instance, all the conic sections can be exactly constructed by projective transformations of piecewise quadratic curves. Given the B-spline basis function $N_{i,p}(\xi)$, the one-dimensional NURBS basis functions can be constructed directly by

$$R_i^p(\xi) = \frac{w_i N_{i,p}(\xi)}{\sum_{\hat{i}=1}^{n} w_{\hat{i}} N_{\hat{i},p}(\xi)}, \tag{1.25}$$

where w_i is referred to as the i-th weight. The function $R_i^p(\xi)$ is a piecewise rational function that inherits most of the properties of B-splines (continuity, support, pointwise nonnegative, and partition of unity). The two- and three-dimensional NURBS basis functions are constructed analogously. For example, the two-dimensional NURBS basis functions are given by

$$R_{i,j}^{p,q}(\xi,\eta) = \frac{w_{i,j} N_{i,p}(\xi) M_{j,q}(\eta)}{\sum_{\hat{i}=1}^{n} \sum_{\hat{j}=1}^{m} w_{\hat{i},\hat{j}} N_{\hat{i},p}(\xi) M_{\hat{j},q}(\eta)}, \tag{1.26}$$

where the notation is identical to the one used in equation (1.24). The values $w_{i,j}$ are the weights. The 2D and 3D rational basis functions also inherit their properties from B-splines. The weights play an important role in the definition of the basis, though they lack any explicit geometric interpretation. Note that if the weights are all equal, $R_i^p(\xi) = N_{i,p}(\xi)$. The derivatives of the rational functions depend on the derivatives of the non-rational counterparts and are calculated by applying the quotient rule to equation (1.25). Higher order derivatives may be expressed in terms of the lower-order derivatives by following the classic derivation rules.

The construction of NURBS curves, surfaces, and volumes is analogous to the case of B-splines. They are created by the linear combination of a control mesh and the piecewise basis functions. For instance, NURBS curves $\mathbf{C}$ and surfaces $\mathbf{S}$ may be expressed as

$$\mathbf{C}(\xi) = \sum_{i=1}^{n} \mathbf{B}_i R_i^p(\xi), \tag{1.27}$$

$$\mathbf{S}(\xi,\eta) = \sum_{i=1}^{n} \sum_{j=1}^{m} \mathbf{B}_{i,j} R_{i,j}^{p,q}(\xi,\eta), \tag{1.28}$$

where $\{\mathbf{B}_i\}$ and $\{\mathbf{B}_{i,j}\}$ are the control points, with $i = 1, 2, ..., n$ and $j = 1, 2, ..., m$.

Analysis framework

We have two notions of mesh in IGA: the physical mesh and the control mesh. The physical mesh represents the exact geometry (i.e., the physical domain), while the control mesh is an scaffold that interpolates the control points (i.e., the parametric domain). A *patch* is a macro-element or subdomain that can be divided into knot spans (also known as *elements*). IGA is an isoparametric method that uses the same basis functions for the geometry and the unknown variables of the problem. In this thesis we use rectangular or cubic elements, so we can overlook the mapping from parametric to physical space. In this thesis we use uniform knot vectors, which form regular and fixed geometries. Since we are not considering deformable geometries, we can overlook the definition of the geometry. The IGA solution of the unknown u in the physical domain may be expressed as

$$u(\mathbf{x}) = \sum_{A=1}^{n_b} u_A N_A(\mathbf{x}), \tag{1.29}$$

where u_A are the *control variables* or degrees of freedom. N_A denotes a generic NURBS (or B-spline) basis function defined on the physical space and n_b is the number of basis functions. The properties of the function u are derived directly from the properties of N_A. The integration of the Galerkin form is performed by standard Gaussian quadrature rules, although novel rules have been recently proposed (Gomez and De Lorenzis, 2016; Hughes *et al.*, 2010), which could improve the efficiency of the computational methods proposed here.

Periodicity

Most of the examples shown in this thesis correspond to problems with periodic boundary conditions. Periodicity is usually enforced by building a system of constraints on the degrees of freedom of the problem. However, periodicity in IGA may be built into the function space due to its simplicity and generality. Periodic boundary conditions are achieved by unclamping[15] the knot vector. Let us consider an open (clamped) knot vector $\Xi = \{\xi_1, \xi_2, ..., \xi_{n+p+1}\}$ that encodes a set of B-spline basis functions $\{N_{i,p}\}_{i=1,...,n}$ of degree p. There are several algorithms (Dalcin *et al.*, 2016) that unclamp the knot vector on the left and right ends for a desired order of continuity $\mathcal{C}^k$, for $0 \geq k \geq p-1$. Figure 1.15 shows the basis functions resulting from unclamping the knot vector with different orders of continuity across the boundary. Note that the number of control variables decreases according to the order of continuity increased across the boundary[16]. In figure 1.15c the continuity across the boundary is $\mathcal{C}^{p-1}$, which is the periodic boundary condition considered in this thesis. In that case, all the basis functions are identical.

[15]Unclamping is a term coined in Piegl and Tiller (2012) through which a knot vector ceases to be open.

[16]From another point of view: the number of control variables does not decrease, but the first and the last control variables take the same values.

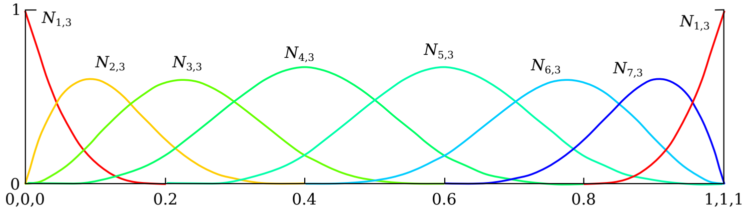

(a) $\mathcal{C}^0$ *periodicity, with* $\Xi' = \{-0.2, 0, 0, 0, 0.2, 0.4, 0.6, 0.8, 1, 1, 1, 1.2\}$.

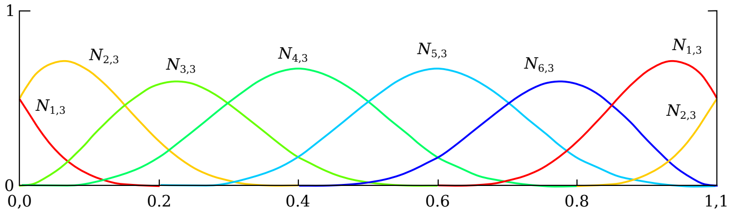

(b) $\mathcal{C}^1$ *periodicity, with* $\Xi' = \{-0.4, -0.2, , 0, 0, 0.2, 0.4, 0.6, 0.8, 1, 1, 1.2, 1.4\}$.

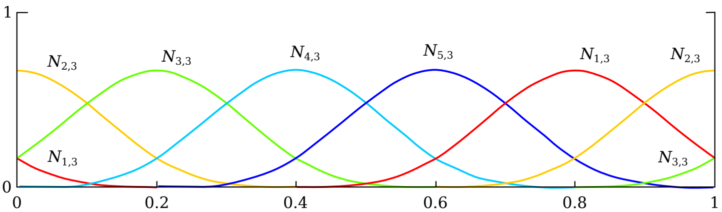

(c) $\mathcal{C}^2$ *periodicity, with* $\Xi' = \{-0.6, -0.4, -0.2, 0, 0.2, 0.4, 0.6, 0.8, 1, 1.2, 1.4, 1.6\}$.

Figure 1.15. Periodicity in B-spline spaces. *Periodic boundary conditions are achieved by modifying the basis functions. The number of basis functions and, hence, the number of control variables are reduced. The examples shown result from unclamping the open knot vector* $\Xi = \{0, 0, 0, 0, 0.2, 0.4, 0.6, 0.8, 1, 1, 1, 1\}$*, which has polynomial order* $p = 3$*. (Adapted from Dalcin* et al.*, 2016)*

1.4 Thesis overview

The rest of the thesis is organized as follows: Chapter 2 introduces a phase-field model applied to the spontaneous migration of a single mesenchymal cell. Chapter 2 also develops the numerical formulation employed throughout the thesis. This formulation constitutes the basis for the numerical methods used in the rest of the chapters. The examples shown in chapter 2 correspond to stationary states of moving keratocytes and different types of periodic migration. In chapter 3 we extend the previous model and propose a mathematical model that accounts for amoeboid motion. We show that our model results are in quantitative agreement with experiments and analyze cell migration in microchannels. We also show a three-dimensional example of cell motion within a fibrous environment. In chapter 4 we extend the model of amoeboid motion and propose a three-dimensional model for chemotactic motion of amoeboid cells. We show two- and three-dimensional simulations of cell migration on planar substrates, flat surfaces with obstacles, and fibrous networks. The results show that our model reproduces the main features of chemotactic amoeboid motion. The results also unveil a complicated interplay between the geometry of the cell's environment and the chemoattractant dynamics that tightly regulates cell motion. Finally, in chapter 5 we present a summary and the conclusions of the thesis. We also indicate the future lines of research originated by this thesis.

At the end of this document, the reader may find a list of publications that resulted from the work in this thesis, the appendices, and the bibliography.

Chapter 2

Phase-field model of mesenchymal cellular migration

In this chapter we present a phase-field model of the spontaneous migration of a single mesenchymal cell. The biochemical interactions between the cellular agents are described through dynamic, nonlinear partial-differential equations. These equations are coupled with a momentum balance law that accounts for the forces involved in cell motion. We also propose a computational method based on isogeometric analysis. The numerical method, which employs $\mathcal{C}^2$-global continuity, permits a robust treatment of the phase-field framework by using a single fixed mesh only. We show numerical examples proving that our phase-field model accurately reproduces mesenchymal cell motility. The examples correspond to stationary states of moving keratocytes and different types of periodic migration in microchannels.

2.1 Introduction

Mesenchymal cell migration (Friedl and Wolf, 2003, 2009) is a very interesting problem in its own right and one that has triggered significant interest in the experimental and theoretical communities. Mesenchymal motion is usually studied by way of experiments with keratocytes (Barnhart *et al.*, 2011; Fournier *et al.*, 2010; Keren *et al.*, 2008). These cells move spontaneously (without any external stimulus) over flat substrates by extending a stationary lamellipodium composed of actin filaments at the leading edge; see figure 2.1a. The end of the filaments pointing to the cell's front is continuously extending due to its polymerization. Meanwhile, myosin contraction causes the displacement of the frontal F-actin network towards the cell's rear, i.e., a backward movement known as retrograde flow (see figure 2.1b). The speed difference between the F-actin assembly and the retrograde flow defines the net velocity at which the cell membrane moves at the cell's front. Thus, cell motion results from the balance between protrusive and contractile forces. Force transmission to the substrate is achieved by integrins, which connect the F-actin network and the substrate; see figure 2.1b. Adhesions are initiated at the cell front and undergo a process of maturation driven by the actomyosin network which leads to the formation of focal adhesions (Choi *et al.*, 2008). These adhesions break down at the cell's rear. As we show later in this chapter, keratocytes exhibit a variety of different motions that the model is able to replicate.

The phase-field method has been previously applied to mesenchymal motion in works, such as, e.g., Camley *et al.* (2013); Löber *et al.* (2014); Shao *et al.* (2012, 2010). The solution of the high-order equations that constitute the phase-field problem, which can not be solved by classical finite element methods that use $\mathcal{C}^0$-continuous basis functions, poses a number of computational challenges. In addition, the definition of the phase field (it takes the value 0 outside the cell)

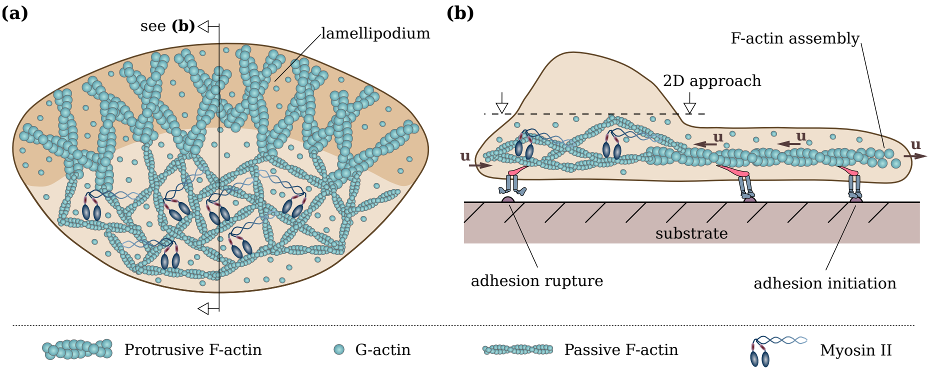

Figure 2.1. Conceptual model of mesenchymal motion. *(a) Mesenchymal motion is produced by the extension of the lamellipodium at the front of the cell and the retraction of the cell's rear caused by myosin. (b) F-actin assembly at the cell's front pushes the membrane forward, while myosin contraction at the cell's body drives the protrusive network inwards (that backwards displacement is called retrograde flow). Cell-substrate adhesion is mediated by integrin. The velocity* **u** *represents the movement of the F-actin network.*

leads to null values of the problem variables in large regions of the domain. The presence of these vanishing values may cause singularities in the equations that must be treated somehow. To our knowledge, this is the first work that develops a numerical method based on IGA to solve phase-field problems of cell migration. Besides the use of IGA, the model presented in this chapter may be appealing for two more reasons: (1) A novel description of the actin dynamics and actin phase transformations. The actin behavior is controlled by a free-energy functional that is rather intuitive and replicates the wave-pinning model of Mori *et al.* (2008); Otsuji *et al.* (2007). (2) Our continuous model incorporates cell-obstacle contact by means of a repulsive force acting in the cell's membrane. This approach is different from other woks that include cell-obstacle interaction through, e.g., a repulsive potential (Zhang *et al.*, 2009), or imposing a vanishing velocity condition (Hecht *et al.*, 2011a) that introduces a discrete component in the model.

The rest of the chapter is organized as follows: we describe the phase-field model of mesenchymal motion in section 2.2. Then, we present the numerical method used to solve the problem in section 2.3. In section 2.4 we test the applicability of the diffuse domain approach to the problem of cell migration and we also show several 2D numerical examples of keratocyte motion. We finalize with the conclusions in section 2.5.

2.2 The model

Our model may be divided into four main compartments describing the cell's motion, the myosin dynamics, the dynamics and phase transformations of actin, and the rheology of the actomyosin network. In what follows, we describe each of these compartments separately. The cytosolic machinery is described by the fields $\rho_f(\mathbf{x}, t)$, $\rho_g(\mathbf{x}, t)$, and $\rho_m(\mathbf{x}, t)$, which represent the density of actin filaments (F-actin), globular actin subunits (G-actin), and myosin II, respectively (see figure 2.1). The actin filament network, which plays a major role in cellular motion, is treated as a viscous fluid with velocity $\mathbf{u}(\mathbf{x}, t)$; see Shao *et al.* (2012) for a rationale.

2.2.1 Cell motion

To define the cell location, we employ the phase-field variable $\phi(\mathbf{x}, t)$. The function ϕ undergoes a smooth but quick transition from 0 (outside the cell) to 1 (inside the cell); see figure 2.2. To leading order ϕ takes a hyperbolic tangent profile in the direction normal to the cell's membrane. The membrane is associated to the

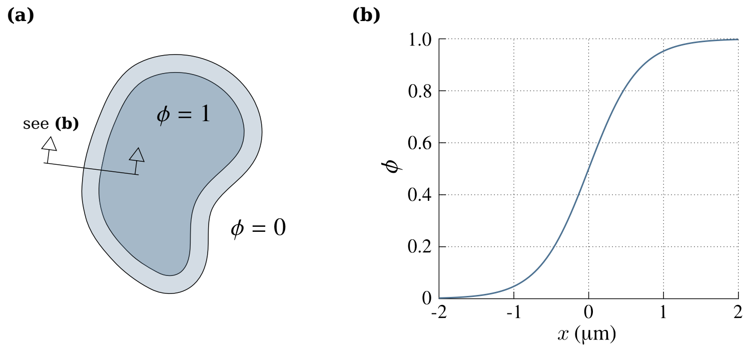

Figure 2.2. Conceptual description of the diffuse domain framework used in the model. *(a) The cell location is implicitly defined by the phase-field variable ϕ. (b) Value of ϕ across the membrane. The plot corresponds to $\varepsilon = 2\,\mu$m.*

diffuse interface defined by the phase field. The dynamics of ϕ are governed by the equation

$$\frac{\partial \phi}{\partial t} + \mathbf{u} \cdot \nabla \phi = \Gamma_\phi \left(\varepsilon \nabla^2 \phi - \frac{G'(\phi)}{\varepsilon} + c\varepsilon |\nabla \phi| \right), \tag{2.1}$$

where Γ_ϕ is a parameter setting the strength of the right hand side, $\mathbf{u}$ is the velocity of the actin network, ε is a length scale that defines the steepness of the diffuse interface, $G(\phi) = 18\phi^2(1-\phi)^2$ is a double well potential with local minima at $\phi = 0$ and $\phi = 1$ (see Shao *et al.*, 2012, 2010), and $c = -\nabla \cdot (\nabla\phi/|\nabla\phi|)$ denotes the curvature of the membrane. The right hand side of equation (2.1) is $\mathcal{O}(\varepsilon)$ and forces the field ϕ to maintain a hyperbolic tangent profile in the direction orthogonal to the cell's membrane. Essentially, equation (2.1) moves the cell's membrane with velocity $\mathbf{u}$, while maintaining a hyperbolic tangent profile. For a full understanding of equation (2.1), the reader is referred to Biben *et al.* (2005); Gomez and van der Zee (2017).

2.2.2 Myosin dynamics

In our model, myosin is transported by the actin network velocity and diffuses throughout the cell. The dynamics of ρ_m are governed by the equation

$$\frac{\partial(\phi\rho_m)}{\partial t} + \nabla \cdot (\phi\rho_m \mathbf{u}) - \nabla \cdot [D_m(\rho_f)\phi\nabla\rho_m] = 0. \tag{2.2}$$

Here, $D_m(\rho_f) = D_m^{\max}/(1+K_m^2\rho_f^2)$, where $D_m^{\max}$ and K_m are constants. Note that ρ_f will usually vary in space, producing a non-constant myosin diffusivity. Since

ρ_f tends to be lower at the back of the cell, D_m will be higher there. This will produce an effective advection of myosin toward the back end of the cell, which is consistent with experimental evidence.

2.2.3 Actin dynamics

Actin undergoes phase transformations between a globular (G-actin) and a filamentous state (F-actin). In addition, F-actin may be in the form of a passive structure or exhibit a protrusive behavior (see figure 2.1). To describe these two forms of F-actin we employ a bistable equation. Passive structures are associated to a stable homogeneous solution of the governing equation and protrusive structures to the other one. Protrusive structures are identified with areas of high F-actin concentration that represent the lamellipodium. We also know that the total amount of actin in the cell, that is,

$$\mathcal{N}[\rho_f, \rho_g] = \int_\Omega \phi(\rho_f + \rho_g) \mathrm{d}\Omega \tag{2.3}$$

must remain constant in time. Thus, we propose the energy functional

$$\mathcal{F}[\rho_f, \rho_g] = \int_\Omega \phi\left[\frac{\varepsilon_f^2}{2}|\nabla\rho_f|^2 + \frac{\varepsilon_g^2}{2}|\nabla\rho_g|^2 + F(\rho_f, \rho_g)\right]\mathrm{d}\Omega + \frac{\alpha_N}{2}(\mathcal{N}_0 - \mathcal{N})^2, \tag{2.4}$$

where ε_f and ε_g represent the diffusive length scales of ρ_f and ρ_g, respectively. The quantity $\mathcal{N}_0$ denotes the total amount of actin at the initial time, that is, $\mathcal{N}_0 = \mathcal{N}[\rho_f(\cdot, 0), \rho_g(\cdot, 0)]$. Therefore, the last term of equation (2.4) energetically penalizes the variations of $\mathcal{N}$ with respect to time and α_N is a suitable penalty constant. The function F controls actin phase transitions and is defined as

$$F(\rho_f, \rho_g) = 10(\rho_f - \rho_f^{\mathrm{pr}})^2(\rho_f - \rho_f^{\mathrm{pa}})^2 + 7.5(\rho_g - \rho_g^{\mathrm{eq}})^2. \tag{2.5}$$

The constants $\rho_f^{\mathrm{pr}} = 3/2$, $\rho_f^{\mathrm{pa}} = 1/2$, and $\rho_g^{\mathrm{eq}} = 1$ represent, respectively, the F-actin concentration associated to protrusive and passive filamentous structures, and the G-actin equilibrium concentration. Using the framework of non-conserved dynamics (see subsection 1.3.2), we derive the evolution equations

$$\frac{\partial(\phi\rho_f)}{\partial t} + \nabla\cdot(\phi\rho_f\mathbf{u}) = -\Gamma_f\frac{\delta\mathcal{F}}{\delta\rho_f} = \Gamma_f\left[\varepsilon_f^2\nabla\cdot(\phi\nabla\rho_f) - \phi\frac{\partial F}{\partial\rho_f} - \alpha_N\phi\big(\mathcal{N} - \mathcal{N}_0\big)\right], \tag{2.6}$$

$$\frac{\partial(\phi\rho_g)}{\partial t} + \nabla\cdot(\phi\rho_g\mathbf{u}) = -\Gamma_g\frac{\delta\mathcal{F}}{\delta\rho_g} = \Gamma_g\left[\varepsilon_g^2\nabla\cdot(\phi\nabla\rho_g) - \phi\frac{\partial F}{\partial\rho_g} - \alpha_N\phi\big(\mathcal{N} - \mathcal{N}_0\big)\right], \tag{2.7}$$

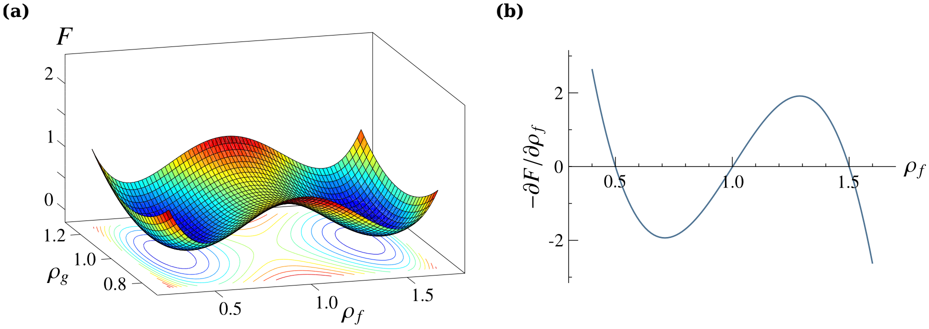

Figure 2.3. Actin free-energy functional. *(a) The minima of the function F establish the stable densities of F-actin and G-actin. (b) The bistable function $-\partial F/\partial \rho_f$ provides the densities for the passive and protrusive F-actin structures.*

where Γ_f and Γ_g are constants. $\delta\mathcal{F}/\delta\rho_f$ and $\delta\mathcal{F}/\delta\rho_g$ denote the variational derivatives of the functional $\mathcal{F}$ with respect to F-actin and G-actin density, respectively.

To gain insight into the dynamics of equations (2.6) and (2.7), we have plotted the function F in figure 2.3a. It may be observed that for a non-moving cell ($\mathbf{u} = 0$) with $\alpha_N = 0$, the homogeneous (constant in space and time) solutions to equations (2.6) and (2.7) are given by the local minima of F. Equation (2.5) shows that F is a convex function of ρ_g.The term $\frac{\partial F}{\partial \rho_g}$, which acts as a driving force in equation (2.7), vanishes at $\rho_g = \rho_g^{\mathrm{eq}}$, which makes this homogeneous state an attractor of the solution. The dynamics of F-actin are more complex because the filaments can undergo phase transformations from a passive to a protrusive structure and vice versa depending on the global state of the cell. F is a non-convex function of ρ_f with $\frac{\partial F}{\partial \rho_f}$ vanishing at $\rho_f = \rho_f^{\mathrm{pr}}$ and $\rho_f \approx \rho_f^{\mathrm{pa}}$; see figure 2.3b. The value $\rho_f = \rho_f^{\mathrm{pr}}$ is associated to protrusive structures which represent the lamellipodium, while the value $\rho_f \approx \rho_f^{\mathrm{pa}}$ is associated to passive networks. The reaction-diffusion system of equations (2.6) and (2.7), which results from the actin free energy proposed in equation (2.4), is equivalent to the wave-pinning model for cell polarity proposed in Otsuji *et al.* (2007) or Mori *et al.* (2008).

2.2.4 Actin flow

The actin filament network is treated as a viscous fluid governed by a Stokes-type equation. At the cellular scale the Reynolds number is very small and we can neglect the nonlinear convective term and inertial forces[1]. Following the rationale presented in Rubinstein *et al.* (2009) we also neglect the pressure term. Therefore, the governing equation is given by

$$\nabla \cdot (\boldsymbol{\sigma} + \boldsymbol{\sigma}_{\mathrm{myo}} + \boldsymbol{\sigma}_{\mathrm{prot}}) + \mathbf{F}_{\mathrm{adh}} + \mathbf{F}_{\mathrm{mem}} + \mathbf{F}_{\mathrm{rep}} = 0, \tag{2.8}$$

where $\boldsymbol{\sigma}$, $\boldsymbol{\sigma}_{\mathrm{myo}}$, and $\boldsymbol{\sigma}_{\mathrm{prot}}$ are Cauchy stress tensors that define the rheology of the actin filament network. $\mathbf{F}_{\mathrm{adh}}$, $\mathbf{F}_{\mathrm{mem}}$, and $\mathbf{F}_{\mathrm{rep}}$ are additional forces acting on the filament network. These include adhesion forces, the membrane forces, and repulsion forces created by rigid obstacles in the cell's path. These forces will be described later. A conceptual description of the forces may be found in figure 2.4. Let us focus first on the rheology of the actin network.

Rheology of the actin network

The stress tensor

$$\boldsymbol{\sigma} = \phi \left[\mu \left(\nabla \mathbf{u} + \nabla \mathbf{u}^T \right) + \lambda (\nabla \cdot \mathbf{u}) \boldsymbol{I} \right] \tag{2.9}$$

is the classical stress tensor of a Newtonian fluid with viscosity coefficients μ and λ. The prefactor ϕ is added to apply the diffuse domain method. The tensor $\boldsymbol{\sigma}_{\mathrm{prot}}$ accounts for F-actin protrusive structures and is given by

$$\boldsymbol{\sigma}_{\mathrm{prot}} = -\phi \rho_f \eta_f(\rho_f) \delta_f \nabla \phi \otimes \nabla \phi. \tag{2.10}$$

Here, ϕ is included again to use the diffuse domain method. The term $\rho_f \eta_f(\rho_f)$, where

$$\eta_f(\rho_f) = \overline{\alpha}_f \overline{\eta}_f + (1 - \overline{\alpha}_f) \overline{\eta}_f \mathcal{H}(\rho_f - \overline{\rho}_f), \tag{2.11}$$

controls the protrusive stress such that it is only significant for large values of ρ_f (lamellipodium). In equation (2.11), $\overline{\alpha}_f$, $\overline{\eta}_f$, and $\overline{\rho}_f = (\rho_f^{\mathrm{pr}} + \rho_f^{\mathrm{pa}})/2$ are constants, while $\mathcal{H}$ is a smoothed-out Heaviside function[2]. The term δ_f annihilates protrusive stresses in the vicinity of rigid obstacles. We take $\delta_f(\mathbf{x}) = \mathcal{H}\left(d_o(\mathbf{x}) - d_o^f\right)$ where $d_o(\mathbf{x})$ is the distance from the point $\mathbf{x}$ to the closest rigid obstacle and d_o^f is a constant that represents an effective distance at which the presence of an obstacle starts to suppress protrusion forces. Since the normal to the cell's membrane $\mathbf{n}_{\Gamma_c}$ is parallel to $\nabla \phi$, it may be easily shown that the traction $\boldsymbol{\sigma}_{\mathrm{prot}} \mathbf{n}_{\Gamma_c}$ is normal to the membrane. In addition, the term $\nabla \phi \otimes \nabla \phi$ localizes $\boldsymbol{\sigma}_{\mathrm{prot}}$ to a neighborhood of the cell's membrane.

[1]Note that due to negligible inertia, cells have to permanently produce forces in order to move.

[2]Throughout this thesis, the smoothed-out Heaviside function is defined as $\mathcal{H}(x) = 0.5 + 0.5 \tanh(7x)$. We use smooth approximations of the Heaviside function to increase the convergence rate of our Newton–Raphson algorithm.

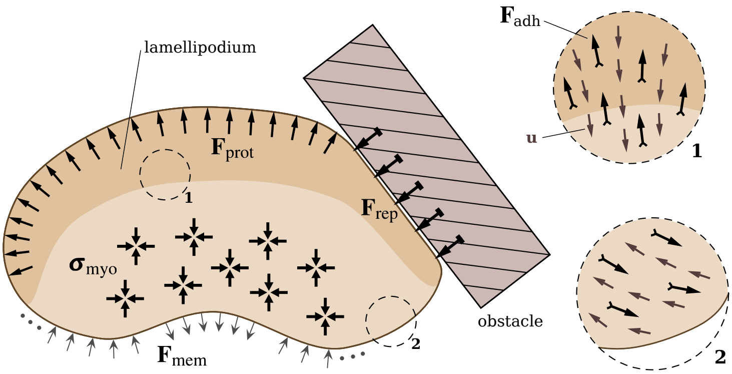

Figure 2.4. Forces acting in the mesenchymal cell. *We consider the protrusion caused by the lamellipodium, the contraction caused by myosin, and the surface tension and bending energy of the membrane. We include a repulsive force generated by the cell-obstacle contact and an adhesive force between the cell and the substrate.*

The tensor $\boldsymbol{\sigma}_{\text{myo}}$ accounts for the isotropic contractile stresses produced by myosin. We propose the expression

$$\boldsymbol{\sigma}_{\text{myo}} = \phi \rho_m \eta_m(\rho_m) \boldsymbol{I}, \tag{2.12}$$

where $\boldsymbol{I}$ is the identity tensor and $\eta_m(\rho_m) = \overline{\alpha}_m \overline{\eta}_m + (1 - \overline{\alpha}_m)\overline{\eta}_m \mathcal{H}(\rho_m - \overline{\rho}_m)$ is a function producing greater stress where myosin concentration is higher. The parameters $\overline{\alpha}_m$, $\overline{\eta}_m$, and $\overline{\rho}_m = 0.9$ play a similar role to $\overline{\alpha}_f$, $\overline{\eta}_f$, and $\overline{\rho}_f$ in equation (2.11).

Membrane forces

The term $\mathbf{F}_{\text{mem}}$ represents the forces exerted by the membrane. Our starting point to derive $\mathbf{F}_{\text{mem}}$ is the so-called Helfrich membrane energy (Canham, 1970; Helfrich, 1973). Let us define a closed surface Γ_c that represents the cell's membrane. For vanishing spontaneous curvature, the Helfrich energy is defined as

$$\mathcal{F}_H[\Gamma_c] = \mathcal{F}_H^B[\Gamma_c] + \mathcal{F}_H^T[\Gamma_c], \tag{2.13}$$

where

$$\mathcal{F}_H^B[\Gamma_c] = \frac{K_c}{2} \int_{\Gamma_c} c^2 \mathrm{d}\Gamma \quad \text{and} \quad \mathcal{F}_H^T[\Gamma_c] = \gamma \int_{\Gamma_c} \mathrm{d}\Gamma. \tag{2.14}$$

Here, K_c is the bending rigidity of the membrane, c is the additive curvature of the surface, and γ denotes the surface tension. Computing the membrane energy (and eventually membrane forces) using equation (2.14) requires an explicit tracking of the membrane. However, we wish to use a formulation consistent with that of the rest of the model and avoid any explicit interface tracking. To do so, we will use the phase-field method, describing Γ_c by the level set $\phi = 1/2$. We will also use several properties of the phase-field method; see Gomez and van der Zee (2017) for a rationale. One of the most useful properties of the phase-field method is that it allows to replace integrals on surfaces with integrals on volumes. For example, it may be shown that

$$\mathcal{F}_H^T[\Gamma_c] = \lim_{\varepsilon \to 0} \mathcal{F}_\varepsilon^T[\phi^\varepsilon]. \tag{2.15}$$

Here,

$$\mathcal{F}_\varepsilon^T[\phi] = \gamma \int\limits_\Omega \left(\frac{G(\phi)}{\varepsilon} + \frac{\varepsilon}{2} |\nabla \phi|^2 \right) \mathrm{d}\Omega \tag{2.16}$$

and $\phi^\varepsilon(\mathbf{x}) = \tanh(d_{\Gamma_c}(\mathbf{x})/\varepsilon)$, where $d_{\Gamma_c}(\mathbf{x})$ is a scaled distance from the point $\mathbf{x}$ to the surface Γ_c and Ω is a sufficiently large subset of $\mathbb{R}^{d_s}$ which may be associated to our computational domain. The advantage of the functional $\mathcal{F}_\varepsilon^T$ with respect to $\mathcal{F}_H^T$ is that the integral in $\mathcal{F}_\varepsilon^T$ is defined on a known and fixed domain. We will also make use of an important property of phase fields referred to as *equipartition of energy* (Fried, 2006), that is,

$$G(\phi^\varepsilon) - \frac{\varepsilon^2}{2} |\nabla \phi^\varepsilon|^2 \to 0 \quad \text{as} \quad \varepsilon \to 0. \tag{2.17}$$

The equipartition property allows us to find alternative expression for $\mathcal{F}_\varepsilon^T$. For example, we know that

$$\mathcal{F}_\varepsilon^T[\phi] \to \gamma \int\limits_\Omega \varepsilon |\nabla \phi|^2 \mathrm{d}\Omega \quad \text{as} \quad \varepsilon \to 0 \tag{2.18}$$

if ϕ is of the form of ϕ^ε, which is guaranteed because equation (2.1) produces solutions with a hyperbolic tangent profile. We can also express the additive curvature of Γ_c, namely c, implicitly in terms of the phase field ϕ. From basic differential geometry, we know

$$c = \nabla_{\Gamma_c} \cdot \mathbf{n}_{\Gamma_c}, \tag{2.19}$$

where $\nabla_{\Gamma_c} \cdot$ denotes the divergence operator on the surface Γ_c. The vector $\mathbf{n}_{\Gamma_c}$ can be expressed in terms of the phase field as $\mathbf{n}_{\Gamma_c} = -\nabla\phi/|\nabla\phi|$ and standard identities of differential geometry may be used to show that

$$c = -\frac{1}{|\nabla \phi|} \left(\nabla^2 \phi - \frac{1}{2|\nabla \phi|^2} \nabla \phi \cdot \nabla(|\nabla \phi|^2) \right). \tag{2.20}$$

Utilizing the property of equipartition of energy, this can be simplified to

$$c \approx -\frac{1}{|\nabla\phi|}\left(\nabla^2\phi - \frac{1}{\varepsilon^2}G'(\phi)\right). \tag{2.21}$$

Using equations (2.18) and (2.21), it may be shown that

$$\mathcal{F}_H^B[\Gamma_c] \approx \mathcal{F}_\varepsilon^B[\phi] = \frac{K_c}{2}\int_\Omega \varepsilon\left(\nabla^2\phi - \frac{1}{\varepsilon^2}G'(\phi)\right)^2 \mathrm{d}\Omega. \tag{2.22}$$

From equation (2.16), we conclude that

$$\mathcal{F}_H^T[\Gamma_c] \approx \mathcal{F}_\varepsilon^T[\phi] = \gamma\int_\Omega \left(\frac{G(\phi)}{\varepsilon} + \frac{\varepsilon}{2}|\nabla\phi|^2\right) \mathrm{d}\Omega. \tag{2.23}$$

Defining $\mathcal{F}_\varepsilon[\phi] = \mathcal{F}_\varepsilon^T[\phi] + \mathcal{F}_\varepsilon^B[\phi] \approx \mathcal{F}_H[\Gamma_c]$, the membrane forces per unit volume may be computed as

$$\mathbf{F}_{\mathrm{mem}} = -\frac{\delta\mathcal{F}_\varepsilon[\phi]}{\delta\Gamma_c}, \tag{2.24}$$

where $\frac{\delta\mathcal{F}_\varepsilon[\phi]}{\delta\Gamma_c}$ denotes the variational derivative of $\mathcal{F}_\varepsilon[\phi]$ with respect to variations of the surface Γ_c in its normal direction. This may be also expressed as

$$\mathbf{F}_{\mathrm{mem}} = \frac{\delta\mathcal{F}_\varepsilon[\phi]}{\delta\phi}\nabla\phi. \tag{2.25}$$

Membrane forces can be split as $\mathbf{F}_{\mathrm{mem}} = \mathbf{F}_{\mathrm{bend}} + \mathbf{F}_{\mathrm{ten}}$ where

$$\mathbf{F}_{\mathrm{bend}} = \frac{\delta\mathcal{F}_\varepsilon^B[\phi]}{\delta\phi}\nabla\phi = K_c\varepsilon\nabla\phi\left[\nabla^2\left(\nabla^2\phi - \frac{G'(\phi)}{\varepsilon^2}\right) - \frac{G''(\phi)}{\varepsilon^2}\left(\nabla^2\phi - \frac{G'(\phi)}{\varepsilon^2}\right)\right], \tag{2.26}$$

$$\mathbf{F}_{\mathrm{ten}} = \frac{\delta\mathcal{F}_\varepsilon^T[\phi]}{\delta\phi}\nabla\phi = \gamma\nabla\phi\left(\frac{G'(\phi)}{\varepsilon} - \varepsilon\nabla^2\phi\right). \tag{2.27}$$

It may be easily shown that $\mathbf{F}_{\mathrm{ten}}$ is a force orthogonal to the cell's membrane and proportional to its curvature.

Adhesion and contact forces

The force $\mathbf{F}_{\mathrm{adh}} = -\varsigma\mathbf{u}$ models a friction force between the cell and the underlying substrate[3], with ς being the friction coefficient. In the biological problem, this force is accomplished by the transmembrane protein family called integrin.

[3] In the case of a three-dimensional simulation, this force may be interpreted as a hydrodynamic drag between actin filaments within the cell.

The force $\mathbf{F}_{\text{rep}}$ models repulsive contact forces produced by rigid solid obstacles in the cell's path. It may be expressed as

$$\mathbf{F}_{\text{rep}} = \nabla \cdot \boldsymbol{\sigma}_{\text{rep}} = \nabla \cdot \left(\phi \eta_{\text{rep}} \delta_{\text{rep}} \nabla \phi \otimes \nabla \phi\right), \tag{2.28}$$

where η_{rep} is a constant and δ_{rep} is a function that depends on the position and acts as a localizer of obstacles. We take

$$\delta_{\text{rep}} = \mathcal{H}\left(d_o^{\text{ef}} - d_o(\mathbf{x})\right), \tag{2.29}$$

where $d_o(\mathbf{x})$ is the distance between the point $\mathbf{x}$ and the closest obstacle and d_o^{ef} is a small constant that represents an effective distance at which the cells feel an obstacle. It can be easily shown that $\mathbf{F}_{\text{rep}}$ is a force normal to the membrane and pointing towards the interior of the cell.

2.2.5 Continuous problem in strong form

Let $\Omega \subset \mathbb{R}^{d_s}$ be an open set that represents our computational domain. Unless otherwise stated, Ω is simply a box sufficiently large to enclose the cell. Let Γ be the boundary of Ω, assumed sufficiently smooth. The strong form of the problem can be stated as: Given a time interval of interest $[0, T]$ and suitable initial and boundary conditions, find $\phi : \overline{\Omega} \times (0,T) \to \mathbb{R}$, $\rho_m : \overline{\Omega} \times (0,T) \to \mathbb{R}$, $\rho_f : \overline{\Omega} \times (0,T) \to \mathbb{R}$, $\rho_g : \overline{\Omega} \times (0,T) \to \mathbb{R}$, and $\mathbf{u} : \overline{\Omega} \times (0,T) \to \mathbb{R}^{d_s}$ such that

$$\frac{\partial \phi}{\partial t} + \mathbf{u} \cdot \nabla \phi = \Gamma_\phi \left(\varepsilon \nabla^2 \phi - \frac{G'(\phi)}{\varepsilon} + c\varepsilon |\nabla \phi| \right) \quad \text{in} \quad \Omega \times (0,T), \tag{2.30}$$

$$\frac{\partial(\phi \rho_m)}{\partial t} + \nabla \cdot (\phi \rho_m \mathbf{u}) = \nabla \cdot \left[D_m(\rho_f) \phi \nabla \rho_m \right] \quad \text{in} \quad \Omega \times (0,T), \tag{2.31}$$

$$\begin{aligned} &\frac{\partial(\phi \rho_f)}{\partial t} + \nabla \cdot (\phi \rho_f \mathbf{u}) = \\ &\quad = \Gamma_f \left[\varepsilon_f^2 \nabla \cdot (\phi \nabla \rho_f) - \phi \frac{\partial F}{\partial \rho_f} - \alpha_N \phi \big(\mathcal{N} - \mathcal{N}_0 \big) \right] \quad \text{in} \quad \Omega \times (0,T), \end{aligned} \tag{2.32}$$

$$\begin{aligned} &\frac{\partial(\phi \rho_g)}{\partial t} + \nabla \cdot (\phi \rho_g \mathbf{u}) = \\ &\quad = \Gamma_g \left[\varepsilon_g^2 \nabla \cdot (\phi \nabla \rho_g) - \phi \frac{\partial F}{\partial \rho_g} - \alpha_N \phi \big(\mathcal{N} - \mathcal{N}_0 \big) \right] \quad \text{in} \quad \Omega \times (0,T), \end{aligned} \tag{2.33}$$

$$\nabla \cdot (\boldsymbol{\sigma} + \boldsymbol{\sigma}_{\text{myo}} + \boldsymbol{\sigma}_{\text{prot}}) + \mathbf{F}_{\text{adh}} + \mathbf{F}_{\text{mem}} + \mathbf{F}_{\text{rep}} = 0 \quad \text{in} \quad \Omega \times (0,T). \tag{2.34}$$

2.3 Numerical formulation

2.3.1 Continuous problem in weak form

Let $\mathcal{S} = \{\, \phi \mid \phi(\cdot,t) \in \mathcal{H}^3(\Omega) \}$ be the trial solution space. Here, $\mathcal{H}^3(\Omega)$ denotes the Sobolev space of square-integrable functions with square-integrable first, second, and third derivatives. Analogously, we define a weighting function space $\mathcal{V} = \{\, w \mid w \in \mathcal{H}^3(\Omega) \}$.

We derive a weak form of equations (2.30) to (2.34) by multiplying them with weighting functions and integrating by parts repeatedly. We work under the assumptions of periodic boundary conditions and sufficient regularity. Let $(\cdot,\cdot)_\Omega$ denote the $\mathcal{L}^2$ inner product with respect to the domain Ω. We call $n_{\text{dof}} = 4 + d_s$ the number of scalar unknowns. Thus, the problem can be stated as: Find $\mathbf{U} = \{\phi, \rho_m, \rho_f, \rho_g, \mathbf{u}\} \in \mathcal{S}^{n_{\text{dof}}}$ such that for all $\mathbf{W} = \{p, q, r, s, \mathbf{w}\} \in \mathcal{V}^{n_{\text{dof}}}$

$$\mathcal{B}(\mathbf{W},\mathbf{U}) = 0 \tag{2.35}$$

with

$$\begin{aligned}
\mathcal{B}(\mathbf{W},\mathbf{U}) = & \left(p, \frac{\partial \phi}{\partial t}\right)_\Omega + \left(q, \phi\frac{\partial \rho_m}{\partial t}\right)_\Omega + \left(q, \rho_m\frac{\partial \phi}{\partial t}\right)_\Omega + \left(r, \phi\frac{\partial \rho_f}{\partial t}\right)_\Omega \\
& + \left(r, \rho_f\frac{\partial \phi}{\partial t}\right)_\Omega + \left(s, \phi\frac{\partial \rho_g}{\partial t}\right)_\Omega + \left(s, \rho_g\frac{\partial \phi}{\partial t}\right)_\Omega + \left(p, \mathbf{u}\cdot\nabla\phi\right)_\Omega \\
& + \left(\nabla p, \Gamma_\phi \varepsilon \nabla\phi\right)_\Omega + \left(p, \Gamma_\phi \frac{G'}{\varepsilon}\right)_\Omega - \left(\nabla p, \Gamma_\phi \varepsilon \nabla\phi\right)_\Omega \\
& - \left(p, \frac{\Gamma_\phi \varepsilon}{|\nabla\phi|}\nabla\phi\cdot\nabla\left(|\nabla\phi|\right)\right)_\Omega - \left(\nabla q, \phi\rho_m\mathbf{u}\right)_\Omega + \left(\nabla q, D_m\phi\nabla\rho_m\right)_\Omega \\
& - \left(\nabla r, \phi\rho_f\mathbf{u}\right)_\Omega + \left(\nabla r, \Gamma_f\varepsilon_f^2\phi\nabla\rho_f\right)_\Omega + \left(r, \Gamma_f\phi\frac{\partial F}{\partial \rho_f}\right)_\Omega \\
& + \left(r, \Gamma_f\alpha_N\phi\left(\mathcal{N}-\mathcal{N}_0\right)\right)_\Omega - \left(\nabla s, \phi\rho_g\mathbf{u}\right)_\Omega + \left(\nabla s, \Gamma_g\varepsilon_g^2\phi\nabla\rho_g\right)_\Omega \\
& + \left(s, \Gamma_g\phi\frac{\partial F}{\partial \rho_g}\right)_\Omega + \left(s, \Gamma_g\alpha_N\phi\left(\mathcal{N}-\mathcal{N}_0\right)\right)_\Omega \\
& - \left(\nabla \mathbf{w}, \phi\left[\mu\left(\nabla\mathbf{u}+\nabla\mathbf{u}^T\right)+\lambda\left(\nabla\cdot\mathbf{u}\right)\boldsymbol{I}\right]\right)_\Omega - \left(\nabla\mathbf{w}, \phi\rho_m\eta_m\boldsymbol{I}\right)_\Omega
\end{aligned}$$

$$
\begin{aligned}
&+\left(\nabla \mathbf{w}, \phi \rho_f \eta_f \delta_f \nabla \phi \otimes \nabla \phi\right)_\Omega - \left(\mathbf{w}, \varsigma \mathbf{u}\right)_\Omega \\
&- \left(\mathbf{w}, \gamma \left(\varepsilon \nabla^2 \phi - \frac{G'}{\varepsilon}\right) \nabla \phi\right)_\Omega - \left(\nabla \left(\mathbf{w} \cdot \nabla \phi\right), K_c \varepsilon \nabla \left(\nabla^2 \phi\right)\right)_\Omega \\
&+ \left(\nabla \left(\mathbf{w} \cdot \nabla \phi\right), \frac{K_c}{\varepsilon} G'' \nabla \phi\right)_\Omega - \left(\mathbf{w}, \frac{K_c}{\varepsilon} G'' \nabla^2 \phi \nabla \phi\right)_\Omega \\
&+ \left(\mathbf{w}, \frac{K_c}{\varepsilon^3} G' G'' \nabla \phi\right)_\Omega - \left(\nabla \mathbf{w}, \phi \eta_{\mathrm{rep}} \delta_{\mathrm{rep}} \nabla \phi \otimes \nabla \phi\right)_\Omega .
\end{aligned} \tag{2.36}
$$

2.3.2 Semidiscrete formulation

The discretization of equations (2.35) and (2.36) cannot be done using classical finite elements because the discrete trial and weight function spaces need to be a subset of $\mathcal{H}^3(\Omega)$; otherwise the integrals in equation (2.36) are not well defined. Classical finite element spaces spanned by basis functions which are $\mathcal{C}^0$-continuous across element boundaries do not permit to generate discrete spaces contained in $\mathcal{H}^3$. To overcome this limitation, we make use of isogeometric analysis (Cottrell *et al.*, 2009; Hughes *et al.*, 2005); see subsection 1.3.3. IGA uses B-splines or non-uniform B-splines (NURBS) to define the discrete spaces. B-splines and NURBS have controllable global continuity which permits to define discrete spaces that are subsets of $\mathcal{H}^3(\Omega)$. The discretization of equations (2.35) and (2.36) requires the use of at least cubic splines with $\mathcal{C}^2$-global continuity. These functions can be easily generated as shown in Piegl and Tiller (2012). Let us call $\mathcal{S}^h$ and $\mathcal{V}^h$ the trial and weighting function discrete spaces, which are assumed to be identical. The spline basis functions are generically denoted by N_A so that $\mathcal{S}^h = \mathcal{V}^h = \mathrm{span}\{N_A\}_{A=1}^{n_b}$, where n_b is the dimension of the discrete space.

The discrete problem can be stated as: Find $\mathbf{U}^h = \{\phi^h, \rho_m^h, \rho_f^h, \rho_g^h, \mathbf{u}^h\} \in (\mathcal{S}^h)^{n_{\mathrm{dof}}}$ such that for all $\mathbf{W}^h = \{p^h, q^h, r^h, s^h, \mathbf{w}^h\} \in (\mathcal{V}^h)^{n_{\mathrm{dof}}}$

$$
\mathcal{B}(\mathbf{W}^h, \mathbf{U}^h) = 0 \tag{2.37}
$$

where

$$
\phi^h(\mathbf{x}, t) = \sum_{A=1}^{n_b} \phi_A(t) N_A(\mathbf{x}), \qquad p^h(\mathbf{x}) = \sum_{A=1}^{n_b} p_A N_A(\mathbf{x}). \tag{2.38}
$$

The rest of the variables in $\mathbf{U}^h$ and $\mathbf{W}^h$ are defined analogously.

Remark:

1. In subsection 2.4.2 we will show that the bending resistance of the membrane is negligible with respect to the remaining acting forces. In all sections other than *Influence of the bending energy of the membrane* in subsection 2.4.2, our computations do not include the bending energy and, therefore, the discrete space needs to be $\mathcal{H}^2$-conforming only. In this case, employing quadratic NURBS basis functions, which are globally $\mathcal{C}^1$-continuous, the Galerkin form is well defined and the computations are usually faster in our implementation[4].

2.3.3 Time discretization and numerical implementation

At this stage, our formulation remains continuous in time. Here, we describe our time-stepping scheme, which is based on the generalized-α method. The generalized-α method was originally derived in Chung and Hulbert (1993) for the equations of structural dynamics and subsequently applied to turbulence computations (Jansen *et al.*, 2000) and to the Cahn–Hilliard phase-field model in Gómez *et al.* (2008).

Time stepping scheme

To illustrate our method, let us divide the time interval of interest $[0, T]$ into a sequence of subintervals (t_n, t_{n+1}) with fixed time-step size $\Delta t = t_{n+1} - t_n$. We define the following residual vectors

$$\mathbf{R}^\Phi = \left\{R_A^\Phi\right\}, \quad \mathbf{R}^M = \left\{R_A^M\right\}, \quad \mathbf{R}^F = \left\{R_A^F\right\}, \quad \mathbf{R}^G = \left\{R_A^G\right\}, \quad \mathbf{R}^U = \left\{R_{A,j}^U\right\}. \tag{2.39}$$

Here, $A \in \{1, \ldots, n_b\}$ is a control-variable index, and j is a dimension index which runs from 1 to d_s. The components of the residual vector are given by

$$R_A^\Phi = \mathcal{B}\left(\{N_A, 0, 0, 0, 0\}, \{\phi^h, \rho_m^h, \rho_f^h, \rho_g^h, \mathbf{u}^h\}\right), \tag{2.40}$$

$$R_A^M = \mathcal{B}\left(\{0, N_A, 0, 0, 0\}, \{\phi^h, \rho_m^h, \rho_f^h, \rho_g^h, \mathbf{u}^h\}\right), \tag{2.41}$$

$$R_A^F = \mathcal{B}\left(\{0, 0, N_A, 0, 0\}, \{\phi^h, \rho_m^h, \rho_f^h, \rho_g^h, \mathbf{u}^h\}\right), \tag{2.42}$$

[4] $\mathcal{C}^2$-continuous cubic functions are slower than $\mathcal{C}^1$ quadratics due to the use of sub-optimal element-based Gaussian quadrature in our implementation. Alternative quadratures and/or assembly methods can be used that speed up the computations dramatically (Calabrò *et al.*, 2017). Another alternative is to use collocation methods (Auricchio *et al.*, 2010). An important feature of IGA that was recently noticed is that it is possible to define collocation points that render the Galerkin solution exactly (Gomez and De Lorenzis, 2016).

$$R^G_A = \mathcal{B}\left(\{0,0,0,N_A,0\},\{\phi^h,\rho^h_m,\rho^h_f,\rho^h_g,\mathbf{u}^h\}\right), \tag{2.43}$$

$$R^U_{A,j} = \mathcal{B}\left(\{0,0,0,0,N_A\mathbf{e}_j\},\{\phi^h,\rho^h_m,\rho^h_f,\rho^h_g,\mathbf{u}^h\}\right), \tag{2.44}$$

where $\mathbf{e}_j$ denotes the j-th unit vector of the Cartesian basis. Let us call $\mathbf{V}$ and $\dot{\mathbf{V}}$ the global vector of control variables of the degrees of freedom and its time derivative. Let us denote $\mathbf{V}_n$ and $\dot{\mathbf{V}}_n$ the time-discrete approximations of $\mathbf{V}$ and $\dot{\mathbf{V}}$ at time t_n. Using this notation, our time-integration algorithm may be defined as follows: Given $\dot{\mathbf{V}}_n$, $\mathbf{V}_n$, and Δt, find $\dot{\mathbf{V}}_{n+1}$, $\mathbf{V}_{n+1}$, $\dot{\mathbf{V}}_{n+\alpha_m}$, and $\mathbf{V}_{n+\alpha_f}$ such that

$$\mathbf{R}^\Phi\left(\dot{\mathbf{V}}_{n+\alpha_m},\mathbf{V}_{n+\alpha_f}\right) = 0, \tag{2.45}$$

$$\mathbf{R}^M\left(\dot{\mathbf{V}}_{n+\alpha_m},\mathbf{V}_{n+\alpha_f}\right) = 0, \tag{2.46}$$

$$\mathbf{R}^F\left(\dot{\mathbf{V}}_{n+\alpha_m},\mathbf{V}_{n+\alpha_f}\right) = 0, \tag{2.47}$$

$$\mathbf{R}^G\left(\dot{\mathbf{V}}_{n+\alpha_m},\mathbf{V}_{n+\alpha_f}\right) = 0, \tag{2.48}$$

$$\mathbf{R}^U\left(\dot{\mathbf{V}}_{n+\alpha_m},\mathbf{V}_{n+\alpha_f}\right) = 0, \tag{2.49}$$

$$\dot{\mathbf{V}}_{n+\alpha_m} = \dot{\mathbf{V}}_n + \alpha_m\left(\dot{\mathbf{V}}_{n+1} - \dot{\mathbf{V}}_n\right), \tag{2.50}$$

$$\mathbf{V}_{n+\alpha_f} = \mathbf{V}_n + \alpha_f\left(\mathbf{V}_{n+1} - \mathbf{V}_n\right), \tag{2.51}$$

$$\mathbf{V}_{n+1} = \mathbf{V}_n + \Delta t\dot{\mathbf{V}}_n + \chi\Delta t\left(\dot{\mathbf{V}}_{n+1} - \dot{\mathbf{V}}_n\right), \tag{2.52}$$

where α_m, α_f, and χ are real-valued parameters that define the method. These parameters are selected based on considerations of accuracy and stability. Jansen *et al.* (2000) proved that, for a model problem, second-order accuracy in time is achieved if

$$\chi = \frac{1}{2} + \alpha_m - \alpha_f, \tag{2.53}$$

while unconditional stability is attained if

$$\alpha_m \geq \alpha_f \geq \frac{1}{2}. \tag{2.54}$$

The method parameters can be expressed in terms of ϱ_∞, the spectral radius of the amplification matrix as $\Delta t \to \infty$, by way of the relations

$$\alpha_m = \frac{1}{2}\left(\frac{3-\varrho_\infty}{1+\varrho_\infty}\right), \tag{2.55}$$

$$\alpha_f = \frac{1}{1+\varrho_\infty}. \tag{2.56}$$

Setting χ according to equation (2.53), a family of second-order accurate and unconditionally A-stable time integration schemes is defined in terms of the parameter $\varrho_\infty \in [0,1]$. The value $\varrho_\infty = 0.5$ has proved an effective choice for turbulence computations and for the Cahn–Hilliard phase-field model (Gómez *et al.*, 2008). We adopt this value for all the simulations presented in this thesis.

The nonlinear system of equations (2.45) to (2.52) is approximated by using Newton–Raphson's method. Our initial guesses for the control variables at time t_{n+1} are:

$$\mathbf{V}_{n+1,(0)} = \mathbf{V}_n, \tag{2.57}$$

$$\dot{\mathbf{V}}_{n+1,(0)} = \frac{\chi - 1}{\chi}\dot{\mathbf{V}}_n. \tag{2.58}$$

Then, we perform the nonlinear iterations by repeating the following steps for $i = 1, 2, \cdots, i_{\max}$, or until convergence is achieved:

1. Evaluate the global unknowns at intermediate time levels

$$\mathbf{V}_{n+\alpha_f,(i)} = \mathbf{V}_n + \alpha_f \left(\mathbf{V}_{n+1,(i-1)} - \mathbf{V}_n\right), \tag{2.59}$$

$$\dot{\mathbf{V}}_{n+\alpha_m,(i)} = \dot{\mathbf{V}}_n + \alpha_m \left(\dot{\mathbf{V}}_{n+1,(i-1)} - \dot{\mathbf{V}}_n\right). \tag{2.60}$$

2. Use the intermediate time levels of the i-th Newton iteration to compute the tangent matrix $\mathbf{K}_{,(i)}$ and the residual vector $\mathbf{R}_{,(i)}$. Once the tangent matrix and the residual vector are computed, the global linear system

$$\mathbf{K}_{,(i)}\Delta\mathbf{V}_{n+1,(i)} = -\mathbf{R}_{,(i)}, \tag{2.61}$$

   is solved up to a given tolerance using the GMRES method (Saad and Schultz, 1986) with the incomplete LU preconditioner (Chan and Van der Vorst, 1997).

3. Use $\Delta\mathbf{V}_{n+1,(i)}$ to update the Newton–Raphson iterates as follows

$$\mathbf{V}_{n+1,(i)} = \mathbf{V}_{n+1,(i-1)} + \Delta\mathbf{V}_{n+1,(i)}, \tag{2.62}$$

$$\dot{\mathbf{V}}_{n+1,(i)} = \dot{\mathbf{V}}_{n+1,(i-1)} + \frac{1}{\chi\Delta t}\mathbf{V}_{n+1,(i)}. \tag{2.63}$$

   This completes one nonlinear iteration.

The nonlinear iterative algorithm is repeated until the norm of each of the residual vectors $\mathbf{R}^\Phi$, $\mathbf{R}^M$, $\mathbf{R}^F$, $\mathbf{R}^G$, and $\mathbf{R}^U$ has been reduced to a given tolerance. In our computations, we set this tolerance to 10^{-4}.

Redefinition of the tangent matrix and the residual vector to avoid singularities

Due to the use of the diffuse domain method, we embedded the cell in a larger computational box. Outside of the cell most of the unknowns approach the value zero and the governing equations are not relevant. This increases dramatically the condition number of the tangent matrix, leading to an inefficient algorithm. The unknowns that create this problem outside the cell ($\phi \approx 0$) are ρ_m, ρ_f, and ρ_g. To overcome this problem we propose the following procedure. After assembling the global residual vector and tangent matrix, we proceed as follows:

(i) Establish the threshold $\phi^T = 10^{-8}$ using the current nonlinear iteration of ϕ at the α_f time level; see figure 2.5.

(ii) Define the spatial domain $\Omega_\phi = \{\, \mathbf{x} \mid \phi > \phi^T \}$.

(iii) Denote by $k_{\max} = n_b\, n_{\mathrm{dof}}$ the number of entries of the global vector of control variables $\mathbf{V}$. Let V_k be the k-th entry of $\mathbf{V}$. For $k = 1, \cdots, k_{\max}$, proceed as follows:

   1. If V_k is a control variable of the unknowns ρ_m, ρ_f, or ρ_g associated to the basis function N_A, compute the support of N_A and denote it by Ω_A.

   2. If $\Omega_\phi \cap \Omega_A = \varnothing$, then, perform the following two steps:

      2.1. Replace the row k of the global tangent matrix by the row k of the $k_{\max} \times k_{\max}$ identity matrix.

      2.2. Replace the k-th entry of the global residual vector by 0.

(iv) Solve the linear system of equation (2.61) with the updated tangent matrix and residual vector.

We found that this strategy worked successfully in all of our numerical examples and rendered tangent matrices with acceptable condition numbers.

Remarks:

1. Note that the entries of the tangent matrix and residual vector corresponding to velocity control variables are not modified in the procedure outlined above. This is because the adhesion force has been defined as $\mathbf{F}_{\mathrm{adh}} = -\varsigma \mathbf{u}$. This produces a contribution to the tangent matrix that is proportional to the mass matrix. Therefore, those blocks of the tangent matrix are well defined. The Stokes-type equation (2.34) essentially becomes $\varsigma \mathbf{u} \approx 0$ outside the cell,

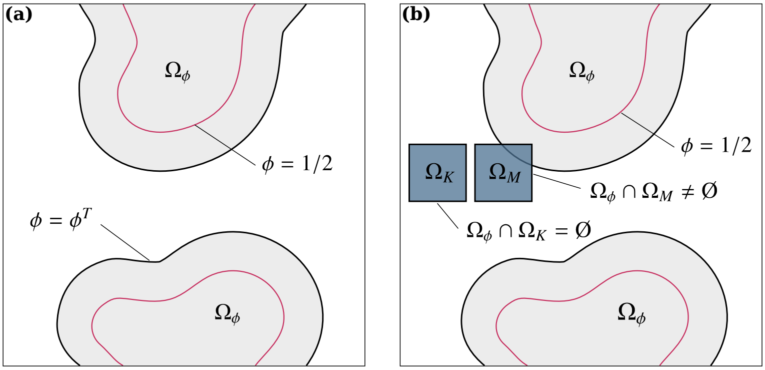

Figure 2.5. Different subdomains defined in the mesenchymal problem. *(a) Ω_ϕ is the region where the entries of the residual and the tangent associated to the unknowns ρ_m, ρ_f, and ρ_g are not modified. (b) Ω_M and Ω_K are the supports of the basis functions N_M and N_K. Ω_M overlaps with Ω_ϕ, while Ω_K does not.*

which leads to a vanishing velocity away from the cell. Having said this, we acknowledge that perhaps a more conceptually consistent strategy would have been to define $\mathbf{F}_{\text{adh}} = -\varsigma\phi\mathbf{u}$ and use the redefinition of the tangent and residual described before also for the velocity control variables. We have opted for simplicity rather than conceptual consistency in this case.

2. Note that the term $(\nabla p, \Gamma_\phi \varepsilon \nabla\phi)$ appears twice with opposite sign in equation (2.36), and we have not suppressed them. This is because they come from different addends in equation (2.30) and one of them is subject to the following procedure: The quantity $\Gamma_\phi c\varepsilon|\nabla\phi|$ of the phase-field equation (2.30) produces the term $-\left(\nabla N_A, \Gamma_\phi\varepsilon\nabla\phi\right) - \left(N_A, \frac{\Gamma_\phi\varepsilon}{|\nabla\phi|}\nabla\phi\cdot\nabla\left(|\nabla\phi|\right)\right)$ in the component R_A^Φ of the residual vector. At regions far from the membrane, where $|\nabla\phi| \approx 0$, the above-mentioned term of the residual as well as its contribution to the tangent are not well defined. To overcome this problem, we have set the term $\Gamma_\phi c\varepsilon|\nabla\phi|$ to zero when computing the residual and tangent in the region $\Omega_{|\nabla\phi|} = \{\, \mathbf{x} \mid |\nabla\phi| < |\nabla\phi|^T\}$ with $|\nabla\phi|^T = 10^{-8}$. In the subdomain $\Omega_{|\nabla\phi|}$, equation (2.30) becomes the Allen–Cahn equation (Allen and Cahn, 1979) that keeps stable the values $\phi = 0$ and $\phi = 1$, producing the desired solution. Note that there are other ways to achieve a similar result, e.g., using for the control variables of ϕ a similar procedure to that used for the control variables of ρ_m, ρ_f, and ρ_g, but in the spatial domain $\Omega\backslash\Omega_{|\nabla\phi|}$; see *Redefinition of the tangent matrix and the residual vector to avoid singularities* in subsection 2.3.3. Unless otherwise stated, this rationale applies to the numerical implementation of the models proposed

in the following chapters.

3. The term δ_{rep} in equation (2.28) is a marker that localizes the obstacles; see equation (2.29). To provide the net distance between the obstacle and the cell membrane we replace $d_o(\mathbf{x})$ with $d_o^\star(\mathbf{x})$ in equation (2.29), where the field $d_o^\star(\mathbf{x})$ is a constant extension of the field $d_o(\mathbf{x})$ at the level set $\phi = 1/2$ in the direction orthogonal to the membrane. Mathematically, this can be expressed as $d_o^\star(\mathbf{x}) = d_o\left(\boldsymbol{\Psi}(\mathbf{x})\right)$ where $\boldsymbol{\Psi}(\mathbf{x})$ is the closest point to $\mathbf{x}$ such that $\phi\left(\boldsymbol{\Psi}(\mathbf{x})\right) = 1/2$; see figure 2.6a.

4. Our numerical experiments indicate that it may be beneficial to treat explicitly, rather than implicitly, some of the terms of the residual vector. This implies that some of the terms in the residual vector are evaluated at time t_n, rather than $t_{n+\alpha_f}$ as indicated in equations (2.45) to (2.49). In particular, treating explicitly $\mathcal{N}$ and δ_{rep} speeds up the computations significantly without compromising the accuracy and stability of the algorithm. In all the numerical examples presented in this thesis we treated $\mathcal{N}$ and δ_{rep} explicitly.

5. The cells that we analyze in this study can move up to a distance equivalent to their diameter in one minute. Therefore, to perform simulations for a time interval of $\sim 20\,\text{min}$, which is what we are interested on, we would need a computational box with side length 20 times larger than the cell if we want to avoid the cell touching the boundary. This is not viable from the computational point of view, so we use periodic boundary conditions. The use of periodic boundary conditions solves the problem, but we have to consider two important points: (1) The periodic box should be large enough to avoid that the cell front touches the cell back. (2) Some of the

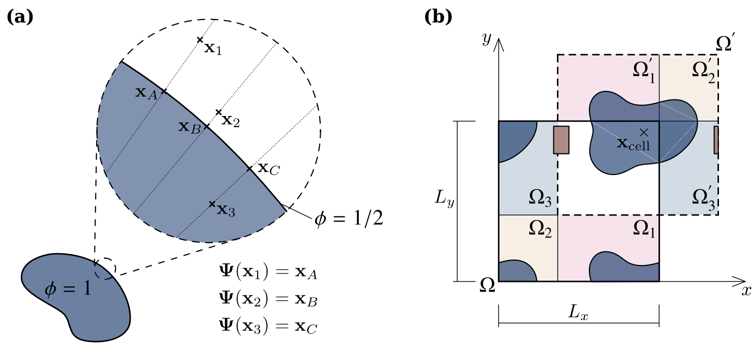

Figure 2.6. Techniques used in the numerical implementation. *(a) Definition of the mapping $\boldsymbol{\Psi}$ that projects a given point to its closest point on the membrane. (b) Mapping redefining the domain. Computational domain Ω and translated domain Ω'.*

terms in the governing equations depend on distances. On a periodic box, the cell may, e.g., exit the box through the right boundary and enter again through the left side. At an intermediate step the cell may look like "broken" in the computational box. In a situation like this, we proceed as follows: Consider the 2D example presented in figure 2.6b, in which the cell is split into four pieces. The solid square represents the computational domain $\Omega = [0, L_x] \times [0, L_y]$. Right after computing every time step, we define the domain Ω' (dashed line in figure 2.6b), which has the same geometry as Ω, but is centered at the cell's center of mass $\mathbf{x}_{\text{cell}}$. Once Ω' is determined, we can define Ω_1, Ω_2, and Ω_3 as shown in figure 2.6b. To reconstitute the cell and all field variables in the domain Ω', we define the transformation $\Sigma(\mathbf{x})$ such that $\mathbf{x}' = \Sigma(\mathbf{x})$ where

$$\Sigma(\mathbf{x}) = \begin{cases} \mathbf{x} + \{0, L_y\}^T & \text{if } \mathbf{x} \in \Omega_1 \\ \mathbf{x} + \{L_x, L_y\}^T & \text{if } \mathbf{x} \in \Omega_2 \\ \mathbf{x} + \{L_x, 0\}^T & \text{if } \mathbf{x} \in \Omega_3 \\ \mathbf{x} & \text{otherwise.} \end{cases} \tag{2.64}$$

Then, a function $f(\mathbf{x})$ defined in Ω can be defined in Ω' as $f\left(\Sigma^{-1}(\mathbf{x}')\right)$. Once all the relevant fields are defined in Ω', we can directly compute distances. Note that in a problem of cellular migration with obstacles, the transformation Σ also needs to be applied to the obstacles; see figure 2.6b where we represented a rigid rectangular obstacle in brown color. Although we illustrated the concept in 2D, the procedure can be easily extended to 3D problems. The mapping Σ is applied in all the examples presented in this thesis that consider periodic boundary conditions.

6. The algorithm explained above to avoid singularities in the tangent matrix may be replaced by another procedure that we found to be more efficient computationally. The alternative procedure modifies the strong form of the problem by redefining the variables such that $\hat{\rho}_m = \phi\rho_m$, $\hat{\rho}_f = \phi\rho_f$, and $\hat{\rho}_g = \phi\rho_g$. This requires posing the equations of the new system in different subdomains of Ω. A complete description of this procedure may be found in appendix B. The procedure, though complex, avoids the redefinition of the tangent matrix and the residual vector, which speeds up the numerics.

2.4 Numerical examples

In this section we present several 2D numerical examples computed using our proposed model and discretization scheme. We used different computational domains and meshes, but we took the same time step $\Delta t = 0.05\,\text{s}$ for all the numerical examples. The code used to perform these simulations has been developed on top of PetIGA (Collier *et al.*, 2013b; Vignal *et al.*, 2013). PetIGA adds NURBS discretization capabilities and integration of forms to the scientific library PETCs (Balay *et al.*, 2016), which allows for parallel computing.

2.4.1 Diffuse domain approach

Here, we show how the diffuse domain approach can be utilized to solve PDEs on moving domains using a fixed background mesh only. We focus on an idealized case in which a perfectly circular cell is traveling with constant velocity $\mathbf{u}_\phi$. Since the cell's velocity is known and fixed, we neglect the actin flow and the presence of membrane-bound components. We consider only a generic cytosolic compound ρ_c that diffuses within the cell. To test the diffuse domain approach we compute a reference solution by solving the problem: Find $\rho_c : \overline{\Omega}_R \times (0,T) \to \mathbb{R}$ such that

$$\frac{\partial \rho_c}{\partial t} = D\nabla^2 \rho_c, \quad \text{in} \quad \Omega_R \times (0,T) \tag{2.65}$$

$$\nabla \rho_c \cdot \mathbf{n}_{\Gamma_R} = 0, \quad \text{on} \quad \Gamma_R \times (0,T) \tag{2.66}$$

$$\rho_c(\mathbf{x},0) = \rho_c^0(\mathbf{x}), \quad \text{in} \quad \overline{\Omega}_R \tag{2.67}$$

where $\rho_c^0 : \overline{\Omega}_R \to \mathbb{R}$ is a function that represents the initial value of ρ_c and Ω_R is a fixed circular domain. Γ_R denotes the boundary of Ω_R and $\mathbf{n}_{\Gamma_R}$ its unit outward normal. The circle Ω_R is centered at the origin of coordinates and its radius is 10 µm. The reference solution is computed as $\rho_c^{\mathrm{Ref}}(\mathbf{x},t) = \rho_c(\mathbf{x}-\mathbf{u}_\phi t, t)$ to account for the cell's motion. The boundary-value problem (2.65)–(2.67) is solved using a NURBS mesh that represents exactly the circular domain Ω_R. We used quadratic functions with 200 elements in the circumferential direction and 100 elements in the radial direction; see figure 2.7a.

To solve this problem using the diffuse domain method (see subsection 1.3.2) we define the box $\overline{\Omega} = [-L,L]^2$ where $L = 20$ µm and we solve the problem: Find $\phi : \overline{\Omega} \times (0,T) \to \mathbb{R}$ and $\hat{\rho}_c : \overline{\Omega} \times (0,T) \to \mathbb{R}$ such that

$$\frac{\partial \phi}{\partial t} + \mathbf{u}_\phi \cdot \nabla\phi = \Gamma_\phi \left(\varepsilon \nabla^2 \phi - \frac{G'(\phi)}{\varepsilon} + c\varepsilon |\nabla \phi| \right), \quad \text{in} \quad \Omega \times (0,T) \tag{2.68}$$

$$\frac{\partial (\phi \hat{\rho}_c)}{\partial t} + \nabla \cdot (\phi \hat{\rho}_c \mathbf{u}_\phi) = \nabla \cdot (D\phi \nabla \hat{\rho}_c), \quad \text{in} \quad \Omega \times (0,T) \tag{2.69}$$

$$\phi(\mathbf{x},0) = \phi_0(\mathbf{x}), \quad \text{in} \quad \overline{\Omega} \tag{2.70}$$

$$\hat{\rho}_c(\mathbf{x},0) = \rho_c^0(\mathbf{x}), \quad \text{in} \quad \overline{\Omega} \tag{2.71}$$

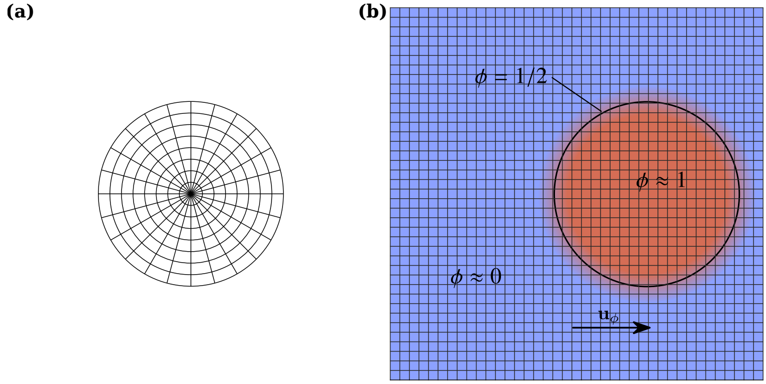

Figure 2.7. Diffuse domain approach. *(a) NURBS mesh used to solve the boundary-value problem (2.65)–(2.67). (b) NURBS mesh used to solve problem (2.68)–(2.71) and implicit representation of the circular cell using the phase-field ϕ. Both meshes are coarser than the meshes used in the actual computations to allow for a clearer visualization.*

with periodic boundary conditions in all directions. Here, $\hat{\rho}_c$ is meant to be an approximation to ρ_c^{Ref} and $\phi_0 : \overline{\Omega} \to \mathbb{R}$ is a phase field that defines the initial position of the cell. More specifically, we took $\phi_0(\mathbf{x}) = \frac{1}{2} - \frac{1}{2}\tanh\left[\frac{2\sqrt{2}}{\varepsilon}\left(d_c(\mathbf{x}) - R_c\right)\right]$ where $R_c = 10\,\mu\text{m}$ is the cell radius and $d_c(\mathbf{x})$ is the distance between the point $\mathbf{x}$ and the origin of coordinates. Note that the field ϕ_0 takes the value ~ 1 in Ω_R and ~ 0 in the rest of the box; see figure 2.7b. Equation (2.68) essentially moves the cell with velocity $\mathbf{u}_\phi$ while maintaining a hyperbolic tangent profile in the direction orthogonal to the membrane. We meshed the computational domain Ω using 400^2 quadratic NURBS elements.

We used the parameters $D = 10\,\mu\text{m}^2\text{s}^{-1}$ and $\mathbf{u}_\phi = \{0.6, 0\}^T\,\mu\text{m}\,\text{s}^{-1}$ for both the reference solution and the diffuse domain approach. For the diffuse domain approach we also set $\varepsilon = 1.0\,\mu\text{m}$ and $\Gamma_\phi = 0.4\,\mu\text{m}\,\text{s}^{-1}$, which provides a reasonable compromise between accuracy and computational time for the purpose of this section.

We first solved the problem taking $\rho_c^0(\mathbf{x}) = 10H\left(5.0 - d_c(\mathbf{x})\right)$ where H denotes the Heaviside function. Figure 2.8a shows contour lines of ρ_c^{Ref} and $\hat{\rho}_c$ in the cell's interior at times 0, 10, 20, and 30 s. The solution provided by the diffuse domain method is indistinguishable from the reference solution at the scale of the plots. More accurate results could be obtained using a finer mesh and a smaller value of ε.

We performed a similar computation using as initial distribution of ρ_c the function

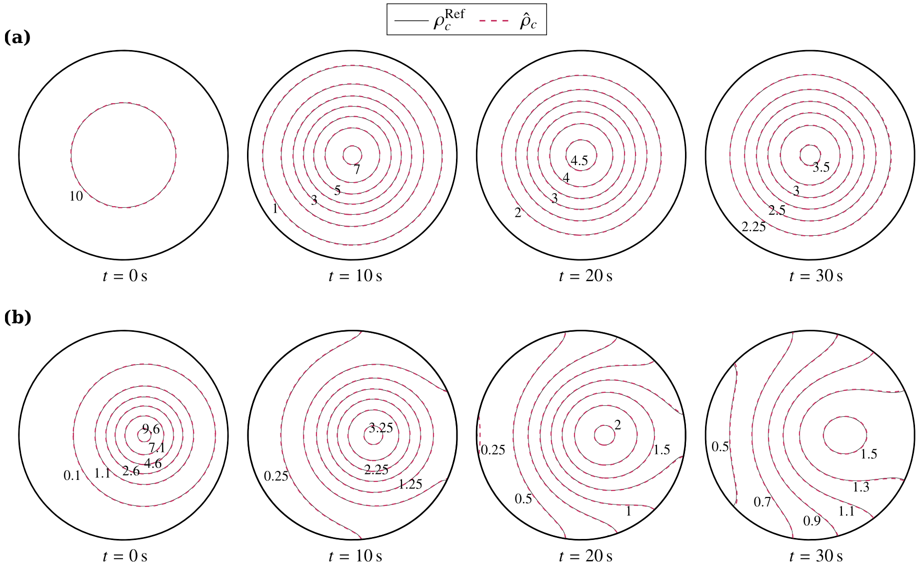

Figure 2.8. Diffusion of a chemical substance in a perfectly circular cell moving with constant velocity. *Comparison of the classical method that uses a mesh conforming to the geometry of the cell (ρ_c^{Ref}, black line) and the diffuse domain method which uses a fixed background mesh ($\hat{\rho}_c$, pink line). (a) Solutions corresponding to the initial condition $\rho_c^0(\mathbf{x}) = 10H\,(5.0 - d_c(\mathbf{x}))$. (b) Solutions corresponding to the initial condition $\rho_c^0(\mathbf{x}) = 10\exp\left(-0.1d_p^2(\mathbf{x})\right)$.*

$\rho_c^0(\mathbf{x}) = 10\exp\left(-0.1d_p^2(\mathbf{x})\right)$ where $d_p(\mathbf{x})$ denotes the distance between $\mathbf{x}$ and $C_p = (2,0)\,\mu\mathrm{m}$. Using this initial condition, the solution does not exhibit circular symmetry anymore, which allows to check the accuracy of the diffuse domain method to impose the boundary condition (2.66). Figure 2.8b shows contour lines of ρ_c^{Ref} and $\hat{\rho}_c$. Again, the solutions are almost indistinguishable, but it may be observed that the error is larger close to the membrane; see, e.g., $t = 20\,\mathrm{s}$, level set 0.25.

In all, this example shows that the diffuse domain method can be safely used for cellular migration problems, introducing negligible errors with respect to the uncertainties in the biological model and the values of the parameters.

Table 2.1. *Keratocyte motion parameters. Some parameter values are taken from experimental data and other computational works of cell motility. The rest of the parameter values have been estimated to account for the biological problem. See Moure and Gomez (2016, 2017) for further details.*

Symbol	Description	Value
Γ_ϕ	Parameter enforcing a hyperbolic tangent profile	$0.52\,\mu\mathrm{m\,s^{-1}}$
ε	Phase-field interfacial length scale	$2\,\mu\mathrm{m}$
$D_m^{\max}$	Myosin diffusion scale	$4.16\,\mu\mathrm{m^2 s^{-1}}$
K_m	Decay rate of myosin diffusion	$1.55\,\mu\mathrm{m}^2$
ε_f	Diffusive length scale of F-actin	$0.707\,\mu\mathrm{m}$
ε_g	Diffusive length scale of G-actin	$3.16\,\mu\mathrm{m}$
α_N	Penalty parameter for actin conservation	$0.06\,\mu\mathrm{m}^{-2}$
Γ_f	F-actin mobility	$0.52\,\mathrm{s}^{-1}$
Γ_g	G-actin mobility	$0.52\,\mathrm{s}^{-1}$
μ	Dynamic viscosity coefficient	$1500\,\mathrm{pN\,s}\,\mu\mathrm{m}^{-1}$
λ	Bulk viscosity coefficient	$-500\,\mathrm{pN\,s}\,\mu\mathrm{m}^{-1}$
$\overline{\alpha}_f$	Range of protrusive forces	$0.076\,59$
d_o^f	Effective distance for protrusion suppression	$1.6\,\mu\mathrm{m}$
$\overline{\alpha}_m$	Range of contractile forces	1.0
γ	Surface tension coefficient	$50\,\mathrm{pN}$
ς	Substrate friction coefficient	$0.7\,\mathrm{pN\,s}\,\mu\mathrm{m}^{-3}$
d_o^{ef}	Effective distance for obstacle repulsion	$0.7\,\mu\mathrm{m}$

2.4.2 Stationary states of free movement

Consistently with what is observed in experiments of keratocytes, our model of mesenchymal motion predicts stationary states of free motion[5]. These stationary states correspond to a cell that migrates with constant velocity and fixed shape. To understand how the equilibrium cell shapes and velocities depend on the parameters, we conducted several simulations. We used the computational domain $\overline{\Omega} = [-L, L]^2$ with $L = 20\,\mu\mathrm{m}$ and a mesh composed of 200 $\mathcal{C}^1$-continuous quadratic elements in each direction. The values of all the model parameters except $\overline{\eta}_m$ and $\overline{\eta}_f$ (which are used for a parametric study) are listed in table 2.1. Note that a realistic value of the substrate friction coefficient ς for mesenchymal motion should be probably higher than the value used in table 2.1. Larger values of ς do not modify qualitatively the results (only a mild reduction of the velocity is observed). In addition, we initially assumed that $K_c = 0$. We will show at the end of this section that this hypothesis is acceptable.

[5]By free motion we refer to spontaneous migration on a planar substrate without obstacles.

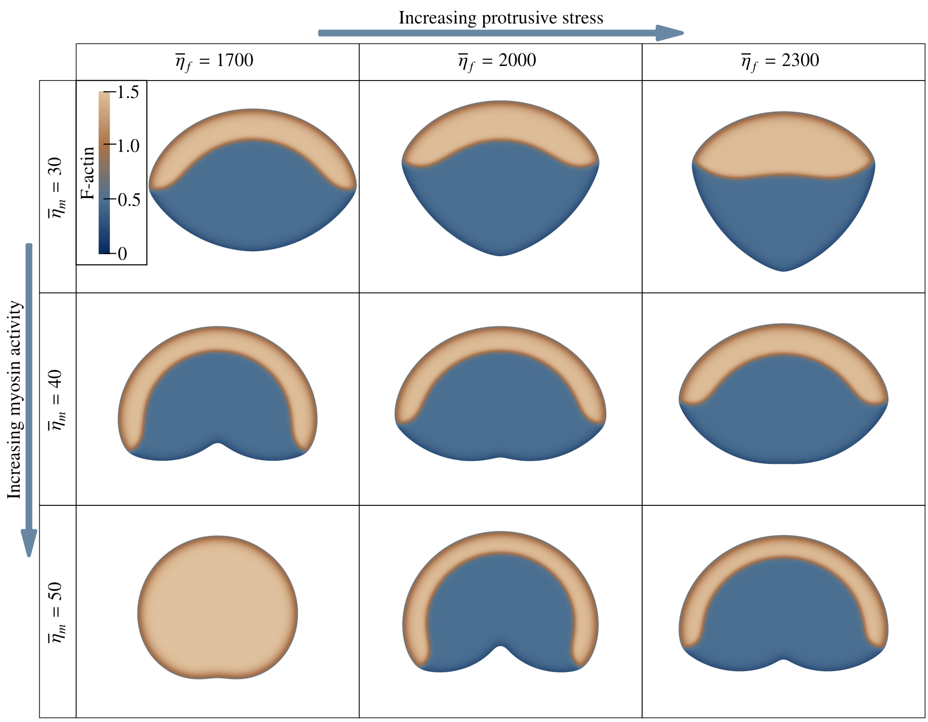

Figure 2.9. Stationary states of keratocyte free motion. F-actin density. *The equilibrium cell shape depends on the balance between contractile and protrusive forces. The color scale represents the F-actin density.*

The initial conditions are the same in all simulations. They represent a circular cell of radius $R_c = 9\,\mu\text{m}$ with vanishing velocity and uniform distribution of myosin and G-actin densities. The distribution of F-actin is non-uniform to produce the cell's polarization and trigger the motion. Specifically, we take

$$\phi(\mathbf{x},0) = 0.5 - 0.5\tanh\left[\frac{2\sqrt{2}}{\varepsilon}\left(d_c(\mathbf{x}) - R_c\right)\right], \tag{2.72}$$

$$\rho_m(\mathbf{x},0) = \phi(\mathbf{x},0), \tag{2.73}$$

$$\rho_f(\mathbf{x},0) = \begin{cases} 1.5\,\phi(\mathbf{x},0) & \text{if } y \geq 0, \\ 0.5\,\phi(\mathbf{x},0) & \text{if } y < 0, \end{cases} \tag{2.74}$$

$$\rho_g(\mathbf{x},0) = 1.1\,\phi(\mathbf{x},0), \tag{2.75}$$

$$\mathbf{u}(\mathbf{x},0) = 0, \tag{2.76}$$

where $d_c(\mathbf{x})$ represents the distance between $\mathbf{x}$ and the coordinates origin. All

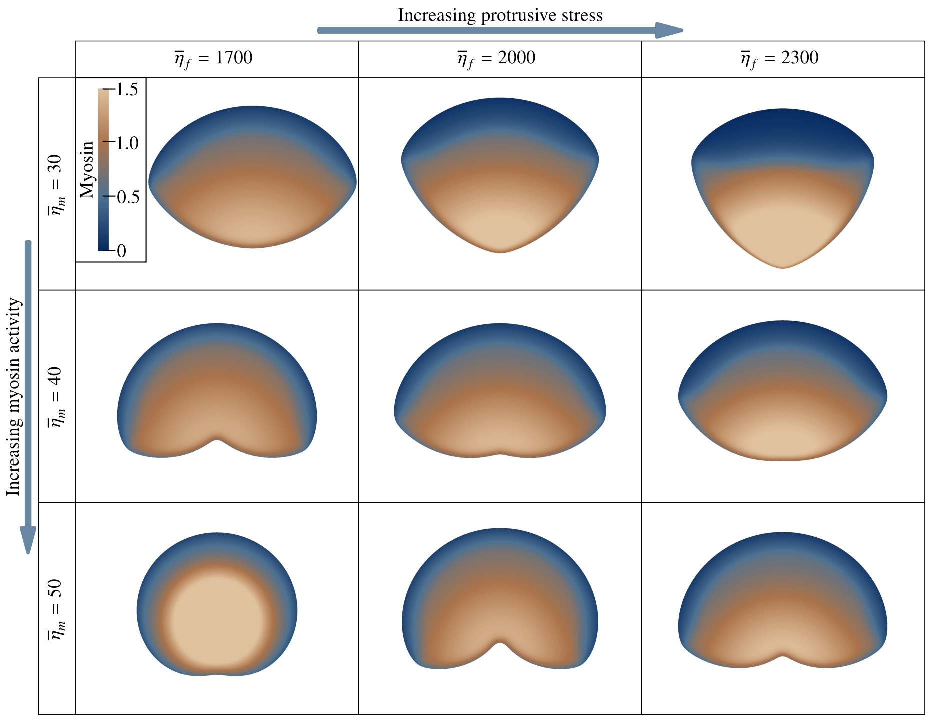

Figure 2.10. Stationary states of keratocyte free motion. Myosin density. *The equilibrium cell shape depends on the balance between contractile and protrusive forces. The color scale represents the myosin density.*

the simulations reach a stationary state at time $t \approx 120\,\mathrm{s}$. Figures 2.9 and 2.10 show, respectively, the stationary F-actin (ρ_f) and myosin (ρ_m) distributions for different values of $\overline{\eta}_m$ and $\overline{\eta}_f$.

The plots show the cell's polarization: while the lamellipodium (associated to areas of large F-actin concentration) is pushing the front of the cell (figure 2.9), myosin is located at the back of the cell (figure 2.10) producing its contraction. The different equilibrium shapes adopted by the cell depend on the balance between protrusive and contractile forces. The three simulations corresponding to $\overline{\eta}_f = 2000\,\mathrm{pN\,\mu m^3}$ (see figure 2.9 or figure 2.10) clearly show the influence of $\overline{\eta}_m$. For higher values of $\overline{\eta}_m$, which produce greater contractile forces exerted by myosin, the cell even loses its convex shape (bottom row, middle column). Increasing the value of $\overline{\eta}_f$ the lack of convexity can be alleviated as shown in the bottom-right panel. The bottom left image corresponds to an extreme case in which the contractile forces

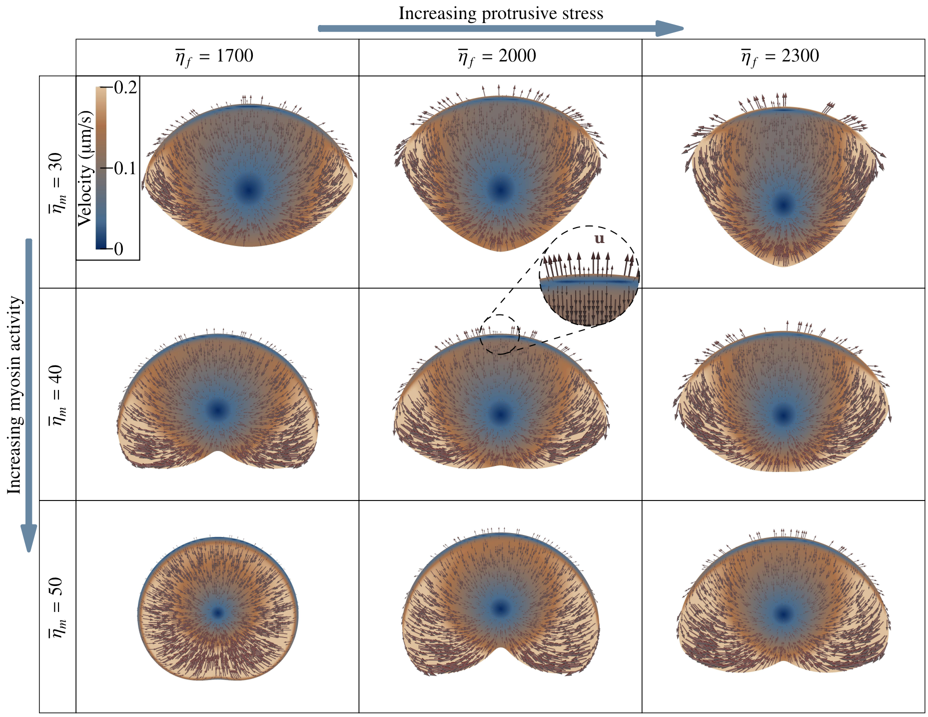

Figure 2.11. Stationary states of keratocyte free motion. Velocity distribution. *The equilibrium cell shape depends on the balance between contractile and protrusive forces. The color scale represents the velocity magnitude. In some random points, we also show the velocity field with arrows.*

are so strong compared to the protrusive ones that the cell loses its polarization and the lamellipodium extends all over the cytoplasm. However, myosin is still concentrated at the back of the cell, which produces a slow steady motion.

Figure 2.11 shows the stationary velocity field for all values of $\overline{\eta}_m$ and $\overline{\eta}_f$. The color scale represents the velocity magnitude. We also added arrows at random locations. The plots show that the lamellipodium undergoes retrograde flow as observed in experiments (Barnhart *et al.*, 2011); see, in particular, the zoomed in region in the central panel. The zoomed in area clearly shows that the membrane velocity points upwards, but the velocity at nearby points of the cytosol has opposite sign. Figure 2.12 displays the area, aspect ratio (width/length), and the global velocity of the cell for the stationary states. We can see that if the cell is fully polarized, its area remains fairly constant (figure 2.12a). The aspect ratio increases as contractile forces become larger with respect to protrusive forces, except when the cell is not fully polarized. As expected, the unpolarized cell breaks the trend again; see figure 2.12b. The cell's velocity increases with increasing values of protrusive forces and with decreasing values of contractile forces. This is true even in the case of the unpolarized cell.

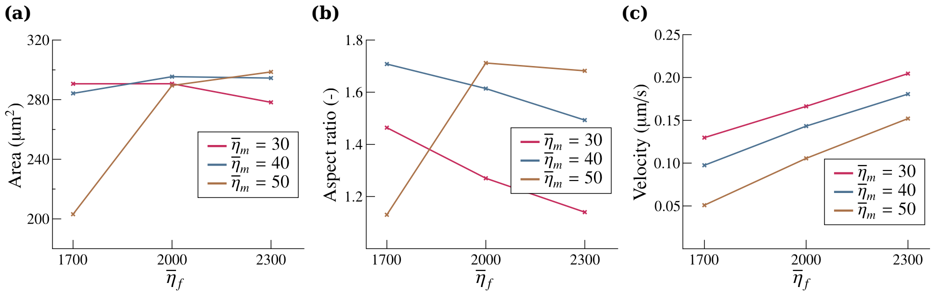

Figure 2.12. Results analysis of keratocyte free motion. *(a) Area of the cell. (b) Aspect ratio. (c) Global cell velocity.*

Influence of the bending energy of the membrane

To analyze the influence of the membrane bending energy, we compute again some of the stationary states using different values for the bending rigidity K_c. We will show that the bending rigidity of the membrane does not play a significant role in the solution as anticipated. We maintained the time step and the number of elements, but now we use cubic splines with $\mathcal{C}^2$ global continuity to be able to generate discrete spaces in $\mathcal{H}^3$ and compute the integrals in equation (2.37). Figure 2.13 shows the results along with the control parameters for the analysis (all examples correspond to $\overline{\eta}_f = 2000\,\mathrm{pN\,\mu m^3}$). The figure also shows the cell's equilibrium shape by displaying the level set $\phi = 1/2$. We observe that even the value $K_c = 80\,\mathrm{pN\,\mu m^2}$, which is much greater than measured values (Dimova, 2014; Simson *et al.*, 1998), produces negligible variations of the equilibrium shape. Figure 2.14 shows that the cell's area, aspect ratio, and global velocity depend on the bending rigidity very mildly. We conclude, in agreement with other computational works (Marth and Voigt, 2014), that bending forces can be neglected in the computations. Therefore, all the subsequent computations in this thesis assume $K_c = 0$. From the computational point of view, this has the advantage that $\mathcal{C}^1$-continuous quadratic functions can be used in the computations. This reduces the computational time in our implementation.

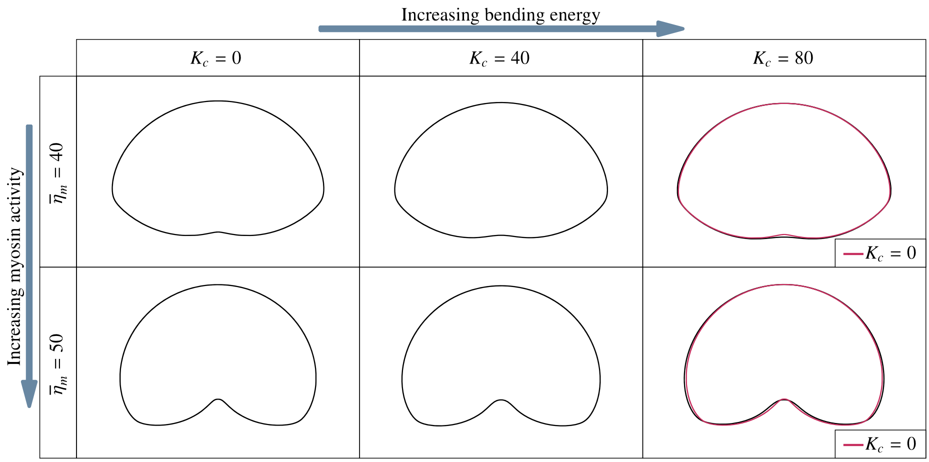

Figure 2.13. Influence of the membrane's bending resistance on the stationary cell shape for different values of $\overline{\eta}_m$. *The cell is represented by the level set $\phi = 1/2$. The rightmost column shows the solutions for $K_c = 80\,\mathrm{pN}\,\mu\mathrm{m}^2$ (black line) and $K_c = 0$ (red line).*

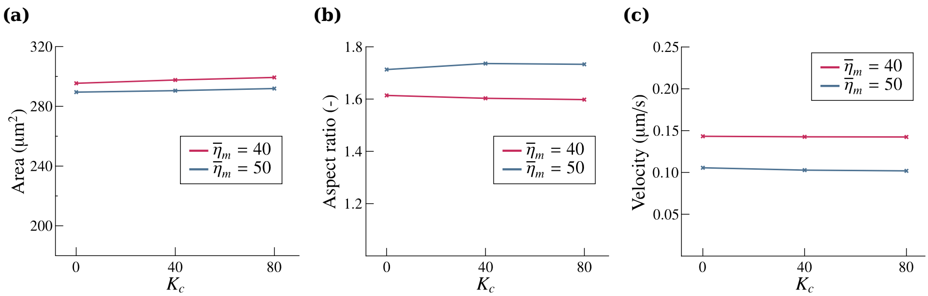

Figure 2.14. Results analysis of the influence of the membrane's bending rigidity. *(a) Area of the cell. (b) Aspect ratio. (c) Cell's global velocity.*

2.4.3 Oscillatory motion

This section shows that our model can reproduce oscillatory motion of keratocytes confined in a microchannel geometry (Camley *et al.*, 2013). We place a microchannel of width 10 µm oriented in the vertical direction and symmetrically located in the domain. We use the same computational domain as in subsection 2.4.2, $\overline{\Omega} = [-L, L]^2$ with $L = 20\,\mu\mathrm{m}$ and a mesh composed of 200 $\mathcal{C}^1$-continuous quadratic elements in each direction. The microchannel walls are modeled as two linear obstacles that exert forces on the cell through the term $\mathbf{F}_{\text{rep}}$ in equation (2.8). We place a polarized, elongated cell in the interior of the microchannel and let the simulation evolve. The cell displays an oscillatory motion which alternates migrations downwards and upwards in the channel. The model parameters are defined in table 2.1 with $\eta_{\text{rep}} = 4550\,\text{pN}\,\mu\text{m}$, $\overline{\eta}_f = 2000\,\text{pN}\,\mu\text{m}^3$, and $\overline{\eta}_m = 30\,\text{pN}\,\mu\text{m}$. The initial conditions are:

$$\phi(\mathbf{x},0) = \left\{0.5 - 0.5\tanh\left[\tfrac{2\sqrt{2}}{\varepsilon}(|x| - w/2)\right]\right\}\left\{0.5 - 0.5\tanh\left[\tfrac{2\sqrt{2}}{\varepsilon}(|y| - l/2)\right]\right\}, \tag{2.77}$$

$$\rho_m(\mathbf{x},0) = \begin{cases} 0 & \text{if } y \geq 0, \\ 2.1\,\phi(\mathbf{x},0) & \text{if } y < 0, \end{cases} \tag{2.78}$$

$$\rho_f(\mathbf{x},0) = \begin{cases} 1.5\,\phi(\mathbf{x},0) & \text{if } y \geq 0, \\ 0.5\,\phi(\mathbf{x},0) & \text{if } y < 0, \end{cases} \tag{2.79}$$

$$\rho_g(\mathbf{x},0) = 1.1\,\phi(\mathbf{x},0), \tag{2.80}$$

$$\mathbf{u}(\mathbf{x},0) = 0, \tag{2.81}$$

where $w = 10\,\mu\text{m}$ and $l = 20\,\mu\text{m}$ are, respectively, the width (x-direction size) and the length (y-direction size) of the cell. Figures 2.15a and 2.15b show, respectively, the distributions of F-actin and myosin at several times. For a clearer

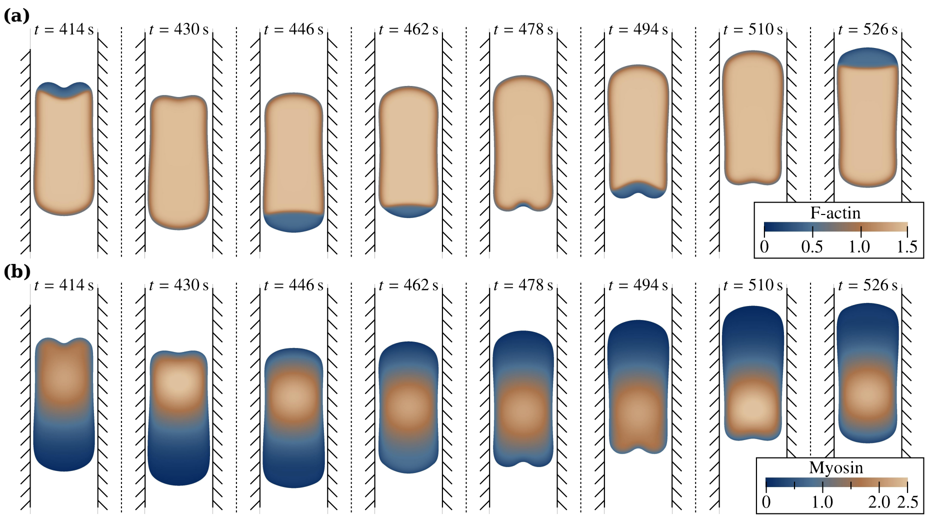

Figure 2.15. Oscillatory motion of keratocytes in a microchannel. *(a) F-actin distribution. (b) Myosin distribution.*

visualization, we only show the relevant part of the computational domain. The snapshots corresponding to $t = 414\,\mathrm{s}$ and $t = 494\,\mathrm{s}$ represent a similar cell shape as well as F-actin and myosin distributions, but with the cell moving in opposite directions. Figure 2.16 shows the time evolution of the cell's area, its global (vertical) velocity, and the y-coordinate of its center of mass. We observe that the cell's area (figure 2.16a) displays variations of up to $\sim 15\%$ as observed in experiments (Keren *et al.*, 2008). Figure 2.16b shows that the vertical velocity changes sign periodically, producing the oscillatory motion. Between each two sign changes the velocity presents a non-trivial time evolution; see, e.g., the time interval $t \in [440, 515]\,\mathrm{s}$. The reason for this is that when F-actin depolarizes for the first time in the time interval ($t \approx 478\,\mathrm{s}$) myosin has not moved to the back of the cell yet and the cell gets polarized in the same direction again ($t \approx 494\,\mathrm{s}$). When F-actin depolarizes for the second time ($t \approx 510\,\mathrm{s}$) myosin is at the back and the cell is able to reverse motion. The time evolution of the vertical position of the cell's center of mass (y_{cell} in figure 2.16c) is simpler and shows a plain oscillatory motion with period $\sim 160\,\mathrm{s}$. By modifying the parameters $\overline{\eta}_f$ or $\overline{\eta}_m$ the model can produce oscillatory motions with different periods as well as stick-slip motion (Löber *et al.*, 2014) (data not shown).

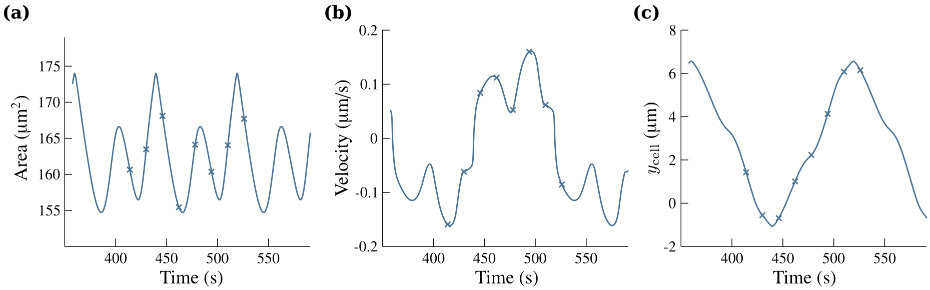

Figure 2.16. Results analysis of the oscillatory motion of keratocytes in a microchannel. *(a) Area of the cell. (b) Global velocity. (c) y-coordinate of the cell's mass center. The cross marks in the plots correspond to the snapshots in figure 2.15.*

2.4.4 Bipedal motion

Using exactly the same setup as in subsection 2.4.3 and changing the initial conditions only, the model predicts bipedal motion (Barnhart *et al.*, 2010). The initial cell's position defined by $\phi(\mathbf{x}, 0)$ is the same as before; see equation (2.77). The initial velocity is set to zero as in equation (2.81) and the G-actin density is given by equation (2.80). The distributions of myosin and F-actin are given by

$$\rho_m(\mathbf{x},0) = \phi(\mathbf{x},0), \tag{2.82}$$

$$\rho_f(\mathbf{x},0) = \begin{cases} 1.5\,\phi(\mathbf{x},0) & \text{if } y \geq -2x, \\ 0.5\,\phi(\mathbf{x},0) & \text{if } y < -2x. \end{cases} \tag{2.83}$$

The reason why these initial conditions enable bipedal motion is that the F-actin distribution is non-symmetric in the vertical and horizontal directions. Figures 2.17a and 2.17b show several snapshots of the F-actin and myosin distributions while the cell is moving upwards. It may be observed that the back part of the cell leaves behind a tail that oscillates from left to right giving rise to the bipedal motion. The plots show that the cell remains polarized throughout the entire time interval although the lamellipodium extends over a large area of the cytosol. Figures 2.18a and 2.18b show, respectively, the time evolution of the cell's area and the x- and y-position of its center of mass. Figure 2.18b shows that the bipedal motion is characterized by a quasi-constant vertical velocity and an oscillatory retraction of one side of the cell body out of phase with the other side (Barnhart *et al.*, 2010) —the latter is reflected in the time evolution of the x-coordinate of the cell's center of mass. Figure 2.18c shows the trajectory of the cell's center of mass.

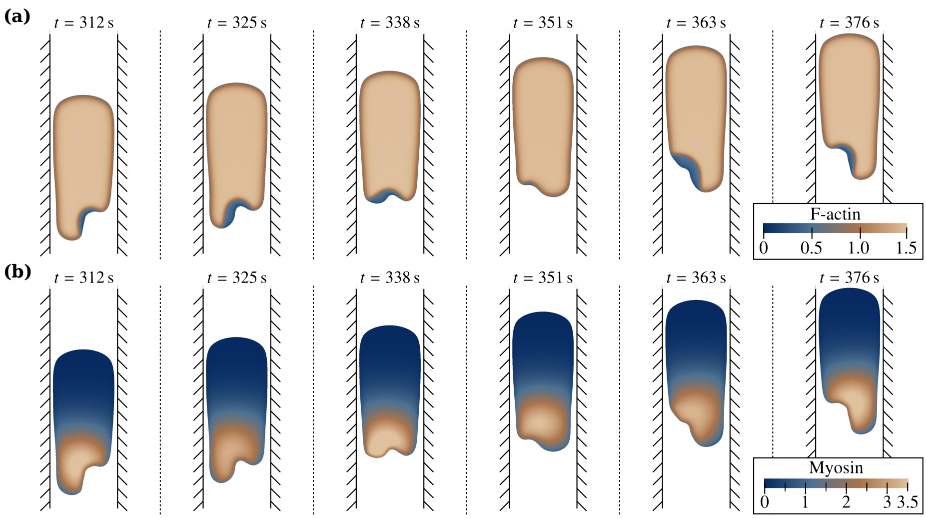

Figure 2.17. Bipedal motion of keratocytes in a microchannel. *(a) F-actin distribution. (b) Myosin distribution.*

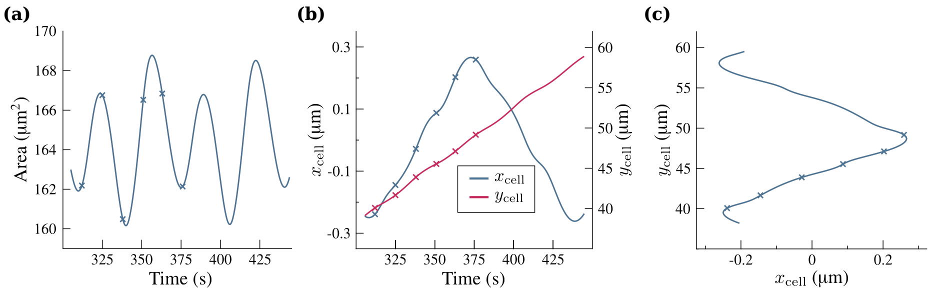

Figure 2.18. Results analysis of the bipedal motion of keratocytes in a microchannel. *(a) Time evolution of the cell's area. (b) Time evolution of the position of the cell's center of mass (x and y-coordinates). (c) Trajectory of the cell. The cross marks in the plots correspond to the snapshots in figure 2.17.*

2.5 Conclusions

We proposed a phase-field model of mesenchymal migration that accounts for the interactions of the cytosolic compounds and the forces acting in the actomyosin network. From a mechanical point of view, the cell's membrane is modeled as a vesicle and the actin network as a viscous Newtonian fluid. The discretization of the model poses significant challenges to conventional numerical schemes, such as, e.g., solving equations on moving and deformable domains or approximating higher-order differential operators. The first challenge is addressed utilizing the diffuse domain method, which allows to use a fixed mesh only. The second one is handled through the use of globally continuous splines constructed using the concept of isogeometric analysis. We applied the model to the migration of mesenchymal cells. The results show that the model for actin phase transformations proposed here effectively reproduces the behavior of actin in keratocytes. The simpler case of mesenchymal migration on flat substrates produces stationary states of motion that are in good agreement with experiments. Moreover, by considering the presence of obstacles, we are able to reproduce complex modes of motion observed in microchannels, such as, e.g., oscillatory and bipedal motion.

Both the model and the numerical formulation of this chapter open a number of new opportunities to study cell migration computationally. The following chapters are devoted to some of the possible extensions of the model, while other remaining extensions are considered for future work. Therefore, the mathematical framework developed in this chapter serves as a starting point for the remaining mathematical models of this thesis.

Chapter 3

Amoeboid motion: coupling membrane and cytosol dynamics

In this chapter we extend the previous model of mesenchymal migration and propose a mathematical model that accounts for amoeboid motion. Contrary to mesenchymal cells, amoeboid cells undergo large deformations caused by the emergence and retraction of actin-rich protrusions. This highly orchestrated process is mediated by the membrane signaling molecules that interact with the cytosol. The diffuse domain method allows to model the coupled interaction of the membrane and the cytosol dynamics using a simple methodology. The model results are in quantitative agreement with experiments and show how cells may take advantage of the geometry of their microenvironment to migrate more efficiently. We also present a three-dimensional example of cell motion within a fibrous network of obstacles.

3.1 Introduction

This chapter deals with pseudopodial amoeboid motion of a single cell, a mode of migration where locomotion is achieved by rapidly protruding and retracting extensions generally called *pseudopods*. This kind of crawling-like motion is often studied by performing experiments with *Dictyostelium discoideum*. *Distyostelium* is an elongated and extraordinarily deformable cell that translocates via rapidly alternating cycles of morphological expansion and myosin-induced contraction (see figure 3.1). These cells produce dynamic actin-rich protrusions at their leading edge, the aforementioned pseudopods, which locally drive the edge of the cell outwards. The dynamic nature of pseudopods may be attributed to the ability of actin to assemble and disassemble quickly.

Our philosophy follows the so-called *pseudopod-centered view*, in which external signals are not necessary for pseudopod formation (Insall, 2010). The motion of *Distyostelium* is the result of an ordered sequence of expansion and retraction steps. Each expansion step corresponds to the formation of a new pseudopod, which may occur by splitting an existing protrusion or by generating one *de novo* (Bosgraaf and Van Haastert, 2009b); see figure 3.1a. The growth of pseudopods is controlled by membrane signaling molecules, such as for example, PIP3 (Van Haastert and Devreotes, 2004). These substances are bound to the cell's membrane. In our

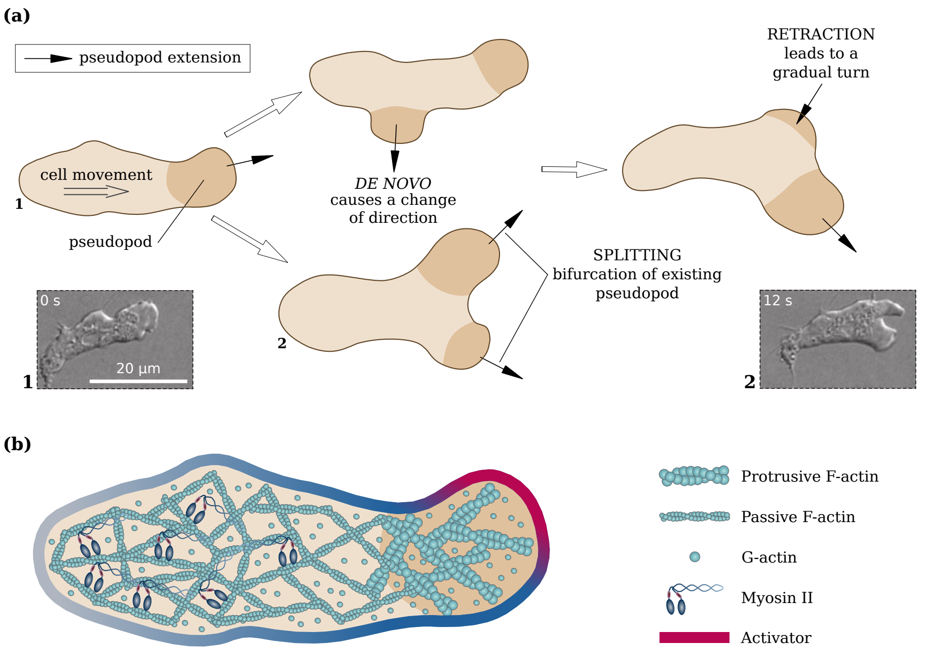

Figure 3.1. Conceptual model of amoeboid motion. *(a) Amoeboid motion is produced by periodic extensions/retractions of pseudopods at the cell's front and contractions at the cell's rear. The dashed rectangles show experimental images taken from Insall (2010). (b) Main elements considered in our model.*

model, they are conceptualized as a single substance that undergoes biochemical reactions within the membrane. We call this substance *activator*; see figure 3.1b. The way in which the growth of new pseudopods is orchestrated leads to the so-called persistent motion. Persistence is the cell's tendency to keep moving in the same direction for a period of time (Potel and Mackay, 1979). Classical experiments (Gail and Boone, 1970; Potel and Mackay, 1979) show that persistent cells are able to colonize farther environments than cells that move in uncorrelated directions (random motion without persistence). This could have implications in many biological processes.

There has been abundant work modeling the membrane mechanics and its signaling activity (Elliott *et al.*, 2012; Hecht *et al.*, 2011b; Levchenko and Iglesias, 2002; Meinhardt, 1999). There are also models that describe in detail the cytosol dynamics (Dreher *et al.*, 2014; Shao *et al.*, 2012, 2010), though most of them have focused on mesenchymal motility. However, coupled models including the cytosolic machinery and membrane dynamics have received little attention, even though they are critical to understand cell migration (Danuser *et al.*, 2013). Moreover, the three-dimensional simulation of amoeboid motion poses a number of computational challenges. The traditional computational approach would be to solve the three-dimensional equations that govern the biochemomechanical processes on the cell's interior using a moving-mesh method. This problem would be coupled to partial-differential equations (PDEs) posed on a moving surface representing the membrane that control the dynamics of the activator. Here, we propose a computational method entirely based on the phase-field theory, which solves PDEs on the time-dependent cell geometry without generating a mesh conforming to the cell shape. We show that modeling the *coupled* interaction of the membrane signaling activity and the cytosol dynamics allows to understand the mechanisms that control pseudopod formation and, thus, amoeboid motion. Our theory predicts realistic myosin and actin distributions within the cell and reproduces experimental laws of spreading. The coupled model allows to study how external forces exerted on the membrane (e.g., those caused by rigid obstacles) modify the cytosol dynamics. The model also explains how cells may exploit particular geometric features of their environment to find more efficient migration strategies. Finally, we present a three-dimensional example of cell motion within a fibrous network that may be seen as a preliminary step for the computational study of cellular migration in the extracellular matrix.

This chapter is organized as the previous chapter: We first present the model for amoeboid motion. Then, we introduce the numerical formulation. We analyze the two-dimensional migration of *Dictyostelium* by means of our numerical results. We also study amoeboid motion in confined environments. We finally show an example of three-dimensional migration in a fibrous network and draw some conclusions.

3.2 The model

In the following, we present the model for amoeboid motion, which is an extension of the model proposed in the previous chapter for mesenchymal motion. Since both models share common characteristics, some concepts are referred to their description in section 2.2. We divide the model in three modules describing the cell's motion, the activator dynamics, and the cytosol biochemomechanics. We use the phase-field $\phi(\mathbf{x}, t)$ to track the cell's location. We simplify the membrane signaling dynamics by using a single membrane-located activator $a(\mathbf{x}, t)$ that triggers the growth of new pseudopods. The cytosolic machinery is described by the fields $\rho_f(\mathbf{x}, t)$, $\rho_g(\mathbf{x}, t)$, and $\rho_m(\mathbf{x}, t)$, that represent the density of F-actin, G-actin, and myosin, respectively. The actin filament network is treated as a viscous fluid, whose velocity $\mathbf{u}(\mathbf{x}, t)$ is governed by a Stokes-type equation (Rubinstein *et al.*, 2009).

3.2.1 Cell motion

The cell's position is given by the phase field $\phi(\mathbf{x}, t)$. The function ϕ transitions smoothly from 0 (outside the cell) to 1 (inside the cell); see figure 3.2. The cell's membrane is defined by the level set $\phi = 1/2$ and moves driven by the velocity of the actin network $\mathbf{u}$. The evolution equation for ϕ is

$$\frac{\partial \phi}{\partial t} + \mathbf{u} \cdot \nabla \phi = \Gamma_\phi \left(\varepsilon \nabla^2 \phi - \frac{G'(\phi)}{\varepsilon} + c\varepsilon |\nabla \phi| \right), \tag{3.1}$$

which is the same equation that we used for mesenchymal motion; see equation (2.1). A detailed description of equation (3.1) and its terms may be found in subsection 2.2.1.

3.2.2 Activator dynamics

The growth of pseudopods is controlled by membrane signaling molecules (e.g., PIP3; see Van Haastert and Devreotes, 2004), which trigger actin nucleation. We model the membrane signaling dynamics by using a single membrane-located compound that we call activator $a(\mathbf{x}, t)$. Although we simplify the model by taking into account one compound only, it would be interesting to propose a more complex model, such as that presented in Ribeiro *et al.* (2017). Compared to Ribeiro *et al.* (2017), our model simplifies the interaction of four signaling components into a single activator. Besides, instead of solving stochastic equations at the molecular level, we solve a continuous equation at the cellular level, where all the stochastic processes are included into a single term.

We make use of the diffuse domain method to localize the activator dynamics to the membrane without resorting to surface PDEs (Teigen *et al.*, 2009); see subsection 1.3.2. This is accomplished by using the smooth membrane marker

$$\delta_m(\phi) = \exp\left[-\varphi(\phi - 1/2)^2\right], \tag{3.2}$$

which has been plotted in figure 3.2. The constant parameter φ defines the thickness of the marker. Our model for the activator dynamics is given by the equation

$$\frac{\partial(\delta_m a)}{\partial t} + \nabla \cdot (\delta_m a \mathbf{u}) = \nabla \cdot (D_a \delta_m \nabla a) - r_a \delta_m a + b_a \delta_m S_a, \tag{3.3}$$

which accounts for the advective transport, diffusion throughout the membrane (with diffusion constant D_a), a natural decay (with rate r_a), and a growth term S_a whose strength is controlled by the parameter b_a. A fundamental model of the term S_a requires knowledge about the mechanisms that control the autocatalysis of membrane-bound activators. Since these mechanisms are not well understood (Insall, 2010), we resort to experimental data (Bosgraaf and Van Haastert, 2009b). These data consist of several probability distribution functions that control the position and time at which the activator triggers actin nucleation. For simplicity, we initially describe this procedure in a 2D scenario. The probability distributions (see figure 3.3) are used to define S_a, which creates peaks in the activator concentration at certain points in space and time. In particular, we take

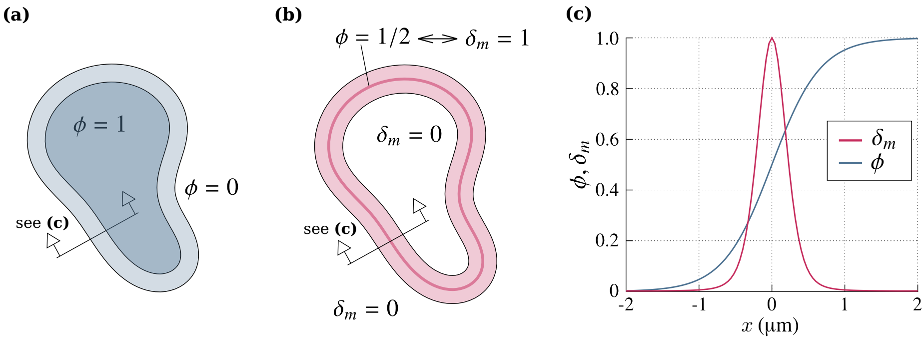

Figure 3.2. Conceptual description of the diffuse domain framework used in the model. *(a) The cell location is implicitly defined by the phase-field variable ϕ. (b) The cell membrane marker δ_m is defined in terms of ϕ (see equation (3.2)). (c) ϕ and δ_m values across the membrane. The plot corresponds to $\varepsilon = 2\,\mu$m and $\varphi = 25$.*

$S_a = (a_{\max} - a) \sum_i \delta^a_{\mathbf{x},i} \delta^a_{t,i}$ that drives a to $a_{\max}$ at certain time intervals ($\delta^a_{t,i}$) and spatial areas ($\delta^a_{\mathbf{x},i}$) of the membrane. To define the temporal localizers we make use of the *interval* and the *growth time*. The interval $\Delta\tau_i$ represents the period of time between the extension of two consecutive pseudopods. Therefore we can define the set of times $\{\tau_{0,1}, \tau_{0,2}, ...\}$, where $\tau_{0,1} = 0$ and $\tau_{0,i} = \tau_{0,i-1} + \Delta\tau_i$, such that $\tau_{0,i}$ indicates the time at which the activator peak i is switched on. Each peak will be active during a growth time ΔT_i. Thus, the temporal localizer is defined by $\delta^a_{t,i} = \mathcal{H}(\Delta T_i - (t - \tau_{0,i}))$, for $t > \tau_{0,i}$. The growth time (ΔT_i) and the interval ($\Delta\tau_i$) are two random variables given by the probability functions plotted in figures 3.3a and 3.3b, respectively. Note that there may be none, one, or more than one active sources at the same time. The spatial location is given by the function $\delta^a_{\mathbf{x},i} = \mathcal{H}(R_a - d^a_i(\mathbf{x}))$, where d^a_i represents the distance to the center of the activator source i ($\mathbf{s}_i$) and R_a is its approximate radius. In the case of a two-dimensional problem, the location of $\mathbf{s}_i$ is derived from the probability

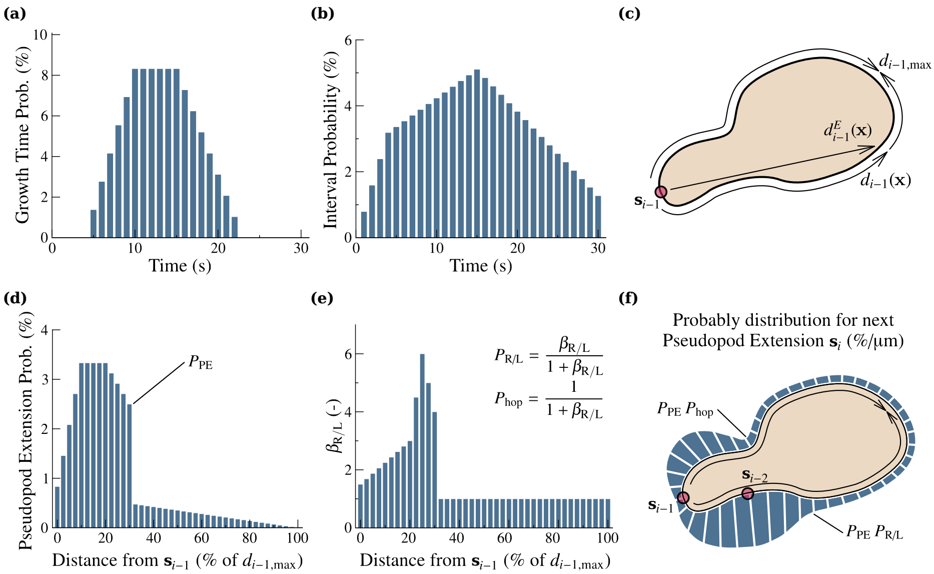

Figure 3.3. Determination of pseudopod formation. *The probability distributions are derived from Bosgraaf and Van Haastert (2009b). (a) Pseudopod growth time probability. (b) Pseudopod interval time distribution. (c) Perimeter distance $d_{i-1}(\mathbf{x})$ and Euclidean distance $d^E_{i-1}(\mathbf{x})$ from previous source. (d) Probability distribution for next pseudopod location in terms of the perimeter distance. (e) Right/left bias function. (f) Probability distribution for next pseudopod extension.*

function plotted in figure 3.3f that depends on the location of the two previous sources ($\mathbf{s}_{i-1}$ and $\mathbf{s}_{i-2}$). To establish the location of a new peak ($\mathbf{s}_i$), we need to define the probability distribution along the membrane using the functions in figures 3.3d and 3.3e. The probability function will be $P_{\text{PE}}\, P_{\text{R/L}}$ on the side of the membrane where $\mathbf{s}_{i-2}$ is located, and $P_{\text{PE}}\, P_{\text{hop}}$ on the other side of the membrane. Note that each source moves together with the membrane and therefore, the probability distribution in figure 3.3f changes over time. In addition, we consider that the membrane receptors are able to sense the presence of an obstacle and prevent the activation of the signaling molecules that trigger actin nucleation. Thus, the cell-obstacle contact impedes pseudopod formation (Nagel *et al.*, 2014) modifying the probability function such that $P_{\text{PE}}(\mathbf{x}) = 0$ if $d_o(\mathbf{x}) < d_o^a$. In summary, each time a new peak emerges, we select three random values using the probability distributions shown in figure 3.3. These quantities represent growth time (time during which the peak is active), interval (permits to compute the time at which the next peak will arise), and location of pseudopod extension.

The extension of this procedure to 3D problems is not straightforward, primarily due to the absence of experimental data in three dimensions. To avoid computing the probability distribution over the entire cell surface, in the case of a 3D calculation, we proceed as follows: We compute the growth time and the interval as before. Then, we determine the distance between $\mathbf{s}_{i-1}$ and each point of the cell's surface. From this computation, we obtain $d_{i-1,\text{max}}$ as shown in figure 3.3c for the 2D case. Once we have $d_{i-1,\text{max}}$, we generate a random number using the probability distribution in figure 3.3d. This number represents the actual value of the distance between $\mathbf{s}_{i-1}$ and $\mathbf{s}_i$ that we call d_{i-1}^i. We can now enter in figure 3.3e with d_{i-1}^i and obtain $P_{\text{R/L}}$ and P_{hop}. Knowing the probabilities of the cell to alternate left and right ($P_{\text{R/L}}$) or to hop (P_{hop}), we can use a random number generator to determine if the cell will alternate left and right or hop. Then, we can compute the locus of the points of the membrane that are located at a distance d_{i-1}^i of $\mathbf{s}_{i-1}$. The locus of these points is one (or several) curve(s) that we denote by l_d. The source activator $\mathbf{s}_i$ will be located on the curve(s) l_d. The next step is to compute two points of l_d, namely C_{l_d} and D_{l_d}. The point C_{l_d} (respectively, D_{l_d}) is the closest (respectively, the farthest) point of l_d to $\mathbf{s}_{i-2}$. If the cell is to alternate left and right (respectively, hop) the location of $\mathbf{s}_i$ will be determined by a normal probability distribution that is centered at C_{l_d} (respectively, D_{l_d}).

Remark:

1. Ideally, in the procedure explained for 3D problems, the distance $d_{i-1}(\mathbf{x})$ should be computed following the shortest path contained in the membrane. To reduce the computational time, in our 3D simulations we use the Euclidean distance $d_{i-1}^E(\mathbf{x})$ (see figure 3.3c) rather than geodesics of the cell's

membrane. Thus, we define the probability distributions of figures 3.3d to 3.3f in function of $d^E_{i-1}(\mathbf{x})$ and $d^E_{i-1,\max}$ instead of $d_{i-1}(\mathbf{x})$ and $d_{i-1,\max}$, respectively.

3.2.3 Cytosol biochemomechanics

In our model, the activator triggers pseudopod formation. Pseudopods are localized regions of F-actin in the form of protrusive structures that push the membrane outwards. Myosin, in contrast, produces contractile forces in the cell rear. A conceptual description of the model is plotted in figure 3.4.

Myosin dynamics

We assume that myosin is transported by the actin network velocity and diffuses throughout the cell. By using the phase-field method, we resort to the evolution equation

$$\frac{\partial(\phi\rho_m)}{\partial t} + \nabla\cdot(\phi\rho_m\mathbf{u}) - \nabla\cdot[D_m(\rho_f)\phi\nabla\rho_m] = 0, \tag{3.4}$$

which is identical to equation (2.2). The function $D_m(\rho_f)$ is defined in subsection 2.2.2.

Actin dynamics

We extend the model presented in subsection 2.2.3 to incorporate the interactions with the signaling proteins that control pseudopod formation. The model

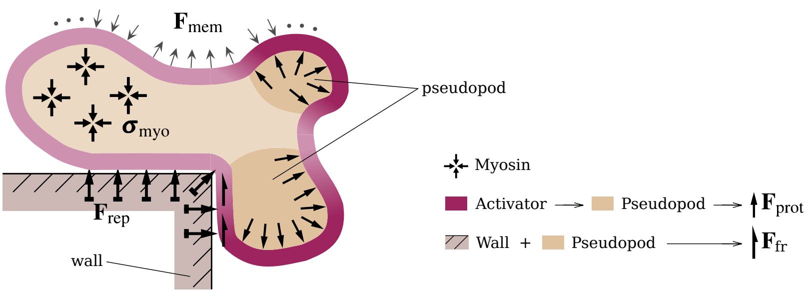

Figure 3.4. Computational model for amoeboid motion. *Forces acting in the amoeboid cell.*

accounts for the phase transformations between G-actin and F-actin, and also for transitions between a protrusive and a passive states of the F-actin network. In this chapter, the protrusive structures are identified with pseudopods and their growth is triggered by the activator. We make use of the phase-field theory to propose a new model of actin dynamics based on the free energy functional

$$\mathcal{F}[\rho_f,\rho_g]=\int_\Omega \phi\left[\frac{\varepsilon_f^2}{2}|\nabla\rho_f|^2+\frac{\varepsilon_g^2}{2}|\nabla\rho_g|^2+F\left(\rho_f,\rho_g,a\right)\right]\mathrm{d}\Omega+\frac{\alpha_N}{2}\left(\mathcal{N}_0-\mathcal{N}\right)^2, \tag{3.5}$$

where all the terms other than the function $F(\rho_f,\rho_g,a)$ are defined in subsection 2.2.3. The function F controls the phase transitions in terms of the activator concentration, and can be expressed as

$$\begin{aligned} F\left(\rho_f,\rho_g,a\right)=&10\left(\rho_f-\rho_f^{\mathrm{pr}}\right)^2\left(\rho_f-\rho_f^{\mathrm{pa}}\right)^2+7.5\left(\rho_g-\rho_g^{\mathrm{eq}}\right)^2\\ &+I(a)(\rho_f-\rho_f^{\mathrm{pr}})^2\left[\rho_f+\kappa(a)I(a)\right]. \end{aligned} \tag{3.6}$$

where $I(a)=a^2-2\exp(-4a)$, $\beta(a)=0.5[1-(a-1.8)^2/1.8^2]$, and the constants $\rho_f^{\mathrm{pr}}=3/2$, $\rho_f^{\mathrm{pa}}=1/2$, and $\rho_g^{\mathrm{eq}}=1$ take the same values as in the previous chapter. F is a convex function of ρ_g with a unique minimum at $\rho_g=\rho_g^{\mathrm{eq}}$, which represents the stable density of G-actin. However, F may be a convex or non-convex function of ρ_f depending on the value of a. When a is small, F is a double well potential; see figure 3.5b. The wells correspond to two stable densities of F-actin, one associated to protrusive structures (higher density, $\rho_f=\rho_f^{\mathrm{pr}}$) and another to passive networks (lower density, $\rho_f\approx\rho_f^{\mathrm{pa}}$). Within the range of small values of a, the well representing protrusive structures is energetically favored for larger values of a; see figure 3.5c. The opposite happens for smaller values of a; see figure 3.5a. If a is sufficiently large (see figure 3.5d), F becomes a convex function with only one local minimum associated to protrusive structures.

According to equation (3.5), a should be a compound living on the cytosol. Conceptually, in our model, a is a generic membrane-bound protein (e.g., PIP3) that triggers a set of reactions inside the cell close to the membrane. This involves the production of pro-nucleation factors a_{PNF} (e.g., Rac1), which are the accessory proteins that effectively cause actin polymerization. Thus, in the previous formulation we should use a_{PNF} instead of a. However, we suppose that pro-nucleation factors concentrate mainly near the membrane. We further suppose that a_{PNF} is proportional to a, which allows us to use a in equations (3.5) and (3.6) thanks to the diffuse domain approach.

Using the free energy functional equation (3.5), we can utilize the framework of classical non-conserved dynamics to derive the evolution equations

$$\frac{\partial(\phi\rho_f)}{\partial t} + \nabla\cdot(\phi\rho_f\mathbf{u}) = -\Gamma_f\frac{\delta\mathcal{F}}{\delta\rho_f} = \Gamma_f\left[\varepsilon_f^2\nabla\cdot(\phi\nabla\rho_f) - \phi\frac{\partial F}{\partial\rho_f} - \alpha_N\phi\big(\mathcal{N}-\mathcal{N}_0\big)\right], \tag{3.7}$$

$$\frac{\partial(\phi\rho_g)}{\partial t} + \nabla\cdot(\phi\rho_g\mathbf{u}) = -\Gamma_g\frac{\delta\mathcal{F}}{\delta\rho_g} = \Gamma_g\left[\varepsilon_g^2\nabla\cdot(\phi\nabla\rho_g) - \phi\frac{\partial F}{\partial\rho_g} - \alpha_N\phi\big(\mathcal{N}-\mathcal{N}_0\big)\right], \tag{3.8}$$

where Γ_f and Γ_g are constants, and $\delta\mathcal{F}/\delta\rho_f$ and $\delta\mathcal{F}/\delta\rho_g$ are the variational derivatives of the energy with respect to F-actin and G-actin concentration, respectively.

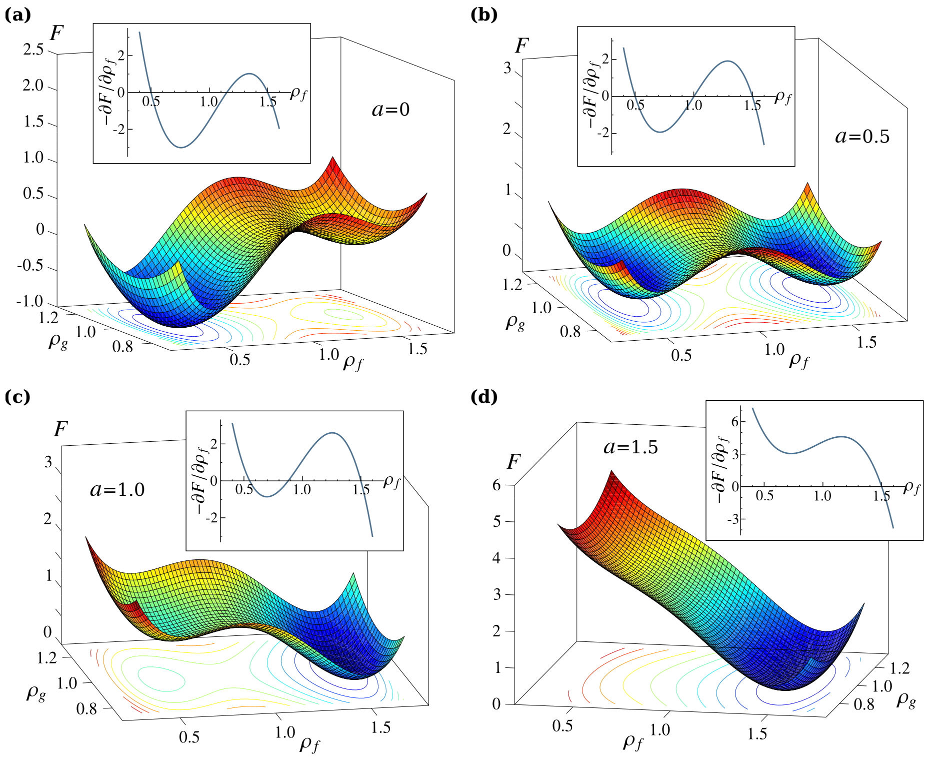

Figure 3.5. Actin free-energy functional. *Function F and its derivative with respect to the F-actin density, depending on the activator concentration. (a) $a = 0$. (b) $a = 0.5$. (c) $a = 1.0$. (d) $a = 1.5$.*

Actin flow

The actin filament network is treated as a viscous flow governed by a Stokes-type equation augmented with forces specific to amoeboid motion; see figure 3.4. We propose the equation

$$\nabla \cdot (\boldsymbol{\sigma} + \boldsymbol{\sigma}_{\text{myo}} + \boldsymbol{\sigma}_{\text{prot}}) + \mathbf{F}_{\text{adh}} + \mathbf{F}_{\text{mem}} + \mathbf{F}_{\text{wall}} = 0. \tag{3.9}$$

The description of $\boldsymbol{\sigma}$, $\boldsymbol{\sigma}_{\text{myo}}$, and $\boldsymbol{\sigma}_{\text{prot}}$ may be found in subsection 2.2.4. The force $\mathbf{F}_{\text{adh}} = -\varsigma \mathbf{u}$ models a hydrodynamic drag[1]. $\mathbf{F}_{\text{mem}}$ accounts for the forces exerted by the cell's membrane. We neglect bending forces (see subsection 2.4.2) and consider only the force induced by surface tension. This force is proportional to the membrane's curvature and is oriented in the direction orthogonal to the membrane. Using the phase-field theory (see subsection 2.2.4) we can get the expression $\mathbf{F}_{\text{mem}} = \gamma \left(G'(\phi)/\varepsilon - \varepsilon \nabla^2 \phi \right) \nabla \phi$ that accounts for the surface tension forces, where γ is the surface tension coefficient. Finally, $\mathbf{F}_{\text{wall}}$ represents the contact forces exerted on the cell by a rigid obstacle. We express this force as $\mathbf{F}_{\text{wall}} = \mathbf{F}_{\text{rep}} + \mathbf{F}_{\text{fr}}$, where $\mathbf{F}_{\text{rep}}$ and $\mathbf{F}_{\text{fr}}$ are, respectively, repulsion and friction forces (Hawkins and Voituriez, 2010; Wilson *et al.*, 2013). Repulsion forces are orthogonal to the solid obstacle, while friction forces are tangential. Repulsive forces may be expressed as $\mathbf{F}_{\text{rep}} = \nabla \cdot \boldsymbol{\sigma}_{\text{rep}}$ with $\boldsymbol{\sigma}_{\text{rep}} = \phi \eta_{\text{rep}} \delta_{\text{rep}} \nabla \phi \otimes \nabla \phi$, whose terms have been previously defined in subsection 2.2.4. Friction forces may be modeled as $\mathbf{F}_{\text{fr}} = -\varsigma_{\text{fr}} \delta_{\text{fr}} \mathbf{t}$, where $\mathbf{t}$ is the unit tangent vector to the wall pointing in the direction of the cell's velocity. $\mathbf{F}_{\text{fr}}$ is non-zero only when a pseudopod is pushing the wall (Gabriele *et al.*, 2009), which is accomplished with the localizer δ_{fr}. The localizer δ_{fr} may be expressed as

$$\delta_{\text{fr}} = \delta_{\text{mem}} \delta_{\text{wall}} \delta_{\text{ps}} \quad \text{with} \quad \begin{cases} \delta_{\text{mem}} & = & \mathcal{H}\left(0.45 - |\phi - 1/2|\right), \\ \delta_{\text{wall}} & = & \mathcal{H}\left(1.0 - d_o(\mathbf{x})\right), \\ \delta_{\text{ps}} & = & \mathcal{H}(\rho_f - \overline{\rho}_f), \end{cases} \tag{3.10}$$

where $d_o(\mathbf{x})$ is the distance to the closest obstacle and $\overline{\rho}_f = (\rho_f^{\text{pr}} + \rho_f^{\text{pa}})/2$, both terms introduced in subsection 2.2.4. The marker δ_{fr} activates the friction force in the cell membrane (defined by δ_{mem})[2] when a pseudopod (marked by δ_{ps}) is pushing the wall (δ_{wall}). ς_{fr} is a function of the cell velocity given by $\varsigma_{\text{fr}}(\mathbf{u}_{\text{cell}}) = \varsigma_{\text{fr}}^M \left[1 - \exp(-K_u \mathbf{u}_{\text{cell}})\right]$ (Gerbal *et al.*, 2000; Preira *et al.*, 2013), where ς_{fr}^M and K_u are constants, and $\mathbf{u}_{\text{cell}}$ is the velocity of the center of mass of the cell.

[1] In a two-dimensional simulation that represents cell motion on a planar substrate, this force may be interpreted as a friction force between the cell and the underlying substrate. In the biological problem, this force is accomplished by integrins.

[2] Note that both δ_{mem} and δ_m [see equation (3.2)] are membrane markers. For a given ε, δ_{mem} displays a fixed membrane width, while the width defined by δ_m depends on φ. We opted for localizing the friction forces to a fixed width of the membrane independent of φ.

3.2.4 Model discussion

Our model presents several differences and advantages in comparison with other models. The first one is the description of the actin dynamics through the functional $\mathcal{F}$; see equation (3.5). Here, the actin behavior is similar to the wave-pinning model (Mori *et al.*, 2008; Shao *et al.*, 2012), but including a dependence on the activator. Since we introduce this dependence in the energy functional, the relationship between actin and the activator in the evolution equations follows directly from our variational derivation. Most amoeboid motility models have focused on the membrane dynamics (Levchenko and Iglesias, 2002; Meinhardt, 1999) and have simulated the cell as an evolving surface (Elliott *et al.*, 2012; Hecht *et al.*, 2011b) resorting to surface PDEs, a moving mesh, and even employing more than one mesh (Neilson *et al.*, 2011b). Most of them do not account for cytosolic components explicitly. However, our model considers both membrane and cytosolic compounds by using a single fixed mesh, thanks to the phase-field framework. Other feature of our model is the cell-obstacle interaction that we simply introduce through the force $\mathbf{F}_{\text{wall}}$. Previous approaches to do this include the introduction of a repulsive potential (Zhang *et al.*, 2009), but this complicates the coupling with other components of the model. Other authors model the cell's membrane as a set of nodes whose velocity vanishes where the cell is in contact with the obstacle (Hecht *et al.*, 2011a), but this introduces a discrete component in the model and our goal was to derive a continuous model. Finally, the coupling between the cytosol and the membrane allows to represent different behaviors of the intracellular compounds that can not be captured by uncoupled models. As we will show in subsection 3.4.4, when the cell is subjected to compressive forces (e.g., those exerted by the walls of a narrow channel) the F-actin network extends over the entire cytosol rather than over localized areas. The coupling is essential to capture this process.

3.2.5 Continuous problem in strong form

Let $\Omega \subset \mathbb{R}^{d_s}$ be an open set that represents our computational domain. Unless otherwise stated, Ω is simply a box sufficiently large to enclose the cell. Let Γ be the boundary of Ω, assumed sufficiently smooth. The strong form of the problem can be stated as: Given a time interval of interest $[0,T]$ and suitable initial and boundary conditions, find $\phi : \overline{\Omega} \times (0,T) \to \mathbb{R}$, $\rho_m : \overline{\Omega} \times (0,T) \to \mathbb{R}$, $\rho_f : \overline{\Omega} \times (0,T) \to \mathbb{R}$, $\rho_g : \overline{\Omega} \times (0,T) \to \mathbb{R}$, $a : \overline{\Omega} \times (0,T) \to \mathbb{R}$, and $\mathbf{u} : \overline{\Omega} \times (0,T) \to \mathbb{R}^{d_s}$ such that

$$\frac{\partial \phi}{\partial t} + \mathbf{u} \cdot \nabla \phi = \Gamma_\phi \left(\varepsilon \nabla^2 \phi - \frac{G'(\phi)}{\varepsilon} + c\varepsilon |\nabla \phi| \right) \quad \text{in} \quad \Omega \times (0,T), \qquad (3.11)$$

$$\frac{\partial(\delta_m a)}{\partial t} + \nabla\cdot(\delta_m a\mathbf{u}) = \\ = \nabla\cdot(D_a\delta_m\nabla a) - r_a\delta_m a + b_a\delta_m S_a \quad \text{in} \quad \Omega\times(0,T), \tag{3.12}$$

$$\frac{\partial(\phi\rho_m)}{\partial t} + \nabla\cdot(\phi\rho_m\mathbf{u}) = \nabla\cdot[D_m(\rho_f)\phi\nabla\rho_m] \quad \text{in} \quad \Omega\times(0,T), \tag{3.13}$$

$$\frac{\partial(\phi\rho_f)}{\partial t} + \nabla\cdot(\phi\rho_f\mathbf{u}) = \\ = \Gamma_f\left[\varepsilon_f^2\nabla\cdot(\phi\nabla\rho_f) - \phi\frac{\partial F}{\partial\rho_f} - \alpha_N\phi\big(\mathcal{N}-\mathcal{N}_0\big)\right] \quad \text{in} \quad \Omega\times(0,T), \tag{3.14}$$

$$\frac{\partial(\phi\rho_g)}{\partial t} + \nabla\cdot(\phi\rho_g\mathbf{u}) = \\ = \Gamma_g\left[\varepsilon_g^2\nabla\cdot(\phi\nabla\rho_g) - \phi\frac{\partial F}{\partial\rho_g} - \alpha_N\phi\big(\mathcal{N}-\mathcal{N}_0\big)\right] \quad \text{in} \quad \Omega\times(0,T), \tag{3.15}$$

$$\nabla\cdot(\boldsymbol{\sigma} + \boldsymbol{\sigma}_{\text{myo}} + \boldsymbol{\sigma}_{\text{prot}}) + \mathbf{F}_{\text{adh}} + \mathbf{F}_{\text{mem}} + \mathbf{F}_{\text{wall}} = 0 \quad \text{in} \quad \Omega\times(0,T). \tag{3.16}$$

3.3 Numerical formulation

3.3.1 Weak form and semidiscrete formulation

Let $\mathcal{S} = \left\{\,\phi \mid \phi(\cdot,t)\in\mathcal{H}^2(\Omega)\right\}$ be the trial solution space. Analogously, we define a weighting function space $\mathcal{V} = \left\{\,w \mid w\in\mathcal{H}^2(\Omega)\right\}$.

We derive a weak form of equations (3.11) to (3.16) by multiplying them with weighting functions and integrating by parts repeatedly. We work under the assumptions of periodic boundary conditions and sufficient regularity. We call $n_{\text{dof}} = 5 + d_s$ the number of scalar unknowns. Thus, the problem can be stated as: Find $\mathbf{U} = \{\phi, a, \rho_m, \rho_f, \rho_g, \mathbf{u}\}\in\mathcal{S}^{n_{\text{dof}}}$ such that for all $\mathbf{W} = \{p, q, r, s, v, \mathbf{w}\}\in\mathcal{V}^{n_{\text{dof}}}$

$$\mathcal{B}(\mathbf{W},\mathbf{U}) = 0 \tag{3.17}$$

with

$$\mathcal{B}(\mathbf{W},\mathbf{U}) = \left(p, \frac{\partial\phi}{\partial t}\right)_\Omega + \left(q, \delta_m\frac{\partial a}{\partial t}\right)_\Omega + \left(q, a\delta_m'\frac{\partial\phi}{\partial t}\right)_\Omega + \left(r, \phi\frac{\partial\rho_m}{\partial t}\right)_\Omega \\ + \left(r, \rho_m\frac{\partial\phi}{\partial t}\right)_\Omega + \left(s, \phi\frac{\partial\rho_f}{\partial t}\right)_\Omega + \left(s, \rho_f\frac{\partial\phi}{\partial t}\right)_\Omega + \left(v, \phi\frac{\partial\rho_g}{\partial t}\right)_\Omega \\ + \left(v, \rho_g\frac{\partial\phi}{\partial t}\right)_\Omega + \left(p, \mathbf{u}\cdot\nabla\phi\right)_\Omega + \left(\nabla p, \Gamma_\phi\varepsilon\nabla\phi\right)_\Omega + \left(p, \Gamma_\phi\frac{G'}{\varepsilon}\right)_\Omega$$

$$
\begin{aligned}
&-\left(\nabla p, \Gamma_\phi \varepsilon \nabla \phi\right)_\Omega - \left(p, \frac{\Gamma_\phi \varepsilon}{|\nabla \phi|} \nabla \phi \cdot \nabla\left(|\nabla \phi|\right)\right)_\Omega - \left(\nabla q, \delta_m a \mathbf{u}\right)_\Omega \\
&+\left(\nabla q, D_a \delta_m \nabla a\right)_\Omega + \left(q, r_a \delta_m a\right)_\Omega - \left(q, b_a \delta_m S_a\right)_\Omega \\
&-\left(\nabla r, \phi \rho_m \mathbf{u}\right)_\Omega + \left(\nabla r, D_m \phi \nabla \rho_m\right)_\Omega - \left(\nabla s, \phi \rho_f \mathbf{u}\right)_\Omega \\
&+\left(\nabla s, \Gamma_f \varepsilon_f^2 \phi \nabla \rho_f\right)_\Omega + \left(s, \Gamma_f \phi \frac{\partial F}{\partial \rho_f}\right)_\Omega + \left(s, \Gamma_f \alpha_N \phi \left(\mathcal{N} - \mathcal{N}_0\right)\right)_\Omega \\
&-\left(\nabla v, \phi \rho_g \mathbf{u}\right)_\Omega + \left(\nabla v, \Gamma_g \varepsilon_g^2 \phi \nabla \rho_g\right)_\Omega + \left(v, \Gamma_g \phi \frac{\partial F}{\partial \rho_g}\right)_\Omega \\
&+\left(v, \Gamma_g \alpha_N \phi \left(\mathcal{N} - \mathcal{N}_0\right)\right)_\Omega \\
&-\left(\nabla \mathbf{w}, \phi\left[\mu\left(\nabla \mathbf{u} + \nabla \mathbf{u}^T\right) + \lambda\left(\nabla \cdot \mathbf{u}\right) \boldsymbol{I}\right]\right)_\Omega \\
&-\left(\nabla \mathbf{w}, \phi \rho_m \eta_m \boldsymbol{I}\right)_\Omega + \left(\nabla \mathbf{w}, \phi \rho_f \eta_f \delta_f \nabla \phi \otimes \nabla \phi\right)_\Omega - \left(\mathbf{w}, \varsigma \mathbf{u}\right)_\Omega \\
&-\left(\mathbf{w}, \gamma\left(\varepsilon \nabla^2 \phi - \frac{G'}{\varepsilon}\right) \nabla \phi\right)_\Omega - \left(\nabla \mathbf{w}, \phi \eta_{\mathrm{rep}} \delta_{\mathrm{rep}} \nabla \phi \otimes \nabla \phi\right)_\Omega \\
&-\left(\mathbf{w}, \varsigma_{\mathrm{fr}} \delta_{\mathrm{fr}} \mathbf{t}\right)_\Omega . \qquad (3.18)
\end{aligned}
$$

The discretization of equations (3.17) and (3.18) requires the use of at least quadratic splines with $\mathcal{C}^1$-global continuity. As done in the previous chapter, we resort to IGA and employ B-spline basis functions for the spatial discretization. Let us call $\mathcal{S}^h$ and $\mathcal{V}^h$ the trial and weighting function discrete spaces, which are assumed to be identical. The spline basis functions are denoted by N_A so that $\mathcal{S}^h = \mathcal{V}^h = \mathrm{span}\{N_A\}_{A=1}^{n_b}$, where n_b is the dimension of the discrete space.

The discrete problem can be stated as: Find $\mathbf{U}^h = \{\phi^h, a^h, \rho_m^h, \rho_f^h, \rho_g^h, \mathbf{u}^h\} \in (\mathcal{S}^h)^{n_{\mathrm{dof}}}$ such that for all $\mathbf{W}^h = \{p^h, q^h, r^h, s^h, v^h, \mathbf{w}^h\} \in (\mathcal{V}^h)^{n_{\mathrm{dof}}}$

$$
\mathcal{B}(\mathbf{W}^h, \mathbf{U}^h) = 0. \qquad (3.19)
$$

The variables in $\mathbf{U}^h$ and $\mathbf{W}^h$ are defined analogously to what was done in subsection 2.3.2; see equation (2.38).

3.3.2 Time discretization and numerical implementation

The time stepping scheme is analogous to the algorithm described in subsection 2.3.3. The time stepping scheme, based on the generalized-α method, divides the time interval of interest $[0, T]$ into a sequence of subintervals (t_n, t_{n+1}) with fixed time-step size $\Delta t = t_{n+1} - t_n$. The list of residual vectors defined in equation (2.39) is extended with $\mathbf{R}^A = \left\{R_A^A\right\}$, where the sub-index $A \in \{1, \ldots, n_b\}$ is the control-variable index. The components of the residual vector are given by

$$R_A^\Phi = \mathcal{B}\left(\{N_A, 0, 0, 0, 0, 0\}, \{\phi^h, a^h, \rho_m^h, \rho_f^h, \rho_g^h, \mathbf{u}^h\}\right), \tag{3.20}$$

$$R_A^A = \mathcal{B}\left(\{0, N_A, 0, 0, 0, 0\}, \{\phi^h, a^h, \rho_m^h, \rho_f^h, \rho_g^h, \mathbf{u}^h\}\right), \tag{3.21}$$

$$R_A^M = \mathcal{B}\left(\{0, 0, N_A, 0, 0, 0\}, \{\phi^h, a^h, \rho_m^h, \rho_f^h, \rho_g^h, \mathbf{u}^h\}\right), \tag{3.22}$$

$$R_A^F = \mathcal{B}\left(\{0, 0, 0, N_A, 0, 0\}, \{\phi^h, a^h, \rho_m^h, \rho_f^h, \rho_g^h, \mathbf{u}^h\}\right), \tag{3.23}$$

$$R_A^G = \mathcal{B}\left(\{0, 0, 0, 0, N_A, 0\}, \{\phi^h, a^h, \rho_m^h, \rho_f^h, \rho_g^h, \mathbf{u}^h\}\right), \tag{3.24}$$

$$R_{A,j}^U = \mathcal{B}\left(\{0, 0, 0, 0, 0, N_A \mathbf{e}_j\}, \{\phi^h, a^h, \rho_m^h, \rho_f^h, \rho_g^h, \mathbf{u}^h\}\right), \tag{3.25}$$

where $\mathbf{e}_j$ denotes the j-th unit vector of the Cartesian basis. Using the notation indicated in subsection 2.3.3, our time-integration algorithm may be defined as follows: Given $\dot{\mathbf{V}}_n$, $\mathbf{V}_n$, and Δt, find $\dot{\mathbf{V}}_{n+1}$, $\mathbf{V}_{n+1}$, $\dot{\mathbf{V}}_{n+\alpha_m}$, and $\mathbf{V}_{n+\alpha_f}$ such that

$$\mathbf{R}^\Phi\left(\dot{\mathbf{V}}_{n+\alpha_m}, \mathbf{V}_{n+\alpha_f}\right) = 0, \tag{3.26}$$

$$\mathbf{R}^A\left(\dot{\mathbf{V}}_{n+\alpha_m}, \mathbf{V}_{n+\alpha_f}\right) = 0, \tag{3.27}$$

$$\mathbf{R}^M\left(\dot{\mathbf{V}}_{n+\alpha_m}, \mathbf{V}_{n+\alpha_f}\right) = 0, \tag{3.28}$$

$$\mathbf{R}^F\left(\dot{\mathbf{V}}_{n+\alpha_m}, \mathbf{V}_{n+\alpha_f}\right) = 0, \tag{3.29}$$

$$\mathbf{R}^G\left(\dot{\mathbf{V}}_{n+\alpha_m}, \mathbf{V}_{n+\alpha_f}\right) = 0, \tag{3.30}$$

$$\mathbf{R}^U\left(\dot{\mathbf{V}}_{n+\alpha_m}, \mathbf{V}_{n+\alpha_f}\right) = 0, \tag{3.31}$$

$$\dot{\mathbf{V}}_{n+\alpha_m} = \dot{\mathbf{V}}_n + \alpha_m\left(\dot{\mathbf{V}}_{n+1} - \dot{\mathbf{V}}_n\right), \tag{3.32}$$

$$\mathbf{V}_{n+\alpha_f} = \mathbf{V}_n + \alpha_f\left(\mathbf{V}_{n+1} - \mathbf{V}_n\right), \tag{3.33}$$

$$\mathbf{V}_{n+1} = \mathbf{V}_n + \Delta t \dot{\mathbf{V}}_n + \chi \Delta t\left(\dot{\mathbf{V}}_{n+1} - \dot{\mathbf{V}}_n\right), \tag{3.34}$$

where χ, α_m, and α_f are the real-valued parameters defined in equations (2.53), (2.55), and (2.56), respectively, with $\varrho_\infty = 0.5$.

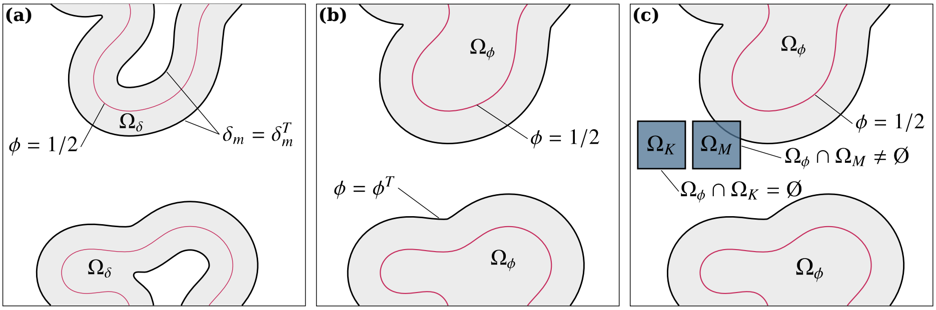

Figure 3.6. Different subdomains defined in the amoeboid problem. *(a) Ω_δ is the region where the entries of the residual and the tangent associated to the unknown a are not modified. (b) Ω_ϕ is similar to Ω_δ, but for the unknowns ρ_m, ρ_f, and ρ_g. (c) Ω_M and Ω_K are the supports of the basis functions N_M and N_K. Ω_M overlaps with Ω_ϕ, while Ω_K does not.*

The nonlinear system of equations (3.26) to (3.34) is approximated by using the Newton–Raphson's method described in subsection 2.3.3. We consider that convergence is achieved when each one of the residual vectors is reduced to 10^{-4} of its initial value.

Redefinition of the tangent matrix and the residual vector to avoid singularities

As explained in the previous chapter, the global linear system solved by the Newton–Raphson algorithm is ill-conditioned. The unknown a also contributes to this issue, since a approaches the value zero outside of the cell membrane ($\delta_m \approx 0$). Here, we extend the procedure described in subsection 2.3.3 to account for the activator also. After assembling the global residual vector and tangent matrix, we proceed as follows:

(i) Establish the thresholds $\phi^T = 10^{-8}$ and $\delta_m^T = 10^{-4}$ using the current nonlinear iteration of ϕ at the α_f time level; see figure 3.6.

(ii) Define the spatial domains $\Omega_\phi = \{\mathbf{x} \mid \phi > \phi^T\}$ and $\Omega_\delta = \{\mathbf{x} \mid \delta_m > \delta_m^T\}$.

(iii) Denote by $k_{\max} = n_b\, n_{\text{dof}}$ the number of entries of the global vector of control variables $\mathbf{V}$. Let V_k be the k-th entry of $\mathbf{V}$. For $k = 1, \cdots, k_{\max}$, proceed as follows:

   1. If V_k is a control variable of the unknowns ρ_m, ρ_f, ρ_g, or a associated to the basis function N_A, compute the support of N_A and denote it by Ω_A.

2. If $\Omega_\phi \cap \Omega_A = \varnothing$ or $\Omega_\delta \cap \Omega_A = \varnothing$, then, perform the following two steps:

   2.1. Replace the row k of the global tangent matrix by the row k of the $k_{\max} \times k_{\max}$ identity matrix.

   2.2. Replace the k-th entry of the global residual vector by 0.

(iv) Solve the linear system defined in equation (2.61) with the updated tangent matrix and residual vector.

This strategy works successfully in all the numerical examples shown throughout this chapter. The updated tangent matrices have a significantly lower condition number.

Remarks:

1. To achieve accurate results in the activator equation [equation (3.12)] it is necessary to use a steep marker δ_m (Teigen *et al.*, 2009). A steep marker can be obtained by taking a large value of φ in equation (3.2), but as a consequence, the numerical approximation of the activator equation requires a very fine mesh. The requirement to use a very fine mesh can be bypassed by replacing $\mathbf{u}$ by $\mathbf{u}^\star$ in equation (3.12). The field $\mathbf{u}^\star$ can be defined as a constant extension of the field $\mathbf{u}$ at the level set $\phi = 1/2$ in the direction orthogonal to the membrane. Mathematically, this can be expressed as $\mathbf{u}^\star(\mathbf{x}) = \mathbf{u}\left(\mathbf{\Psi}(\mathbf{x})\right)$ where $\mathbf{\Psi}(\mathbf{x})$ is the closest point to $\mathbf{x}$ such that $\phi\left(\mathbf{\Psi}(\mathbf{x})\right) = 1/2$; see figure 2.6a. We found that this procedure significantly speeds up the computations, introducing negligible errors. A similar procedure was also used to compute δ_{rep} and δ_{wall} in equations (2.29) and (3.10), respectively, where we replaced $d_o(\mathbf{x})$ with $d_o^\star(\mathbf{x}) = d_o\left(\mathbf{\Psi}(\mathbf{x})\right)$.

2. As done in the previous chapter, we treat explicitly, rather than implicitly, some of the terms of the residual vector. This implies that some of the terms in the residual vector are evaluated at time t_n, rather than $t_{n+\alpha_f}$ as indicated in equations (3.26) to (3.31). In particular, treating explicitly $\mathcal{N}$, δ_{rep}, δ_{wall}, $\mathbf{u}_{\text{cell}}$, and $\mathbf{u}^\star$ speeds up the computations significantly without compromising the accuracy and stability of the algorithm.

3. The locations of the activator sources move together with the cell's membrane. In our computations, the locations are updated using the midpoint rule and the membrane's velocity $\mathbf{u}^\star$. Thus, for the activator source located at $\mathbf{s}_i$, we assume $\mathbf{s}_i(t_{n+1}) \approx \mathbf{s}_i(t_n) + \frac{\Delta t}{2}\left(\mathbf{u}^\star(t_n) + \mathbf{u}^\star(t_{n+1})\right)$. When we compute the residual in the Newton–Raphson loop, $\mathbf{u}^\star(t_{n+1})$ is replaced by the current approximation of the membrane velocity. The locations of the activator sources that enter the residual are evaluated at α_f time level. When

the centers of the activator sources are sufficiently close to the boundary, we resort to the mapping Σ defined in equation (2.64).

4. An alternative methodology more efficient computationally than the procedure explained above to avoid singularities may be found in appendix B.

3.4 Numerical examples

This section shows numerical examples of amoeboid motion, in particular, *Dictyostelium* migration in 2D and 3D environments. The simulations are computed using the proposed model and discretization scheme. The code as been developed on top of PetIGA, as done for the mesenchymal problem developed in chapter 2. We took the same time step $\Delta t = 0.05\,\mathrm{s}$ for all the examples. We open this section with a quantitative and qualitative analysis of two-dimensional free movement. Then, we show cell migration on a planar surface with obstacles and in confined environments such as, e.g., microchannels. By studying migration in microchannels we show the importance of considering the cytosol interactions along with the membrane dynamics. Finally, we present an example of 3D migration in a fibrous network.

3.4.1 Analysis of amoeboid motion on planar substrates

We initially focus on the free movement of *Dictyostelium* on a planar surface without obstacles. There are a number of experiments that analyze this kind of migration. To compare our results with the experiments, we performed 10 independent simulations, each corresponding to the motion of one cell for 15 minutes. We use the computational domain $\overline{\Omega} = [-L, L]^2$ with $L = 20\,\mu\mathrm{m}$ and a mesh composed of 200 $\mathcal{C}^1$-continuous quadratic elements in each direction. The initial condition defines a circular cell of radius $R_c = 8\,\mu\mathrm{m}$ with no activator on the membrane, uniform ρ_m, ρ_f, and ρ_g densities[3], zero velocity, and random locations for $\mathbf{s}_0$ and $\mathbf{s}_{-1}$, required to define the first pseudopod (associated to $\mathbf{s}_1$). The values of the model parameters are listed in table 3.1.

Figure 3.7 illustrates how our model reproduces larger-scale features and emerging behavior, such as persistent motion. Figure 3.7a shows the predicted tracks of 10 cells compared with experimental results (see the rectangular inset). The cells tracks seem to maintain their direction for certain periods of time, suggesting

[3]More specifically, $\phi(\mathbf{x}, 0) = 0.5 - 0.5 \tanh\left[\frac{2\sqrt{2}}{\varepsilon}\left(d_c(\mathbf{x}) - R_c\right)\right]$ with $d_c(\mathbf{x})$ the distance to the coordinates origin, $\rho_m(\mathbf{x}, 0) = \phi(\mathbf{x}, 0)$, $\rho_f(\mathbf{x}, 0) = 0.5\phi(\mathbf{x}, 0)$, and $\rho_g(\mathbf{x}, 0) = 1.1\phi(\mathbf{x}, 0)$.

Table 3.1. *Dictyostelium two-dimensional motion parameters. In this chapter, some of the parameter values are taken from experiments and computational works of cell motility, while the rest have been estimated to better represent the biological problem; see Moure and Gomez (2016, 2017) for more details.*

Symbol	Description	Value
Γ_ϕ	Parameter enforcing a hyperbolic tangent profile	$0.52\,\mu\mathrm{m\,s}^{-1}$
ε	Phase-field interfacial length scale	$2\,\mu\mathrm{m}$
φ	Scaling of membrane marker width	25
D_a	Diffusion coefficient of activator	$0.195\,\mu\mathrm{m}^2\mathrm{s}^{-1}$
r_a	Decay rate of activator	$0.325\,\mathrm{s}^{-1}$
b_a	Production rate of activator	$7.8\,\mathrm{s}^{-1}$
$a_{\max}$	Saturation of activator	$1.5\,\mu\mathrm{m}^{-2}$
R_a	Radius of activator source	$1\,\mu\mathrm{m}$
d_o^a	Effective distance for pseudopod inhibition	$1.3\,\mu\mathrm{m}$
$D_m^{\max}$	Myosin diffusion constant	$4.16\,\mu\mathrm{m}^2\mathrm{s}^{-1}$
K_m	Decay rate of myosin diffusion	$1.55\,\mu\mathrm{m}^2$
ε_f	Diffusive length scale of F-actin	$0.707\,\mu\mathrm{m}$
ε_g	Diffusive length scale of G-actin	$3.16\,\mu\mathrm{m}$
α_N	Penalty parameter for actin conservation	$0.06\,\mu\mathrm{m}^{-2}$
Γ_f	F-actin mobility	$0.52\,\mathrm{s}^{-1}$
Γ_g	G-actin mobility	$0.52\,\mathrm{s}^{-1}$
μ	Dynamic viscosity coefficient	$1500\,\mathrm{pN\,s}\,\mu\mathrm{m}^{-1}$
λ	Bulk viscosity coefficient	$-500\,\mathrm{pN\,s}\,\mu\mathrm{m}^{-1}$
$\overline{\eta}_f$	Strength of protrusive forces	$1.22\cdot 10^4\,\mathrm{pN}\,\mu\mathrm{m}^3$
$\overline{\alpha}_f$	Range of protrusive forces	0.076 59
d_o^f	Effective distance for protrusion suppression	$1.6\,\mu\mathrm{m}$
$\overline{\eta}_m$	Strength of contractile forces	$22.1\,\mathrm{pN}\,\mu\mathrm{m}$
$\overline{\alpha}_m$	Range of contractile forces	0.4117
ς	Substrate friction coefficient	$0.7\,\mathrm{pN\,s}\,\mu\mathrm{m}^{-3}$
γ	Surface tension coefficient	$78\,\mathrm{pN}$
η_{rep}	Strength of repulsive forces	$4550\,\mathrm{pN}\,\mu\mathrm{m}$
d_o^{ef}	Effective distance for obstacle repulsion	$0.7\,\mu\mathrm{m}$
$\varsigma_{\mathrm{fr}}^M$	Wall friction coefficient	$0.895\,\mathrm{pN}\,\mu\mathrm{m}^{-2}$
K_u	Scaling of frictional cell speed	$30\,\mathrm{s}\,\mu\mathrm{m}^{-1}$

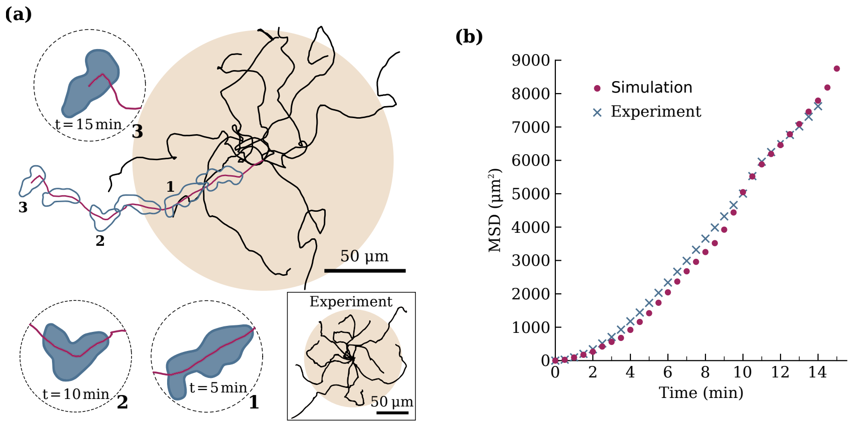

Figure 3.7. ***Dictyostelium*** **free movement results analysis.** *(a) Comparison of cells tracks with the experiment of Bosgraaf and Van Haastert (2009b). Some snapshots of the cell shape corresponding to the red track are zoomed in. (b) Comparison of the computational mean-squared displacement with the experiment of Bosgraaf and Van Haastert (2009b).*

persistent motion. For a more detailed quantitative comparison, we make use of the *mean squared displacement* (MSD) (Gail and Boone, 1970; Potel and Mackay, 1979), a widely used measure of the spatial extent of random motion. More specifically, $\mathrm{MSD}(t) = (\sum_{i=1}^{n_c} |\mathbf{x}_{\mathrm{cell},i}(t) - \mathbf{x}_{\mathrm{cell},i}(0)|^2)/n_c$, where n_c is the number of cells and $\mathbf{x}_{\mathrm{cell},i}(t)$ is the position of the cell's centroid at time t. As shown in figure 3.7b, the time evolution of the MSD exhibits a quasi-quadratic behavior for early times and a linear growth for late times, as expected for persistent motion. The plot shows quantitative agreement with the experiment (Bosgraaf and Van Haastert, 2009b).

Following the quantitative analysis, the pseudopod size and the angle between consecutive pseudopods have been measured according to description in figure 3.9 ($t = 857\,\mathrm{s}$), and have been plotted in figures 3.8a and 3.8b. The results are quite similar to experimental data (Bosgraaf and Van Haastert, 2009b; Li *et al.*, 2008) (note that we have not distinguished between splitting or *de novo* pseudopods) and to other *Dictyostelium* motility models results (Hecht *et al.*, 2011b; Neilson *et al.*, 2011b). This resemblance could seem redundant, since we have introduced the pseudopod formation probability in the model, but it should be noticed that only the initial location of the activator patch is given. Though the correlation between the activator and pseudopod locations is high (as observed in Hecht *et al.*, 2011b), the pseudopod growth is led by the actin dynamics. Therefore, the shape, size, and angle between pseudopods naturally arise in our model. We have also plotted the pairs (θ_i, θ_{i+1}) on a phase space of angles between pseudopods; see

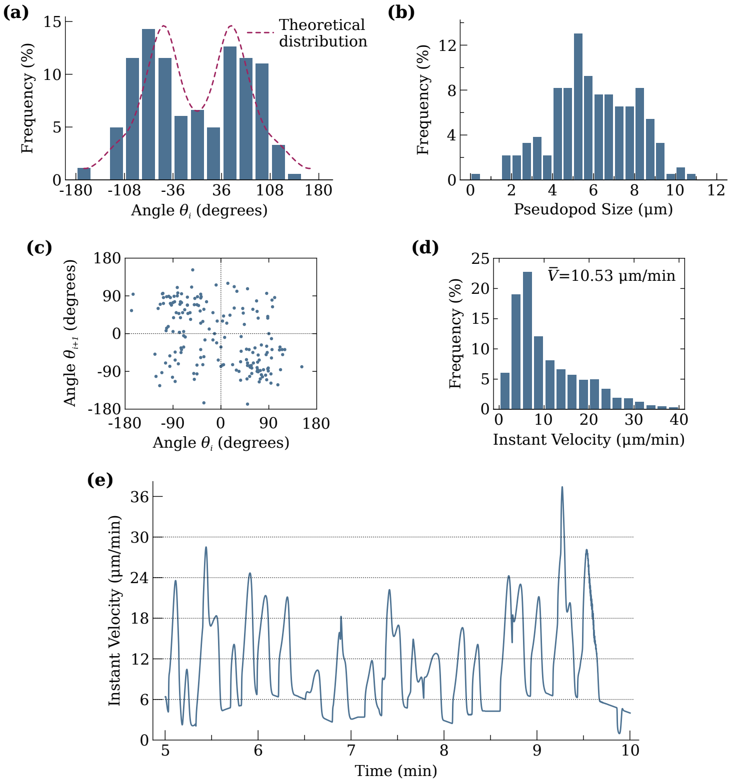

Figure 3.8. *Dictyostelium* free movement results analysis. *(a) Frequency histogram of angle between two consecutive pseudopods (θ_i). (b) Frequency histogram of pseudopod size. (c) θ_i angle plotted against θ_{i+1} angle. (d) Frequency histogram of instant velocity. (e) Temporal evolution of instant velocity.*

figure 3.8c. Here, the top-left and the bottom-right quadrants are denser than the two others, a typical feature of persistent motion (Bosgraaf and Van Haastert, 2009b; Li *et al.*, 2008) (the most frequent sequence is a turn left after a turn right, and vice versa). We have finally analyzed the cell's instant velocity. The average (over time and cell population) takes the value $\overline{V} = 10.53\,\mu\text{m/min}$ in the simulations and $10.4\,\mu\text{m/min}$ in the experiment of Bosgraaf and Van Haastert (2009b). A histogram and a 5 minute-long graph with the temporal evolution of the instant velocity can be found in figures 3.8d and 3.8e. Both of them display great similarities to their respective plots in Jacobelli *et al.* (2010); Li *et al.* (2008), showing the presence of fluctuations around the average velocity, on the time-scale of minutes. In the temporal plot, each peak corresponds to the extension of a pseudopod, causing also peaks in the cell's area and perimeter plots (not shown).

3.4.2 *Dictyostelium* free movement

Here, we present a qualitatively analysis of *Dictyostelium* free movement, which better shows the capabilities of the model. We employ two of the ten simulations performed in the previous section. Let us call them simulation (I) and simulation (II). We use simulation (I) to study short time intervals, in particular, pseudopod dynamics during the growth time ($\sim 14\,\mathrm{s}$). The cell's behavior in a larger time-scale ($\sim 1\,\mathrm{min}$) is analyzed with simulation (II).

We first focus on simulation (I) and analyze the small-scale features of the model, such as the cytosol or activator dynamics within the cell. Figure 3.9 shows the cell shape at four different times: 844, 847, 852, and 857 s (solid and dashed black lines indicate the cell's membrane position at previous times). We represent the F-actin distribution within the cell. Note that we have plotted a strip at the cell's membrane. The color of the strip represents the activator concentration. At $t = 844\,\mathrm{s}$, a new activator peak has just appeared and triggers the formation of a new pseudopod (let us call it $\mathbf{s}_i$), which will grow until $t = 857\,\mathrm{s}$. At that time, the pseudopod is no longer extending, but beginning its retraction. At $t = 847\,\mathrm{s}$, near the initial pseudopod, there is a crescent activator peak that will cause the formation of a new pseudopod ($\mathbf{s}_{i+1}$) by splitting the current one few seconds later. We also compare experimental images taken from Insall (2010) to our results (see the rectangular insets in figure 3.9), and we conclude that qualitative features such as cell shape, F-actin distribution, or the general dynamic behavior exhibit great similarities. The velocity and myosin distributions at times 844, 847, 852, and 857 s are plotted in figure 3.10. We can observe that myosin is concentrated at the rear of the cell, producing the retraction of the membrane (see zoom 1 in figure 3.10), and the F-actin velocity is able to reproduce retrograde flow in regions of growing lamellipodia. Figure 3.11 shows the temporal evolution of the main variables along the membrane, corresponding to the snapshots plotted in figures 3.9 and 3.10. The aforementioned relationship between F-actin and activator can be observed, as well as the decrease of myosin II in areas of pseudopod extension. Note the growth of the membrane and the fluctuation of G-actin around values of $\rho_g^{\mathrm{eq}} = 1$, depending on the global state of the cell and the location of high density patches of F-actin.

Let us focus now on simulation (II). The orchestrated process of growth and retraction of pseudopods produces the highly dynamic motion characteristic of *Dictyostelium*. Figure 3.12 shows several snapshots of the moving cell. In the cell's interior the color scale represents F-actin density. The activator concentration is plotted on the membrane. As expected, a peak in the activator concentration ($t = 490\,\mathrm{s}$) produces a region with high F-actin density, i.e., a pseudopod, in a nearby area of the cell's interior ($t = 498\,\mathrm{s}$). Simultaneously, the previous pseudopods retract ($t = 498\,\mathrm{s}$ and $t = 509\,\mathrm{s}$). The process is periodically repeated with most new pseudopods emerging at the front of the cell as described by the probability distributions displayed in figures 3.3d to 3.3f. This is a particular feature of amoeboid motility that produces persistent motion. However, occasionally, a new protrusive structure grows far from the cell's front giving rise to a so-called *de novo* pseudopod (Bosgraaf and Van Haastert, 2009b), which produces an abrupt change of direction in the cell ($t = 530\,\mathrm{s}$ and $t = 539\,\mathrm{s}$). Figure 3.13 shows the myosin distribution and the membrane's velocity at the same time steps. The plots show how myosin is mostly concentrated at the rear of the cell (Van Haastert and Devreotes, 2004), producing the contraction of the tail as well as the retraction of the pseudopods that are no longer active.

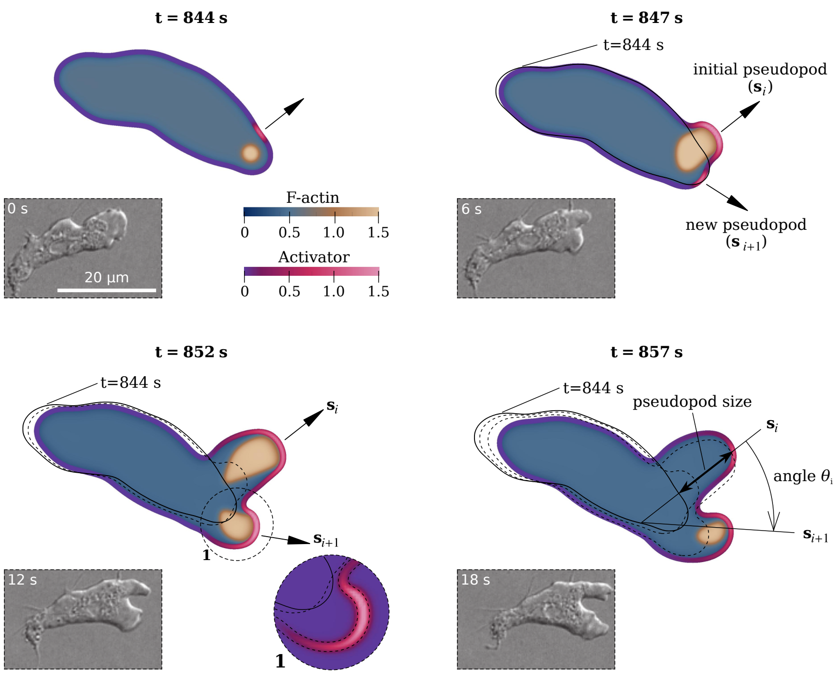

Figure 3.9. *Dictyostelium* free movement (I). F-actin and activator distributions. *F-actin and activator distributions at $t = 844$, 847, 852, and 857 s. The rectangular insets show experimental images taken from Insall (2010). The activator distribution at $t = 852\,\mathrm{s}$ is zoomed in (circular inset 1). The pseudopod size (net distance traveled by $\mathbf{s}_i$ during its growth time) and the angle θ_i are described in the panel $t = 857\,\mathrm{s}$.*

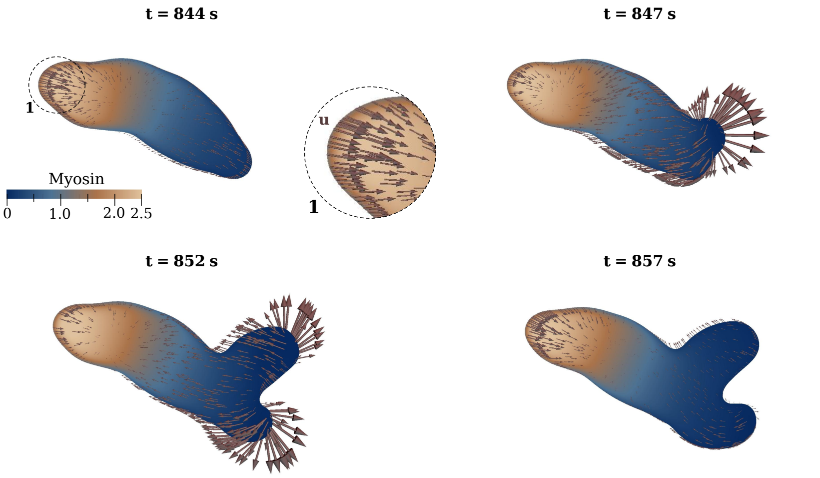

Figure 3.10. *Dictyostelium* free movement (I). Myosin and velocity distributions. *Myosin and velocity distributions at* $t = 844$*,* 847*,* 852*, and* $857\,\mathrm{s}$*. The velocity distribution at* $t = 844\,\mathrm{s}$ *is zoomed in (inset 1).*

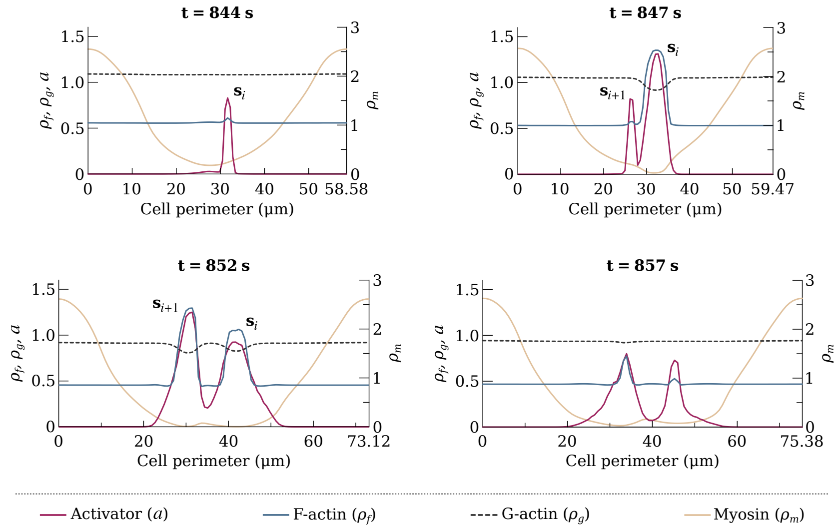

Figure 3.11. *Dictyostelium* free movement (I). Activator, F-actin, G-actin, and myosin distributions along the cell membrane. *The plots correspond to the snapshots shown in figures 3.9 and 3.10.*

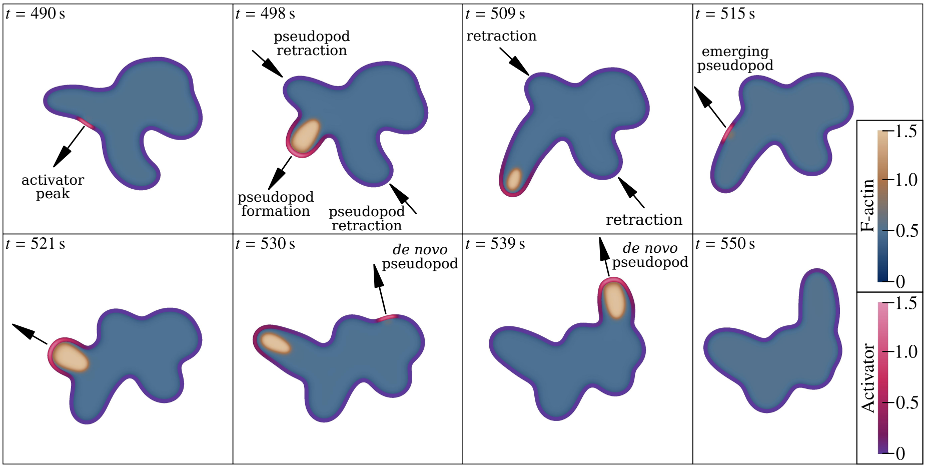

Figure 3.12. ***Dictyostelium* free movement (II). Time evolution of the F-actin and activator distributions.** *The arrows indicate the extension or retraction of pseudopods.*

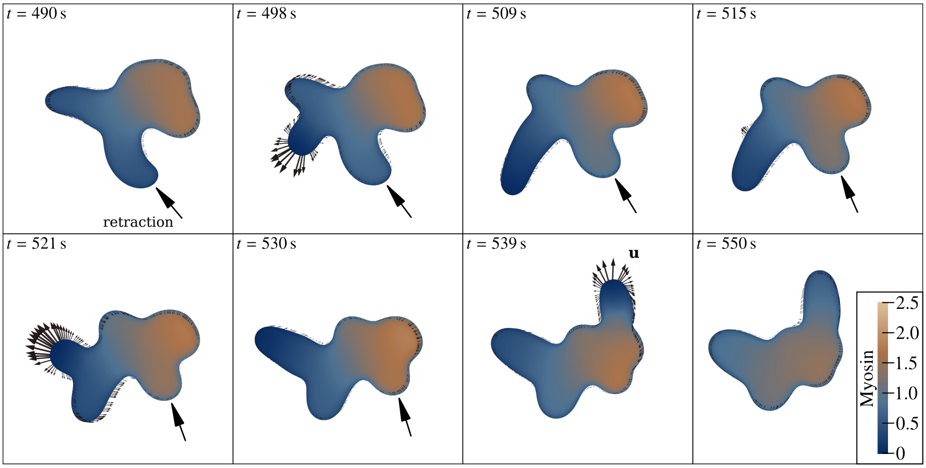

Figure 3.13. ***Dictyostelium* free movement (II). Time evolution of the membrane's velocity and the myosin distribution.** *The arrows indicate the retraction of pseudopods produced by myosin and surface tension.*

3.4.3 Migration on a planar surface with obstacles

Dictyostelium cells are known to migrate effectively on a planar substrate with obstacles. This example shows that the model can successfully reproduce this

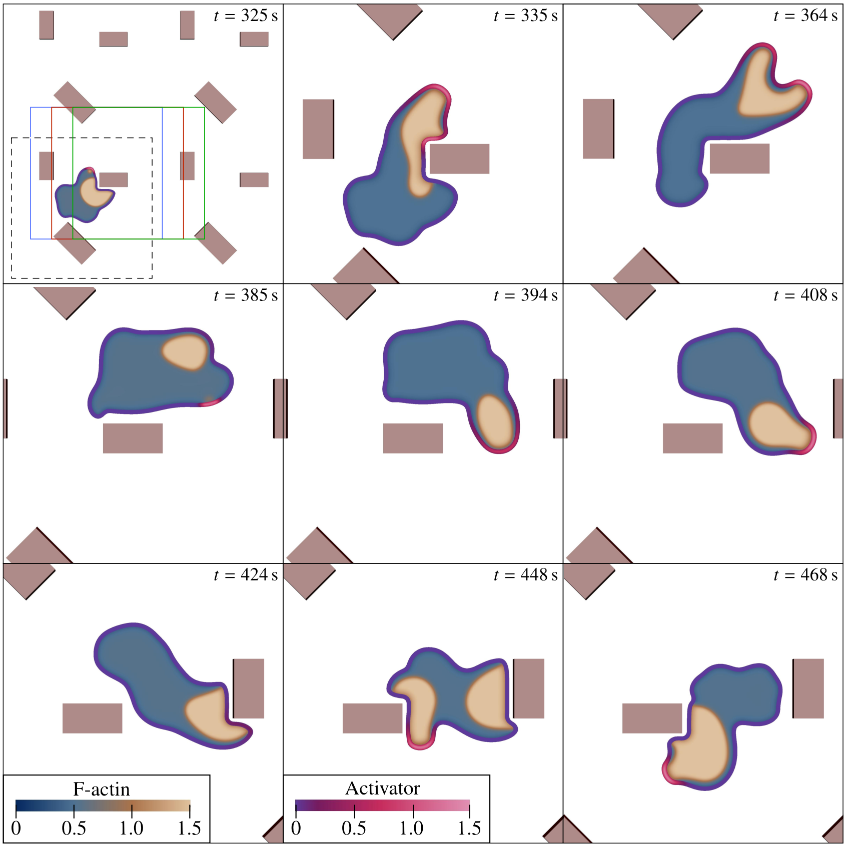

Figure 3.14. *Dictyostelium* migration on a planar surface with obstacles. Time evolution of the F-actin and activator concentrations. *In the top left panel, the computational domain (marked with the dashed square) is expanded four times. The blue, red, and green squares in the top left panel represent the areas plotted in the rest of the top row, middle row, and bottom row, respectively.*

feature of amoeboid motion. We employ the same computational domain and mesh as done in subsection 3.4.1, as well as the same initial conditions. The model parameters are listed in table 3.1. We have disregarded friction forces in this example[4] ($\varsigma_{\rm fr}^{M} = 0$). The top left panel of figure 3.14 shows the computational domain represented by a square plotted with dashed lines. For visualization

[4]Friction forces are produced by adherent F-actin networks observed in confined migration in microchannels (see subsection 3.4.4). We assume that the interaction with isolated obstacles does not produce adherent networks.

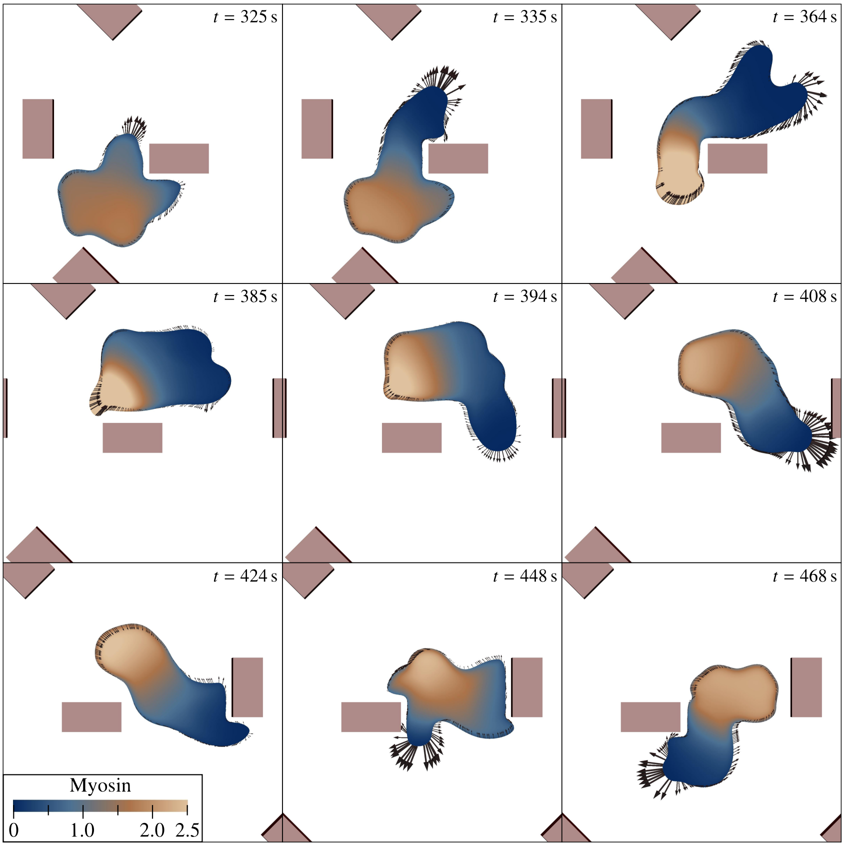

Figure 3.15. *Dictyostelium* migration on a planar surface with obstacles. Time evolution of the membrane's velocity and the myosin distribution. *The snapshots correspond to the same time steps shown in figure 3.14.*

purposes, we have periodically extended the computational domain in both directions, so that the top left panel of figure 3.14 is approximately four times larger than the actual computational domain. The obstacles have rectangular shape, random locations, and have been plotted with brown color. The blue, red, and green squares in the top left panel represent the areas that will be plotted in the rest of the top row, the middle row, and the bottom row, respectively. The color scales in figure 3.14 represent the F-actin and activator concentrations. The first row of the figure shows how the central obstacle exerts forces on the cell; see the term $\mathbf{F}_{\mathrm{wall}}$ in equation (3.9). These forces bend the cell's membrane, avoiding the penetration of the obstacle. $\mathbf{F}_{\mathrm{rep}}$ plays the role of a very simple contact model based on the penalty method. A recent work (Tozluoglu *et al.*, 2013) has proposed a different approach, where no-slip condition between membrane and obstacle is imposed, and a hard wall potential impedes the cell penetration into the obstacles. In our model, the ability of the cell to overcome the obstacle is enhanced by preventing pseudopods to form in the areas of the membrane that are close to the rigid obstacle. This constraint has been built into the model (see subsection 3.2.2) and is based on experimental observations (Nagel *et al.*, 2014). In the snapshots of the middle row the cell is relatively far from the obstacle and is migrating essentially as in an obstacle-free substrate. The bottom row shows how the cell hits the obstacle on the right hand side, and as it tries to reverse its direction, encounters the obstacle on the left hand side. Eventually, the cell manages to move downwards and escape away of the obstacles. Figure 3.15 shows the membrane's velocity and the myosin distribution at the same time steps. It may be observed that the membrane's velocity is very small close to the obstacles due to the absence of protrusive forces.

3.4.4 Confined movement in microchannels

Now we focus on confined movement. We compare our model results with the experiments in Jacobelli *et al.* (2010); Nagel *et al.* (2014), which study cell motility in microchannels (see figure 3.16). The experiments analyze how the microchannel width modifies the ability of cells to spread. In narrow channels, wall friction slows down the cell, whereas in wider channels the cell is unable to contact both sides, reducing its forward protrusion (Wilson *et al.*, 2013) and acquiring a more random phenotype. There seems to be an optimal channel width that maximizes spreading.

To get representative results, we performed 8 simulations of 15 minutes for each channel width (6, 8, 10, 12, 14, and 16 µm). The computational domains employed in the simulations depend on the channel width. We used periodic rectangular domains meshed with quadratic square elements of size 0.2 µm for all the channel widths. The size of the rectangle is adjusted such that the area outside the channel is reduced as much as possible. The parameter values used in the microchannel simulations are shown in table 3.1. The initial conditions correspond to a rectangular cell adjusted to the channel width (with a suitable length so as to keep a physiological area), vanishing activator and velocity distributions, and uniform densities for ρ_m, ρ_f, and ρ_g[5]. Unlike subsection 3.4.1, we locate $\mathbf{s}_0$ and $\mathbf{s}_1$ on the right-hand side of the cell, so that the cell starts moving to the right (i.e., the cell's velocity in the channel's direction is positive at the initial time).

[5]The initial cell geometry is given by a hyperbolic tangent function, $\phi(\mathbf{x}, 0)$, that depends on the channel width. Thus, $\rho_m(\mathbf{x}, 0) = \rho_m^0 \phi(\mathbf{x}, 0)$, $\rho_f(\mathbf{x}, 0) = \rho_f^0 \phi(\mathbf{x}, 0)$, and $\rho_g(\mathbf{x}, 0) = 1.1\phi(\mathbf{x}, 0)$,

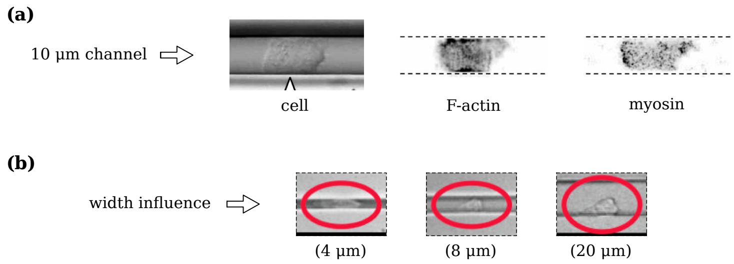

Figure 3.16. Experimental images of confined cellular migration. *(a) Cell shape, F-actin, and myosin experimental images in a* 10 µm *width channel, taken from Nagel* et al. *(2014). (b) Experimental images for different widths, taken from Jacobelli* et al. *(2010).*

Figure 3.17 shows several snapshots of F-actin, activator, velocity and myosin distributions for widths of 6, 10, and 16 µm (cell's membrane positions at previous times are displayed with black lines), which can be compared with the experiments in figure 3.16. In the case of narrow channels, the F-actin network spreads all over the cell, pushing the walls and causing friction on a large surface. For intermediate widths, the sides of the cell contact with a smaller area, which combined with a wider front, results in faster polymerization (Wilson *et al.*, 2013), and thus, faster motion. Comparing with F-actin distributions in experiments (figure 3.16a) we can see how the F-actin network is in contact with both walls of the channel and is widespread across the cell, resulting in a characteristic rectangular shape (Nagel *et al.*, 2014). However, our model is unable to reproduce some detailed dynamics experimentally observed in Nagel *et al.* (2014); Wilson *et al.* (2013), e.g., the presence of two kinds of F-actin networks. One of them, called *free* network, produces protrusions at the leading edge in a highly dynamic fashion. The other one is a denser network that polymerizes perpendicular to the channel wall, remains stationary with respect to the wall, and is called *adherent* network. As shown in figure 3.17b, our model represents just one type of dense F-actin network: both the free and the adherent networks are associated to $\rho_f = \rho_f^{\mathrm{pr}}$. To distinguish the two networks, we should modify the functional $\mathcal{F}$ [see equation (3.5)] to include another stable F-actin density that accounts for the adherent network. In addition, Nagel *et al.* (2014); Wilson *et al.* (2013) suggest that confinement produces a mechanical interaction between the actin networks. We have modeled the cell-wall contact through the membrane-located force $\mathbf{F}_{\mathrm{wall}}$, but we have not incorporated the feedback between confinement and actin dynamics, which could lead to a stationary adherent network. Finally, Nagel *et al.* (2014) describes an alternating zigzag motion at the cell front, while the back advances synchronously.

---

where ρ_m^0 and ρ_f^0 are defined such that $\int_\Omega \phi\rho_m \mathrm{d}\Omega = 250$ and $\mathcal{N}_0 = 430$.

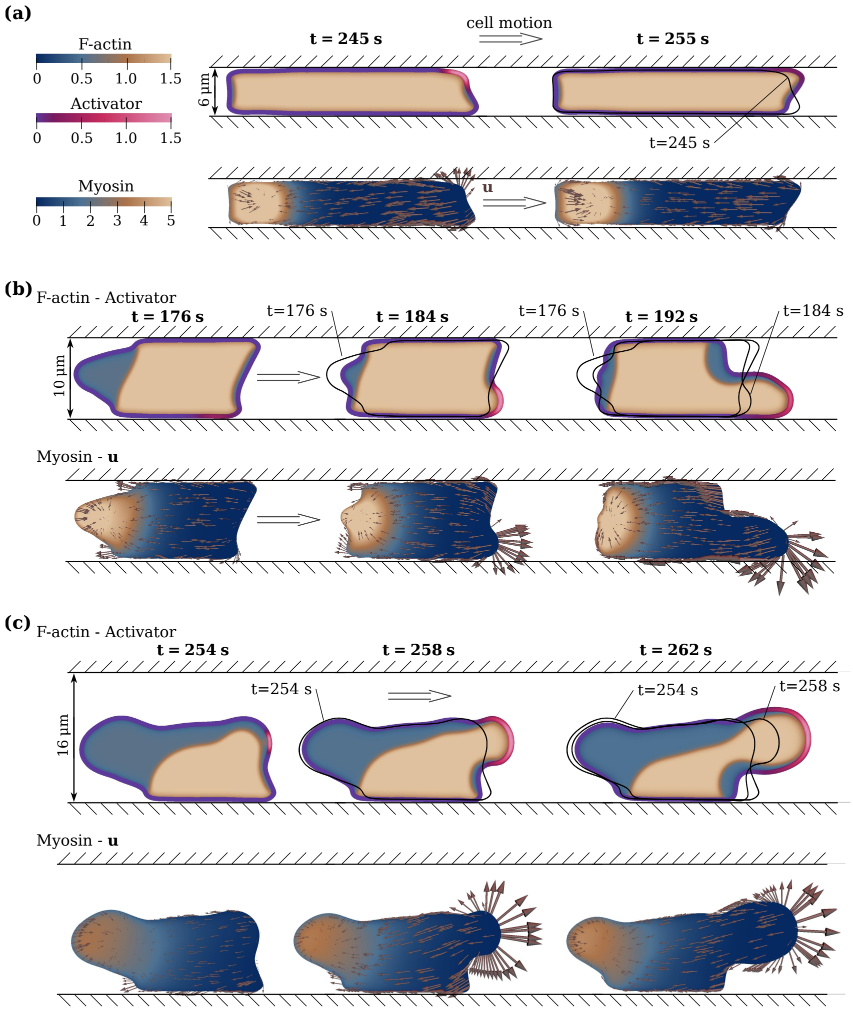

Figure 3.17. Cell motility in microchannels. F-actin and activator distributions (top of each panel), and myosin and velocity distributions (bottom of each panel) at different times. *(a)* $6\,\mu$m *width channel at* $t = 245$ *and* $255\,$s. *(b)* $10\,\mu$m *width channel at* $t = 176$, 184, *and* $192\,$s. *(c)* $16\,\mu$m *width channel at* $t = 254$, 258, *and* $262\,$s.

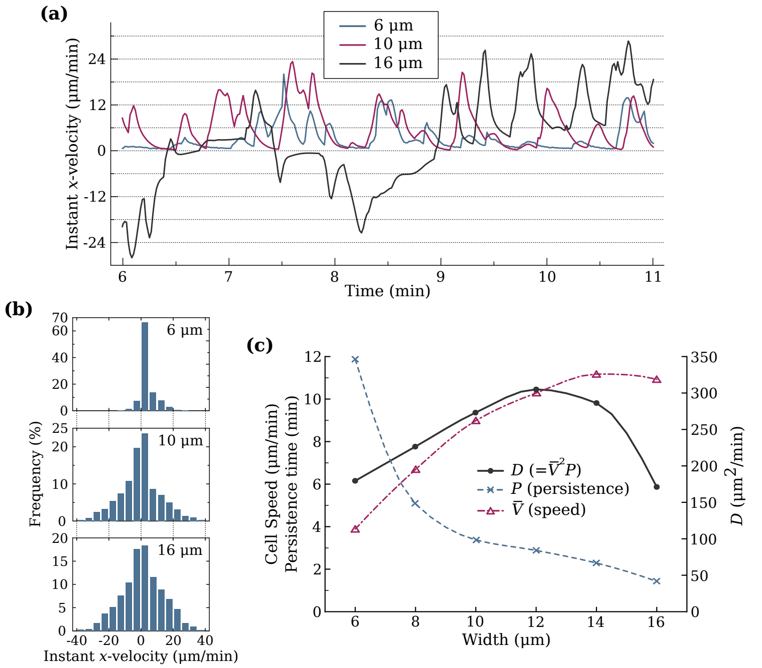

Figure 3.18. Results analysis of cell motility in microchannels. *(a) Temporal evolution of instant x-velocity (in the channel's direction) for* 6, 10, *and* 16 µm *width channels. (b) Histograms of instant x-velocity for* 6 *(top subpanel),* 10 *(mid subpanel), and* 16 µm *(bottom subpanel) width channels. (c) Cell speed, persistence time, and parameter D, depending on channel width.*

This behavior is predicted by our model, mainly caused by the pseudopod extension probability (see figure 3.3d), which is annihilated in regions where the membrane is touching the wall. This constraint is also set in the activator-inhibitor system of Nagel *et al.* (2014), whose activator outcome displays similarities with the dynamics of our activator. A mild alternating motion as well as qualitatively realistic distributions of F-actin and myosin can be observed throughout the simulations (data not shown).

We have measured the cell's instant velocity and the persistence time for the different widths. Figure 3.18 shows how the speed increases as the channel becomes wider, reaching a maximum value that is close to the free-motion velocity. The persistence time decreases as the width increases, showing an obvious trend to random free motion for wider channels. These two features of confined movement can be observed in figure 3.18a: for wide channels, the instant velocity reaches greater values, and the x-velocity (in the channel's direction) sign changes more frequently, which means a decrease in the persistence time. The same conclusion can be drawn from figure 3.18b (note that the initial conditions considered in the simulations imply positive x-velocity); the wider the channel is, the more symmetric the x-velocity histogram will be. The average velocity ($\overline{V}$) and the persistence time (P) for the different widths have been plotted in figure 3.18c. Here, the parameter $D = \overline{V}^2 P$ is known to measure the cells ability to spread and disseminate[6] (Potel and Mackay, 1979; Uhlenbeck and Ornstein, 1930). It may be observed how D reaches a maximum for a channel width of $\sim 12\,\mu\text{m}$. This suggests that cells may exploit the geometry of their microenvironment to find effective migration strategies.

3.4.5 Migration in a three-dimensional fibrous environment

Although many experimental studies of cellular migration are performed on planar substrates, most cells migrate within the extracellular matrix —an intricate network made of fibrous proteins. The cell attaches to the fibers through integrin-mediated junctions. In turn, the fibers deform and might also get degraded due to chemicals secreted by the cell. The simulations presented in this section do not aim at reproducing this phenomenon, but rather, at proposing a much simpler scenario that is computable with the model we developed. In our simulations, the deformable fibers are replaced by rigid obstacles with fibrous geometry. The distance between fibers is probably larger than in the extracellular matrix and fiber degradation is not considered. A more accurate description of the extracellular matrix fibers and their mechanics should be addressed in future research. For example, an elastic or viscoelastic model for the fibers could be coupled with our cell's model. In spite of all these assumptions, we believe that these simulations are the most realistic three-dimensional computations of cellular amoeboid motion that have been reported on heretofore. To make the problem computable we also had to modify the values of some of the parameters. We modified φ and ε_f to increase, respectively, the effective membrane thickness and the F-actin length scale. This allowed us to use coarser meshes. We have also changed the penalty constant α_N to adapt it to 3D computations (α_N is a computational parameter that depends on the number of spatial dimensions). Finally, we reduced $\overline{\eta}_m$ and $\overline{\eta}_f$ to adjust the contractile and protrusive velocities to biological values in

[6] The augmented diffusion constant D is used to fit the MSD of the persistent random motion by the function $\mathrm{MSD}(t) = 2n_d D[t - P(1 - \exp(-t/P))]$, where n_d is the number of dimensions. According to Potel and Mackay (1979), the velocity autocovariance analysis applied to the general case of n_d dimensions leads to $D = \overline{V}^2 P/n_d$. For confined motility inside channels, assuming the width is small enough, we can consider that there is only one direction of dispersal (the channel's direction) and we can take $n_d = 1$.

Table 3.2. *Dictyostelium three-dimensional motion parameters.*

Symbol	Description	Value
Γ_ϕ	Parameter enforcing a hyperbolic tangent profile	$0.52\,\mu\mathrm{m\,s^{-1}}$
ε	Phase-field interfacial length scale	$2\,\mu\mathrm{m}$
φ	Scaling of membrane marker width	15
D_a	Diffusion coefficient of activator	$0.195\,\mu\mathrm{m^2 s^{-1}}$
r_a	Decay rate of activator	$0.325\,\mathrm{s^{-1}}$
b_a	Production rate of activator	$7.8\,\mathrm{s^{-1}}$
$a_{\max}$	Saturation of activator	$1.5\,\mu\mathrm{m^{-3}}$
R_a	Radius of activator source	$1\,\mu\mathrm{m}$
d_o^a	Effective distance for pseudopod inhibition	$1.3\,\mu\mathrm{m}$
$D_m^{\max}$	Myosin diffusion scale	$4.16\,\mu\mathrm{m^2 s^{-1}}$
K_m	Decay rate of myosin diffusion	$1.55\,\mu\mathrm{m^3}$
ε_f	Diffusive length scale of F-actin	$1.0\,\mu\mathrm{m}$
ε_g	Diffusive length scale of G-actin	$3.16\,\mu\mathrm{m}$
α_N	Penalty parameter for actin conservation	$0.03\,\mu\mathrm{m^{-3}}$
Γ_f	F-actin mobility	$0.52\,\mathrm{s^{-1}}$
Γ_g	G-actin mobility	$0.52\,\mathrm{s^{-1}}$
μ	Dynamic viscosity coefficient	$1500\,\mathrm{pN\,s}\,\mu\mathrm{m^{-2}}$
λ	Bulk viscosity coefficient	$-500\,\mathrm{pN\,s}\,\mu\mathrm{m^{-2}}$
$\overline{\eta}_f$	Strength of protrusive forces	$1.1\cdot 10^4\,\mathrm{pN}\,\mu\mathrm{m^3}$
$\overline{\alpha}_f$	Range of protrusive forces	0.076 59
d_o^f	Effective distance for protrusion suppression	$1.6\,\mu\mathrm{m}$
$\overline{\eta}_m$	Strength of contractile forces	$9.95\,\mathrm{pN}\,\mu\mathrm{m}$
$\overline{\alpha}_m$	Range of contractile forces	0.4117
ς	Drag coefficient	$0.7\,\mathrm{pN\,s}\,\mu\mathrm{m^{-4}}$
γ	Surface tension coefficient	$78\,\mathrm{pN}\,\mu\mathrm{m^{-1}}$
η_{rep}	Strength of repulsive forces	$4550\,\mathrm{pN}$
d_o^{ef}	Effective distance for obstacle repulsion	$0.7\,\mu\mathrm{m}$

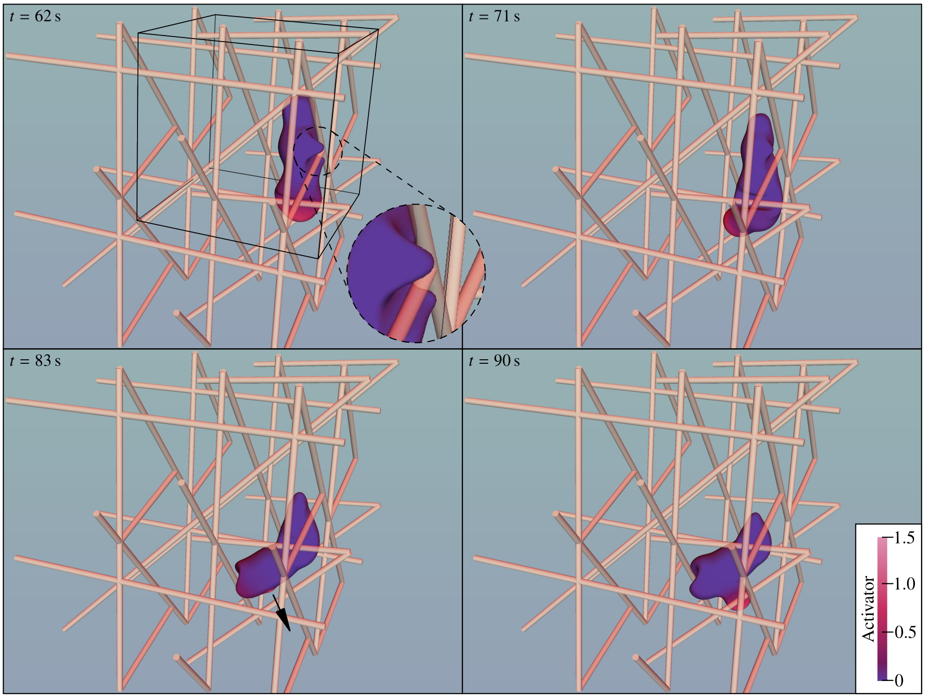

Figure 3.19. Amoeboid migration in a three-dimensional fibrous network. Activator concentration. *Activator distribution on the cell's membrane at $t = 62$, 71, 83, and $90\,\mathrm{s}$. The top left panel shows a box that represents the actual computational domain, which has been periodically extended for visualization purposes. The arrow in the bottom left panel indicates the emergence of a new pseudopod.*

3D moving cells. The parameter values used in the 3D simulation are listed in table 3.2. Following the rationale explained in subsection 3.4.3, we disregard friction forces for migration in a fibrous environment. The computational domain is $\overline{\Omega} = [0, L]^3$ with $L = 32\,\mu\mathrm{m}$. We assume periodic boundary conditions is all directions. We used 100 $\mathcal{C}^1$-quadratic elements in each direction. The initial conditions are the same as in the examples of subsection 3.4.1, but the cell is centered at the point $(16, 16, 16)\,\mu\mathrm{m}$ and has a radius of $7\,\mu\mathrm{m}$. Figure 3.19 shows snapshots of the moving cell with the membrane colored according to the activator concentration. The fibers (brown color) have been assumed to be straight and have a random spatial distribution and orientation. The images show how high concentrations of activator at the membrane give rise to the growth of new pseudopods as in the 2D examples. It may also be observed how the cell deforms locally to adapt to the fibrous environment (see, e.g., the zoom at the right-hand side of the top-left panel). We believe that such a strong cell deformation might not be realistic and may be attributed to our assumption of undeformable fibers. Nevertheless, the image illustrates the interaction between the cell and the obstacles. Figure 3.20 shows the cell at the same times with a different perspective. The membrane is represented by a semi-transparent pink surface that allows to see the cell's interior. The surfaces inside the cell are defined by the equation $\rho_f = \overline{\rho}_f$ and represent pseudopods. This image shows how the model allows to visualize the 3D structure of pseudopods. Figure 3.21 shows the evolution of the myosin distribution throughout the simulation. The highest concentrations are found in the back of the cell as in the 2D examples.

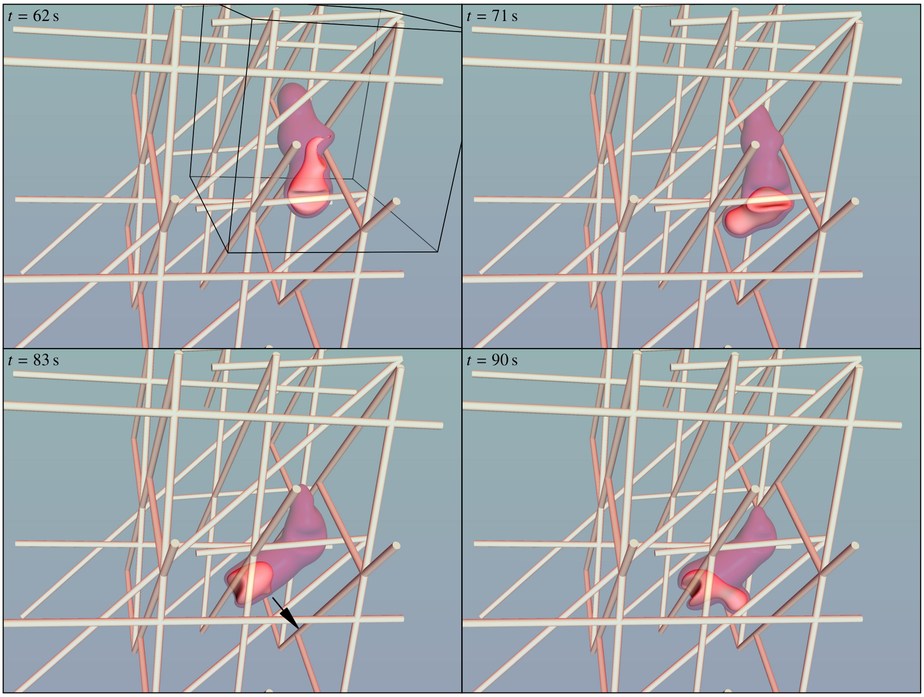

Figure 3.20. Amoeboid migration in a three-dimensional fibrous network. Pseudopod dynamics. *The cell's membrane is represented by a semi-transparent pink surface. The internal surface, defined by $\rho_f = \overline{\rho}_f$, represents the pseudopods. The top left panel shows a box that represents the actual computational domain, which has been periodically extended for visualization purposes. The arrow in the bottom left panel indicates the emergence of a new pseudopod.*

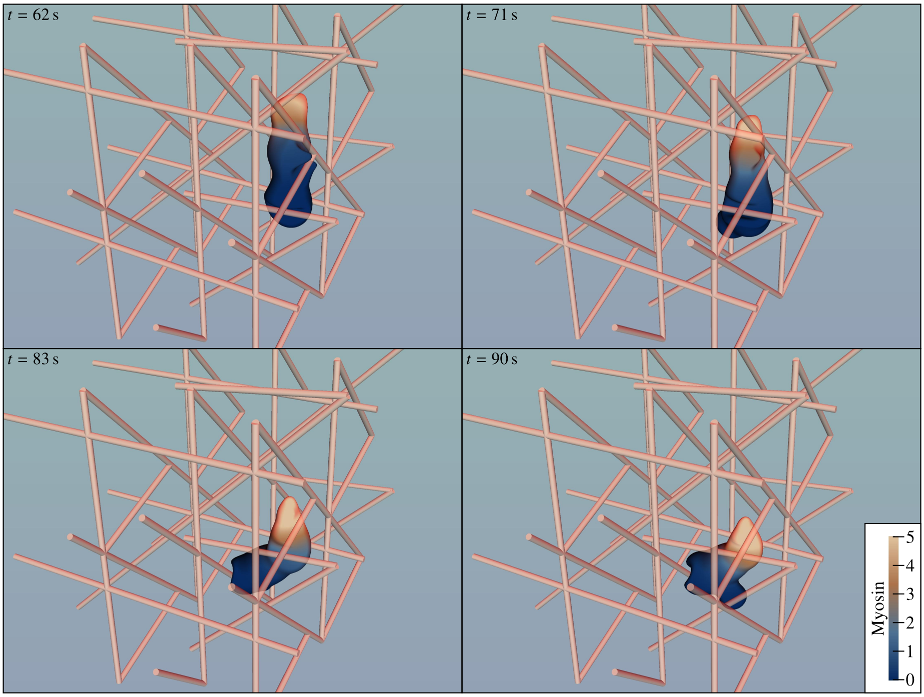

Figure 3.21. Amoeboid migration in a three-dimensional fibrous network. Myosin distribution. *The snapshots show the time evolution of myosin concentration on the cell's surface. The computational domain is oriented as in figure 3.19.*

3.5 Conclusions

We proposed a phase-field model of amoeboid cell migration. The model accounts for a membrane-bound species that interacts with the actin and the myosin present in the cytosol. The dynamics of the membrane signaling compound is controlled by a stochastic process that reproduces pseudopod formation. By including the main cytosolic components involved in cell motion, we are able to represent the intracellular dynamics of amoeboid motility. The use of the phase-field method permits a simple treatment of phase transformations, avoids the use of moving meshes, which is especially important to model membrane dynamics, and simplifies the numerics.

We performed simulations of migration on planar surfaces with and without obstacles. The model results show quantitative agreement with experiments of free and confined amoeboid migration. Our results suggest that coupling intracellular and membrane dynamics is crucial to understand amoeboid motion. We also performed a 3D simulation within a fibrous network of obstacles. We believe this simulation may constitute an initial step toward the computational study of cellular migration in the extracellular matrix.

The model opens new opportunities to study amoeboid cell migration computationally. A simple way to extend the theory would be to include a detailed description of the membrane molecules involved in the signaling pathway. Other option could be to consider deformable obstacles. This would be of special interest for the 3D simulation in a fibrous network because it would lead to a more realistic representation of the extracellular matrix. One of the possible extensions of the model, chemotaxis, is developed in the next chapter. Other extensions, such as, e.g., blebbing migration, are considered for future work.

Chapter 4

Three-dimensional simulation of obstacle-mediated chemotaxis

Amoeboid cells exhibit a highly dynamic motion that can be directed by external chemical signals, through the process of chemotaxis. Here, we extend the model of amoeboid motion presented in the previous chapter and propose a three-dimensional model for chemotactic motion of amoeboid cells. By using the diffuse domain method, we account for the interactions between the extracellular substances, the membrane-bound proteins, and the cytosolic components involved in the signaling pathway that originates cell motility. We show two- and three-dimensional simulations of cell migration on planar substrates, flat surfaces with obstacles, and fibrous networks. The results show that our model reproduces the main features of chemotactic amoeboid motion. Our simulations unveil a complicated interplay between the geometry of the cell's environment and the chemoattractant dynamics that tightly regulates cell motion.

4.1 Introduction

An outstanding feature of motile cells is their ability to perceive external stimuli that can direct their motion. Durotaxis, haptotaxis, or electrotaxis are prime examples of directed cellular motion. In this chapter we study chemotaxis, which is the movement of cells guided by chemical cues. We focus on *Dictyostelium*

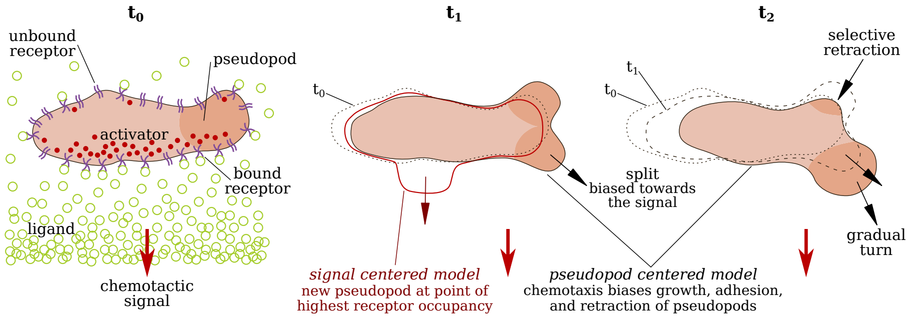

Figure 4.1. Conceptual model of chemotactic amoeboid motion. *Temporal evolution of an amoeboid cell that undergoes chemotaxis. An extracellular ligand binds to the membrane receptors, activating the signaling pathway that produces actin nucleation. According to the pseudopod centered view, pseudopods are self-generated in the cycle that drives motility. Chemotaxis does not alter the cycle, but biases any or all of the steps in the cycle.*

discoideum, which migrates spontaneously but also undergoes chemotaxis when subject to extracellular chemotactic factors (e.g., a gradient of cAMP; see Song *et al.*, 2006). *Dictyostelium* performs amoeboid motion (Lämmermann and Sixt, 2009), which follows the five-step model of cell migration (Friedl and Wolf, 2003). Amoeboid cell motility may be identified by its extraordinary deformability and dynamism, which results from a balance between myosin-induced contraction and rapid membrane extensions caused by pseudopods. Pseudopod extension is driven by actin polymerization, which is regulated by several intracellular pathways (Dawes and Edelstein-Keshet, 2007) affected by extracellular signals. The prevalent model of chemotaxis assumes that pseudopod formation is caused by chemotactic signals. That approach does not explain behaviors such as, e.g., spontaneous migration. Therefore, we follow the pseudopod-centered view (Insall, 2010) that considers pseudopod formation as a self-generated process that does not require external signals. When external chemical signals are indeed present they bias the location of growing and retracting pseudopods; see figure 4.1.

Chemotaxis arises with the association between the extracellular factors and the membrane receptors; see figure 4.1. Variations in the number of bound receptors produce the reactions between the signaling pathways that generate a chemotactic response (Swaney *et al.*, 2010; Van Haastert and Devreotes, 2004). Computational modeling of cell signaling usually focuses on a single pathway. Starting with the extracellular signal, the models provide the chemotactic response to the cytosolic machinery. This kind of models accounts for the reactions occurring in the vicinity of the membrane and may exhibit different levels of complexity. For example, the model presented in Meinhardt (1999) includes a global and a local inhibitors, and an activator that provides the response. Levchenko and Iglesias (2002) proposed a more complex model that accounts for adaptation and signal amplification; see also Subramanian and Narang (2004) and Gamba *et al.* (2005). All of these models consider a fixed geometry for the cell and restrict the signaling reactions to the membrane compounds.

Taking into account cell deformation requires the use of novel methods that entail computational challenges; see section 1.3. The cellular potts model (Marée *et al.*, 2012) or the use of moving bulk and surface meshes (MacDonald *et al.*, 2016) are examples where the dynamics of the signaling molecules are posed on moving cells. To avoid the algorithmic complexity of the use of moving meshes, the level set (Neilson *et al.*, 2011b; Shi *et al.*, 2013) and the phase-field (Moure and Gomez, 2017) methods offer an alternative: they employ a single fixed mesh where an auxiliary field identifies the region occupied by the cell. We use the phase-field method that, besides tracking the cell, permits the localization of the evolution laws of different compounds to the region where they take place; namely, the cytosol, the membrane, or the extracellular medium.

The chemotactic pathway does not end with the response given by the membrane signaling molecules. Chemotaxis finalizes with the motion of the cell, which is accomplished by the cytosolic machinery, mainly by remodeling the actomyosin network. Thus, the bidirectional feedback between the cytosolic elements and the membrane proteins plays a crucial role (Van Haastert and Devreotes, 2004). However, while there is a significant body of literature that studies models of the membrane signaling compounds such as, e.g., Hecht *et al.* (2011b); Shi *et al.* (2013); Vermolen and Gefen (2013), their interaction with the cellular motile machinery has been overlooked. The coupling between the membrane and the cytosolic compounds has been recently included in works such as Marth and Voigt (2014) or Moure and Gomez (2016) which focus on non-chemotactic migration. Models of chemotactic migration have traditionally focused on two-dimensional approaches. It has been recognized that quantitative agreement with experiments will require a refinement of the biochemical mechanisms accounted for in the model, but also three-dimensional simulations. Significant progress has been made in this direction in recent years (Allena and Aubry, 2012; Elliott *et al.*, 2012; Tjhung *et al.*, 2015; Vermolen and Gefen, 2013), but the current state of the art does not yet permit to model cell migration in a collagen matrix (Chen *et al.*, 2014).

This chapter proposes a model of individual amoeboid motion driven by chemotactic signals. The model considers cell migration in three-dimensional environments with rigid obstacles and fibers. Our results reveal a complicated interplay between the matrix geometry and the chemoattractant dynamics that strongly regulate the cell's motion. We take into account the biomechanics of the main cytosolic components involved in cell motility. We also track the dynamics of the membrane signaling molecules and locate the chemotactic factors to the extracellular environment. Since we employ the diffuse domain method, we only need a fixed mesh to solve the continuous problem. The reactions of the signaling cascade are simplified by resorting to a stochastic process that accounts for pseudopod formation.

This chapter is organized as follows: we first present the model for chemotactic migration of *Dictyostelium*. Then we briefly explain the numerical method employed to solve the problem. We analyze the influence of the chemoattractant distribution on the motion of the cells. We also show results where natural cAMP waves guide cell migration. In addition, we present two 3D simulations of a cell migrating on a planar surface and within a fibrous network. Finally, we review the main limitations of the model and draw some conclusions.

4.2 Model of chemotactic amoeboid motion

We propose a mathematical model for chemotactic amoeboid motion based on the theory presented in the previous chapter for spontaneous migration. The model resorts to the diffuse domain method to track the cell, the membrane, and the extracellular medium; as well as to locate the dynamics of the components living on each domain. We organize the model into four blocks: cell motion; biomechanics of the cytosolic compounds; dynamics of the extracellular ligand; and dynamics of a generic membrane-bound activator.

4.2.1 Diffuse domain approach

In our problem, the moving cell determines two different regions that change in time: the cell itself and the extracellular environment. Here, we consider a fixed domain Ω that encloses both time-dependent regions. We make use of the diffuse domain method (see subsection 1.3.2) to distinguish each region. In particular, we employ the phase-field variable $\phi(\mathbf{x}, t)$ for cell location, where t denotes time and $\mathbf{x} \in \mathbb{R}^{d_s}$ is a point in a space of d_s dimensions. Then, we define membrane and extracellular markers by means of ϕ.

Cell motion

The phase-field variable ϕ defines the location of the cell such that $\phi \approx 1$ inside the cell and $\phi \approx 0$ outside the cell; see figure 4.2. The interface (i.e, the cell membrane) displays a smooth transition from 0 to 1 over a width defined by a length scale ε.

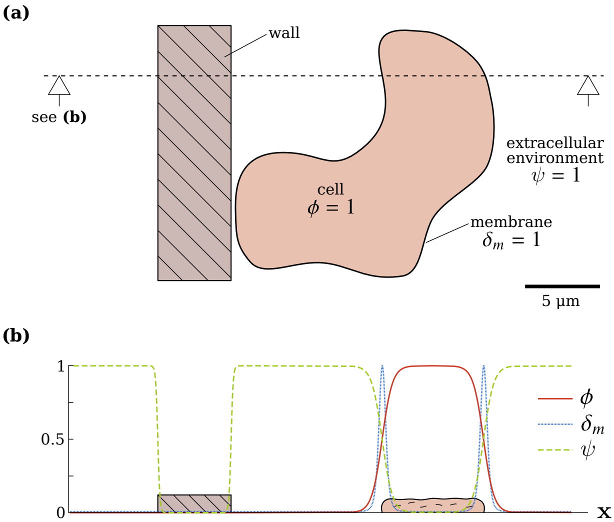

Figure 4.2. Conceptual description of the diffuse domain framework used in the model. *(a) The location of the cell is defined by the phase-field variable ϕ. The membrane of the cell is located by the function δ_m and the extracellular environment by the marker ψ. (b) ϕ, δ_m, and ψ values across the section indicated in panel (a).*

The movement of the membrane is driven by the velocity of the F-actin network $\mathbf{u}$. The evolution equation for ϕ is

$$\frac{\partial \phi}{\partial t} + \mathbf{u} \cdot \nabla \phi = \Gamma_\phi \left(\varepsilon \nabla^2 \phi - \frac{G'(\phi)}{\varepsilon} + c\varepsilon |\nabla \phi| \right), \tag{4.1}$$

which is identical to the equation used for amoeboid motion; see equation (3.1) in subsection 3.2.1.

Membrane marker

The membrane of the cell can be located by employing a smooth function δ_m that takes the value ~ 1 on the membrane and ~ 0 elsewhere. By making use of the phase-field variable ϕ, we define the marker

$$\delta_m(\phi) = \exp\left[-\varphi(\phi - 1/2)^2 \right], \tag{4.2}$$

introduced in the previous chapter and plotted in figure 4.2b. The thickness of the marker is controlled by the parameter φ.

Extracellular marker

Our model considers the presence of obstacles to the cell's motion that represent a simplified notion of the extracellular matrix or external barriers to motility. We consider that these obstacles do not permit the diffusion of any extracellular substance through them. Therefore, we locate regions outside the cell and the obstacles with the spatial marker

$$\psi(\phi, d_o(\mathbf{x})) = (1 - \phi) f_\psi(d_o(\mathbf{x})), \tag{4.3}$$

which takes the value 1 where there is neither cell nor obstacle, and 1 elsewhere; see figure 4.2. The function $f_\psi(d_o(\mathbf{x})) = \mathcal{H}(d_o(\mathbf{x}) - d_o^{\text{ef}})$ locates the obstacles ($f_\psi = 0$ where an obstacle is placed, $f_\psi = 1$ elsewhere). Remember that $\mathcal{H}$ is a smoothed-out Heaviside function that displays a hyperbolic tangent profile, in this case, at obstacle boundaries. $d_o(\mathbf{x})$ is the distance between point $\mathbf{x}$ and its closest obstacle and d_o^{ef} is an effective distance for obstacle detection. Both $d_o(\mathbf{x})$ and d_o^{ef} have been used in the previous chapters; see, e.g., equation (2.29).

4.2.2 Cytosol biomechanics

Inside the cell, we consider myosin $\rho_m(\mathbf{x}, t)$ dynamics, phase transformations between G-actin $\rho_g(\mathbf{x}, t)$ and F-actin $\rho_f(\mathbf{x}, t)$, and the flow of the F-actin network directed by its velocity $\mathbf{u}(\mathbf{x}, t)$. The classic approach would be to solve the evolution equations on a moving domain, i.e., the cell. However, we can pose the equations on a larger and fixed domain Ω by taking advantage of the diffuse domain framework; see subsection 1.3.2. As explained in subsection 1.3.2, the inclusion of ϕ into the space and time differential operators imposes a zero-flux condition on the membrane and restricts dynamics to the cell's interior.

Myosin dynamics

Myosin dynamics is governed by a convection-diffusion equation, where molecular motors are transported by the F-actin network velocity. Simultaneously, myosin diffuses throughout the cell, giving rise to the evolution equation

$$\frac{\partial(\phi\rho_m)}{\partial t} + \nabla \cdot (\phi\rho_m \mathbf{u}) - \nabla \cdot [D_m(\rho_f)\phi\nabla\rho_m] = 0, \tag{4.4}$$

which is identical to equation (2.2).

Actin dynamics

Globular actin (ρ_g) subunits, which diffuse throughout the cell, may polymerize turning into actin filaments (ρ_f), forming an intricate network that spreads over the cell. At the same time, F-actin may disassemble recovering the G-actin state. These transformations are regulated by various signaling proteins. In addition, amoeboid cells exhibit denser actin-rich structures, i.e., the pseudopods, whose protrusive nature differs from the rest of the F-actin network. Here, we model actin dynamics by using the energy functional

$$\mathcal{F}[\rho_f,\rho_g] = \int_\Omega \phi\left[\frac{\varepsilon_f^2}{2}|\nabla\rho_f|^2 + \frac{\varepsilon_g^2}{2}|\nabla\rho_g|^2 + \overline{F}\left(\rho_f,\rho_g,a\right)\right]\mathrm{d}\Omega + \lambda_N\left(\mathcal{N}_0 - \mathcal{N}\right), \quad (4.5)$$

where all the terms other than $\overline{F}$ and λ_N have been previously defined; see equations (2.4) and (3.5). λ_N is a Lagrange multiplier that keeps $\mathcal{N}$ constant throughout the cell motion. $\overline{F}$ is a function that determines the phase transitions between G-actin and F-actin in terms of the activator a (described in subsection 4.2.4), expressed as

$$\begin{aligned}\overline{F}\left(\rho_f,\rho_g,a\right) =& 10\left(\rho_f - \rho_f^{\mathrm{pr}}\right)^2\left(\rho_f - \rho_f^{\mathrm{pa}}\right)^2 + 7.5\left(\rho_g - \rho_g^{\mathrm{eq}}\right)^2 \\ &+ \overline{I}(a)(\rho_f - \rho_f^{\mathrm{pr}})^2\left[\rho_f + \overline{\kappa}(a)\overline{I}(a)\right]. \end{aligned} \quad (4.6)$$

Here, the functions $\overline{I}(a) = -2+2.6\,a$ and $\overline{\kappa}(a) = a/3$ determine the dependence of F-actin stability on the activator concentration. Note that the function $\overline{F}$ is analogous to the function F used for spontaneous amoeboid motion; see equation (3.6). The difference between $\overline{F}$ and F lies in the terms $\overline{I}(a)$ and $\overline{\kappa}(a)$, which are a simplified expression of $I(a)$ and $\kappa(a)$ in equation (3.6), respectively. Regarding the actin phase transitions mediated by the activator, the overall behavior of the actin compounds is analogous to that explained in subsection 3.2.3; see figure 3.5. We have plotted the function $-\partial\overline{F}/\partial\rho_f$ for different values of a in figure 4.3; compare with insets in figure 3.5. Note that the rationale in subsection 3.2.3 that explains the reason why we employ a instead of a cytosolic pro-nucleation factor (shown in figure 4.1, t_0) applies also to this section.

By using the framework of non-conserved dynamics (see subsection 1.3.2), we derive evolution equations for ρ_f and ρ_g using the functional $\mathcal{F}$. This leads to

$$\frac{\partial(\phi\rho_f)}{\partial t} + \nabla\cdot(\phi\rho_f\mathbf{u}) = -\Gamma_f\frac{\delta\mathcal{F}}{\delta\rho_f} = \Gamma_f\left[\varepsilon_f^2\nabla\cdot(\phi\nabla\rho_f) - \phi\frac{\partial\overline{F}}{\partial\rho_f} + \lambda_N\phi\right], \quad (4.7)$$

$$\frac{\partial(\phi\rho_g)}{\partial t} + \nabla\cdot(\phi\rho_g\mathbf{u}) = -\Gamma_g\frac{\delta\mathcal{F}}{\delta\rho_g} = \Gamma_g\left[\varepsilon_g^2\nabla\cdot(\phi\nabla\rho_g) - \phi\frac{\partial\overline{F}}{\partial\rho_g} + \lambda_N\phi\right], \quad (4.8)$$

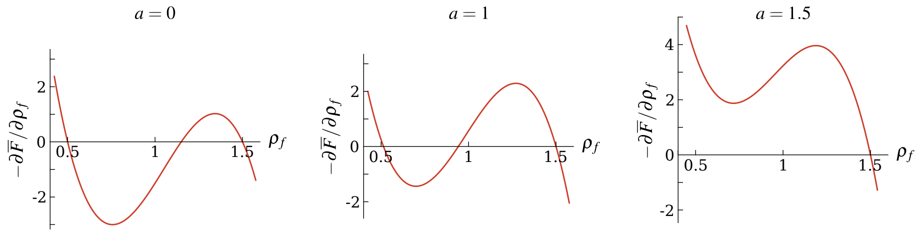

Figure 4.3. Stable densities of F-actin depending on the activator concentration. *Derivative of the function $\overline{F}$ with respect to the F-actin density, depending on the activator. We have plotted the cases $a = 0$, $a = 1$, and $a = 1.5$; c.f. with figure 3.5.*

where Γ_f is a constant and $\delta\mathcal{F}/\delta\rho_f$ is the variational derivative of the functional $\mathcal{F}$ with respect to the F-actin density. Γ_g and $\delta\mathcal{F}/\delta\rho_g$ are defined analogously. We may obtain the value of the Lagrange multiplier λ_N by forcing $\partial\mathcal{N}/\partial t = 0$. Using the definition of $\mathcal{N}$, see equation (2.3), we have $\int_\Omega \partial(\phi\rho_f)/\partial t \, \mathrm{d}\Omega + \int_\Omega \partial(\phi\rho_g)/\partial t \, \mathrm{d}\Omega = 0$. We consider either periodic or Dirichlet ($\phi = 0$) boundary conditions on $\partial\Omega$, which after the integration of equations (4.7) and (4.8) lead to

$$\lambda_N = \frac{\Gamma_f \int_\Omega \phi \frac{\partial\overline{F}}{\partial\rho_f} \mathrm{d}\Omega + \Gamma_g \int_\Omega \phi \frac{\partial\overline{F}}{\partial\rho_g} \mathrm{d}\Omega}{(\Gamma_f + \Gamma_g) \int_\Omega \phi \mathrm{d}\Omega}. \tag{4.9}$$

We further assume that: (1) The Lagrange multiplier λ_N strongly forces $\mathcal{N} = \mathcal{N}_0 \ \forall t$, (2) ε_g is large enough[1] to neglect the spatial variation of G-actin inside the cell, thus $\rho_g(\mathbf{x}, t) \to \rho_g(t)$. Under these hypotheses, we can obtain the value of ρ_g from the identity $\mathcal{N}[\rho_f, \rho_g] = \mathcal{N}_0$, as

$$\rho_g(t) = \frac{\mathcal{N}_0 - \int_\Omega \phi\rho_f \mathrm{d}\Omega}{\int_\Omega \phi \mathrm{d}\Omega}. \tag{4.10}$$

Therefore, in our model, we can replace equation (4.8) by equation (4.10). Neglecting the dependence of ρ_g on space leads to a simpler and faster computational method.

F-actin network flow

We follow the rationale applied in the previous chapters and we treat the F-actin network as a viscous fluid, whose behavior is governed by a Stokes-type equation.

[1] The large diffusion constant of G-actin has been noted in the literature; see Novak *et al.* (2008).

The equation, which is augmented with forces related to the cell motion machinery, may be written as

$$\nabla \cdot (\boldsymbol{\sigma} + \boldsymbol{\sigma}_{\text{myo}} + \boldsymbol{\sigma}_{\text{prot}}) + \mathbf{F}_{\text{adh}} + \mathbf{F}_{\text{mem}} + \mathbf{F}_{\text{rep}} = 0. \tag{4.11}$$

$\boldsymbol{\sigma}$, $\boldsymbol{\sigma}_{\text{myo}}$, and $\boldsymbol{\sigma}_{\text{prot}}$ have been defined in equations (2.9), (2.10), and (2.12), respectively. The definition of the term δ_f in $\boldsymbol{\sigma}_{\text{prot}}$ is different from the previous chapters. In this chapter, excluding the examples computed using periodic boundary conditions, we will assume that the unknown ϕ vanishes on the boundary. In that case, the boundary behaves as a rigid obstacle that impedes the movement of the cell. To define δ_f, we resort to the fields $d_o(\mathbf{x})$ and $d_b(\mathbf{x})$. The field $d_o(\mathbf{x})$ provides the distance to obstacles that we place on the domain and $d_b(\mathbf{x})$ accounts for the distance between point $\mathbf{x}$ and the closest non-periodic boundary. The marker δ_f is expressed as

$$\delta_f = \begin{cases} \mathcal{H}\left(d_o(\mathbf{x}) - d_o^f\right) & \text{if } \ d_o(\mathbf{x}) < d_b(\mathbf{x}) + \Delta d^f \\ \mathcal{H}\left(d_b(\mathbf{x}) - d_b^f\right) & \text{if } \ d_o(\mathbf{x}) \geq d_b(\mathbf{x}) + \Delta d^f, \end{cases} \tag{4.12}$$

where $\Delta d^f = d_o^f - d_b^f$, with the constants d_o^f and d_b^f being effective distances at which the cell starts to suppress protrusive stress when approaching an obstacle and the boundary, respectively. Note that if we consider periodic boundary conditions, $d_b(\mathbf{x}) \to \infty$ and $\delta_f = \mathcal{H}(d_o(\mathbf{x}) - d_o^f)$, which coincides with the expression in subsection 2.2.4.

Adhesive forces between the cell and the environment are included through the term $\mathbf{F}_{\text{adh}}$, where we take into account a continuous drag force and a set of punctual forces such that $\mathbf{F}_{\text{adh}} = \mathbf{F}_{\text{drag}} + \sum_j \mathbf{F}^j_{\text{punct}}$. The drag force $\mathbf{F}_{\text{drag}} = -\varsigma \mathbf{u}$ is proportional to F-actin velocity, with ς the drag coefficient. Each focal adhesion j produces a punctual force $\mathbf{F}^j_{\text{punct}} = -k^j_{\text{grip}}(t)(\mathbf{x}^j - \mathbf{x}^j_0)\,\delta(\mathbf{x} - \mathbf{x}^j)$, applied on the F-actin network at point $\mathbf{x}^j$, where $\delta(\mathbf{x})$ denotes the Dirac delta function. The force is modeled as a spring with one end attached to the substrate ($\mathbf{x}^j_0$) and the other end to the F-actin network ($\mathbf{x}^j$). We include focal adhesion maturation (Choi *et al.*, 2008) by proposing a time-dependent spring constant $k^j_{\text{grip}}(t) = k_{\text{grip}_0}(t - t^j_0)$, where k_{grip_0} is a constant and t^j_0 is the time at which adhesion j clutches. Since we consider a rigid substrate (or rigid fibers), each point $\mathbf{x}^j_0$ remains fixed. However, each point $\mathbf{x}^j$, connected to the F-actin network, moves according to the velocity $\mathbf{u}$. The initial deformation of the spring is zero, that is $\mathbf{x}^j_0 = \mathbf{x}^j(t^j_0)$. We call N_{adh} the number of punctual adhesions active at a particular time. We assume that N_{adh} cannot exceed the value $N^{\max}_{\text{adh}}$. Each focal adhesion is associated to the index j such that $1 \leq j \leq N_{\text{adh}}$. New adhesions are created sufficiently far away from existing adhesions in regions of membrane-substrate (or membrane-fiber) contact according to a random distribution weighted by the F-actin density. The rupture of focal adhesions follows a stochastic model based on Poisson's distribution[2] with average number of events per interval $\lambda_p^j = r_{\text{off}}^j(t - t_0^j)$, where j is the index that identifies the focal adhesion. The disassociation rate $r_{\text{off}}^j = r_{\text{off}_0} \exp(|\mathbf{F}_{\text{punct}}^j|/F_0)$ is modeled using Bell's law (Bell *et al.*, 1978), where r_{off_0} is a constant and F_0 the characteristic adhesive strength. We also consider that if the point $\mathbf{x}^j$ leaves the cell, then the focal adhesion j is broken. The procedure employed to determine focal adhesion behavior (adhesion formation, time evolution, and rupture) is fully explained in subsection 4.3.2. In the 2D case, $\mathbf{F}_{\text{punct}}^j$ and $\mathbf{F}_{\text{drag}}$ play a similar role. Therefore, for the sake of simplicity we neglect $\mathbf{F}_{\text{punct}}^j$ in the 2D examples. In the 3D examples, $\mathbf{F}_{\text{drag}}$ models an hydrodynamic drag between actin filaments within the cell.

Bending forces can be neglected for realistic values of the parameters; see subsection 2.4.2. Therefore, the membrane forces may be expressed as $\mathbf{F}_{\text{mem}} = -\gamma\nabla\phi(\varepsilon\nabla^2\phi - G'(\phi)/\varepsilon)$, where γ is the surface tension coefficient; see the derivation of the membrane forces in subsection 2.2.4. Finally, when the cell approaches an obstacle, a repulsive force acting on the membrane stops its motion[3]. This is accomplished with the repulsive force $\mathbf{F}_{\text{rep}} = \nabla\cdot\boldsymbol{\sigma}_{\text{rep}} = \nabla\cdot(\phi\eta_{\text{rep}}\delta_{\text{rep}}\nabla\phi\otimes\nabla\phi)$, which has been previously introduced in equation (2.28). The term $\delta_{\text{rep}} = \mathcal{H}(d_o^{\text{ef}} - d_o(\mathbf{x}))$ activates this force only in the vicinity of the obstacle. Note that, unlike δ_f [see equation (4.12)], δ_{rep} does not depend on $d_b(\mathbf{x})$. Thus, the repulsive force is not active on the boundary because the boundary condition $\phi = 0$ produces the same effect as $\mathbf{F}_{\text{rep}}$. However, if δ_f does not suppress the protrusive force on the boundary, an instability in the balance of forces appears and the cell undergoes a backward movement not observed in experiments.

4.2.3 Extracellular chemoattractant

Chemotaxis usually originates from the presence of an extracellular substance, generally called ligand or chemoattractant, that is perceived by the cell and guides its motion. Here, we consider a single ligand $q(\mathbf{x}, t)$ that diffuses throughout the extracellular environment, experiences a natural degradation, and reacts with membrane receptors. According to the diffuse domain framework (see subsec-

[2] The Poisson distribution states that the probability of observing k events in an interval is given by the equation $P = \exp(-\lambda_p)\lambda_p^k/k!$, where λ_p is the average number of events per interval. In our adhesion rupture model, $k = 1$ and $\lambda_p^j = r_{\text{off}}^j(t - t_0^j)$, where the index j identifies the focal adhesion.

[3] This chapter does not include simulations of chemotactic migration in microchannels. Therefore, we disregard friction forces.

tion 1.3.2), the governing equation may be written as

$$\frac{\partial(\psi q)}{\partial t} = \nabla \cdot (D_q \psi \nabla q) - r_q \psi q + b_q \psi S_q - k_q \delta_m q, \tag{4.13}$$

where D_q, r_q, and b_q are the chemoattractant diffusion coefficient, degradation rate, and strength of the source term, respectively. The chemoattractant source is defined as $S_q = \sum_i S_i$. Here, $S_i = (q_{\max,i} - q)\delta^q_{\mathbf{x},i}\delta^q_{t,i}$ where $q_{\max,i}$ is a constant, $\delta^q_{\mathbf{x},i}$ gives the spatial location of each source i, and $\delta^q_{t,i}$ is the time localizer. $q_{\max,i}$, $\delta^q_{\mathbf{x},i}$, and $\delta^q_{t,i}$ differ depending on each example[4] and we only consider one chemotactic source active at the same time. We model the ligand-receptor interaction as a consumption proportional to the ligand concentration at the membrane, with rate k_q.

A cell is able to sense extracellular signals through the membrane, in particular, through membrane receptors. The ligand binds to the receptors. The receptors change from inactive to active (see figure 4.1, t_0), at a rate depending on the ligand concentration at the cell surface (Swaney *et al.*, 2010). Variations in the receptor occupancy along the membrane determine the direction of the signal to the cytosolic machinery to a significant extent, but also the average level of occupancy may affect the signaling transduction [e.g., receptor saturation is a consequence of a finite number of receptors (Song *et al.*, 2006)]. Here, we assume that the number of bound receptors is proportional to the chemoattractant density along the membrane (Levine *et al.*, 2006). Based on the previous arguments, we suppose that chemotactic motion is controlled by the *signaling parameters* $\overline{\nabla q}$ and $\overline{q}$, which represent an average chemoattractant gradient and the mean chemoattractant concentration. To define $\overline{\nabla q}$ and $\overline{q}$, we consider the distribution of chemoattractant concentration q along the membrane (see figure 4.4). Let us denote $q_{\min}$ and $q_{\max}$ the minimum and maximum values of q along the membrane. $\mathbf{n}_q$ is a unit vector parallel to the line that joins the points where the values $q_{\min}$ and $q_{\max}$ are attained. We define $|\overline{\nabla q}| = (q_{\max} - q_{\min})/d_q$, where d_q is the distance between the membrane points with minimum and maximum chemoattractant concentration. The vector $\overline{\nabla q}$ is defined as $\overline{\nabla q} = |\overline{\nabla q}|\mathbf{n}_q$. The average chemoattractant concentration is defined as $\overline{q} = (q_{\max} + q_{\min})/2$. As indicated in figure 4.4, we suppose that when the cell touches an obstacle, the ligand does not interact with the membrane in the contact region.

[4] In this chapter, we suppose spherical (circular in 2D) chemoattractant sources. Thus, $\delta^q_{\mathbf{x},i} = \mathcal{H}\left(R_q - d^q_i(\mathbf{x})\right)$, where $R_q = 1\,\mu\text{m}$ and $d^q_i(\mathbf{x})$ denotes the distance from point $\mathbf{x}$ to the center of source i.

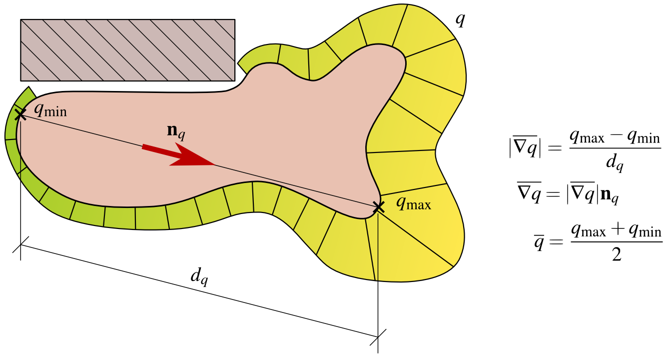

Figure 4.4. Computation of the signaling parameters. *$\overline{\nabla q}$ and $\overline{q}$ are established through the maximum and minimum values of chemoattractant detected by the cell along the membrane. The areas of the membrane that are in contact with a solid obstacle are not considered to compute $\overline{\nabla q}$ and $\overline{q}$.*

4.2.4 Membrane activator

We consider one single membrane signaling compound called activator $a(\mathbf{x}, t)$, which produces actin nucleation. In the formulation, this can be understood by examining the actin energy functional $\mathcal{F}$; see equations (4.5) and (4.6). We make use again of the diffuse domain method to derive an evolution equation for the activator. We propose the model

$$\frac{\partial(\delta_m a)}{\partial t} + \nabla \cdot (\delta_m a \mathbf{u}) = \nabla \cdot (D_a \delta_m \nabla a) - r_a \delta_m a + b_a \delta_m S_a, \tag{4.14}$$

which is identical to equation (3.3); see subsection 3.2.2 for details. The source term $S_a = (a_{\max} - a) \sum_i \delta^a_{\mathbf{x},i} \delta^a_{t,i}$ drives a to $a_{\max}$ at certain regions (defined by $\delta^a_{\mathbf{x},i}$) and interval times (defined by $\delta^a_{t,i}$), producing peaks in the activator concentration and eventually the emergence of pseudopods. Therefore, pseudopod formation is controlled by $\delta^a_{\mathbf{x},i}$ and $\delta^a_{t,i}$, which are calculated through probability functions taken from experimental works (Bosgraaf and Van Haastert, 2009a,b; Fuller *et al.*, 2010; Van Haastert, 2010); see figure 4.5. The functions $\delta^a_{\mathbf{x},i}$ and $\delta^a_{t,i}$, defined in subsection 3.2.2, are smoothed-out step functions that depend on parameters that define the spatio-temporal location of the activator peaks. Since we follow the pseudopod-centered view (Insall, 2010), we first calculate the parameters as if the cell was undergoing spontaneous motion (no chemotaxis) and then modify them using a chemotactic bias. The relevant parameters are the location of the i-th activator peak $\mathbf{s}^*_i$ (used for the spatial localizer $\delta^a_{\mathbf{x},i}$), the time between two consecutive peaks $\Delta\tau^*_i$ (called interval and used to define $\delta^a_{t,i}$), and the growth time of the peak ΔT_i^* (also used in $\delta_{t,i}^a$). Note that we use an asterisk to denote the parameters for spontaneous motion[5]. The values of $\mathbf{s}_i^*$, $\Delta\tau_i^*$, and ΔT_i^* are obtained using the probability functions shown in figure 4.5a, which are taken from experiments, following the procedure explained in subsection 3.2.2. Note that, for consistency with the previous section, we preclude pseudopod formation in regions of cell-obstacle contact such that $P_{\mathrm{PE}}(\mathbf{x}) = 0$ if $d_o(\mathbf{x}) < d_o^a$ or $d_b(\mathbf{x}) < d_o^a - \Delta d^f$. More details on the definition of $\mathbf{s}_i^*$, $\Delta\tau_i^*$, and ΔT_i^* for two-dimensional problems may be found in subsection 3.2.2.

In figure 4.5c (left and middle) we have plotted the probability of pseudopod extension for a theoretical case where the cell shape is an ellipsoid with $\mathbf{s}_{i-1}$ and $\mathbf{s}_{i-2}$ placed in a mean equatorial plane. The plane π_1, which contains $\mathbf{s}_{i-1}$, $\mathbf{s}_{i-2}$, and $\mathbf{x}_{\mathrm{cell}}$ (the mass center of the cell), presents a probability distribution analogous to that of the 2D case. However, the plane π_2, which is orthogonal to π_1 (in particular, orthogonal to the line that joins $\mathbf{s}_{i-1}$ and $\mathbf{x}_{\mathrm{cell}}$), shows that the probability of extension decreases proportional to the distance to the plane π_1. Thus, the probability of extension is zero on a large region of the cell surface; see figure 4.5c (middle). Nevertheless, an actual cell exhibits more complicated shapes. We approximate the theoretical probability distributions as follows: From point $\mathbf{s}_{i-1}$ we compute the geodesic distance over the cell surface to get $d_{i-1,\max}$. We resort to the probability function P_{PE} (see figure 4.5a, middle) to obtain d_{i-1} and the corresponding value of $\beta_{\mathrm{R/L}}$. $\mathbf{s}_i^*$ will be located in l_d, defined as the set of points of the membrane whose distance from $\mathbf{s}_{i-1}$ is d_{i-1} . We select the points C_{l_d} and D_{l_d}, which are the closest and farthest points to $\mathbf{s}_{i-2}$ belonging to l_d, respectively. The probability of extension along l_d presents two triangles centered on C_{l_d} and D_{l_d}. The length of the base of each triangle is 10% of the total length of l_d, and the probability at points C_{l_d} and D_{l_d} is $\beta_{\mathrm{R/L}}/(1+\beta_{\mathrm{R/L}})$ and $1/(1+\beta_{\mathrm{R/L}})$, respectively. The similarity with the theoretical case may be noted if we assume that the view in π_2 corresponds to l_d; see figure 4.5c (middle).

Once the spontaneous motion parameters ($\mathbf{s}_i^*$, $\Delta\tau_i^*$, and ΔT_i^*) have been obtained, we modify them using the signaling parameters $\overline{\nabla q}$ and $\overline{q}$ to obtain $\mathbf{s}_i$, $\Delta\tau_i$, and ΔT_i. The first step in the process is to compute the bias $\beta \in [0, 1]$ using ideas from the stochastic model from Van Haastert (2010). We apply the multiplicative split $\beta = \beta_{\overline{\nabla q}}\beta_{\overline{q}}$ to isolate the effect of the two control parameters that determine the strength of the chemotactic bias. The value of $\beta_{\overline{\nabla q}}$ depends on whether the pseudopod is a split or *de novo*; see figure 4.5b (left) where the value of $\beta_{\overline{\nabla q}}$ approximates the values given by Van Haastert (2010). The value of $\beta_{\overline{q}}$ is also plotted on the left-hand side of figure 4.5b and follows the data of Song *et al.* (2006) and Fuller *et al.* (2010). Let us call $\mathbf{n}_{\mathbf{s}_i^*}$ the normal vector to the membrane

[5]The parameters $\mathbf{s}_i^*$, $\Delta\tau_i^*$, and ΔT_i^* are equivalent to the parameters $\mathbf{s}_i$, $\Delta\tau_i$, and ΔT_i of chapter 3, respectively.

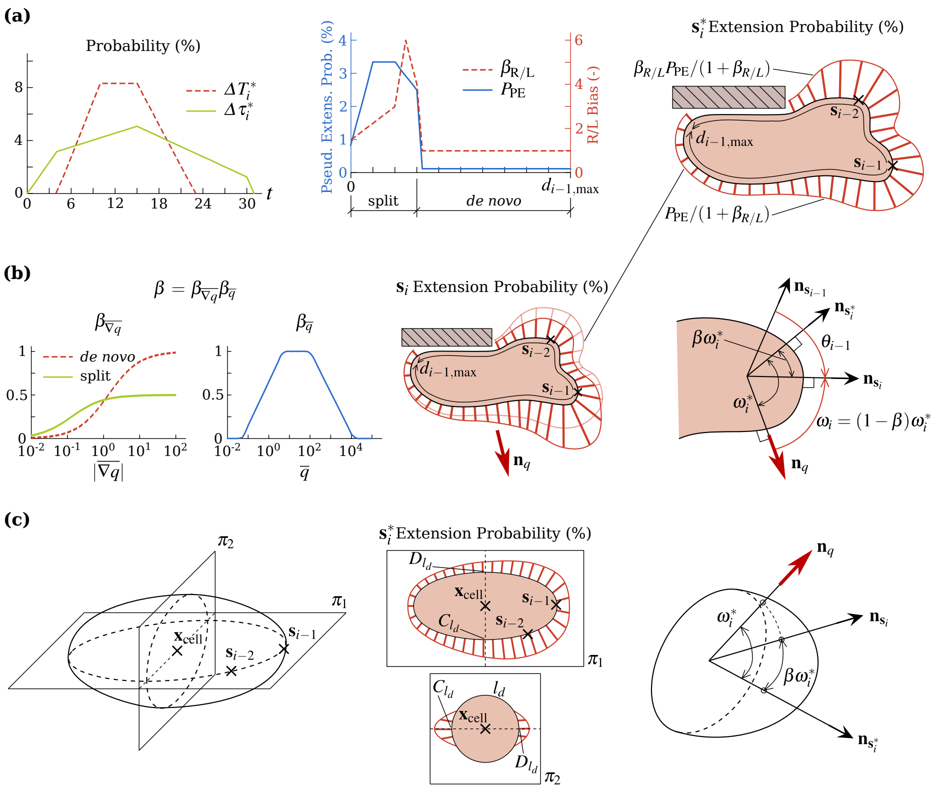

Figure 4.5. Determination of pseudopod formation. *(a) Growth time (ΔT_i^*), interval ($\Delta\tau_i^*$), pseudopod extension (P_{PE}), and right-left bias ($\beta_{\text{R/L}}$) probability distributions, derived from Bosgraaf and Van Haastert (2009b). Probability distribution of $\mathbf{s}_i^*$ given the locations $\mathbf{s}_{i-1}$ and $\mathbf{s}_{i-2}$ in a 2D computation. (b) Chemotactic bias (β) produced by the gradient ($\beta_{\overline{\nabla q}}$) and the average level ($\beta_{\overline{q}}$) of chemoattractant, derived from Fuller et al. (2010); Song et al. (2006); Van Haastert (2010). Probability distribution of $\mathbf{s}_i$ modified by β and the gradient direction $\mathbf{n}_q$. Diagram showing how $\mathbf{n}_{\mathbf{s}_i^*}$ is rotated to determine ω_i and $\mathbf{s}_i$. (c) The process to determine $\mathbf{s}_i$ can be extended to 3D by proceeding analogously to the 2D case on the plane defined by $\mathbf{n}_q$ and $\mathbf{n}_{\mathbf{s}_i^*}$.*

at point $\mathbf{s}_i^*$; see the right-hand side of figure 4.5b. The angle between the vectors $\mathbf{n}_q$ and $\mathbf{n}_{\mathbf{s}_i^*}$ is denoted ω_i^*. The point $\mathbf{s}_i$ is located in the neighborhood of $\mathbf{s}_i^*$ such that the angle between $\mathbf{n}_q$ and $\mathbf{n}_{\mathbf{s}_i}$ is as close as possible to $\omega_i = (1-\beta)\omega_i^*$. This idea can be extended to 3D migration as illustrated on the left-hand side of figure 4.5c, where $\mathbf{n}_q$, $\mathbf{n}_{\mathbf{s}_i^*}$, and $\mathbf{n}_{\mathbf{s}_i}$ belong to the same plane. According to

Bosgraaf and Van Haastert (2009a), the time interval between two consecutive pseudopods is not affected by chemotaxis, that is, $\Delta\tau_i = \Delta\tau_i^*$. However, the life time of pseudopods is greater if they point in the same direction as $\mathbf{n}_q$. We describe this quantitatively using the formula $\Delta T_i = \Delta T_i^*[1 + 0.1\cos(\omega_i)]$.

4.2.5 Continuous problem in strong form

We consider a fixed set $\Omega \subset \mathbb{R}^{d_s}$ that represents our computational domain. The boundary of Ω is Γ. The strong form of the problem can be stated as: Given a time interval of interest $[0, T]$ and suitable initial conditions, find $\phi : \overline{\Omega} \times (0, T) \to \mathbb{R}$, $\rho_m : \overline{\Omega} \times (0, T) \to \mathbb{R}$, $\rho_f : \overline{\Omega} \times (0, T) \to \mathbb{R}$, $\mathbf{u} : \overline{\Omega} \times (0, T) \to \mathbb{R}^{d_s}$, $q : \overline{\Omega} \times (0, T) \to \mathbb{R}$, and $a : \overline{\Omega} \times (0, T) \to \mathbb{R}$ such that

$$\frac{\partial \phi}{\partial t} + \mathbf{u} \cdot \nabla\phi = \Gamma_\phi \left(\varepsilon\nabla^2\phi - \frac{G'(\phi)}{\varepsilon} + c\varepsilon|\nabla\phi| \right) \quad \text{in} \quad \Omega \times (0, T), \tag{4.15}$$

$$\frac{\partial(\phi\rho_m)}{\partial t} + \nabla \cdot (\phi\rho_m\mathbf{u}) = \nabla \cdot [D_m(\rho_f)\phi\nabla\rho_m] \quad \text{in} \quad \Omega \times (0, T), \tag{4.16}$$

$$\begin{aligned} \frac{\partial(\phi\rho_f)}{\partial t} + \nabla \cdot (\phi\rho_f\mathbf{u}) = \\ = \Gamma_f \left[\varepsilon_f^2 \nabla \cdot (\phi\nabla\rho_f) - \phi\frac{\partial \overline{F}}{\partial\rho_f} + \lambda_N\phi \right] \quad \text{in} \quad \Omega \times (0, T), \end{aligned} \tag{4.17}$$

$$\nabla \cdot (\boldsymbol{\sigma} + \boldsymbol{\sigma}_{\text{myo}} + \boldsymbol{\sigma}_{\text{prot}}) + \mathbf{F}_{\text{adh}} + \mathbf{F}_{\text{mem}} + \mathbf{F}_{\text{rep}} = 0 \quad \text{in} \quad \Omega \times (0, T), \tag{4.18}$$

$$\frac{\partial(\psi q)}{\partial t} = \nabla \cdot (D_q\psi\nabla q) - r_q\psi q + b_q\psi S_q - k_q\delta_m q \quad \text{in} \quad \Omega \times (0, T), \tag{4.19}$$

$$\begin{aligned} \frac{\partial(\delta_m a)}{\partial t} + \nabla \cdot (\delta_m a\mathbf{u}) = \\ = \nabla \cdot (D_a\delta_m\nabla a) - r_a\delta_m a + b_a\delta_m S_a \quad \text{in} \quad \Omega \times (0, T). \end{aligned} \tag{4.20}$$

We assume that the unknowns ϕ, ρ_m, ρ_f, and a vanish on the boundary Γ. We also assume stress-free and flux-free conditions on Γ. Mathematically, these can be expressed as $(\boldsymbol{\sigma} + \boldsymbol{\sigma}_{\text{myo}} + \boldsymbol{\sigma}_{\text{prot}})\,\mathbf{n}_\Gamma = 0$ and $\nabla q \cdot \mathbf{n}_\Gamma = 0$, respectively. Here, $\mathbf{n}_\Gamma$ is the unit outward normal vector on Γ. Note that equations (4.9) and (4.10) are also necessary to solve the cell-motion problem, but they do not need to be discretized, as we will show in section 4.3.

4.3 Numerical method

4.3.1 Weak form and spatial discretization

To solve the equations numerically, we use IGA, a spline-based finite element method. We define the trial solution space $\mathcal{S} = \left\{ \phi \mid \phi(\cdot, t) \in \mathcal{H}^2(\Omega) \right\}$ and the weighting function space $\mathcal{V} = \left\{ w \mid w \in \mathcal{H}^2(\Omega) \right\}$. We begin by deriving a weak form of equations (4.15) to (4.20) by multiplying them with weighting functions, integrating over the computational domain, and integrating by parts. We denote $n_{\text{dof}} = 5 + d_s$, the number of scalar unknowns. The problem can be stated as: Find $\mathbf{U} = \{\phi, \rho_m, \rho_f, \mathbf{u}, q, a\} \in \mathcal{S}^{n_{\text{dof}}}$ such that for all $\mathbf{W} = \{l, p, r, \mathbf{w}, s, v\} \in \mathcal{V}^{n_{\text{dof}}}$

$$\mathcal{B}(\mathbf{W}, \mathbf{U}) = 0 \tag{4.21}$$

with

$$\begin{aligned}
\mathcal{B}(\mathbf{W}, \mathbf{U}) = & \left(l, \frac{\partial \phi}{\partial t} \right)_\Omega + \left(p, \phi \frac{\partial \rho_m}{\partial t} \right)_\Omega + \left(p, \rho_m \frac{\partial \phi}{\partial t} \right)_\Omega + \left(r, \phi \frac{\partial \rho_f}{\partial t} \right)_\Omega \\
& + \left(r, \rho_f \frac{\partial \phi}{\partial t} \right)_\Omega + \left(s, \psi \frac{\partial q}{\partial t} \right)_\Omega + \left(s, q \frac{\partial \psi}{\partial t} \right)_\Omega + \left(v, \delta_m \frac{\partial a}{\partial t} \right)_\Omega \\
& + \left(v, a \delta_m' \frac{\partial \phi}{\partial t} \right)_\Omega + \left(l, \mathbf{u} \cdot \nabla \phi \right)_\Omega + \left(\nabla l, \Gamma_\phi \varepsilon \nabla \phi \right)_\Omega + \left(l, \Gamma_\phi \frac{G'}{\varepsilon} \right)_\Omega \\
& - \left(\nabla l, \Gamma_\phi \varepsilon \nabla \phi \right)_\Omega - \left(l, \frac{\Gamma_\phi \varepsilon}{|\nabla \phi|} \nabla \phi \cdot \nabla \left(|\nabla \phi| \right) \right)_\Omega - \left(\nabla p, \phi \rho_m \mathbf{u} \right)_\Omega \\
& + \left(\nabla p, D_m \phi \nabla \rho_m \right)_\Omega - \left(\nabla r, \phi \rho_f \mathbf{u} \right)_\Omega + \left(\nabla r, \Gamma_f \varepsilon_f^2 \phi \nabla \rho_f \right)_\Omega \\
& + \left(r, \Gamma_f \phi \frac{\partial \overline{F}}{\partial \rho_f} \right)_\Omega - \left(r, \Gamma_f \lambda_N \phi \right)_\Omega \\
& - \left(\nabla \mathbf{w}, \phi \left[\mu \left(\nabla \mathbf{u} + \nabla \mathbf{u}^T \right) + \lambda \left(\nabla \cdot \mathbf{u} \right) \boldsymbol{I} \right] \right)_\Omega \\
& - \left(\nabla \mathbf{w}, \phi \rho_m \eta_m \boldsymbol{I} \right)_\Omega + \left(\nabla \mathbf{w}, \phi \rho_f \eta_f \delta_f \nabla \phi \otimes \nabla \phi \right)_\Omega - \left(\mathbf{w}, \varsigma \mathbf{u} \right)_\Omega \\
& + \sum_j \mathbf{w}(\mathbf{x}^j) \cdot \mathbf{F}^j_{\text{punct}} - \left(\mathbf{w}, \gamma \left(\varepsilon \nabla^2 \phi - \frac{G'}{\varepsilon} \right) \nabla \phi \right)_\Omega
\end{aligned}$$

$$
\begin{aligned}
&- \left(\nabla \mathbf{w}, \phi \eta_{\mathrm{rep}} \delta_{\mathrm{rep}} \nabla \phi \otimes \nabla \phi\right)_{\Omega} + \left(\nabla s, D_q \psi \nabla q\right)_{\Omega} + \left(s, r_q \psi q\right)_{\Omega} \\
&- \left(s, b_q \psi S_q\right)_{\Omega} + \left(s, k_q \delta_m q\right)_{\Omega} - \left(\nabla v, \delta_m a \mathbf{u}\right)_{\Omega} \\
&+ \left(\nabla v, D_a \delta_m \nabla a\right)_{\Omega} + \left(v, r_a \delta_m a\right)_{\Omega} - \left(v, b_a \delta_m S_a\right)_{\Omega} . \qquad (4.22)
\end{aligned}
$$

The discretization of equations (4.21) and (4.22) requires the use of at least quadratic splines with $\mathcal{C}^1$-global continuity. As done throughout this thesis, we resort to IGA and employ B-spline basis functions for the spatial discretization. Let us call $\mathcal{S}^h$ and $\mathcal{V}^h$ the trial and weighting function discrete spaces, which are assumed to be identical. The spline basis functions are denoted by N_A so that $\mathcal{S}^h = \mathcal{V}^h = \mathrm{span}\{N_A\}_{A=1}^{n_b}$, where n_b is the dimension of the discrete space.

The discrete problem can be stated as: Find $\mathbf{U}^h = \{\phi^h, \rho_m^h, \rho_f^h, \mathbf{u}^h, q^h, a^h\} \in (\mathcal{S}^h)^{n_{\mathrm{dof}}}$ such that for all $\mathbf{W}^h = \{l^h, p^h, r^h, \mathbf{w}^h, s^h, v^h\} \in (\mathcal{V}^h)^{n_{\mathrm{dof}}}$

$$
\mathcal{B}(\mathbf{W}^h, \mathbf{U}^h) = 0. \qquad (4.23)
$$

The variables in $\mathbf{U}^h$ and $\mathbf{W}^h$ are defined analogously as done in subsection 2.3.2; see equation (2.38).

4.3.2 Time stepping scheme and numerical implementation

The time stepping scheme is analogous to the algorithm described in subsection 2.3.3. The time stepping scheme, based on the generalized-α method, divides the time interval of interest $[0, T]$ into a sequence of subintervals (t_n, t_{n+1}) with time-step size $\Delta t = t_{n+1} - t_n$. The list of residual vectors defined in equation (2.39) is extended with $\mathbf{R}^Q = \left\{R_A^Q\right\}$ and $\mathbf{R}^A = \left\{R_A^A\right\}$, where $A \in \{1, \ldots, n_b\}$ is the control-variable index. The components of the residual vector are given by

$$
\begin{aligned}
R_A^{\Phi} &= \mathcal{B}\left(\{N_A, 0, 0, 0, 0, 0\}, \{\phi^h, \rho_m^h, \rho_f^h, \mathbf{u}^h, q^h, a^h\}\right), && (4.24)\\
R_A^{M} &= \mathcal{B}\left(\{0, N_A, 0, 0, 0, 0\}, \{\phi^h, \rho_m^h, \rho_f^h, \mathbf{u}^h, q^h, a^h\}\right), && (4.25)\\
R_A^{F} &= \mathcal{B}\left(\{0, 0, N_A, 0, 0, 0\}, \{\phi^h, \rho_m^h, \rho_f^h, \mathbf{u}^h, q^h, a^h\}\right), && (4.26)\\
R_{A,j}^{U} &= \mathcal{B}\left(\{0, 0, 0, N_A \mathbf{e}_j, 0, 0\}, \{\phi^h, \rho_m^h, \rho_f^h, \mathbf{u}^h, q^h, a^h\}\right), && (4.27)\\
R_A^{Q} &= \mathcal{B}\left(\{0, 0, 0, 0, N_A, 0\}, \{\phi^h, \rho_m^h, \rho_f^h, \mathbf{u}^h, q^h, a^h\}\right), && (4.28)\\
R_A^{A} &= \mathcal{B}\left(\{0, 0, 0, 0, 0, N_A\}, \{\phi^h, \rho_m^h, \rho_f^h, \mathbf{u}^h, q^h, a^h\}\right), && (4.29)
\end{aligned}
$$

where $\mathbf{e}_j$ denotes the j-th unit vector of the Cartesian basis. Using the notation indicated in subsection 2.3.3, our time-integration algorithm may be defined as follows: Given $\dot{\mathbf{V}}_n$, $\mathbf{V}_n$, and Δt, find $\dot{\mathbf{V}}_{n+1}$, $\mathbf{V}_{n+1}$, $\dot{\mathbf{V}}_{n+\alpha_m}$, and $\mathbf{V}_{n+\alpha_f}$ such that

$$\mathbf{R}^{\Phi}\left(\dot{\mathbf{V}}_{n+\alpha_m}, \mathbf{V}_{n+\alpha_f}\right) = 0, \tag{4.30}$$

$$\mathbf{R}^{M}\left(\dot{\mathbf{V}}_{n+\alpha_m}, \mathbf{V}_{n+\alpha_f}\right) = 0, \tag{4.31}$$

$$\mathbf{R}^{F}\left(\dot{\mathbf{V}}_{n+\alpha_m}, \mathbf{V}_{n+\alpha_f}\right) = 0, \tag{4.32}$$

$$\mathbf{R}^{U}\left(\dot{\mathbf{V}}_{n+\alpha_m}, \mathbf{V}_{n+\alpha_f}\right) = 0, \tag{4.33}$$

$$\mathbf{R}^{Q}\left(\dot{\mathbf{V}}_{n+\alpha_m}, \mathbf{V}_{n+\alpha_f}\right) = 0, \tag{4.34}$$

$$\mathbf{R}^{A}\left(\dot{\mathbf{V}}_{n+\alpha_m}, \mathbf{V}_{n+\alpha_f}\right) = 0, \tag{4.35}$$

$$\dot{\mathbf{V}}_{n+\alpha_m} = \dot{\mathbf{V}}_n + \alpha_m\left(\dot{\mathbf{V}}_{n+1} - \dot{\mathbf{V}}_n\right), \tag{4.36}$$

$$\mathbf{V}_{n+\alpha_f} = \mathbf{V}_n + \alpha_f\left(\mathbf{V}_{n+1} - \mathbf{V}_n\right), \tag{4.37}$$

$$\mathbf{V}_{n+1} = \mathbf{V}_n + \Delta t\dot{\mathbf{V}}_n + \chi\Delta t\left(\dot{\mathbf{V}}_{n+1} - \dot{\mathbf{V}}_n\right), \tag{4.38}$$

where α_m, α_f, and χ are the real-valued parameters defined in subsection 2.3.3, calculated with $\varrho_\infty = 0.5$.

The nonlinear system of equations (4.30) to (4.38) is approximated by using the Newton–Raphson's method described in subsection 2.3.3. We stop the iterative solver after i_{max} iterations or if convergence is achieved. We consider that convergence is attained if each of the residual vectors has been reduced to a given tolerance. We set the tolerance to 10^{-4}.

Remark:

1. All the terms of the residual are treated implicitly, except those which require non-local computations, such as, for example, calculating integrals or distances. In particular, we treat implicitly the terms λ_N defined in equation (4.9), ρ_g defined in equation (4.10), δ_{rep}, and the velocity $\mathbf{u}^\star$ used in the activator equation; see *Remark 3* below.
2. We use a simple adaptive time stepping scheme in which the time step size is modified based on the convergence of the Newton–Raphson solver. When the convergence is slow, the algorithm reduces the time step size for a given time interval. When the convergence is fast, the time step is slowly increased.

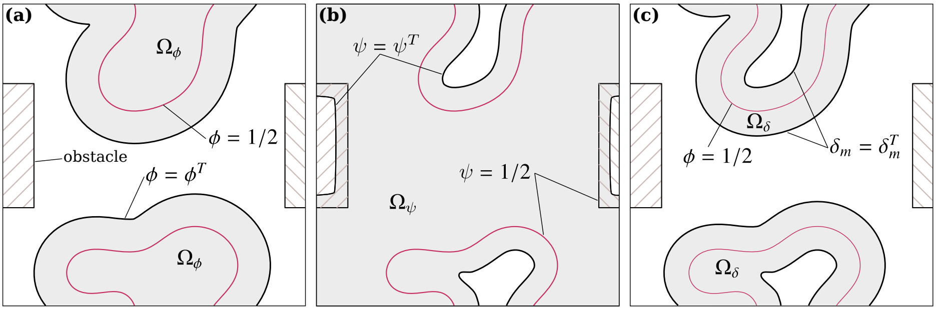

Figure 4.6. Different subdomains defined in the chemotactic problem. *(a) Ω_ϕ is the region where the entries of the residual and the tangent associated to the unknowns ρ_m and ρ_f are not modified. (b) Ω_ψ is similar to Ω_ϕ, but for the unknown q. (c) Ω_δ is the corresponding region to the unknown a.*

Redefinition of the tangent matrix and the residual vector to avoid singularities

As explained in subsection 3.3.2, some of the terms in the weak form become singular outside of the cell and the membrane. The unknown q also contributes to this issue, since q approaches the value zero inside the cell and the obstacles ($\psi \approx 0$). Here, we extend the procedure explained in subsection 3.3.2 to account for the chemoattractant also. After assembling the global residual vector and tangent matrix, we proceed as follows:

(i) Establish the thresholds $\phi^T = 10^{-8}$, $\psi^T = 10^{-8}$, and $\delta_m^T = 10^{-4}$ using the current nonlinear iteration of ϕ at the α_f time level; see figure 4.6.

(ii) Define the spatial domains $\Omega_\phi = \{\mathbf{x} \mid \phi > \phi^T\}$, $\Omega_\psi = \{\mathbf{x} \mid \psi > \psi^T\}$, and $\Omega_\delta = \{\mathbf{x} \mid \delta_m > \delta_m^T\}$.

(iii) Denote by $k_{\max} = n_b\, n_{\text{dof}}$ the number of entries of the global vector of control variables $\mathbf{V}$. Let V_k be the k-th entry of $\mathbf{V}$. For $k = 1, \cdots, k_{\max}$, proceed as follows:

1. If V_k is a control variable of the unknowns ρ_m, ρ_f, q, or a associated to the basis function N_A, compute the support of N_A and denote it by Ω_A.
2. If $\Omega_\phi \cap \Omega_A = \varnothing$, $\Omega_\psi \cap \Omega_A = \varnothing$, or $\Omega_\delta \cap \Omega_A = \varnothing$, then, perform the following two steps:

   2.1. Replace the row k of the global tangent matrix by the row k of the $k_{\max} \times k_{\max}$ identity matrix.

2.2. Replace the k-th entry of the global residual vector by 0.

(iv) Solve the linear system defined in equation (2.61) with the updated tangent matrix and residual vector.

Remarks:

3. We replace $\mathbf{u}$ by $\mathbf{u}^\star$ in the activator equation [equation (4.20)], where $\mathbf{u}^\star(\mathbf{x})$ may be defined as $\mathbf{u}^\star(\mathbf{x}) = \mathbf{u}\left(\boldsymbol{\Psi}(\mathbf{x})\right)$. $\boldsymbol{\Psi}(\mathbf{x})$ is the closest point to $\mathbf{x}$ such that $\phi\left(\boldsymbol{\Psi}(\mathbf{x})\right) = 1/2$; see figure 2.6a. By using $\mathbf{u}^\star$ we can employ coarser meshes without compromising the accuracy of the activator equation. We also replace $d_o(\mathbf{x})$ with $d_o^\star(\mathbf{x}) = d_o\left(\boldsymbol{\Psi}(\mathbf{x})\right)$ in the term δ_{rep} (see subsection 4.2.2) to provide the net distance between the cell membrane and the obstacle.

4. When we advance from t_n to t_{n+1} in our time-stepping scheme, we update the punctual adhesion states as follows:

   (i) Determine the position of the N_{adh} points $\mathbf{x}^j$ at time t_{n+1}:

$$\mathbf{x}^j(t_{n+1}) = \mathbf{x}^j(t_n) + \int_{t_n}^{t_{n+1}} \mathbf{u}(\mathbf{x}^j(\tau), \tau)\, \mathrm{d}\tau. \tag{4.39}$$

   Equation (4.39) may be replaced by the approximation $\mathbf{x}^j(t_{n+1}) = \mathbf{x}^j(t_n) + \mathbf{u}(\mathbf{x}^j, t_n + \Delta t/2)\Delta t$.

   (ii) Determine which focal adhesions will break during the current time step. The rupture of focal adhesions follows a stochastic model based on Poisson's distribution with average number of events per interval $\lambda_p^j = r_{\text{off}}^j(t_{n+1} - t_0^j)$, where j is the index that identifies the focal adhesion and $r_{\text{off}}^j = r_{\text{off}_0}\exp(|\mathbf{F}_{\text{punct}}^j|/F_0)$, where r_{off_0} is a constant and F_0 the characteristic adhesive strength. We also consider that if the point $\mathbf{x}^j$ leaves the cell ($\phi(\mathbf{x}^j) < 1/4$), then the focal adhesion j is broken.

   (iii) Remove broken focal adhesions and update N_{adh}.

   (iv) If $N_{\text{adh}} < N_{\text{adh}}^{\text{max}}$, find new points $\mathbf{x}^j$ such that:

   - $\phi(\mathbf{x}^j) \sim 1/2$.
   - $d_o(\mathbf{x}^j) \lesssim d_o^{\text{ef}}$ or $d_b(\mathbf{x}^j) \lesssim \varepsilon/2$ ($\mathbf{x}^j$ falls in the substrate or fiber).
   - $\mathbf{x}^j$ is sufficiently far away from existing adhesions. In particular, we only permit new focal adhesions on elements of the computational

mesh where no active adhesions are located. In addition, we only permit one new focal adhesion per element.

If the set of points that verify these conditions provides more points than required to reach $N_{\mathrm{adh}}^{\max}$, we choose a subset using a random distribution weighted by the F-actin density, so that those points with a higher F-actin density are more likely to become new adhesions. Otherwise, all points in the set become active adhesions.

(v) Update N_{adh}.

When computing the residual and the tangent matrix, we replace $\mathbf{u}(\mathbf{x}^j, t_{n+1})$ by the current approximation at the intermediate time level.

5. The integration demanded by the numerical method is done through element-based Gaussian quadrature. The evaluation of any unknown on points other than Gauss points slows down the computations. Hence, instead of applying each punctual adhesive force $\mathbf{F}_{\mathrm{punct}}^j$ at $\mathbf{x}^j$, we apply $\mathbf{F}_{\mathrm{punct}}^j$ at the closest Gauss point to $\mathbf{x}^j$. Regarding the pseudopod formation description (see subsection 4.2.4), $\mathbf{s}_i^*$ is placed at the closest Gauss point to its theoretical position. To obtain $\mathbf{s}_i$, we need to compute angles and normal vectors to the membrane. To speed up the computations, we only do that at Gauss points. We resort to penalty functions to select the Gauss point that best adjusts to the point $\mathbf{s}_i$ we seek. Let us call $G_M = \{\mathbf{x}_i^G\}_{i=1,\dots,N_G}$ the set of Gauss points located at the cell's membrane and sufficiently far away from obstacles, that is, $\phi(\mathbf{x}_i^G) \approx 1/2$, $d_o(\mathbf{x}_i^G) \geq d_o^a$, and $d_b(\mathbf{x}_i^G) \geq d_o^a - \Delta d^f$. In 2D we replace $\mathbf{s}_i$ with the point of G_M that minimizes the penalty function $PF_{2\mathrm{D}}(\mathbf{x}_i^G) = |\widehat{\mathbf{n}_q, \mathbf{n}_{\mathbf{x}_i^G}} - \omega_i| + 1.5 d_{\mathbf{s}_i^*}(\mathbf{x}_i^G)$, where $\widehat{\mathbf{n}_q, \mathbf{n}_{\mathbf{x}_i^G}}$ is the angle formed by $\mathbf{n}_q$ and $\mathbf{n}_{\mathbf{x}_i^G}$ in degrees, and $d_{\mathbf{s}_i^*}(\mathbf{x}_i^G)$ is the distance between $\mathbf{s}_i^*$ and $\mathbf{x}_i^G$ in µm. Here, $\mathbf{n}_{\mathbf{x}_i^G}$ is the outward normal vector to the membrane at point $\mathbf{x}_i^G$. Note that the penalty function is sensitive to the signs of the angles that must be consistently measured. For the 3D case, we proceed analogously, but the penalty function is given by $PF_{3\mathrm{D}}(\mathbf{x}_i^G) = |\widehat{\mathbf{n}_q, \mathbf{n}_{\mathbf{x}_i^G}} - \omega_i| + |\widehat{\mathbf{n}_{\mathbf{s}_i^*}, \mathbf{n}_{\mathbf{x}_i^G}} - \beta\omega_i^*| + 1.5 d_{\mathbf{s}_i^*}(\mathbf{x}_i^G) + 100\,[\mathbf{n}_q, \mathbf{n}_{\mathbf{s}_i^*}, \mathbf{n}_{\mathbf{x}_i^G}]$ where $[\mathbf{n}_q, \mathbf{n}_{\mathbf{s}_i^*}, \mathbf{n}_{\mathbf{x}_i^G}]$ represents the volume of the parallelepiped defined by the vectors $\mathbf{n}_q$, $\mathbf{n}_{\mathbf{s}_i^*}$, and $\mathbf{n}_{\mathbf{x}_i^G}$ in µm^3.

6. An alternative methodology more efficient computationally than the procedure explained above to avoid singularities may be found in appendix B.

4.4 Results and discussion

In this section we show the ability of our method to reproduce amoeboid chemotactic motion. We present several 2D and 3D computations. For a particular initial cell geometry, given by the function $\phi(\mathbf{x}, 0)$, the cytosolic components are initialized in all examples as $\rho_m(\mathbf{x}, 0) = \phi(\mathbf{x}, 0)$, $\rho_f(\mathbf{x}, 0) = 0.5\phi(\mathbf{x}, 0)$, and $\rho_g(\mathbf{x}, 0) = \alpha_g \phi(\mathbf{x}, 0)$ with $\alpha_g = 1.1$ in the 2D examples and $\alpha_g = 0.9$ in the 3D computations. The chemoattractant and activator concentrations as well as the velocity are assumed to vanish at the initial time in all examples. The parameter values used in the two- and three-dimensional simulations may be found in tables 4.1 and 4.2, respectively.

4.4.1 Analysis of chemotactic motion

We initially analyze the behavior of cells under different chemotactic conditions neglecting the chemoattractant dynamics. Thus, we disregard equation (4.19) and assume that $|\overline{\nabla q}|$, $\overline{q}$, and $\mathbf{n}_q$ are constants imposed *a priori*. We will take $\mathbf{n}_q = \{1, 0\}^T$ in all simulations and vary $|\overline{\nabla q}|$ and $\overline{q}$. In order to study chemotaxis in large environments without employing unaffordable computational domains, we resort to periodic boundary conditions. We use a 2D computational domain $\overline{\Omega} = [-L, L]^2$ with $L = 25\,\mu\text{m}$. The domain is discretized using 200 $\mathcal{C}^1$-continuous quadratic elements in each direction. We take an initial time step $\Delta t = 0.05\,\text{s}$. The initial cell geometry is given by a circle[6] of radius $R_c = 8\,\mu\text{m}$ centered at the origin of coordinates.

First, we analyze the influence of $|\overline{\nabla q}|$. Thus, we keep constant $\overline{q} = 80\,\text{nM}$ and perform 10 independent simulations for each value of $|\overline{\nabla q}|$. We study the interval $[0, T]$, where $T = 15\,\text{min}$. We consider three values of $|\overline{\nabla q}|$, namely, 0.1, 1, and $10\,\text{nM}/\mu\text{m}$. The results are plotted in figure 4.7, where each column corresponds to a value of $|\overline{\nabla q}|$, increasing from left to right. Figure 4.7a shows the tracks of the cells. As $|\overline{\nabla q}|$ increases, the cells lose their characteristic persistent random motion and exhibit a movement guided by $\mathbf{n}_q$. We define the chemotactic index CI as the displacement in the gradient direction over the total distance traveled in the simulation[7]. The average CI over the cell population increases with $|\overline{\nabla q}|$, as shown in the plot. Figure 4.7b shows the frequency histogram of the angle ω_i (red bars) and the average pseudopod size (blue crosses) as a function of ω_i. The

[6] A circular cell is described using a smooth function given by $\phi(\mathbf{x}, 0) = 0.5 - 0.5 \tanh[\frac{2\sqrt{2}}{\varepsilon}(d_c(\mathbf{x}) - R_c)]$, where $d_c(\mathbf{x})$ is the distance to the center of the cell. Similar initial conditions based on hyperbolic tangents will be used throughout the chapter.

[7] More precisely, $CI = d_{\mathbf{n}_q}/d_{\text{cell}}$, where $d_{\mathbf{n}_q} = \int_0^T \mathbf{u}_{\text{cell}} \cdot \mathbf{n}_q \text{d}t$ and $d_{\text{cell}} = \int_0^T |\mathbf{u}_{\text{cell}}| \text{d}t$, with $\mathbf{u}_{\text{cell}}$ the velocity of the mass center of the cell.

Table 4.1. *Parameters used for two-dimensional chemotactic motion. In this chapter, some of the parameter values are taken from experiments and computational works of cell motility, while the rest have been estimated to better represent the biological problem; see Moure and Gomez (2016, 2017) for more details.*

Symbol	Description	Value
Γ_ϕ	Parameter enforcing a hyperbolic tangent profile	$0.52\,\mu\mathrm{m\,s^{-1}}$
ε	Phase-field interfacial length scale	$2\,\mu\mathrm{m}$
φ	Scaling of membrane marker width	20
d_o^{ef}	Effective distance for obstacle repulsion	$1.7\,\mu\mathrm{m}$
$D_m^{\max}$	Myosin diffusion scale	$4.16\,\mu\mathrm{m^2 s^{-1}}$
K_m	Decay rate of myosin diffusion	$1.55\,\mu\mathrm{m}^2$
ε_f	Diffusive length scale of F-actin	$1.0\,\mu\mathrm{m}$
ε_g	Diffusive length scale of G-actin	$3.16\,\mu\mathrm{m}$
Γ_f	F-actin mobility	$0.52\,\mathrm{s}^{-1}$
Γ_g	G-actin mobility	$0.52\,\mathrm{s}^{-1}$
μ	Dynamic viscosity coefficient	$1500\,\mathrm{pN\,s}\,\mu\mathrm{m}^{-1}$
λ	Bulk viscosity coefficient	$-500\,\mathrm{pN\,s}\,\mu\mathrm{m}^{-1}$
$\overline{\eta}_m$	Strength of contractile forces	$22\,\mathrm{pN}\,\mu\mathrm{m}$
$\overline{\alpha}_m$	Range of contractile forces	0.41
$\overline{\eta}_f$	Strength of protrusive forces	$1.2{\cdot}10^4\,\mathrm{pN}\,\mu\mathrm{m}^3$
$\overline{\alpha}_f$	Range of protrusive forces	0.075
d_o^f	Effective distance to obstacles for protrusion suppression	$2.6\,\mu\mathrm{m}$
d_b^f	Effective distance to the boundary for protrusion suppression	$1.8\,\mu\mathrm{m}$
ς	Substrate drag coefficient	$0.7\,\mathrm{pN\,s}\,\mu\mathrm{m}^{-3}$
γ	Surface tension coefficient	$78\,\mathrm{pN}$
η_{rep}	Strength of repulsive forces	$6000\,\mathrm{pN}\,\mu\mathrm{m}$
r_q	Decay rate of chemoattractant	$0.1\,\mathrm{s}^{-1}$
b_q	Production rate of chemoattractant	$500\,\mathrm{s}^{-1}$
k_q	Production rate of chemoattractant	$10\,\mathrm{s}^{-1}$
D_a	Diffusion coefficient of activator	$0.2\,\mu\mathrm{m^2 s^{-1}}$
r_a	Decay rate of activator	$0.32\,\mathrm{s}^{-1}$
b_a	Production rate of activator	$7.8\,\mathrm{s}^{-1}$
$a_{\max}$	Saturation of activator	$1.5\,\mu\mathrm{m}^{-2}$
R_a	Radius of activator source	$1\,\mu\mathrm{m}$
d_o^a	Effective distance for pseudopod inhibition	$2.35\,\mu\mathrm{m}$

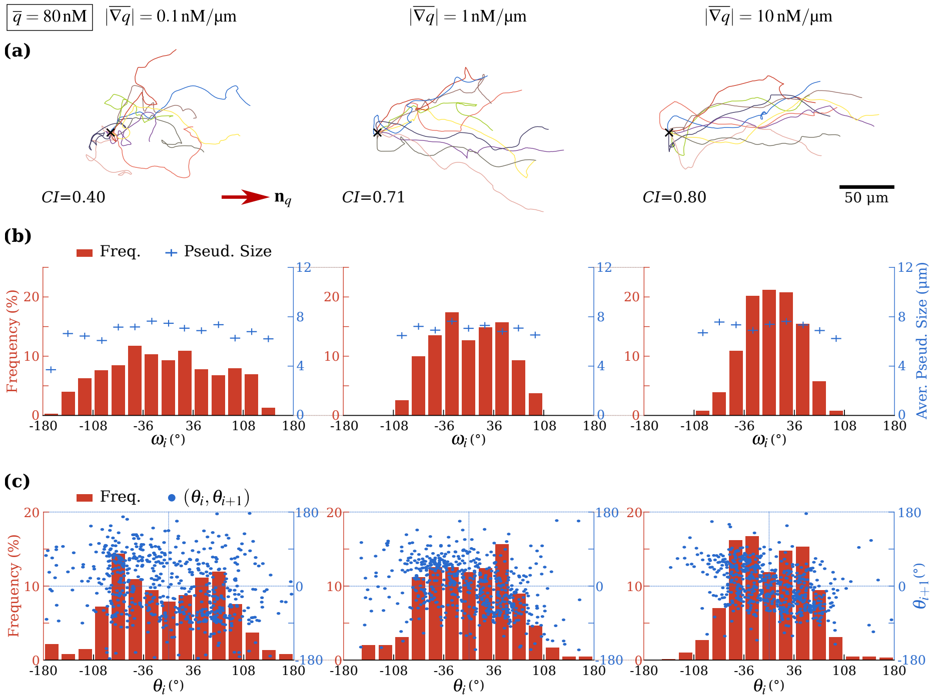

Figure 4.7. Analysis of chemotactic motion. Influence of $|\overline{\nabla q}|$. *Results corresponding to $|\overline{\nabla q}| = 0.1\,\mathrm{nM}/\mu\mathrm{m}$ (left column), $|\overline{\nabla q}| = 1\,\mathrm{nM}/\mu\mathrm{m}$ (middle column), and $|\overline{\nabla q}| = 10\,\mathrm{nM}/\mu\mathrm{m}$ (right column); with $\overline{q} = 80\,\mathrm{nM}$ for all cases. (a) Tracks of the cells and chemotactic index (CI). (b) Frequency histogram of ω_i and average pseudopod size as a function of ω_i. (c) Frequency histogram of θ_i and distribution of the pairs (θ_i, θ_{i+1}). See figure 4.5b for a description of angles ω_i and θ_i.*

angle ω_i has been measured as shown in figure 4.5b (right) and pseudopod size has been estimated as the net distance traveled by $\mathbf{s}_i$ during its growth time ΔT_i. The histogram of ω_i is approximately symmetric, with the highest frequencies concentrating around $\omega_i \sim 0°$ as $|\overline{\nabla q}|$ increases. For example, for $|\overline{\nabla q}| = 0.1\,\mu\mathrm{M}/\mu\mathrm{m}$ the histogram spreads almost over the entire range of ω_i, namely $[-180°, 180°]$, but for $|\overline{\nabla q}| = 10\,\mu\mathrm{M}/\mu\mathrm{m}$ all the non-zero frequencies fall into the interval $[-108°, 108°]$. Pseudopod size is fairly independent of ω_i, though it displays a slight increase in the neighborhood of $\omega_i = 0°$ (Bosgraaf and Van Haastert, 2009a).

To further analyze the chemotactic motion, we study the angles between consecutive pseudopods. We use θ_i, which is the angle between $\mathbf{n}_{\mathbf{s}_i}$ and $\mathbf{n}_{\mathbf{s}_{i+1}}$ (see figure 4.5b, right), as a measure of the angle between pseudopods. Figure 4.7c shows the frequency histogram of θ_i (red bars) as well as the distribution of the pairs (θ_i, θ_{i+1}) on a two-dimensional space (blue dots). In non-chemotactic amoeboid motion, the histogram of θ_i usually presents a symmetric distribution with respect to $\theta_i = 0°$ with two peaks around $\theta_i = \pm 55°$, while the plot of the pairs (θ_i, θ_{i+1}) is denser in the top-left and bottom-right quadrants (Bosgraaf and Van Haastert, 2009b). In chemotactic motion, the histogram of θ_i remains approximately symmetric, but the two peaks are closer to $\theta_i = 0°$ as $|\overline{\nabla q}|$ increases. The distribution of the pairs (θ_i, θ_{i+1}) is still denser on the top-left and bottom-right quadrants, but is more populated in the region that corresponds to smaller angles. Note that, once the cell is moving in the direction of $\mathbf{n}_q$, the probability distribution of pseudopod extension affected by the chemotactic bias displays very low values at the back and the sides of the cell. These values are lower as $|\overline{\nabla q}|$ increases. This is the reason why it is difficult to observe abrupt changes in the cell direction, i.e., angles θ_i close to $-180°$ and $180°$, for high values of $|\overline{\nabla q}|$; see figure 4.7c (right).

The influence of $\overline{q}$ on chemotactic cell motility is studied through 10 independent simulations with a 15 minute duration. We take $|\overline{\nabla q}| = 1\,\text{nM/µm}$ for all simulations and analyze the cases given by $\overline{q} = 80$, 800, and 8000 nM. Figure 4.8 shows the results using the same format as in the previous figure. Notably, the results show that the chemotactic index CI decreases as we increase $\overline{q}$. This is a phenomenon that has also been observed experimentally. It is thought to be a consequence of receptor saturation (Song *et al.*, 2006). Cells have a finite number of receptors. If the extracellular ligand concentration is high, most of them will be bound and the cell will find it difficult to establish differences in the level of receptor occupancy. The same argument applies for low values of $\overline{q}$; with a small amount of bound receptors the cell can not distinguish variations in occupancy along the membrane[8] (Fuller *et al.*, 2010). Figure 4.8b shows that the histogram of ω_i becomes more and more uniform as $\overline{q}$ increases. In figure 4.8c, the histogram of θ_i features two symmetric peaks for all values of $\overline{q}$, which are located approximately at $\theta_i = \pm 55°$ for the largest value of $\overline{q}$, showing again a feature of non-chemotactic motion. The distribution of the pairs (θ_i, θ_{i+1}) for a given chemotactic index is consistent with experimental observations and the data presented in figure 4.7.

[8] We checked that the model also reproduces this experimental observation (data not shown).

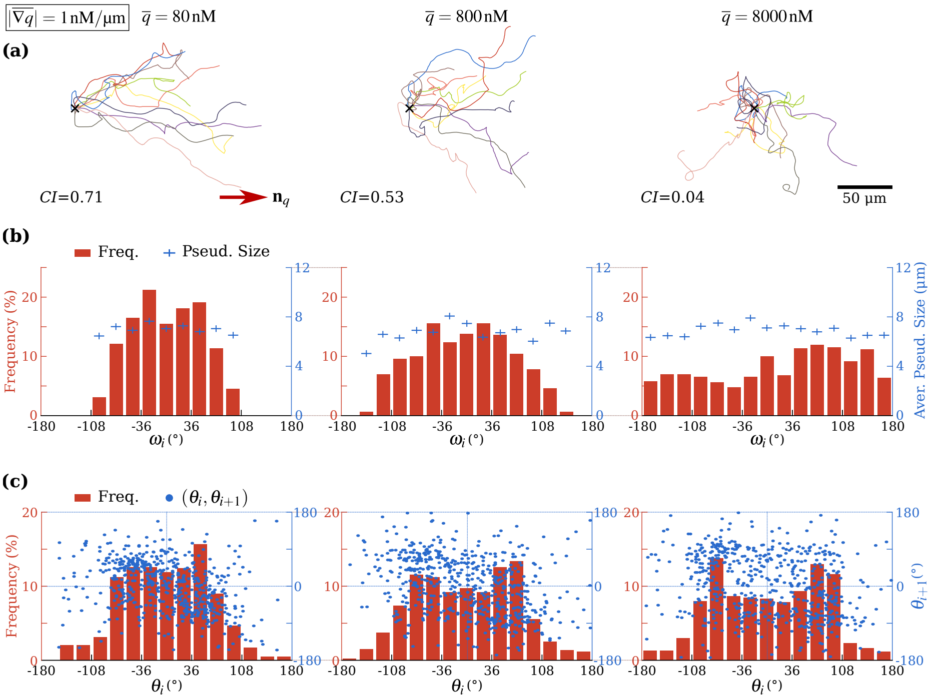

Figure 4.8. Analysis of chemotactic motion. Influence of $\overline{q}$. *Results corresponding to $\overline{q} = 80\,\mathrm{nM}$ (left column), $\overline{q} = 800\,\mathrm{nM}$ (middle column), and $\overline{q} = 8000\,\mathrm{nM}$ (right column); with $|\nabla q| = 1\,\mathrm{nM}/\mu\mathrm{m}$ for all cases. (a) Tracks of the cells and chemotactic index (CI). (b) Frequency histogram of ω_i and average pseudopod size as a function of ω_i. (c) Frequency histogram of θ_i and distribution of the pairs (θ_i, θ_{i+1}). See figure 4.5b for a description of angles ω_i and θ_i.*

4.4.2 *Dictyostelium* aggregation mediated by natural waves

Social *Dictyostelium discoideum*, after nutrient deprivation, may experience a process called aggregation. During aggregation, cells come together guided by a signaling molecule called cAMP, secreted by the cells themselves. Individual cells located far from the aggregation center move under the influence of traveling waves of cAMP. These waves are released with a period $T_w \sim 6\,\mathrm{min}$ and travel outward from the aggregation center without significant dissipation. Although cAMP waves are symmetric, cells are able to produce effective migration towards the wave source. This is known as the back-of-the-wave problem: even though the gradient reverses in the back half of the wave, cells do not exhibit effective migration away from the aggregation center. This behavior may be explained through the concept of adaptation: cells respond better to increases of chemoattractant concentration. When the chemoattractant concentration decreases, the chemotactic response diminishes (Van Haastert and Devreotes, 2004). Thus, when cells encounter the cAMP wave, although the gradient strength is the same in both halves of the wave, the chemotactic response is weaker in the back half because the chemoattractant concentration decreases. It has been suggested, see, e.g., Goldstein (1996), that adaptation features a characteristic time, identified as the time the cell needs to recover its initial state of chemotactic response. Adaptation may be also thought of as a long-term memory with characteristic time scale similar to the adaptation time. The chemotactic long-term memory plays a similar role to that of the persistence time in spontaneous (non chemotactic) *Dictyostelium* migration; i.e., maintaining the direction of the motion for a certain time. Skoge *et al.* (2014) explains the process of aggregation assuming that the adaptation time is similar to the period of the cAMP wave. Their experiments show that waves with greater period than the adaptation time produce reverse motion in the cell population. Our model does not include adaptation explicitly, but we show that the persistence of the motion alone enables an effective aggregation process for cAMP waves of up to $\sim$6 min.

To replicate the nondissipating waves of the experiments in Skoge *et al.* (2014), we ignore the chemoattractant dynamics (as done in subsection 4.4.1) and simply impose *a priori* a distribution $q(\mathbf{x}, t)$ that represents the traveling waves used in the experiments. The waves travel in the direction of a channel, which we assume to be aligned with the x axis. The chemoattractant wave has a wavelength $\lambda_q = 1300\,\mu\mathrm{m}$, a maximum concentration $Q = 700\,\mathrm{nM}$, and moves with velocity $\{-\lambda_q/T_w, 0\}^T \mu\mathrm{m/s}$, where T_w is the period of the wave. The concentration of a single wave can be defined as

$$q_w(x,t) = Q \exp\left[-0.5\left(\frac{x + \frac{\lambda_q}{T_w}t - \frac{\lambda_q}{2}}{\sigma_q}\right)^2\right], \tag{4.40}$$

with the constant $\sigma_q = 101.12\,\mu\mathrm{m}$. If we consider a set of waves that are λ_q away from each other in the x-direction, the concentration of each wave i is given by

$$q_{w,i}(x,t) = Q \exp\left[-0.5\left(\frac{x + \frac{\lambda_q}{T_w}t - (2i-1)\frac{\lambda_q}{2}}{\sigma_q}\right)^2\right], \tag{4.41}$$

where i is a positive integer that identifies each wave. The distribution q used in this section can be computed as $q(x,t) = \sum_i q_{w,i}(x,t)$, where i accounts for the waves with non-zero concentration in the vicinity of the cell.

To reduce the computational time we use a rather small computational domain, $\overline{\Omega} = [-L, L]^2$ with $L = 25\,\mu\mathrm{m}$, but assume periodic boundary conditions in all

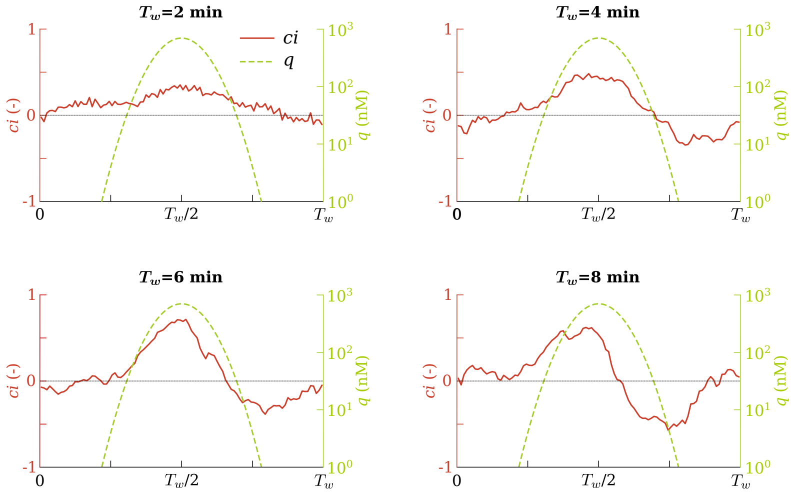

Figure 4.9. *Dictyostelium* aggregation mediated by natural waves. *Temporal evolution of the average instantaneous chemotactic index (ci) and cAMP concentration (q) for different values of the wave period T_w.*

directions. We consider the same initial cell geometry as in the previous section. We perform 5 independent simulations of duration $6T_w$ for each wave period $T_w = 2$, 4, 6, and 8 min. To analyze the results we define the instantaneous chemotactic index $ci(t) = \mathbf{u}_{\text{cell}}(t) \cdot \mathbf{n}_q / |\mathbf{u}_{\text{cell}}(t)|$. Here, $\mathbf{u}_{\text{cell}}(t)$ is the velocity of the cell's center of mass. We assumed that the aggregation center is located at the point $(\infty, 0)$. Thus, we expect chemotactic motion along the horizontal direction and we take $\mathbf{n}_q = \{1, 0\}^T$. Figure 4.9 shows the time evolution of the instantaneous chemotactic index (red line) and the cAMP concentration (dashed green line). The reported value of $ci(t)$ is the average of the 30 periods that we computed (5 simulations, with duration $6T_w$). The results show that for short periods ($T_w \sim 2$ min) the cell always moves toward the aggregation center, that is, $ci(t) > 0$ for all t. As T_w increases, $ci(t)$ attains negative values, which indicates reverse migration at the back half of the wave. For the largest period $T_w = 8$ min the positive and negative peaks of $ci(t)$ reach similar values and the net motion of the cell toward the aggregation center is small. Our results are in agreement with the experiments reported in Skoge *et al.* (2014) although the efficiency of the aggregation process deteriorates earlier in our simulations. This suggests that the time scale of the adaptation process is larger than the persistence time. In subsection 4.4.7 we discuss how to incorporate adaptation into our model to obtain better quantitative agreement with the experiments of cAMP traveling waves.

4.4.3 Chemotactic migration on a planar surface

Here, we aim at illustrating the behavior of a cell moving along a chemoattractant gradient as well as the cell-chemoattractant interaction. Thus, this example, in contrast with those analyzed so far, considers the dynamics of the extracellular ligand described by equation (4.19). The simulation will show how a cell follows a moving chemoattractant source as observed in experiments. We perform a simulation with duration 25 minutes on a 2D computational domain $\overline{\Omega} = [0, L]^2$, where $L = 100\,\mu\text{m}$. The source term S_q in equation (4.19) is defined as $S_q = \sum_{i=1}^{5} S_i$. The source term S_i is a Gaussian function in space centered at point $\mathbf{S}_i^c$ and is non-zero in a particular time interval only. The centers are given by $\mathbf{S}_1^c = (50, 97)$, $\mathbf{S}_2^c = (97, 3)$, $\mathbf{S}_3^c = (3, 97)$, $\mathbf{S}_4^c = (50, 3)$, and $\mathbf{S}_5^c = (97, 97)\,\mu\text{m}$; see figure 4.10. The different sources S_i with $i = 1, ..., 5$ are active, respectively, in the time intervals $(0, 300)$, $(300, 600)$, $(600, 900)$, $(900, 1200)$, and $(1200, 1500)\,\text{s}$. The main panel in figure 4.10 shows the entire computational domain and the numerical solution at time $t = 513\,\text{s}$. The cell's interior shows the F-actin density and the membrane displays the activator concentration. Outside the cell, the color corresponds to the chemoattractant concentration. The plot also includes three rectangular insets that show the cell's location, shape and biochemical state (ρ_f and a) at different times ($t = 104$, 1012, and $1500\,\text{s}$). The insets also show the chemoattractant concentration in a small rectangular region of the domain around the cell. The main panel also shows the path followed by the cell's center of mass over the entire simulation. The path is divided into 5 sections represented by different line types. The section changes when the active source changes. The figure shows the section changes with crosses in the path line as well as the location of each S_i and its interval of activity. For each time, the plot shows the cell's center of mass with a small circle as well as the values of $|\overline{\nabla q}|$, $\overline{q}$, and the chemotactic direction $\mathbf{n}_q$ (red arrow). Figure 4.10 shows the main features of our amoeboid motion model: the membrane-bound activator triggers the emergence of pseudopods (regions of high F-actin density; see $t = 513$ and $1012\,\text{s}$) that push forward the membrane producing the cell motion. In this example, the signaling parameters detected by the cell display a range of values ($|\overline{\nabla q}| \sim 1\,\text{nM}/\mu\text{m}$ and $\overline{q} \sim 40\,\text{nM}$) that strongly bias the movement of the cell. The cell carries out a well-directed migration towards the chemoattractant source that is active at each time, with the exception of the interval $(400, 600)\,\text{s}$. During the interval $(400, 600)\,\text{s}$, the cell actually moves in the opposite direction to $\mathbf{n}_q$, highlighting the chaotic nature of cell motion observed in experiments (e.g., Tweedy *et al.*, 2013). Even a strong chemoattractant gradient cannot guarantee a rapid and straight displacement towards the source. In figure 4.10 we can also observe the interaction between the cell and the chemoattractant. The chemoattractant undergoes reactions with the membrane receptors and does not diffuse through the cell, which produces a

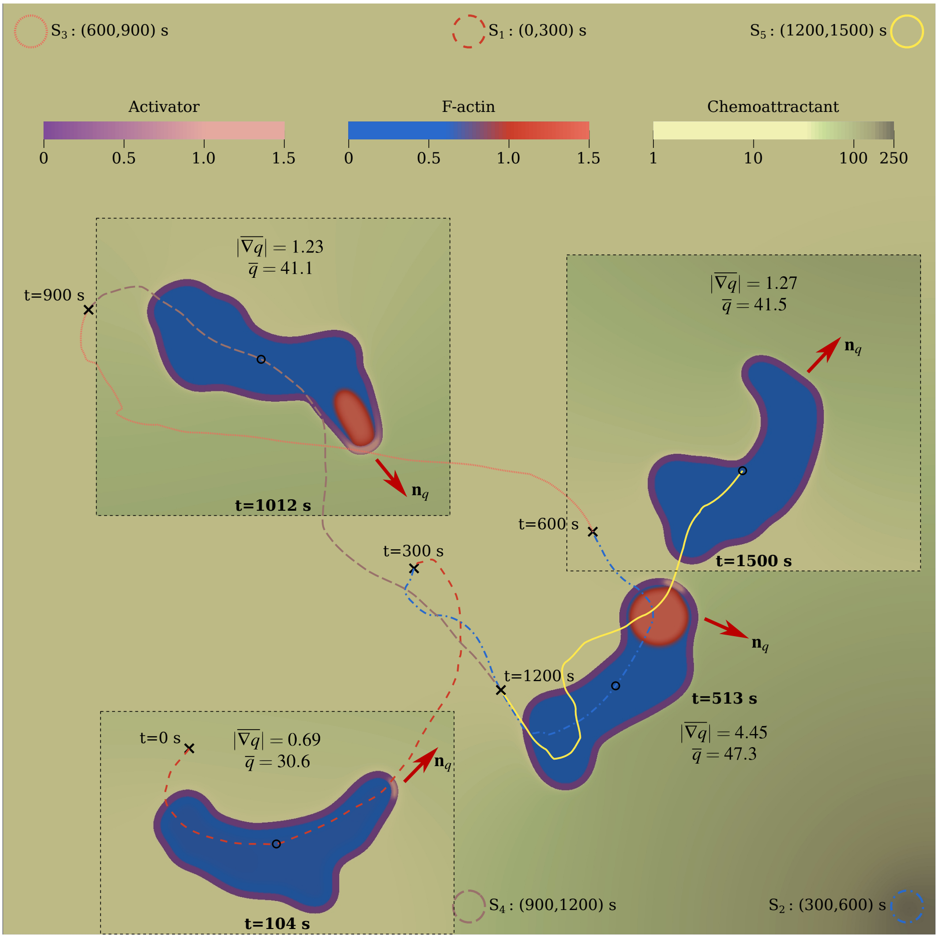

Figure 4.10. Chemotactic migration on a planar substrate. Activator, F-actin, and chemoattractant distributions. *Simulation performed on a mesh composed of* 400 $\mathcal{C}^1$*-continuous quadratic elements in each direction. The initial time step is* $\Delta t = 0.05\,\mathrm{s}$*. The cell is initially centered at the point* $(20, 20)\,\mu\mathrm{m}$ *with a circular geometry of radius* $R_c = 8\,\mu\mathrm{m}$*. We set* $D_q = 500\,\mu\mathrm{m}^2\mathrm{s}^{-1}$ *and* $q_{\max,i} = 250\,\mathrm{nM}$ *for* $i = 1, \ldots, 5$*. The main panel shows the distributions of* a*,* ρ_f*, and* q *at* $t = 513\,\mathrm{s}$*. The three insets show the distributions of* a*,* ρ_f*, and* q *in the neighborhood of the cell at* $t = 104$*, 1012, and 1500 s. The circles close to the domain boundary represent the spatial location of the chemotactic sources (*S_1*,* S_2*,* S_3*,* S_4*, and* S_5*), along with the interval time they are active. The cell's path is divided into five segments according to the active source. The division points are marked with crosses.* $\mathbf{n}_q$ *(red arrow),* $|\overline{\nabla q}|$*, and* $\overline{q}$ *(units nM/µm and nM, respectively) are indicated for the considered times* $t = 104$*, 513, 1012, and 1500 s. The position of the cell's center of mass is marked with a small circle.*

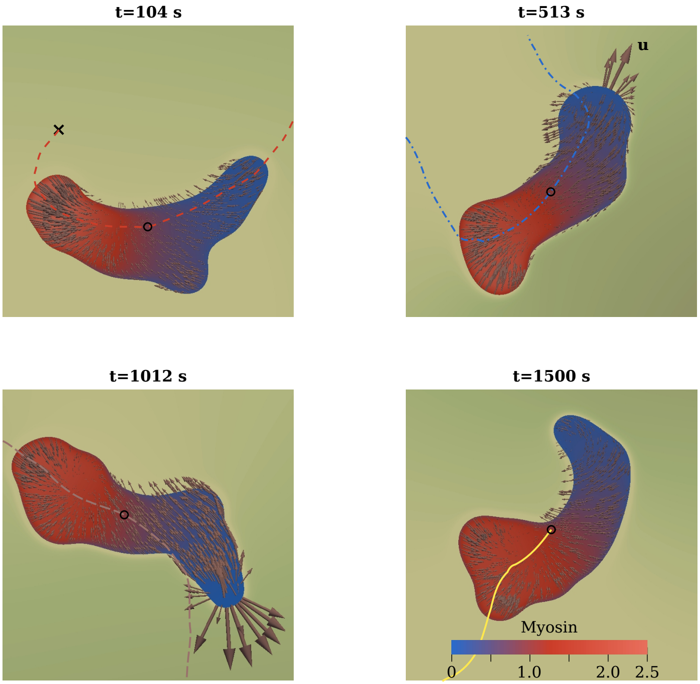

Figure 4.11. Chemotactic migration on a planar substrate. *Myosin distribution and F-actin network velocity (grey arrows) at the same times as shown in figure 4.10 (*$t = 104$, 513, 1012*, and* $1500\,\mathrm{s}$*). The chemoattractant concentration outside the cell is plotted using the same color scale as in figure 4.10.*

small track of low chemoattractant density behind the cell (slightly visible, e.g., at $t = 1012\,\mathrm{s}$). Figure 4.11 shows the myosin distribution inside the cell at times $t = 104$, 513, 1012, and $1500\,\mathrm{s}$. For simplicity, we only show a small region of the computational domain at each time. In figure 4.11 we also show the F-actin velocity $\mathbf{u}$ inside the cell, represented by arrows distributed at random points. All the snapshots show the accumulation of myosin at the back of the cell, causing its retraction. However, at times $t = 104$ and $1500\,\mathrm{s}$, one cannot appreciate significant protrusive velocities because there are no pseudopods pushing the membrane at those times; c.f. with figure 4.10.

4.4.4 Maze-solving by chemotactic migration

We study chemotactic migration on a planar surface with rigid obstacles. The obstacle layout is intricate, so that the cell essentially has to migrate in a maze-like environment. The computational domain is a square of side 100 µm. The chemoattractant source is a Gaussian function located at the center of the domain and active throughout the entire time span of the simulation. Figure 4.12 shows the simulation results using the same format as in figure 4.10. The main panel displays the results at time $t = 370\,\text{s}$, with the color outside the cell indicating the chemoattractant concentration. The color scales inside the cell and the membrane represent, respectively, F-actin density and activator concentration. There is also a yellow line showing the path followed by the cell's center of mass throughout the simulation. The black crosses on the track indicate the location of the cell's center of mass at times $t = 0$, 200, 400, 600, and 800 s. The rectangular insets marked with dashed black line show the cell's location and biochemical state as well as the chemoattractant concentration is a small region around the cell at times $t = 238$, 576, and 723 s. The plot shows that at early times ($t < 200\,\text{s}$) the cell performs an inefficient migration around its initial position. The initial motion is inefficient mainly for two reasons: First, the chemotactic source is located at a large effective distance to the cell because the chemoattractant cannot penetrate the obstacles. This produces low chemoattractant gradients in the neighborhood of the cell. Second, and foremost, the chemoattractant approaches the cell from two opposite sides —left and right. As a consequence, the point of the membrane where $q_{\max}$ is located is on the left or right side of the cell, but $q_{\min}$ is attained somewhere else than left or right. Thus, the direction of $\mathbf{n}_q$, which is a unit vector pointing from $q_{\min}$ to $q_{\max}$, is not horizontal and the cell moves neither right nor left which are the two only ways out. After $t \sim 200\,\text{s}$, the cell migrates towards the chemotactic source following a nearly optimal path. In particular, as the cell approaches the chemotactic source, the value of $|\overline{\nabla q}|$ becomes greater, increasing the efficiency of the motion. The strong interaction between the cell and the chemoattractant is apparent in figure 4.12. The chemoattractant binds to the cell's receptors, so that the membrane acts as a chemoattractant sink. As the same time, the extracellular ligand cannot penetrate the cell. The results clearly show that the obstacles have a strong impact on the cell motion directly, but also through the chemoattractant distribution. This is particularly visible in the insets that correspond to $t = 576\,\text{s}$ and $t = 723\,\text{s}$. At $t = 576\,\text{s}$, the chemoattractant concentration at the back of the cell is significantly lower than at the front. This happens because the boundary on the left and the obstacle on the right block chemoattractant flow producing a much higher gradient than what would be attained in obstacle-free motion. Thus, our results suggest that the presence of obstacles increases the efficiency of chemotactic migration.

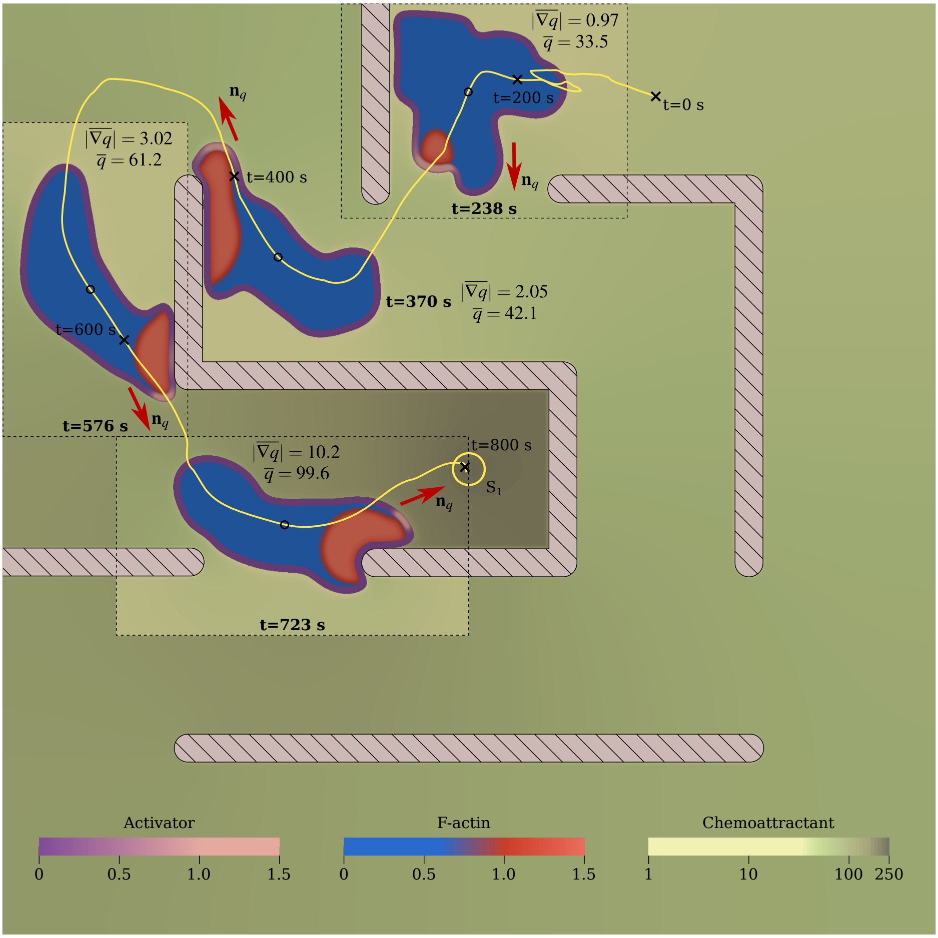

Figure 4.12. Maze-solving by chemotactic migration. Activator, F-actin, and chemoattractant distributions. *We use the same mesh, initial cell geometry and time step as the simulation shown in figure 4.10. The cell is initially centered at the point* $(70, 90)\,\mu$m. *We set* $D_q = 1000\,\mu\text{m}^2\text{s}^{-1}$ *and* $q_{\max,1} = 250\,$nM. *The chemotactic source* S_1 *(yellow circle) is active throughout the entire simulation. The walls are represented as striped grey regions (the width of the walls has been slightly modified for visualization purposes). The main panel shows the distributions of* a, ρ_f, *and* q *at* $t = 370\,$s. *The three insets show the distributions of* a, ρ_f, *and* q *in the neighborhood of the cell at* $t = 238$, 576, *and* 723 s. *The cell's path is drawn with a yellow line. Black crosses represent the position of the mass center of the cell at* $t = 0$, 200, 400, 600, *and* 800 s. $\mathbf{n}_q$ *(red arrow),* $|\overline{\nabla q}|$ *and* $\overline{q}$ *(units* nM/μm *and* nM, *respectively) are indicated for the considered times* $t = 238$, 370, 576, *and* 723 s. *The position of the cell's center of mass is marked with a small circle.*

4.4.5 Three-dimensional migration on a planar substrate

In subsection 4.4.3 we simulated migration on a planar substrate using a 2D computational model. While using a 2D simulation for this problem is common practice and produces indeed a reasonably accurate solution (see Ziebert and Aranson, 2016), we show here that a 3D simulation allows to gain further insight into the process. In particular, the 2D approach somehow assumes that the entire surface of the cell is in contact with the substrate. However, experiments with *Dictyostelium* show that the cell displays irregular elongated shapes (Wessels *et al.*, 2004), that produce only a few localized areas of contact with the substrate. The most common situation is that of two contact areas, where most of the adhesive forces are located. The contact regions are at the front and the back of the cell with forces pointing in opposite directions and producing the so-called dipole of forces (Del Alamo *et al.*, 2007). Cell motion is a consequence of forces pointing forward being greater than forces pointing backwards. To better understand this process, we use our 3D computational model considering punctual adhesive forces on the substrate. Our computational domain is the box shown in figure 4.13. Since the cell location is defined using a diffuse interface representation, where the cell membrane has a thickness of order $\sim\varepsilon$, we consider the substrate to be the plane $z = \varepsilon/2 = 1\,\mu\text{m}$. The remaining boundaries of the domain (lateral and top) are non-adhesive walls where contact forces are not considered. To mimic a quasi-2D motion, we only allow the formation of new pseudopods in the region $z \in (z_{\text{cell}} - 1, z_{\text{cell}} + 1)\,\mu\text{m}$, where z_{cell} is the z-coordinate of the cell's center of mass. The chemotactic source S_q is defined as $S_q = S_1 + S_2$, where S_1 and S_2 have the usual spatial distribution and are centered at the points $\mathbf{S}_1^c = (41.2, 62.8, 2.5)$, $\mathbf{S}_2^c = (2, 2, 2.5)\,\mu\text{m}$. S_1 and S_2 are active, respectively, in the time intervals $(0, 150)$ and $(150, 230)\,\text{s}$. Figure 4.13 shows the activator distribution on the cell's membrane and the chemoattractant concentration on the substrate as well as on two lateral boundaries. The plot also shows the path followed by the cell's center of mass throughout the simulation and the location of the active chemoattractant source at each time. The line representing the cell's path is divided in two sections, corresponding to the time intervals of activity of the chemoattractant sources. In the simulation, the signaling parameters $|\overline{\nabla q}|$ and $\overline{q}$ attain values ($|\overline{\nabla q}| \sim 0.5\,\text{nM}/\mu\text{m}$ and $\overline{q} \sim 20\,\text{nM}$) that effectively bias the cell movement as illustrated by the cell's path. Figure 4.14 shows myosin concentration on the cell's membrane at the same times. As expected, myosin concentration is higher at the back of the cell. Figure 4.14 shows also insets with the punctual adhesive forces acting on the F-actin network[9]. The insets display the regions where the cell touches the substrate (black solid line) and the adhesive forces

[9] There are forces of equal strength and opposite direction acting on the substrate but we do not plot them for clarity.

Table 4.2. *Parameters used for three-dimensional chemotactic motion.*

Symbol	Description	Value
Γ_ϕ	Parameter enforcing a hyperbolic tangent profile	$0.52\,\mu\mathrm{m\,s^{-1}}$
ε	Phase-field interfacial length scale	$2\,\mu\mathrm{m}$
φ	Scaling of membrane marker width	20
d_o^{ef}	Effective distance for obstacle repulsion	$1.7\,\mu\mathrm{m}$
$D_m^{\max}$	Myosin diffusion scale	$4.16\,\mu\mathrm{m}^2\mathrm{s}^{-1}$
K_m	Decay rate of myosin diffusion	$1.55\,\mu\mathrm{m}^3$
ε_f	Diffusive length scale of F-actin	$1.0\,\mu\mathrm{m}$
ε_g	Diffusive length scale of G-actin	$3.16\,\mu\mathrm{m}$
Γ_f	F-actin mobility	$0.52\,\mathrm{s}^{-1}$
Γ_g	G-actin mobility	$0.52\,\mathrm{s}^{-1}$
μ	Dynamic viscosity coefficient	$1500\,\mathrm{pN\,s}\,\mu\mathrm{m}^{-2}$
λ	Bulk viscosity coefficient	$-500\,\mathrm{pN\,s}\,\mu\mathrm{m}^{-2}$
$\overline{\eta}_m$	Strength of contractile forces	$9.9\,\mathrm{pN}\,\mu\mathrm{m}$
$\overline{\alpha}_m$	Range of contractile forces	0.41
$\overline{\eta}_f$	Strength of protrusive forces	$1.14{\cdot}10^4\,\mathrm{pN}\,\mu\mathrm{m}^3$
$\overline{\alpha}_f$	Range of protrusive forces	0.075
d_o^f	Effective distance to obstacles for protrusion suppression	$2.6\,\mu\mathrm{m}$
d_b^f	Effective distance to the boundary for protrusion suppression	$1.8\,\mu\mathrm{m}$
ς	Drag coefficient	$0.7\,\mathrm{pN\,s}\,\mu\mathrm{m}^{-4}$
k_{grip_0}	Gripping coefficient	$1.5\,\mathrm{pN\,s}^{-1}\mu\mathrm{m}^{-1}$
$N_{\mathrm{adh}}^{\max}$	Maximum number of adhesions	100
r_{off_0}	Disassociation rate of adhesions	$0.002\,\mathrm{s}^{-1}$
F_0	Characteristic adhesive strength	$12\,\mathrm{pN}\,\mu\mathrm{m}^{-3}$
γ	Surface tension coefficient	$78\,\mathrm{pN}\,\mu\mathrm{m}^{-1}$
η_{rep}	Strength of repulsive forces	$6000\,\mathrm{pN}$
r_q	Decay rate of chemoattractant	$0.1\,\mathrm{s}^{-1}$
b_q	Production rate of chemoattractant	$500\,\mathrm{s}^{-1}$
k_q	Production rate of chemoattractant	$10\,\mathrm{s}^{-1}$
D_a	Diffusion coefficient of activator	$0.2\,\mu\mathrm{m}^2\mathrm{s}^{-1}$
r_a	Decay rate of activator	$0.32\,\mathrm{s}^{-1}$
b_a	Production rate of activator	$7.8\,\mathrm{s}^{-1}$
$a_{\max}$	Saturation of activator	$1.5\,\mu\mathrm{m}^{-3}$
R_a	Radius of activator source	$2\,\mu\mathrm{m}$
d_o^a	Effective distance for pseudopod inhibition	$2.35\,\mu\mathrm{m}$

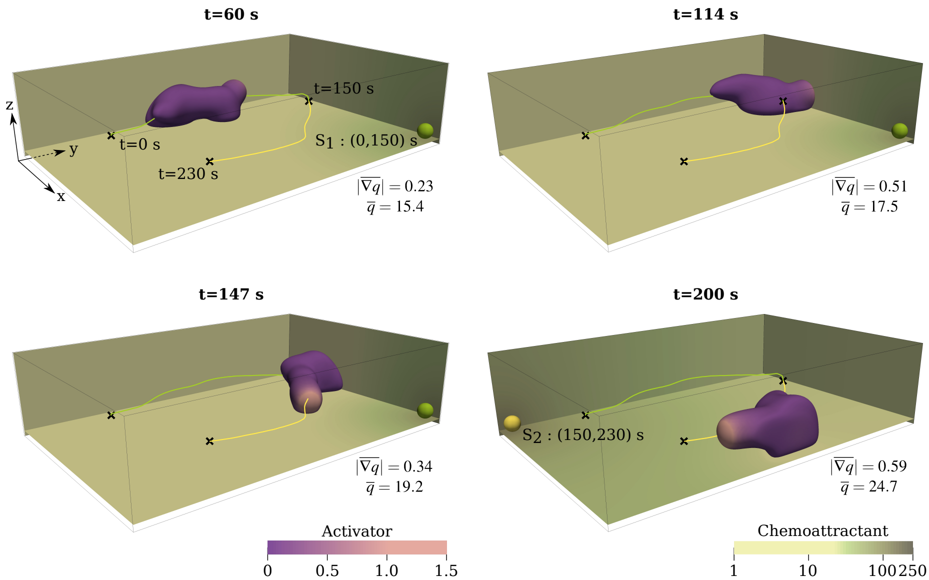

Figure 4.13. 3D migration on a planar substrate. Activator density on the cell's membrane. *Simulation performed on the box* $[0, L_x] \times [0, L_y] \times [0, L_z]$ *with* $L_x = 43.2$, $L_y = 64.8$, *and* $L_z = 15.6\,\mu\text{m}$. *The mesh is composed of* $144 \times 216 \times 52$ $\mathcal{C}^1$*-continuous quadratic elements. The initial time step is* $\Delta t = 0.1\,\text{s}$. *The initial cell geometry is a cylinder of radius* $R_c = 8\,\mu\text{m}$ *and height* $h_c = 7\,\mu\text{m}$ *centered at the point* $(12, 12, 4.5)\,\mu\text{m}$. *We set* $D_q = 400\,\mu\text{m}^2\text{s}^{-1}$, $q_{\text{max},1} = 150\,\text{nM}$, *and* $q_{\text{max},2} = 250\,\text{nM}$. *The activator concentration is plotted on the cell membrane and the chemoattractant distribution on the planes* $x = 0$, $y = L_y$, *and* $z = 1\,\mu\text{m}$, *at* $t = 60$, 114, 147, *and* 200 s. *We also show the chemoattractant sources* S_1 *(green sphere) and* S_2 *(yellow sphere). The cell's path is divided into two segments according to the active source (*S_1 *green line,* S_2 *yellow line). The two sections are delimited with crosses.*

acting on them. The punctual forces are predominantly horizontal, effectively contributing to the cell's motion. At times $t = 60\,\text{s}$ and $t = 147\,\text{s}$ the dipole of forces seen experimentally emerges naturally in the simulations, although the imbalance of forces seems to be greater than in experiments (Del Alamo *et al.*, 2007). In particular, the contractile pole exerts much smaller forces than the protrusive pole; see $t = 147\,\text{s}$. At some points ($t = 114\,\text{s}$ and $t = 200\,\text{s}$), the cell's tail even detaches from the substrate and there is no contractile pole. These observations indicate that future modeling efforts should be directed at improving our description of focal adhesions. We also believe that this example can be an important benchmark as the field of computational cell migration transitions from 2D to 3D simulations.

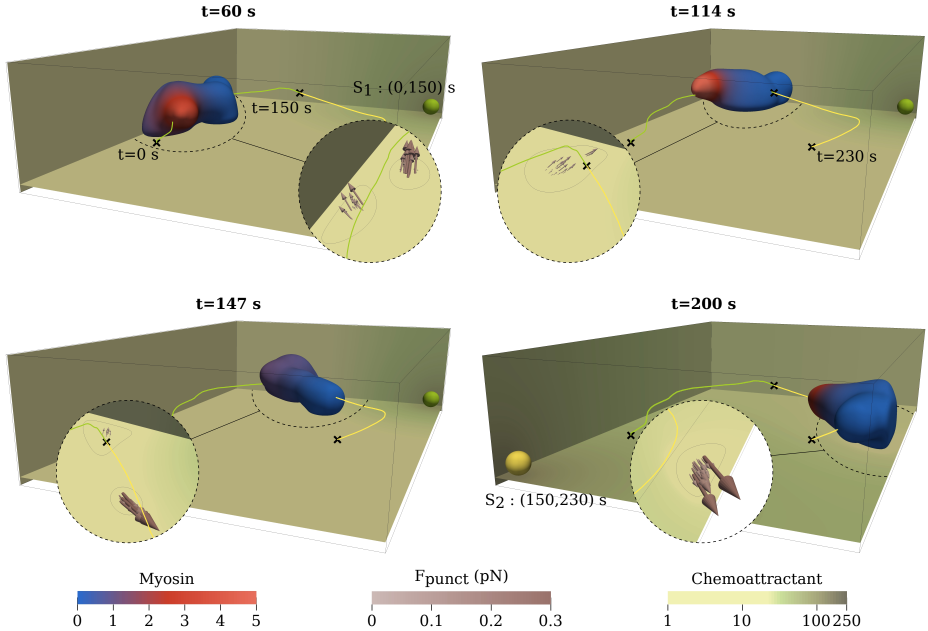

Figure 4.14. 3D migration on a planar substrate. *Myosin distribution on the cell membrane and chemoattractant concentration on the planes $x = 0$, $y = L_y$, and $z = 1\,\mu$m. The circular insets show the punctual adhesive forces $\mathbf{F}^j_{\text{punct}}$ (grey arrows) and the region of cell-substrate contact (black solid line).*

4.4.6 Three-dimensional migration in a fibrous environment

Our previous examples focus on cell motion on a planar substrate, but most cells actually migrate within the extracellular matrix interacting chemically and mechanically with a fibrous network. While migrating through the extracellular matrix, cells establish focal adhesions and remodel the fibers by deforming and degrading them. Our current model cannot handle all of these phenomena, but we aim at reproducing a much simpler scenario in which the fibers are rigid and the cell is unable to degrade them. In our simplified computation, the fibers are represented by cylindrical objects where the cells can establish focal adhesions. The layout of the fibers can be observed in figure 4.15, where the width of the fibers has been slightly reduced for a better visualization of the cell. The computation was performed on a cubic domain. The boundaries of the cube are assumed to be non-adherent walls, where the cell cannot establish focal adhesions. The cell's migration is driven by the chemotactic source $S_q = S_1 + S_2$, where the S_i's have

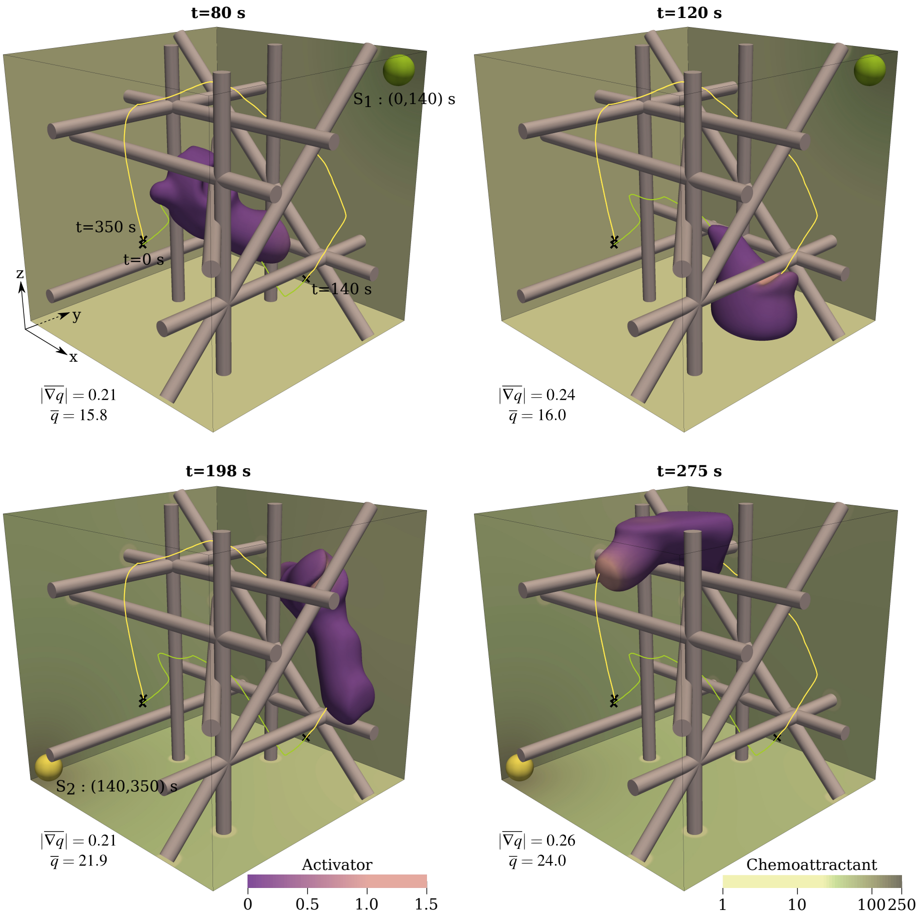

Figure 4.15. 3D migration in a fibrous environment. *The simulation is performed on the cube* $[0, L]^3$ *with* $L = 38.4\,\mu\text{m}$*. The mesh is comprised of 128* $\mathcal{C}^1$*-continuous quadratic elements in each direction. The initial time step is* $\Delta t = 0.1\,\text{s}$ *and the initial cell geometry is a sphere of radius* $R_c = 7\,\mu\text{m}$ *centered at the point* $(12, 12, 12)\,\mu\text{m}$*. We set* $D_q = 400\,\mu\text{m}^2\text{s}^{-1}$*,* $q_{\text{max},1} = 150\,\text{nM}$*, and* $q_{\text{max},2} = 250\,\text{nM}$*. The activator density is plotted on the cell membrane and the chemoattractant distribution on three walls of the domain, at* $t = 80$*, 120, 198, and 275 s. We also plot the chemotactic sources* S_1 *(green sphere) and* S_2 *(yellow sphere). The fibers width has been slightly reduced for visualization purposes. The cell's path is divided into two sections corresponding to the different active sources (green line for* S_1*, yellow line for* S_2*). The crosses on the cell's path mark the position of the cell's center of mass at* $t = 0$*, 140, and 350 s.*

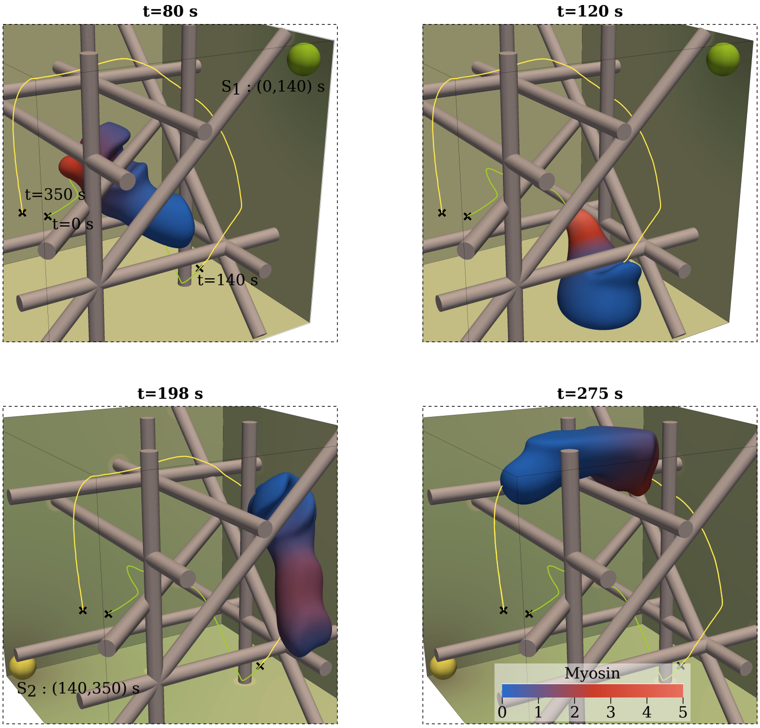

Figure 4.16. 3D migration in a fibrous environment. Myosin distribution. *The myosin distribution is plotted on the cell membrane and the chemoattractant concentration on three walls of the domain.*

the usual form. The sources are centered at $\mathbf{S}_1^c = (36, 36, 36)$ and $\mathbf{S}_2^c = (2, 2, 2)$ µm. The chemoattractant sources S_1 and S_2 are active in the time intervals $(0, 140)$ and $(140, 350)$ s, respectively. Figure 4.15 shows the activator distribution on the cell's membrane. The plot also displays the location of the active chemoattractant source with a small sphere. Three faces of the cube have been colored according to the chemoattractant concentration. Figure 4.16 follows the same format, but shows the myosin concentration on the cell's membrane using a reduced view from a different perspective. From the figures, we can see that the values of the signaling parameters ($|\overline{\nabla q}| \sim 0.2\,\mathrm{nM}/\mu\mathrm{m}$ and $\overline{q} \sim 20\,\mathrm{nM}$) fall within a range where significant chemotactic bias is expected. Thus, despite the presence of the fibers that impede a more straight migration, the cell gradually approaches the active chemoattractant source as illustrated by the path traveled by the cell's center of mass. Throughout the simulation, the cell touches the fibers and the boundary.

The cell-fiber interaction modifies the motion of the cell, as well as the cell shape (see, e.g., $t = 80\,\mathrm{s}$ where a fiber is surrounded by the cell's body). In addition, the interaction with fibers gives rise to punctual adhesions, which produce an increase of the cell-fiber adhesiveness (see, e.g., $t = 198\,\mathrm{s}$ where the tail of the cell remains attached to the fibers producing a noticeable deformation of the cell's body).

4.4.7 Model limitations

Signaling mechanisms of chemotaxis

We have simplified the reactions of the signaling compounds by considering a single activator. In our model, the activator dynamics is controlled by statistical data (see figure 4.5) that are biased according to extracellular signals. Thus, the activator displays a phenomenological behavior based on statistics taken from 2D experiments. Such data does not seem to be available in 3D. Therefore, we proposed an extension to 3D of the functions shown in figure 4.5a, but this remains to be validated.

Cellular chemotaxis features signal amplification and adaptation: Small variations ($\sim 2\%$) in the chemoattractant concentration over the cell's length produce chemotaxis due to the amplification of the external signal (Janetopoulos *et al.*, 2004). Although the exact mechanisms that control signal amplification are not understood, our model is able to replicate amplification through the signaling parameters, as shown in the simulations. However, as seen in subsection 4.4.2, the model is unable to reproduce adaptation, i.e., the change of the chemotactic response as a function of the time evolution of the chemoattractant concentration. Adaptation not only explains *Dictyostelium* aggregation, but also the cell's behavior after the exposure to a uniform chemoattractant concentration (Van Haastert and Devreotes, 2004): A moving cell exposed to a sudden increase in the chemoattractant concentration undergoes actin polymerization along the entire membrane for a short period of time ($\sim 6\,\mathrm{s}$). Due to the polymerization of the entire membrane, the cell stops its motion and remains still for some time. After that, even if the chemoattractant concentration remains constant, a gradual actin depolymerization takes place, permitting the cell to return to its original polarized and motile state. Adaptation could be incorporated to our model by considering a more accurate description of the dynamics of the membrane signaling compounds; see, e.g., Levchenko and Iglesias (2002) or Ribeiro *et al.* (2017).

Focal adhesions

The adhesion between the cell and the extracellular environment is a complex process carried out by a family of transmembrane proteins called integrins. Focal adhesion formation involves a series of steps (initiation, integrin clustering, growth, and maturation) highly regulated by actomyosin contractility and extra- and intra-cellular signals (Geiger *et al.*, 2009). In this chapter, we have simplified focal adhesions as gripping forces whose spring constants increase with time. In our model, focal adhesions disassemble following Bell's law. To improve the model, myosin contractility and F-actin network dynamics should be taken into account in the process of maturation and rupture. In addition, focal adhesions usually change the mechanism of force transmission between a gripping and a slipping mode (Jurado *et al.*, 2005); and we have only considered gripping forces in the model.

Finally, rigid fibers do not reproduce the features of the extracellular matrix where actual cells migrate. Taking into account the elasticity of the fibers, as well as considering extracellular matrix degradation, may lead to more realistic results.

4.5 Conclusions

We propose a phase-field model for chemotactic motion of amoeboid cells. The model, which attains cell motion by considering the forces acting on the actomyosin network, captures the reactions occurring along the signaling pathway. The underlying computational technology is the diffuse domain method, which permits to solve equations posed on deformable domains (i.e., the cytosol, the membrane, and the extracellular medium) by using a fixed mesh only. The results show quantitative agreement with experiments, though some experimentally-observed features of chemotactic motion are not observed due to the stochastic description used for pseudopod formation. In addition, including the cell-substrate (or cell-fiber) interaction leads to realistic 3D migration on substrates (or in fibrous networks). The results also suggest that coupling the extracellular, membrane, and cytosol dynamics is crucial to better understand chemotaxis, especially in case of migration in confined environments. The model may be improved by including a deterministic theory for the membrane signaling molecules reactions. Also, considering fiber elasticity and matrix degradation, along with the focal adhesions may provide new insights and extend the model to other directional migrations, such as haptotaxis or durotaxis.

Chapter 5

Summary, conclusions, and furture work

In this chapter we present a brief summary and the general conclusions of the thesis. We also propose a selection of lines for further research that continue the work developed in this thesis.

5.1 Summary

We develop a summary of the thesis according to the main objectives proposed in chapter 1:

Modeling We proposed three phase-field models that account for three different kinds of individual cell migration. A model for mesenchymal migration is proposed in chapter 2. In that model, we have considered the main cytosolic compounds involved in mesenchymal cell motion, i.e., the molecular motors (myosin) and the actin compounds (G-actin and F-actin). The dynamics of these compounds is governed by PDEs posed on a fixed domain. The actin behavior is controlled by a free-energy functional that accounts for the actin phase transformations. We assumed that the actomyosin network behaves as a viscous fluid governed by a Stokes-type equation augmented with forces caused by the cell motion machinery (e.g., the surface tension of the membrane, myosin contraction, cell-substrate adhesion, and actin-driven protrusion). We have also studied migration with obstacles, which may represent fibers or walls. The cell-obstacle interaction is modeled with a repulsive force acting on the cell's membrane. The movement of the cell is caused by the flow of the F-actin network. In chapter 3 we have extended the model to reproduce spontaneous amoeboid migration. The new model accounts for the coupling between the cytosolic and the membrane signaling molecules that trigger amoeboid motion. The reactions along the signaling pathway have been simplified by considering the dynamics of a single activator controlled by statistical data. In chapter 4 we presented an extension of the model proposed in chapter 3. The extended model accounts for the chemotactic migration of amoeboid cells. Besides the cytosolic and membrane compounds, we consider the presence of an extracellular chemoattractant capable of biasing the movement of the cell. In addition, we incorporate focal adhesions that are modeled as punctual forces acting in the F-actin network.

Developing numerical algorithms The use of the phase-field method permits to solve the equations posed on the different domains (i.e., the cytosol, the membrane, and the extracellular medium) by using a fixed mesh only. We developed a numerical implementation for the model proposed in chapter 2. The methodology developed for the models proposed in chapters 3 and 4 is analogous. The spatial discretization of the higher-order equations is based on IGA, which employs B-splines as basis functions. B-spline functions possess arbitrary degrees of inter-element continuity for any spatial dimension, which permits a direct derivation of the Galerkin form. The time integration algorithm is based on the generalized-α method. We proposed a time-stepping scheme that employs a fixed time step in most of the examples[1]. The resulting non-linear system is solved using the iterative Newton-Raphson method. All terms are treated implicitly, except those that require non-local computations, such as, for example, calculating integrals or distances. The condition number of the tangent matrix is very large, which leads to an inefficient algorithm. This is because most of the unknowns approach to zero in different regions of the domain. We proposed a simple procedure that produces equivalent residual vector and tangent matrix with acceptable condition number.

Application Throughout this thesis we have tested the phase-field framework in a number of examples. For instance, in subsections 2.4.1 and 4.4.4 we showed examples that prove the effectiveness of the phase-field method to model moving

[1] In chapter 4 we implemented a simple adaptive time stepping scheme, motivated by the presence of Dirichlet boundary conditions that slow down the convergence of the Newton–Raphson solver.

domains. In chapter 2 we have reproduced mesenchymal motion by means of two-dimensional simulations of keratocytes. These examples correspond to cells moving on flat surfaces and in microchannels. In chapters 3 and 4 we have devoted our efforts to simulate the migration of an amoeboid cell called *Dictyostelium*. We performed a detailed analysis of the chemotactic and non-chemotactic motion results, which shows good agreement with experiments. We showed two-dimensional results of cells moving on planar surfaces with and without obstacles, as well as migration in microchannels. These results allow to analyze the coupling between the cytosol, the membrane, and the extracellular compounds; and also the influence of the obstacles on the motion of the cells. We also showed three-dimensional examples of cells moving on planar substrates and fibrous networks. These examples may constitute a first approach toward the simulation of cellular migration in the ECM.

5.2 General conclusions

The conclusions that can be extracted from the work developed in the thesis are the following:

- From a mechanical point of view, the cell's membrane is modeled as a vesicle and the actin network as a viscous Newtonian fluid. The model proposes evolution equations in the form of PDEs for the myosin and actin compounds (posed on the cytosol), the membrane-bound species (posed on the membrane), and the chemoattractant (posed on the extracellular medium). The model also accounts for the interactions between the elements that live in the different domains. The movement of the cell's membrane is driven by the flow of the actin network underneath the membrane.

- The Stokes-type equation that governs the actin-network dynamics includes the forces produced during cellular motion. This formulation allows to account for contractile and protrusive stresses, punctual adhesive forces, and forces caused by external obstacles. The formulation also allows to extend the model by considering the stiffness or adhesiveness of the substrate, or the elasticity and degradation of the fibers. Those extensions may be directly coupled to the cell's dynamics through forces acting in the actin network.

- The computational challenges associated to the solution of equations on moving and deformable domains are addressed utilizing the phase-field method. We can solve the equations posed on the cytosol, the membrane, and the extracellular medium by using a fixed mesh only.

- The phase-field method is also employed to derive the evolution equations for the actin compounds. We propose an energy functional that accounts for the actin phase transformations occurring within the cell, which depend on the signaling molecules activated along the signaling cascade. According to the examples shown throughout this thesis, the proposed model effectively reproduces the actin behavior observed in experiments, with the exception of some experimentally-observed features of confined migration in microchannels.

- The reactions occurring along the signaling pathway are simplified by resorting to a single membrane-bound protein. The dynamics of this membrane signaling compound, which is coupled to other cytosolic and extracellular signaling elements, is controlled by a stochastic process that reproduces pseudopod formation. The model may be improved by including a deterministic theory for the membrane signaling molecules reactions.

- We developed a numerical method based on the concept of isogeometric analysis. The method has proven to be efficient, accurate, and robust. The numerical method allowed us to investigate the models presented in the thesis in a number of biologically relevant simulations. In particular, the method provided us a way to study individual cell migration in three-dimensional environments, which has been overlooked in most of the models found in the literature. To our knowledge, this is the first work that has developed a numerical method based on IGA for problems of cell motility. We have also developed the subsequent code to implement the numerical formulation and perform the simulations.

- The simulations of mesenchymal motion show that the simpler case of keratocyte's migration on flat substrates produces stationary states of motion, which are in good agreement with experiments. Moreover, by considering the presence of obstacles, we are able to reproduce complex modes of motion observed in microchannels, such as, e.g., oscillatory and bipedal motion.

- The model results of spontaneous amoeboid motion show quantitative agreement with experiments of free and confined migration. The results corresponding to chemotactic migration also show quantitative agreement with experiments, though some experimentally-observed features of chemotactic motion are not observed due to the stochastic description used for pseudopod formation.

- The results attained for amoeboid migration in microchannels and maze-like environments also suggest that coupling the extracellular, membrane, and cytosol dynamics is crucial to better understand chemotaxis and amoeboid motion, especially in case of migration in confined environments. Models that overlook the bidirectional feedback (cytosol-membrane and membrane-extracellular medium) may be unable to capture some particular features of motile cells. In that sense, our results of confined migration suggest that cells may exploit the geometry of their microenvironment to find effective migration strategies.

- We have performed three-dimensional simulations that correspond to cells moving on a planar substrate and within a fibrous network of obstacles. The incorporation of cell-substrate (or cell-fiber) interaction leads to realistic three-dimensional migration on substrates (or in fibrous networks). The example corresponding to migration on a planar substrate represents the classic two-dimensional approach of cell migration, though performed in a three-dimensional domain. This example can be an important benchmark as the field of computational cell migration transitions from two- to three-dimensional simulations. In addition, the examples of cells moving in a fibrous network may be thought of as a first approach to model cell migration in the ECM.

5.3 Ongoing and further work

Throughout this thesis we have mentioned possible extensions of the model and future lines of work. In the following paragraphs we summarize the main lines of research opened by the work presented in this thesis.

Introduce ECM dynamics In the thesis we have treated the ECM as a network composed of rigid fibers. As shown in subsection 1.2.2, the ECM is a complex substance that displays viscoelastic properties and possesses, among other compounds, fibrous proteins. In addition, cells are able to degrade and reorganize the ECM. This behavior should be coupled to our model in a robust and consistent way. A possible approach could be to include an elastic or viscoelastic model for the fibers. Another possibility could be the use of an immersed boundary method to model the cell-ECM interaction.

Haptotaxis and durotaxis Haptotaxis is the movement of cells directed by a gradient of cellular adhesion sites. In the case of durotaxis, cell migration depends on the rigidity of the substrate. In this thesis, we have considered substrates (or fibers) of infinite stiffness and uniform density of adhesion sites. To simulate both types of motion, a detailed description of the dynamics of the focal adhesions is required; see subsection 4.4.7. A detailed model of the punctual adhesions and the incorporation of the density of adhesions sites could lead to reproduce haptotaxis. In case of durotaxis, besides the model for focal adhesions, we should include the elasticity of the substrate (or fibers).

Blebbing motion Blebbing migration is a type of amoeboid motion where the membrane extensions (called blebs) are not caused by the polymerization of F-actin. A disruption in the cortex-membrane connection may be the origin of a bleb; see figure 5.1. When the hydrostatic pressure in the cytoplasm increases, the membrane detaches from the cortex in the aforementioned location and the cytoplasmic fluid produces a sudden extension of the membrane, as shown in figure 5.1. In blebbing motion, the cytoplasmic fluid, not the F-actin network, drives cell migration. As well, the intracellular pressure and the membrane-actin connection play a crucial role. The model presented in this thesis needs to be adapted to blebbing migration, although the phase-field methodology, the derivation of the membrane forces, the presence of membrane-bound proteins, and the assumption of a Newtonian fluid that deforms the membrane still apply.

3D mesenchymal motion on planar substrates In the thesis, we have shown examples of three-dimensional migration corresponding to amoeboid motion. However, it would be interesting to simulate three-dimensional migration of keratocytes, i.e., mesenchymal migration, on planar substrates. This kind of migration is usually modeled using a two-dimensional approach because the lamellipodium, the F-actin structure that drives the motion, forms a two-dimensional sheet parallel to the substrate; see, e.g., figure 2.1. The model proposed in chapter 2 is unable to reproduce the lamellipodium dynamics in three-dimensional simulations. We believe that minor changes in the actin free-energy functional,

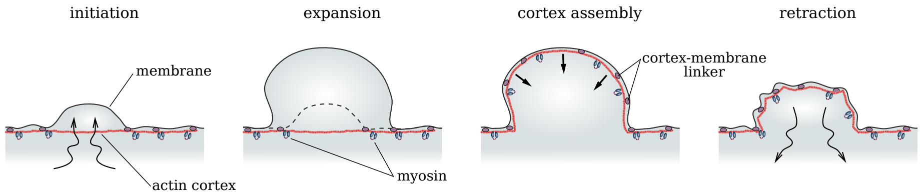

Figure 5.1. Bleb formation. *The bleb life cycle is subdivided into three phases. Initiation: local detachment of the cortex from the membrane (or local rupture of the cortex, not shown). Expansion* (5 *to* 30 s)*: hydrostatic pressure in the cytoplasm drives the membrane expansion. A new actin cortex reforms under the bleb membrane. Retraction* (60 *to* 120 s)*: caused by myosin recruitment. (Adapted from Charras and Paluch, 2008)*

the description of the forces, and the dynamics of the focal adhesions could lead to simulate keratocyte migration in 3D.

Signaling molecules dynamics on a deformable cell The phase-field framework proposed in this thesis can be used to solve other models of individual cell motility on three-dimensional deformable geometries. In particular, we refer to models that account for the signaling events that occur in the vicinity of the membrane. Frequently, those models have been solved in one- and two-dimensional fixed geometries. Also, it would be interesting to couple those signaling compounds with the chemoattractant and the cytosolic compounds considered in our model. This could lead to more realistic three-dimensional simulations because the stochastic description used for the membrane activator would be replaced with a deterministic theory.

Appendices

Appendix A

List of publications

The development of this thesis has produced several peer-reviewed publications in international journals and contributions in international conferences. In the following, we list the publications and contributions, and also mention the collaborations done in other works.

A.1 Articles in peer-reviewed international journals

The following journal articles are directly related to this thesis:

- Moure, A. and Gomez, H. 2017. Phase-field model of cellular migration: Three-dimensional simulations in fibrous networks. *Computer Methods in Applied Mechanics and Engineering,* vol. 320, pp. 162–197. Associated with chapters 2 and 3.
- Moure, A. and Gomez, H. 2016. Computational model for amoeboid motion: Coupling membrane and cytosol dynamics. *Physical Review E,* vol. 94(4), p. 042423. Associated with chapter 3.
- Moure, A. and Gomez, H. Three-dimensional simulation of obstacle-mediated chemotaxis. *Biomechanics and modeling in mechonobiology,* submitted. Associated with chapter 4.

A.2 Contributions in international conferences

The work of this thesis was presented in the following international conferences:

- 5th International Conference on Computational and Mathematical Biomedical Engineering. Computational modeling of amoeboid motion: *Dictyostelium* in chemotactic environments. Pittsburgh, Pensilvania (USA), April 10-12, 2017.
- Mechanobiology across Networks. Computational modeling of amoeboid motion: Chemotaxis and free movement in different environments. Barcelona (Spain), October 6-7, 2016.
- 12th World Congress on Computational Mechanics (WCCM XII). Computational modeling of amoeboid motion: Chemotaxis and free movement in different environments. Seoul (Republic of Korea), July 24-29, 2016.
- 21th Congress of the European Society of Biomechanics. Computational modeling of cellular motility: Chemotaxis and movement in confined environments. Prague (Czech Republic), July 5-8, 2015.
- Kick-off Meeting – Spanish Network of Excellence in Mechanobiology. An overview of our work on modeling and simulation on cancer growth. Barcelona (Spain), February 24-25, 2015.

A.3 Collaborations in other works

During the last year of this thesis, the author has participated in another research project related to cancer growth. In particular, we apply the phase-field method to the proliferation-invasion-hypoxia-necrosis-angiogenesis model (Swanson *et al.*, 2011), which accounts for the growth of gliomas (a type of malignant brain tumor). The phase-field method allows for an implicit definition of the brain geometry, which avoids the use of complex meshes. Up to now, this work has resulted in the contribution:

- Dominguez-Frojan, P., Moure, A., and Gomez, H. 2017. Patient-specific computational modeling of glioma growth. In *Congress on Numerical Methods in Engineering CMN2017*, vol. 3, p. 5.

Appendix B

Alternative methodology to avoid singularities in the linear systems

We have developed an alternative methodology that avoids the presence of singularities in the residual vector and the tangent matrix and provides well-conditioned tangent matrices. The procedure presented here is applied to the model of chapter 4, and is completely analogous for the models of chapters 2 and 3.

Original strong form

We consider a fixed set $\Omega \subset \mathbb{R}^{d_s}$ that represents our computational domain. The boundary of Ω is Γ. The strong form of the problem can be stated as: Given a time interval of interest $[0,T]$ and suitable initial conditions, find $\phi : \overline{\Omega} \times (0,T) \to \mathbb{R}$, $\rho_m : \overline{\Omega} \times (0,T) \to \mathbb{R}$, $\rho_f : \overline{\Omega} \times (0,T) \to \mathbb{R}$, $\mathbf{u} : \overline{\Omega} \times (0,T) \to \mathbb{R}^{d_s}$, $q : \overline{\Omega} \times (0,T) \to \mathbb{R}$, and $a : \overline{\Omega} \times (0,T) \to \mathbb{R}$ such that

$$\frac{\partial \phi}{\partial t} + \mathbf{u} \cdot \nabla \phi = \Gamma_\phi \left(\varepsilon \nabla^2 \phi - \frac{G'(\phi)}{\varepsilon} + c\varepsilon |\nabla \phi| \right) \quad \text{in} \quad \Omega \times (0,T), \tag{B.1}$$

$$\frac{\partial (\phi \rho_m)}{\partial t} + \nabla \cdot (\phi \rho_m \mathbf{u}) = \nabla \cdot [D_m(\rho_f) \phi \nabla \rho_m] \quad \text{in} \quad \Omega \times (0,T), \tag{B.2}$$

$$\begin{aligned} \frac{\partial (\phi \rho_f)}{\partial t} + \nabla \cdot (\phi \rho_f \mathbf{u}) = \\ = \Gamma_f \left[\varepsilon_f^2 \nabla \cdot (\phi \nabla \rho_f) - \phi \frac{\partial \overline{F}}{\partial \rho_f} + \lambda_N \phi \right] \quad \text{in} \quad \Omega \times (0,T), \end{aligned} \tag{B.3}$$

B · Alternative methodology to avoid singularities in the linear systems

$$\nabla \cdot (\boldsymbol{\sigma} + \boldsymbol{\sigma}_{\mathrm{myo}} + \boldsymbol{\sigma}_{\mathrm{prot}}) + \mathbf{F}_{\mathrm{adh}} + \mathbf{F}_{\mathrm{mem}} + \mathbf{F}_{\mathrm{rep}} = 0 \quad \text{in} \quad \Omega \times (0,T), \tag{B.4}$$

$$\frac{\partial(\psi q)}{\partial t} = \nabla \cdot (D_q \psi \nabla q) - r_q \psi q + b_q \psi S_q - k_q \delta_m q \quad \text{in} \quad \Omega \times (0,T), \tag{B.5}$$

$$\begin{aligned}\frac{\partial(\delta_m a)}{\partial t} &+ \nabla \cdot (\delta_m a \mathbf{u}) = \\ &= \nabla \cdot (D_a \delta_m \nabla a) - r_a \delta_m a + b_a \delta_m S_a \quad \text{in} \quad \Omega \times (0,T).\end{aligned} \tag{B.6}$$

We assume that the unknowns ϕ, ρ_m, ρ_f, and a vanish on the boundary Γ. We also assume stress-free and flux-free conditions on Γ. Mathematically, these can be expressed as $(\boldsymbol{\sigma} + \boldsymbol{\sigma}_{\mathrm{myo}} + \boldsymbol{\sigma}_{\mathrm{prot}})\,\mathbf{n}_\Gamma = 0$ and $\nabla q \cdot \mathbf{n}_\Gamma = 0$, respectively. Here, $\mathbf{n}_\Gamma$ is the unit outward normal vector on Γ.

Change of variables

We define the new unknowns:

$$\hat{\rho}_m = \phi \rho_m, \tag{B.7}$$

$$\hat{\rho}_f = \phi \rho_f, \tag{B.8}$$

$$\hat{q} = \psi q, \tag{B.9}$$

$$\hat{a} = \delta_m a. \tag{B.10}$$

We replace ρ_m, ρ_f, q, and a in equations (B.1) to (B.6) with the variables defined in equations (B.7) to (B.10). The new strong form of the problem can be stated as: Given a time interval of interest $[0,T]$ and suitable initial conditions, find $\phi : \overline{\Omega} \times (0,T) \to \mathbb{R}$, $\hat{\rho}_m : \overline{\Omega} \times (0,T) \to \mathbb{R}$, $\hat{\rho}_f : \overline{\Omega} \times (0,T) \to \mathbb{R}$, $\mathbf{u} : \overline{\Omega} \times (0,T) \to \mathbb{R}^{d_s}$, $\hat{q} : \overline{\Omega} \times (0,T) \to \mathbb{R}$, and $\hat{a} : \overline{\Omega} \times (0,T) \to \mathbb{R}$ such that

$$\frac{\partial \phi}{\partial t} + \mathbf{u} \cdot \nabla \phi = \Gamma_\phi \left[\varepsilon \nabla^2 \phi - \frac{G'(\phi)}{\varepsilon} - \nabla \cdot \left(\frac{\nabla \phi}{|\nabla \phi|} \right) \varepsilon |\nabla \phi| \right] \quad \text{in } \Omega \times (0,T), \tag{B.11}$$

$$\frac{\partial \hat{\rho}_m}{\partial t} + \nabla \cdot (\hat{\rho}_m \mathbf{u}) = \nabla \cdot \left(\hat{D}_m \nabla \hat{\rho}_m \right) - \nabla \cdot \left(\hat{D}_m \frac{\hat{\rho}_m}{\phi} \nabla \phi \right) \quad \text{in } \Omega \times (0,T), \tag{B.12}$$

$$\begin{aligned}\frac{\partial \hat{\rho}_f}{\partial t} &+ \nabla \cdot (\hat{\rho}_f \mathbf{u}) = \\ &= \Gamma_f \left[\varepsilon_f^2 \nabla \cdot (\nabla \hat{\rho}_f) - \varepsilon_f^2 \nabla \cdot \left(\frac{\hat{\rho}_f}{\phi} \nabla \phi \right) - \phi \frac{\partial \widehat{\overline{F}}}{\partial \rho_f} + \lambda_N \phi \right] \quad \text{in } \Omega \times (0,T),\end{aligned} \tag{B.13}$$

$$\nabla \cdot (\boldsymbol{\sigma} + \hat{\boldsymbol{\sigma}}_{\mathrm{myo}} + \hat{\boldsymbol{\sigma}}_{\mathrm{prot}}) + \mathbf{F}_{\mathrm{adh}} + \mathbf{F}_{\mathrm{mem}} + \mathbf{F}_{\mathrm{rep}} = 0 \quad \text{in } \Omega \times (0,T), \tag{B.14}$$

$$\frac{\partial \hat{q}}{\partial t} = \nabla \cdot (D_q \nabla \hat{q}) - \nabla \cdot \left(D_q \frac{\hat{q}}{\psi} \nabla \psi \right)$$

$$-r_q\hat{q} + b_q\hat{S}_q - k_q\delta_m\frac{\hat{q}}{\psi} \quad \text{in } \Omega\times(0,T), \tag{B.15}$$

$$\frac{\partial\hat{a}}{\partial t} + \nabla\cdot(\hat{a}\mathbf{u}) =$$
$$= \nabla\cdot(D_a\nabla\hat{a}) - \nabla\cdot\left(D_a\frac{\hat{a}}{\delta_m}\nabla\delta_m\right) - r_a\hat{a} + b_a\hat{S}_a \quad \text{in } \Omega\times(0,T). \tag{B.16}$$

Note that we have used the identity $c = -\nabla\cdot(\nabla\phi/|\nabla\phi|)$ in equation (B.11) and we have introduced the following notation:

$$\hat{D}_m = \frac{\phi^2 D_m^{\max}}{\phi^2 + K_m^2\hat{\rho}_f^2}, \tag{B.17}$$

$$\widehat{\frac{\partial F}{\partial\rho_f}} = \frac{40}{\phi^3}\left(\hat{\rho}_f - \phi\rho_f^{\mathrm{pr}}\right)\left(\hat{\rho}_f - \phi\rho_f^{\mathrm{pa}}\right)\left(\hat{\rho}_f - \phi\frac{\rho_f^{\mathrm{pa}}+\rho_f^{\mathrm{pr}}}{2}\right) + \frac{3\hat{I}}{\phi^2}\left(\hat{\rho}_f - \phi\rho_f^{\mathrm{pr}}\right)\left[\hat{\rho}_f - \tfrac{1}{3}\phi\rho_f^{\mathrm{pr}} - \tfrac{2}{3}\phi\hat{\kappa}\hat{I}\right], \tag{B.18}$$

$$\hat{I} = \frac{\hat{a}}{3\delta_m}, \tag{B.19}$$

$$\hat{\kappa} = -2 + 2.6\frac{\hat{a}}{\delta_m}, \tag{B.20}$$

$$\hat{\boldsymbol{\sigma}}_{\mathrm{prot}} = -\hat{\rho}_f\hat{\eta}_f\delta_f\nabla\phi\otimes\nabla\phi, \tag{B.21}$$

$$\hat{\eta}_f = \overline{\alpha}_f\overline{\eta}_f + (1-\overline{\alpha}_f)\overline{\eta}_f\mathcal{H}\left(\frac{\hat{\rho}_f}{\phi} - \overline{\rho}_f\right), \tag{B.22}$$

$$\hat{\boldsymbol{\sigma}}_{\mathrm{myo}} = \hat{\rho}_m\hat{\eta}_m\boldsymbol{I}, \tag{B.23}$$

$$\hat{\eta}_m = \overline{\alpha}_m\overline{\eta}_m + (1-\overline{\alpha}_m)\overline{\eta}_m\mathcal{H}\left(\frac{\hat{\rho}_m}{\phi} - \overline{\rho}_m\right), \tag{B.24}$$

$$\hat{S}_q = \sum_i\hat{S}_i = \sum_i\left(\psi q_{\max,i} - \hat{q}\right)\delta_{\mathbf{x},i}^q\delta_{t,i}^q, \tag{B.25}$$

$$\hat{S}_a = (\delta_m a_{\max} - \hat{a})\sum_i\delta_{\mathbf{x},i}^a\delta_{t,i}^a. \tag{B.26}$$

We assume that the unknowns ϕ, $\hat{\rho}_m$, $\hat{\rho}_f$, and $\hat{a}$ vanish on the boundary Γ. We employ stress-free and flux-free conditions on Γ, i.e., $(\boldsymbol{\sigma} + \hat{\boldsymbol{\sigma}}_{\mathrm{myo}} + \hat{\boldsymbol{\sigma}}_{\mathrm{prot}})\,\mathbf{n}_\Gamma = 0$ and $\nabla\hat{q}\cdot\mathbf{n}_\Gamma = 0$, respectively. Equations (B.11) to (B.16) include terms that are ill-defined in different regions of the domain (e.g., outside the cell, where $\phi\approx 0$). To solve this issue, we divide the domain Ω in different subdomains where we will reformulate the equations.

B · Alternative methodology to avoid singularities in the linear systems

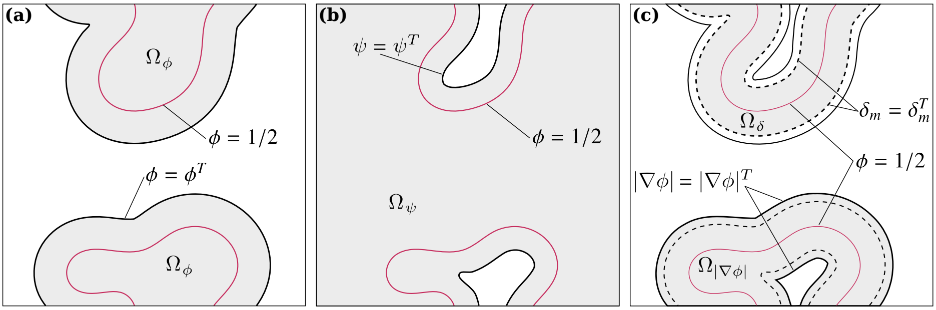

Figure B.1. Different subdomains defined in the alternative procedure to avoid singularities. *(a) Ω_ϕ. (b) Ω_ψ. (c) Ω_δ and $\Omega_{|\nabla\phi|}$.*

Definition of the subdomains

We use the thresholds ϕ^T, ψ^T, $|\nabla\phi|^T$, and δ_m^T to define the regions (see figure B.1):

- $\Omega_\phi = \{\mathbf{x} \mid \phi > \phi^T\}$,
- $\Omega_\psi = \{\mathbf{x} \mid \psi > \psi^T\}$,
- $\Omega_\delta = \{\mathbf{x} \mid \delta_m > \delta_m^T\}$,
- $\Omega_{|\nabla\phi|} = \{\mathbf{x} \mid |\nabla\phi| > |\nabla\phi|^T\}$.

In our computations, we used the values $\phi^T = \psi^T = |\nabla\phi|^T = 10^{-8}$ and $\delta_m^T = 10^{-4}$. Note that we can choose the values $|\nabla\phi|^T$ and δ_m^T such that $\Omega_{|\nabla\phi|} = \Omega_\delta$; see figure B.1c. For the sake of simplicity, from here on we assume that $\Omega_{|\nabla\phi|} = \Omega_\delta$.

Update of the strong form

Equations (B.11) to (B.16) are reformulated and posed in different subdomains to avoid the singularities. The idea is to locate the original equation in the region of interest. In that region, all the terms of the equation are well-defined. In the rest of the domain, we reformulate the equation such that we disregard the terms that are not well-defined. The modified equation does not affect the solution in the region of interest. In addition, the solution of the modified equation is equivalent to the original equation, as we show below.

- Equation (B.11) is expressed as

$$\frac{\partial \phi}{\partial t} + \mathbf{u} \cdot \nabla \phi = \Gamma_\phi \left[\varepsilon \nabla^2 \phi - \frac{G'(\phi)}{\varepsilon} - \nabla \cdot \left(\frac{\nabla \phi}{|\nabla \phi|} \right) \varepsilon |\nabla \phi| \right] \quad \text{in } \Omega_\delta, \tag{B.27}$$

$$\frac{\partial \phi}{\partial t} + \mathbf{u} \cdot \nabla \phi = \Gamma_\phi \left(\varepsilon \nabla^2 \phi - \frac{G'(\phi)}{\varepsilon} \right) \quad \text{in } \Omega/\Omega_\delta. \tag{B.28}$$

  Equation (B.28) is the Allen–Cahn equation, which keeps stable the values $\phi = 0$ and $\phi = 1$, producing the desired solution in Ω/Ω_δ (away from the membrane).

- Equation (B.12) is written as

$$\frac{\partial \hat{\rho}_m}{\partial t} + \nabla \cdot (\hat{\rho}_m \mathbf{u}) = \nabla \cdot \left(\hat{D}_m \nabla \hat{\rho}_m \right) - \nabla \cdot \left(\hat{D}_m \frac{\hat{\rho}_m}{\phi} \nabla \phi \right) \quad \text{in } \Omega_\phi, \tag{B.29}$$

$$\frac{\partial \hat{\rho}_m}{\partial t} + \nabla \cdot (\hat{\rho}_m \mathbf{u}) = 0 \quad \text{in } \Omega/\Omega_\phi. \tag{B.30}$$

  From equation (B.30), we have $\partial \hat{\rho}_m / \partial t \approx 0$ outside the cell (we show bellow that $\mathbf{u} \approx 0$ outside the cell).

- Equation (B.13) is redefined in three subdomains because the term $\widehat{\partial \overline{F}} / \partial \rho_f$ can produce singularities inside the cell and away from the membrane:

$$\frac{\partial \hat{\rho}_f}{\partial t} + \nabla \cdot (\hat{\rho}_f \mathbf{u}) =$$
$$\Gamma_f \left[\varepsilon_f^2 \nabla \cdot (\nabla \hat{\rho}_f) - \varepsilon_f^2 \nabla \cdot \left(\frac{\hat{\rho}_f}{\phi} \nabla \phi \right) - \phi \frac{\widehat{\partial \overline{F}}}{\partial \rho_f} + \lambda_N \phi \right] \quad \text{in } \Omega_\delta, \tag{B.31}$$

$$\frac{\partial \hat{\rho}_f}{\partial t} + \nabla \cdot (\hat{\rho}_f \mathbf{u}) = \Gamma_f \left[\varepsilon_f^2 \nabla \cdot (\nabla \hat{\rho}_f) - \varepsilon_f^2 \nabla \cdot \left(\frac{\hat{\rho}_f}{\phi} \nabla \phi \right) + \lambda_N \phi \right] \text{ in } \Omega_\phi/\Omega_\delta, \tag{B.32}$$

$$\frac{\partial \hat{\rho}_f}{\partial t} + \nabla \cdot (\hat{\rho}_f \mathbf{u}) = \Gamma_f \lambda_N \phi \quad \text{in } (\Omega/\Omega_\phi) \cap (\Omega/\Omega_\delta). \tag{B.33}$$

  The union of the three subdomains considered in equations (B.31) to (B.33) is Ω and their intersections are the empty set. Outside the cell, the evolution equation of $\hat{\rho}_f$ becomes $\partial \hat{\rho}_f / \partial t \approx 0$; see equation (B.33).

- Equation (B.14) is written as

$$\nabla \cdot (\boldsymbol{\sigma} + \hat{\boldsymbol{\sigma}}_{\text{myo}} + \hat{\boldsymbol{\sigma}}_{\text{prot}}) + \mathbf{F}_{\text{adh}} + \mathbf{F}_{\text{mem}} + \mathbf{F}_{\text{rep}} = 0 \quad \text{in } \Omega_\phi, \tag{B.34}$$

$$\nabla \cdot \boldsymbol{\sigma} + \mathbf{F}_{\text{adh}} + \mathbf{F}_{\text{mem}} + \mathbf{F}_{\text{rep}} = 0 \quad \text{in } \Omega/\Omega_\phi. \tag{B.35}$$

  Outside the cell, we have $\phi \approx 0$ and $|\nabla \phi| \approx 0$. Therefore, we get $-\varsigma \mathbf{u} \approx 0$.

- Equation (B.15) is reformulated as

$$\frac{\partial \hat{q}}{\partial t} = \nabla \cdot (D_q \nabla \hat{q}) - \nabla \cdot \left(D_q \frac{\hat{q}}{\psi} \nabla \psi \right) - r_q \hat{q} + b_q \hat{S}_q - k_q \delta_m \frac{\hat{q}}{\psi} \quad \text{in } \Omega_\psi, \tag{B.36}$$

$$\frac{\partial \hat{q}}{\partial t} = -r_q \hat{q} + b_q \hat{S}_q \quad \text{in } \Omega / \Omega_\psi. \tag{B.37}$$

  Outside the extracellular medium, equation (B.37) drives q to zero.

- Finally, equation (B.16) is expressed as

$$\frac{\partial \hat{a}}{\partial t} + \nabla \cdot (\hat{a}\mathbf{u}) = \nabla \cdot (D_a \nabla \hat{a}) - \nabla \cdot \left(D_a \frac{\hat{a}}{\delta_m} \nabla \delta_m \right) - r_a \hat{a} + b_a \hat{S}_a \quad \text{in } \Omega_\delta, \tag{B.38}$$

$$\frac{\partial \hat{a}}{\partial t} + \nabla \cdot (\hat{a}\mathbf{u}) = -r_a \hat{a} + b_a \hat{S}_a \quad \text{in } \Omega / \Omega_\delta. \tag{B.39}$$

  Equation (B.39) drives a to zero outside the membrane. According to the definition of δ_m [see equation (3.2)], the term $\frac{\nabla \delta_m}{\delta_m}$ in equation (B.16) takes the value $-2\varphi(\phi - 1/2)$, which does not produce singularities. Thus, the reformulation of equation (B.16) is not necessary. However, we have included equations (B.38) and (B.39) in case the membrane marker δ_m is defined differently.

At this point, we replace equations (B.11) to (B.16) of the strong form with equations (B.27) to (B.39). The updated system of equations is equivalent to the original problem.

Weak form

Using the same notation as in section 4.3, the problem can be stated as: Find $\mathbf{U} = \{\phi, \hat{\rho}_m, \hat{\rho}_f, \mathbf{u}, \hat{q}, \hat{a}\} \in \mathcal{S}^{n_{\text{dof}}}$ such that for all $\mathbf{W} = \{l, p, r, \mathbf{w}, s, v\} \in \mathcal{V}^{n_{\text{dof}}}$

$$\mathcal{B}(\mathbf{W}, \mathbf{U}) = 0 \tag{B.40}$$

with

$$\begin{aligned}\mathcal{B}(\mathbf{W}, \mathbf{U}) = &\left(l, \frac{\partial \phi}{\partial t} \right)_\Omega + \left(p, \frac{\partial \hat{\rho}_m}{\partial t} \right)_\Omega + \left(r, \frac{\partial \hat{\rho}_f}{\partial t} \right)_\Omega + \left(s, \frac{\partial \hat{q}}{\partial t} \right)_\Omega + \left(v, \frac{\partial \hat{a}}{\partial t} \right)_\Omega \\ &+ \left(l, \mathbf{u} \cdot \nabla \phi \right)_\Omega + \left(\nabla l, \Gamma_\phi \varepsilon \nabla \phi \right)_\Omega + \left(l, \Gamma_\phi \frac{G'}{\varepsilon} \right)_\Omega - \left(\nabla l, \Gamma_\phi \varepsilon \nabla \phi \right)_{\Omega_\delta}\end{aligned}$$

$$
\begin{aligned}
&-\left(l, \frac{\Gamma_\phi \varepsilon}{|\nabla \phi|} \nabla \phi \cdot \nabla\left(|\nabla \phi|\right)\right)_{\Omega_\delta} - \left(\nabla p, \hat{\rho}_m \mathbf{u}\right)_{\Omega} + \left(\nabla p, \hat{D}_m \nabla \hat{\rho}_m\right)_{\Omega_\phi} \\
&-\left(\nabla p, \hat{D}_m \frac{\hat{\rho}_m}{\phi} \nabla \phi\right)_{\Omega_\phi} - \left(\nabla r, \hat{\rho}_f \mathbf{u}\right)_{\Omega} + \left(\nabla r, \Gamma_f \varepsilon_f^2 \nabla \hat{\rho}_f\right)_{\Omega_\phi} \\
&-\left(\nabla r, \Gamma_f \varepsilon_f^2 \frac{\hat{\rho}_f}{\phi} \nabla \phi\right)_{\Omega_\phi} + \left(r, \Gamma_f \phi \widehat{\frac{\partial \overline{F}}{\partial \rho_f}}\right)_{\Omega_\delta} - \left(r, \Gamma_f \lambda_N \phi\right)_{\Omega} \\
&-\left(\nabla \mathbf{w}, \phi\left[\mu\left(\nabla \mathbf{u} + \nabla \mathbf{u}^T\right) + \lambda\left(\nabla \cdot \mathbf{u}\right) \boldsymbol{I}\right]\right)_{\Omega} - \left(\nabla \mathbf{w}, \hat{\rho}_m \hat{\eta}_m \boldsymbol{I}\right)_{\Omega_\phi} \\
&+\left(\nabla \mathbf{w}, \hat{\rho}_f \hat{\eta}_f \delta_f \nabla \phi \otimes \nabla \phi\right)_{\Omega_\phi} - \left(\mathbf{w}, \varsigma \mathbf{u}\right)_{\Omega} + \sum_j \mathbf{w}(\mathbf{x}^j) \cdot \mathbf{F}^j_{\text{punct}} \\
&-\left(\mathbf{w}, \gamma\left(\varepsilon \nabla^2 \phi - \frac{G'}{\varepsilon}\right) \nabla \phi\right)_{\Omega} - \left(\nabla \mathbf{w}, \phi \eta_{\text{rep}} \delta_{\text{rep}} \nabla \phi \otimes \nabla \phi\right)_{\Omega} \\
&+\left(\nabla s, D_q \nabla \hat{q}\right)_{\Omega_\psi} - \left(\nabla s, D_q \frac{\hat{q}}{\psi} \nabla \psi\right)_{\Omega_\psi} + \left(s, r_q \hat{q}\right)_{\Omega} - \left(s, b_q \hat{S}_q\right)_{\Omega} \\
&+\left(s, k_q \delta_m \frac{\hat{q}}{\psi}\right)_{\Omega_\psi} - \left(\nabla v, \hat{a} \mathbf{u}\right)_{\Omega} + \left(\nabla v, D_a \nabla \hat{a}\right)_{\Omega_\delta} \\
&-\left(\nabla v, D_a \frac{\hat{a}}{\delta_m} \nabla \delta_m\right)_{\Omega_\delta} + \left(v, r_a \hat{a}\right)_{\Omega} - \left(v, b_a \hat{S}_a\right)_{\Omega}. \qquad \text{(B.41)}
\end{aligned}
$$

Note that the inner products are defined in different domains. When periodic boundary conditions are considered, the weak form of the problem takes the same form as in equations (B.40) and (B.41).

Semidiscrete formulation and numerical implementation

We employ a semidiscrete formulation based on IGA, which is analogous to the one described in chapter 4. Also, we use the time stepping scheme based on the Newton–Raphson method explained in subsection 2.3.3. The subdomains are established using the current nonlinear iteration of ϕ at the α_f time level. The key point is that the tangent matrix is well-conditioned and the singularities have been avoided due to the reformulation of the equations in the different subdomains. The numerical implementation of the formulation presented here is faster than the procedure described in the main text, because we avoid the loop over the global tangent matrix and the global residual vector (see subsection 4.3.2). The improvement is notable in parallel computations, especially in three-dimensional problems and problems that use fine meshes.

Appendix C

Extended summary in Spanish

C.1 Introducción

Una característica fascinante de las células eucariotas es su capacidad para moverse. La movilidad celular controla procesos biológicos cruciales, tales como la nutrición celular, la curación de heridas, la eliminación de patógenos, o la metástasis. Esta tesis está motivada por el importante papel desempeñado por la migración celular en algunos pasos del proceso metastásico. En concreto, durante la transición epitelio-mesénquima las células abandonan el tumor, invaden tejidos cercanos, y penetran en los vasos sanguíneos. De la misma forma, la salida de los capilares y la migración hacia órganos distantes conlleva el movimiento de las células. Los mecanismos que controlan el movimiento de las células cancerígenas son análogos a los de las células sanas. Es por esto que en esta tesis nos centramos en la migración celular de células sanas.

La migración celular a través de tejidos biológicos es un proceso sumamente complejo resultante de la interacción de la célula con su entorno. Los principales elementos que participan en la movilidad celular son el citoesqueleto, los motores moleculares, las proteínas encargadas de la adhesión con otras células y con la matriz extracelular, y un conjunto de proteínas localizadas en la membrana y el citosol que conforman la cascada de señalización. Estas últimas proteínas controlan todas las reacciones que originan el movimiento de las células. Estas proteínas van desde los receptores de membrana hasta los agentes nucleantes que inducen la polimerización de los filamentos del citoesqueleto. En los tipos de migración estudiados en esta tesis, los filamentos del citoesqueleto que desempeñan el papel más destacado son los filamentos de actina. Estos filamentos, formados por la polimerización de pequeños monómeros llamados actina globular, son capaces de constituir diversos tipos de configuraciones (por ejemplo, láminas bidimensionales denominadas lamelipodios o estructuras 3D conocidas como pseudópodos). La actina globular se difunde rápidamente en el citosol, lo que permite repentinos cambios en la geometría y organización interna de la célula. La miosina de tipo II, asociada a los filamentos de actina, es el tipo de motor molecular que realiza la actividad contractiva en las células móviles. Por último, la migración celular se produce en la matriz extracelular, una substancia gelatinosa bastante compleja, formada por una red de macromoléculas. Las células pueden degradar la matriz extracelular, rompiendo e incluso digiriendo las proteínas que conforman la matriz, para facilitar su migración.

La migración celular suele entenderse como un ciclo continuo que consta de cinco pasos interdependientes: la protrusión y elongación del frente de la célula provocadas por la polimerización de la actina; la interacción entre la célula y la matriz extracelular y la formación de adhesiones focales por medio de proteínas transmembrana de adherencia; la degradación de la matriz extracelular causada por proteasas localizadas en la membrana celular; la contracción de la red de actomiosina, generada por miosina de tipo II unida a los filamentos de actina; y el desprendimiento de la parte trasera de la célula y el consecuente deslizamiento hacia delante. La migración celular puede ser dirigida por diferentes estímulos externos percibidos en la membrana por proteínas de membrana. Esos estímulos, que pueden ser substancias químicas o cambios en las propiedades físicas del entorno, producen una respuesta celular que modifica el comportamiento de la célula al moverse. En el caso de substancias químicas, este fenómeno se conoce como quimiotaxis. Además, las células móviles presentan una serie de variantes morfológicas, denominadas modos de migración, que son función de factores endógenos y exógenos, tales como la adherencia célula-célula y célula-matriz extracelular, la degradación de la matriz extracelular, ciertas propiedades de la matriz extracelular (por ejemplo, densidad y orientación de las fibras y rigidez de la matriz), o el tipo de estructura predominante que forma el citoesqueleto. Los modos de migración se clasifican en individuales y colectivos. Los principales modos de migración individual, objeto de estudio en esta tesis, son la migración mesenquimal y la migración ameboidal. La migración mesenquimal se caracteriza por una alta adherencia célula-matriz extracelular, alta actividad contractiva en la red de actomiosina, y degradación de la matriz extracelular. En cambio, la migración ameboidal presenta una baja adherencia célula-matriz extracelular, carece de degradación de la matriz extracelular, y exhibe un comportamiento más dinámico causado por la rápida extensión y retracción de pseudópodos. Las células pueden compensar la pérdida de alguna capacidad motora mediante el desarrollo de nuevas estrategias migratorias, las cuales pueden incluir la transición entre diferentes modos de migración celular.

C.2 Objetivos

El objetivo principal de la tesis es modelar y simular la movilidad celular. Bajo este objetivo general, una serie de objetivos particulares se detallan en los siguientes puntos:

- **Modelización:** El objetivo es desarrollar modelos que representen la dinámica de aquellos componentes del citosol que producen la movilidad celular. Los componentes citosólicos están controlados por un conjunto de proteínas de señalización, cuyas reacciones son desencadenadas por moléculas de membrana. Por lo tanto, el acoplamiento entre el citosol y la membrana debe tenerse en cuenta. También tenemos como objetivo modelar el movimiento de las células en ambientes 3D compuestos por fibras, de tal forma que imiten la matriz extracelular. El primer paso para alcanzar este objetivo es la incorporación de obstáculos rígidos en el modelo usando una descripción continua. Las células no solo interactúan con la matriz extracelular, también con substancias extracelulares que pueden dirigir el movimiento de las células. Acoplar la dinámica de las substancias extracelulares con la membrana celular, y también con las fibras extracelulares, constituye otro objetivo de esta tesis.

- **Desarrollo de algoritmos numéricos:** El seguimiento de dominios móviles plantea una serie de desafíos computacionales. En esta tesis se recurre a una tecnología emergente (el método del campo de fase) que permite reformular problemas con interfases como ecuaciones en derivadas parciales planteadas en dominios fijos en el espacio. Los modelos de campo de fase normalmente incluyen ecuaciones en derivadas parciales de alto orden. Para superar esta limitación, hacemos uso del análisis isogeométrico. El análisis isogeométrico es un método de elementos finitos que usa *B-splines* o *non-uniform B-splines* (NURBS), que poseen continuidad global controlable, como funciones de base. El objetivo es desarrollar un algoritmo numérico robusto que solucione los modelos de campo de fase propuestos de una manera eficiente. Además, la descripción del campo de fase (toma el valor 0 fuera de la célula) produce sistemas mal condicionados. Para alcanzar este objetivo, construimos un código tomando como base PetIGA, que incorpora la capacidad de discretización de las NURBS y la integración de formas a la librería científica PETSc, y que además permite la paralelización del código.

- **Aplicación:** El primer objetivo en este punto es comprobar los modelos y los métodos computacionales propuestos. Esto se realiza comparando resultados 2D de migración mesenquimal y ameboidal con experimentos. También queremos estudiar la compleja interacción que se produce entre las proteínas de membrana y los compuestos citosólicos. En concreto, simulaciones 2D de células en microcanales y en entornos con obstáculos pueden proporcionar una idea sobre las interacciones existentes entre el citosol y la membrana. Otro objetivo es simular quimiotaxis y estudiar la influencia del entorno (de la matriz extracelular) y de la propia célula en la dinámica del quimioatrayente, y viceversa. El objetivo final es realizar simulaciones 3D de células migrando en substratos planos y en medios fibrosos. La movilidad celular en substratos planos se suele analizar usando modelos bidimensionales, pero una aproximación tridimensional puede posibilitar una mejor comprensión de la dinámica celular, sobre todo en relación a la adherencia célula-substrato. En el caso de medios fibrosos, las simulaciones tridimensionales pueden constituir una primera aproximación al estudio de la migración celular en la matriz extracelular.

C.3 Metodología

Una célula en movimiento es un ejemplo destacado de un problema con interfases móviles. La migración unicelular puede considerarse un problema de condición de frontera donde la membrana celular representa el contorno. El tratamiento clásico de este tipo de problemas involucra la solución de ecuaciones en derivadas parciales planteadas en dominios móviles. Estas ecuaciones están acopladas a otras ecuaciones en derivadas parciales por medio de condiciones de contorno planteadas en la interfase móvil, cuya ubicación es *a priori* desconocida. El tratamiento numérico de este tipo de problemas es muy complejo. El método del campo de fase ha surgido como una teoría matemática que permite reformular el problema de frontera libre como ecuaciones en derivadas parciales planteadas en un dominio computacional fijo y conocido. Todos los modelos propuestos en esta tesis están inspirados en el método del campo de fase y su tratamiento numérico es análogo.

El método del campo de fase nos permite solucionar las ecuaciones planteadas en los diferentes dominios (el citosol, la membrana, y el medio extracelular) usando una única malla fija en el espacio. La resolución de las ecuaciones de alto orden derivadas del método del campo de fase implica una serie de desafíos. Para superar esos desafíos, desarrollamos una metodología inspirada en el análisis isogeométrico, una generalización del método de elementos finitos. Para la discretización espacial nos basamos en el análisis isogeométrico y usamos *B-splines* como funciones de base. Las funciones *B-splines* poseen continuidad de grado arbitrario entre elementos para cualquier dimensión espacial, lo que permite una derivación directa de la forma de Galerkin. El algoritmo de integración temporal se basa en el método alfa-generalizado. Proponemos un esquema de integración temporal que utiliza un paso de tiempo fijo en casi todos los ejemplos. Solo para los ejemplos que consideran condiciones de contorno tipo Dirichlet implementamos un algoritmo con paso de tiempo adaptativo. El sistema no lineal resultante se resuelve usando el método de Newton–Raphson. Todos los términos son tratados implícitamente, excepto aquellos que necesiten cálculos no locales, como pueden ser el cálculo de integrales o de distancias. El número de condición de la matriz tangente presenta valores elevados, provocando que el algoritmo numérico sea ineficiente. Esto es debido a que la mayoría de las variables toman valores próximos a cero en diferentes zonas del dominio. Proponemos un método sencillo que genera vectores residuo y matrices tangente con un número de condición aceptable.

En esta tesis hemos propuesto tres modelos matemáticos de migración unicelular. Los modelos representan las interacciones entre los componentes del citosol, de la membrana, y del medio extracelular implicados en la movilidad celular. El movimiento de la célula es producido por las deformaciones de la red de filamentos de actina. Dicha red de filamentos se modela como un fluido Newtoniano sujeto a las fuerzas provocadas por la maquinaria encargada de la movilidad celular. Esas fuerzas son la tensión superficial de la membrana, la adherencia célula-substrato, y la protrusión y contracción causada por los filamentos de actina y la miosina, respectivamente. De la misma forma, una fuerza repulsiva actuando en la membrana representa la interacción con los obstáculos, que pueden simular fibras o paredes.

El primer modelo se centra en la migración mesenquimal. En este modelo consideramos los principales componentes citosólicos que participan en la migración mesenquimal, es decir, los motores moleculares (miosina) y los compuestos de actina (actina globular y filamentos de actina). El modelo propone una descripción innovadora para las transformaciones entre los compuestos de actina basada en un funcional de energía libre. Los resultados muestran que el modelo es capaz de reproducir de una manera efectiva el comportamiento de la actina en los queratocitos. Con este modelo somos capaces de reproducir migración mesenquimal por medio de simulaciones bidimensionales de queratocitos. Los ejemplos mostrados corresponden a células moviéndose en superficies planas y en microcanales.

El segundo modelo se usa para analizar la migración espontánea de células ameboidales. El modelo representa el acoplamiento entre los componentes del citosol y las moléculas de señalización de membrana que causan el movimiento ameboidal. Las reacciones observadas a lo largo de la cascada de señalización son simplificadas al considerar la dinámica de un único activador controlada por un proceso estocástico. El modelo permite simular la migración de un tipo de célula ameboidal llamada *Dictyostelium*. Los resultados correspondientes a migración libre y en microcanales muestran gran concordancia con los experimentos, lo cual sugiere que acoplar la membrana y el citosol es determinante para entender la migración ameboidal. También mostramos simulaciones de células moviéndose en un entorno 3D formado por fibras, que puede interpretarse como una primera aproximación a simular migración celular en la matriz extracelular.

El tercer modelo se centra en la quimiotaxis de células ameboidales. El modelo captura las interacciones que se producen entre el quimioatrayente extracelular, las proteínas de membrana, y los compuestos citosólicos a lo largo de la cascada de señalización, y que provocan el movimiento de la célula. También incorporamos adhesiones focales que se modelan como fuerzas puntuales que actúan en la red de actina. Los resultados 2D reproducen las principales características observadas en la quimiotaxis de células ameboidales. Las simulaciones muestran una complicada interacción entre la geometría del entorno y la dinámica del quimioatrayente, la cual controla la migración celular. También mostramos simulaciones 3D correspondientes a quimiotaxis en substratos planos y en entornos formados por fibras. Estos ejemplos pueden constituir un primer paso hacia la simulación de migración celular en tejidos biológicos.

C.4 Conclusiones

Las conclusiones que se extraen del trabajo desarrollado en esta tesis son:

- Desde un punto de vista mecánico, la membrana se modela como una vesícula y la red de actina como un fluido Newtoniano. El modelo propone ecuaciones en derivadas parciales para las ecuaciones de evolución de la miosina y los compuestos de actina (planteadas en el citosol), las especies localizadas en la membrana (planteadas en la membrana), y el quimioatrayente (planteadas en el entorno extracelular). El modelo también representa las interacciones entre los elementos que habitan en los diferentes dominios. El movimiento de la membrana celular es controlado por las deformaciones de la red de actina en contacto con el interior de la membrana.
- La ecuación de tipo Stokes que controla la dinámica de la red de actina incorpora las fuerzas producidas durante el movimiento celular. Esta formulación permite representar fuerzas de contracción y protrusión, fuerzas de adhesión puntuales, y fuerzas causadas por obstáculos externos. La formulación también permite ampliar el modelo si consideramos la rigidez y adhesividad del substrato, o la elasticidad y degradación de las fibras. Esas

ampliaciones pueden acoplarse directamente a la dinámica de la célula a través de fuerzas que actúan en la red de actina.

- Los desafíos computacionales asociados a la solución de ecuaciones en dominios móviles y deformables se abordan utilizando el método del campo de fase. Las ecuaciones propuestas en el citosol, la membrana, y el medio extracelular se pueden resolver usando una única malla fija en el espacio.

- El método del campo de fase también se usa para obtener las ecuaciones de evolución de los compuestos de actina. En la tesis proponemos un funcional de energía que representa las transformaciones que ocurren en la célula entre los distintos compuestos de actina. Estas transformaciones dependen de moléculas de señalización que se activan a lo largo de la cascada de señalización.

- Las reacciones que ocurren a lo largo de la cascada de señalización se simplifican al recurrir a una única proteína de mebrana. La dinámica de este componente señalizador, que está acoplado al resto de elementos señalizadores del citosol y del exterior de la célula, es controlada por un proceso estocástico que reproduce la formación de pseudópodos. El modelo puede ser mejorado al incluir una teoría determinista que describa las reacciones de las moléculas senalizadoras en el entorno de la membrana.

- Hemos desarrollado un método numérico basado en el análisis isogeométrico. El método ha demostrado ser eficiente, preciso, y robusto. El método numérico nos ha permitido analizar los modelos presentados en esta tesis a través de un gran número de simulaciones destacadas desde el punto de vista biológico. En concreto, el método ha servido de instrumento para estudiar el movimiento de células en medios tridimensionales, lo cual ha sido pasado por alto en la mayoría de los modelos presentes en la literatura. A nuestro entender, este es el primer trabajo que ha desarrollado un método numérico basado en el análisis isogeométrico para problemas de movilidad celular. También hemos desarrollado el consecuente código para implementar la formulación numérica y realizar las simulaciones.

- Las simulaciones de movilidad mesenquimal muestran que el caso de migración de queratocitos en substratos planos produce estados de movilidad estacionarios, que coinciden con observaciones experimentales. Además, al considerar la presencia de obstáculos, somos capaces de reproducir complejos modos de migración observados en microcanales, tales como movimiento oscilatorio y bípedo.

- Los resultados de movimiento espontáneo ameboidal concuerdan cuantitativamente con experimentos de migración en entornos libres y confinados.

Los resultados correspondientes a quimiotaxis también concuerdan cuantitativamente con experimentos, aunque algunas características observadas experimentalmente no se aprecian debido a la descripción estocástica empleada para la formación de pseudópodos.

- Los resultados de migración ameboidal en microcanales y entornos laberínticos también sugieren que acoplar la dinámica del medio extracelular, la membrana, y el citosol es determinante para una mejor comprensión de la quimiotaxis y la movilidad ameboidal, especialmente en el caso de migración en entornos confinados. Los modelos que pasan por alto este acoplamiento bidireccional (citosol-membrana y membrana-medio extracelular) pueden ser incapaces de reproducir algunas características particulares de las células móviles. En este sentido, nuestros resultados de migración en entornos confinados sugieren que las células pueden aprovecharse de su microentorno para buscar estrategias migratorias más efectivas.
- Hemos realizado simulaciones 3D que corresponden a células moviéndose en substratos planos y mallas fibrosas formadas por obstáculos. La incorporación de la interacción célula-substrato (o célula-fibra) supone una migración tridimensional más realista en substratos (o en mallas fibrosas). El ejemplo correspondiente a migración en substratos planos representa la típica aproximación bidimensional de migración celular, aunque realizada en un dominio tridimensional. Este ejemplo puede ser un punto de referencia importante a medida que el campo de la migración celular computacional evolucione de simulaciones 2D a simulaciones 3D.

C.5 Futuras líneas de trabajo

A lo largo de esta tesis hemos mencionado posibles ampliaciones del modelo y futuras líneas de trabajo. A continuación resumimos las principales líneas de investigación abiertas durante el trabajo realizado en esta tesis.

Dinámica de la matriz extracelular En la tesis hemos considerado la matriz extracelular como una malla formada por fibras rígidas. La matriz extracelular es una substancia muy compleja con propiedades viscoelásticas y que posee, entre otros compuestos, proteínas fibrosas. Además, las células son capaces de degradar y reestructurar la matriz extracelular. Este comportamiento debería acoplarse a nuestro modelo de una forma robusta y consistente. Una posibilidad podría ser incluir un modelo elástico o viscoelástico para las fibras. Otra posibilidad sería el uso de un método inmerso para modelar la interacción célula-matriz extracelular.

Haptotaxis y durotaxis La haptotaxis es el movimiento de células dirigido por un gradiente de puntos de adhesión celular. En el caso de durotaxis, la migración celular depende de la rigidez del substrato. En esta tesis, hemos considerado substratos (o fibras) de rigidez infinita y una densidad uniforme de puntos de adhesión. Para simular ambos tipos de migración, es necesaria una descripción más detallada de la dinámica de las adhesiones focales. Un modelo detallado de las adhesiones focales y la incorporación de la densidad de puntos de adhesión podría llevar a reproducir la haptotaxis. En el caso de durotaxis, además del modelo de adhesiones focales, deberíamos incluir la elasticidad del substrato (o fibras).

Migración tipo *bleb* La migración tipo *bleb* es un tipo de migración ameboidal en la cual las extensiones de la membrana (en inglés denominadas *blebs*) no están provocadas por la polimerización de los filamentos de actina. Una ruptura en la conexión del córtex con la membrana suele provocar el origen de un *bleb*. Cuando la presión hidrostática en el citoplasma aumenta, la membrana se separa del córtex en la zona de ruptura y el fluido citoplasmático, no la red de actina, produce el movimiento celular. De la misma forma, la presión intracelular y la conexión membrana-córtex desempeñan un papel importante. El modelo presentado en esta tesis debe ser adaptado a la migración tipo *bleb*, aunque la metodología del campo de fase, la obtención de las fuerzas en la membrana, la presencia de proteínas de membrana, y la consideración de que un fluido Newtoniano deforma la membrana siguen siendo aplicables.

Migración mesenquimal 3D en substratos planos En esta tesis, hemos mostrado ejemplos de migración 3D correspondientes a movilidad ameboidal. Sin embargo, sería interesante simular migración 3D de queratocitos (migración mesenquimal) en substratos planos. Este tipo de migración suele ser modelada usando una aproximación bidimensional porque el lamelipodio, la estructura de filamentos de actina que dirige el movimiento, forma una lámina bidimensional paralela al substrato. El modelo de migración mesenquimal propuesto en la tesis es incapaz de reproducir la dinámica del lamelipodio en simulaciones 3D. Creemos que pequeñas modificaciones en el funcional de energía libre de actina, en la descripción de las fuerzas, y en la dinámica de las adhesiones focales pueden conducir a simular la migración de queratocitos en 3D.

Dinámica de las moléculas de señalización en una célula deformable El marco teórico propuesto en esta tesis en relación al campo de fase puede ser usado para resolver otros modelos de movilidad unicelular en geometrías 3D deformables.

En concreto, nos referimos a modelos que reproducen las reacciones de las moléculas de señalización que ocurren en el entorno de la membrana. Normalmente, esos modelos han sido resueltos en geometrías fijas de una y dos dimensiones. De la misma forma, sería interesante acoplar esas moléculas de señalización con el quimioatrayente y los compuestos citosólicos considerados en nuestro modelo. Así, podríamos obtener simulaciones tridimensionales más realistas porque la descripción estocástica usada para el activador sería reemplazada por una teoría determinista.

Appendix D

Extended summary in Galician

D.1 Introdución

Unha característica fascinante das células eucariotas é a súa capacidade para moverse. A mobilidade celular controla procesos biolóxicos cruciais, como a nutrición celular, a curación de feridas, a eliminación de patóxenos, ou a metástase. Esta tese de doutoramento está motivada polo importante papel xogado pola migración celular nalgúns pasos do proceso metastático. En concreto, durante a transición epitelio-mesénquima as células abandonan o tumor, invaden tecidos próximos, e penetran nos vasos sanguíneos. Da mesma forma, a saída dos capilares e a migración cara órganos distantes implica o movemento das células. Os mecanismos que controlan o movemento das células canceríxenas son análogos aos das células sas. É por iso que nesta tese centrámonos na migración celular de células sas.

A migración celular a través de tecidos biolóxicos é un proceso sumamente complexo resultante da interacción da célula co medio que a rodea. Os principais elementos que participan na mobilidade celular son o citoesqueleto, os motores moleculares, as proteínas encargadas da adhesión con outras células e coa matriz extracelular, e un conxunto de proteínas localizadas na membrana e no citosol que conforman a ruta de sinalización. Estas últimas proteínas controlan tódalas reaccións que orixinan o movemento das células. Estas proteínas van dende os receptores de membrana ata os axentes nucleantes que inducen a polimerización dos filamentos do citoesqueleto. Nos tipos de migración estudados nesta tese, os filamentos do citoesqueleto que xogan o papel máis destacado son os filamentos de actina. Estes filamentos, formados pola polimerización de pequenos monómeros chamados actina globular, son capaces de constituír diversos tipos de configuracións (por exemplo, láminas bidimensionais denominadas lamelipodios ou estruturas 3D coñecidas como pseudópodos). A actina globular difúndese rapidamente no citosol, o que permite cambios repentinos na xeometría e organización interna da célula. A miosina II, asociada aos filamentos de actina, é o tipo de motor molecular que realiza a actividade contráctil nas células móbiles. Por último, a migración celular prodúcese na matriz extracelular, unha substancia xelatinosa bastante complexa, formada por unha rede de macromoléculas. As células poden degradar a matriz extracelular, rompendo e incluso dixerindo as proteínas que conforman a matriz, para facilitar a súa migración.

A migración celular xeralmente enténdese como un ciclo continuo que consta de cinco pasos interdependentes: a protrusión e elongación do frente da célula provocadas pola polimerización da actina; a interacción entre a célula e a matriz extracelular e a formación de adhesións focais por medio de proteínas transmembrana de adherencia; a degradación da matriz extracelular causada por proteases localizadas na membrana celular; a contracción da rede de actomiosina, xerada por miosina II unida aos filamentos de actina; e o desprendemento da parte traseira da célula e o consecuente deslizamento cara adiante. A migración celular pode ser dirixida por diferentes estímulos externos percibidos na membrana por proteínas de membrana. Eses estímulos, que poden ser substancias químicas ou cambios nas propiedades físicas do ambiente, producen unha resposta celular que modifica o comportamento da célula no seu movemento. No caso de substancias químicas, este fenómeno coñécese como quimiotaxe. Ademais, as células móbiles presentan unha serie de variantes morfolóxicas, denominadas modos de migración, que son función de factores endóxenos e exóxenos, como a adherencia célula-célula e célula-matriz extracelular, a degradación da matriz extracelular, certas propiedades da matriz extracelular (por exemplo, densidade e orientación das fibras e rixidez da matriz), ou o tipo de estrutura predominante que forma o citoesqueleto. Os modos de migración clasifícanse en individuais e colectivos. Os principais modos de migración individual, obxecto de estudo nesta tese, son a migración mesenquimal e a migración ameboidal. A migración mesenquimal caracterízase por unha alta adherencia célula-matriz extracelular, alta actividade contráctil na rede de actomiosina, e degradación da matriz extracelular. En cambio, a migración ameboidal presenta unha baixa adherencia célula-matriz extracelular, carece de degradación da matriz extracelular, e exhibe un comportamento máis dinámico causado pola rápida extensión e retracción de pseudópodos. As células poden compensar a perda dalgunha capacidade motora mediante o desenvolvemento de novas estratexias migratorias, que poden incluír a transición entre diferentes modos de migración celular.

D.2 Obxectivos

O obxectivo principal da tese é modelar e simular a mobilidade celular. Baixo este obxectivo xeral, unha serie de obxectivos particulares detállanse nos puntos seguintes:

- **Modelización:** O obxectivo é desenvolver modelos que representen a dinámica daqueles compoñentes do citosol que producen a mobilidade celular. Os compoñentes citosólicos están controlados por un conxunto de proteínas de sinalización, cuxas reaccións son desencadeadas por moléculas de membrana. Polo tanto, o acoplamento entre o citosol e a membrana debe terse en conta. Tamén temos como obxectivo modelar o movemento das células en ambientes 3D compostos por fibras, de tal xeito que imiten a matriz extracelular. O primeiro paso para lograr este obxectivo é a incorporación de obstáculos ríxidos no modelo usando unha descrición continua. As células non só interactúan coa matriz extracelular, tamén con substancias extracelulares que poden dirixir o movemento das células. Acoplar a dinámica das substancias extracelulares coa membrana celular, e tamén coas fibras da matriz extracelular, constitúe outro obxectivo desta tese.

- **Desenvolvemento de algoritmos numéricos:** O seguimento de dominios móbiles supón unha serie de desafíos computacionais. Nesta tese facemos uso dunha tecnoloxía emerxente (o método do campo de fase) que permite reformular problemas con interfases como ecuacións en derivadas parciais propostas en dominios fixos no espacio. Os modelos de campo de fase normalmente inclúen ecuacións en derivadas parciais de alto orde. Para superar esta limitación, facemos uso da análise isoxeométrica. A análise isoxeométrico é un método de elementos finitos que usa *B-splines* ou *non-uniform B-splines* (NURBS), que posúen continuidade global controlable, como funcións de base. O obxectivo é desenvolver un algoritmo numérico robusto que solucione os modelos de campo de fase propostos dunha forma eficiente. Ademais, a descrición do campo de fase (toma o valor 0 fóra da célula) produce sistemas mal condicionados. Para lograr este obxectivo, construímos un código tomando como base PetIGA, que incorpora a capacidade de discretización das NURBS e a integración de formas á librería científica PETSc, e que ademais permite a paralelización do código.

- **Aplicación:** O primeiro obxectivo neste punto é comprobar os modelos e os métodos computacionais propostos. Isto realízase comparando resultados 2D de migración mesenquimal e ameboidal con experimentos. Tamén queremos estudar a complexa interacción que se produce entre as proteínas de membrana e os compostos citosólicos. En concreto, simulacións 2D de células en microcanles e en ambientes con obstáculos poden proporcionar unha idea sobre as interaccións existentes entre o citosol e a membrana. Outro obxectivo é simular quimiotaxe e estudar a influencia do medio (da matriz extracelular) e da propia célula na dinámica do quimioatraente, e viceversa. O obxectivo final é realizar simulacións 3D de células migrando en substratos planos e en medios fibrosos. A mobilidade celular en substratos planos xeralmente analízase usando modelos bidimensionais, mais unha aproximación tridimensional pode posibilitar unha mellor comprensión da dinámica celular, sobre todo en relación á adherencia célula-substrato. No caso de medios fibrosos, as simulacións tridimensionais poden constituír unha primeira aproximación ao estudo da migración celular na matriz extracelular.

D.3 Metodoloxía

Unha célula en movemento supón un exemplo destacado dun problema con interfases móbiles. A migración unicelular pode considerarse un problema de condición de fronteira onde a membrana celular representa o contorno. O tratamento clásico deste tipo de problemas involucra a solución de ecuacións en derivadas parciais propostas en dominios móbiles. Estas ecuacións están acopladas a outras ecuacións en derivadas parciais por medio de condicións de contorno propostas na interfase móbil, cuxa localización é *a priori* descoñecida. O tratamento numérico deste tipo de problemas é moi complexo. O método do campo de fase xorde como unha teoría matemática que permite reformular o problema de fronteira libre como ecuacións en derivadas parciais propostas nun dominio computacional fixo e coñecido. Tódolos modelos propostos nesta tese están inspirados no método do campo de fase e o seu tratamento numérico é análogo.

O método do campo de fase permítenos solucionar as ecuacións propostas nos diferentes dominios (o citosol, a membrana, e o medio extracelular) usando unha única malla fixa no espacio. A resolución das ecuacións de alto orde derivadas do método do campo de fase implica unha serie de desafíos. Para superar eses desafíos, desenvolvemos unha metodoloxía inspirada na análise isoxeométrica, unha xeneralización do método de elementos finitos. Para a discretización espacial baseámonos na análise isoxeométrica e usamos *B-splines* como funcións de base. As funcións *B-splines* posúen continuidade de grado arbitrario entre elementos para calquera dimensión espacial, o que permite unha derivación directa da forma de Galerkin. O algoritmo de integración temporal baséase no método alfa-xeneralizado. Propoñemos un esquema de integración temporal que utiliza un paso de tempo fixo en casi tódolos exemplos. Só para os exemplos que consideran condicións de contorno tipo Dirichlet implementamos un algoritmo con paso de tempo adaptable. O sistema non lineal resultante resólvese usando o método de Newton–Raphson. Tódolos termos son tratados implícitamente, agás aqueles que precisen cálculos non locais, como poden ser o cálculo de integrais ou de distancias. O número de condición da matriz tanxente presenta valores elevados, provocando que o algoritmo numérico sexa ineficiente. Isto débese a que a maioría das variables toman valores próximos a cero en diferentes zonas do dominio. Propoñemos un método sinxelo que xera vectores residuo e matrices tanxente cun número de condición aceptables.

Nesta tese propoñemos tres modelos matemáticos de migración unicelular. Os modelos representan as interaccións entre os compoñentes do citosol, da membrana, e do medio extracelular implicados na mobilidade celular. O movemento da célula é producido polas deformacións da rede de filamentos de actina. Esta rede de filamentos modélase como un fluído Newtoniano suxeito ás forzas provocadas pola maquinaria encargada da mobilidade celular. Esas forzas son a tensión superficial da membrana, a adherencia célula-substrato, e a protrusión e contracción causada polos filamentos de actina e a miosina, respectivamente. Do mesmo xeito, unha forza repulsiva actuando na membrana representa a interacción cos obstáculos, que poden simular fibras ou paredes.

O primeiro modelo céntrase na migración mesenquimal. Neste modelo consideramos os principais compoñentes citosólicos que participan na migración mesenquimal, é dicir, os motores moleculares (miosina) e os compostos de actina (actina globular e filamentos de actina). O modelo propón unha descrición innovadora para as transformacións entre os compostos de actina baseada nun funcional de enerxía libre. Os resultados mostran que o modelo é capaz de reproducir dunha forma efectiva o comportamento da actina nos queratocitos. Con este modelo somos capaces de reproducir migración mesenquimal por medio de simulacións bidimensionais de queratocitos. Os exemplos mostrados corresponden a células movéndose en superficies planas e en microcanles.

O segundo modelo úsase para analizar a migración espontánea de células ameboidais. O modelo representa o acoplamento entre os compoñentes do citosol e as moléculas de sinalización de membrana que causan o movemento ameboidal. As reaccións observadas ao longo da ruta de sinalización son simplificadas ao considerar a dinámica dun único activador controlada por unha descrición estocástica. O modelo permite simular a migración dun tipo de célula ameboidal chamada *Dictyostelium*. Os resultados correspondentes a migración libre e en microcanles mostran gran concordancia cos experimentos, o que suxire que acoplar a membrana e o citosol é determinante para entender a migración ameboidal. Tamén mostramos simulacións de células movéndose nun medio 3D formado por fibras, que pode interpretarse como unha primeira aproximación a simular migración celular na matriz extracelular.

O terceiro modelo céntrase na quimiotaxe de células ameboidais. O modelo captura as interaccións que se producen entre o quimioatraente extracelular, as proteínas de membrana, e os compostos citosólicos ao longo da ruta de sinalización, e que provocan o movemento da célula. Tamén incorporamos adhesións focais que se modelan como forzas puntuais que actúan na rede de actina. Os resultados 2D reproducen as principais características observadas na quimiotaxe de células ameboidais. As simulacións mostran unha complicada interacción entre a xeometría do medio e a dinámica do quimioatraente, que controla a migración celular. Tamén mostramos simulacións 3D correspondentes a quimiotaxe en substratos planos e en ambientes fibrosos. Estes exemplos poden constituír un primeiro paso cara a simulación de migración celular en tecidos biolóxicos.

D.4 Conclusións

As conclusións que se extraen do traballo desenvolto nesta tese son:

- Dende un punto de vista mecánico, a membrana modélase como unha vesícula e a rede de actina como un fluído Newtoniano. O modelo propón ecuacións en derivadas parciais para as ecuacións de evolución da miosina e os compostos de actina (propostas no citosol), as especies localizadas na membrana (propostas na membrana), e o quimioatraente (propostas no medio extracelular). O modelo tamén representa as interaccións entre os elementos que habitan nos diferentes dominios. O movemento da membrana celular é controlado polas deformacións da rede de actina en contacto co interior da membrana.

- A ecuación de tipo Stokes que controla a dinámica da rede de actina incorpora as forzas producidas durante o movemento celular. Esta formulación permite representar forzas de contracción e protrusión, forzas de adhesión puntuais, e forzas causadas por obstáculos externos. A formulación tamén permite ampliar o modelo se consideramos a rixidez e adherencia do substrato, ou a elasticidade e degradación das fibras. Esas ampliacións poden acoplarse directamente á dinámica da célula a través de forzas que actúan na rede de actina.

- Os desafíos computacionais asociados á solución de ecuacións en dominios móbiles e deformables abórdanse utilizando o método do campo de fase. As ecuacións propostas no citosol, na membrana, e no medio extracelular pódense resolver usando unha única malla fixa no espacio.

- O método do campo de fase tamén se usa para obter as ecuacións de evolución dos compostos de actina. Na tese propoñemos un funcional de enerxía que representa as transformacións que ocorren na célula entre os distintos compostos de actina. Estas transformacións dependen de moléculas de sinalización que se activan ao longo da ruta de sinalización.

- As reaccións que ocorren ao longo da ruta de sinalización simplifícanse ao empregar unha única proteína de mebrana. A dinámica deste compoñente sinalizador, que está acoplado ao resto de elementos sinalizadores do citosol e do exterior da célula, é controlada por un proceso estocástico que reproduce a formación de pseudópodos. O modelo pode ser mellorado ao incluír unha teoría determinista que describa as reaccións das moléculas sinalizadoras na zona da membrana.

- Desenvolvemos un método numérico baseado na análise isoxeométrica. O método demostra ser eficiente, preciso, e robusto. O método numérico permítenos analizar os modelos presentados nesta tese a través dun gran número de simulacións destacadas dende o punto de vista biolóxico. En concreto, o método serve de instrumento para estudar o movemento de células en medios tridimensionais, que se ignora na maior parte dos modelos presentes na literatura. Ao noso entender, este é o primeiro traballo que desenvolve un método numérico baseado na análise isoxeométrica para problemas de mobilidade celular. Tamén desenvolvemos o consecuente código para implementar a formulación numérica e realizar as simulacións.

- As simulacións de mobilidade mesenquimal mostran que o caso de migración de queratocitos en substratos planos produce estados de mobilidade estacionarios, que coinciden con observacións experimentais. Ademais, ao considerar a presenza de obstáculos, somos capaces de reproducir complexos modos de migración observados en microcanles, como o movemento oscilatorio e bípede.

- Os resultados de movemento espontáneo ameboidal concordan cuantitativamente con experimentos de migración en ambientes libres e confinados. Os resultados correspondentes a quimiotaxe tamén concordan cuantitativamente cos experimentos, aínda que algunhas características observadas experimentalmente non se aprecian por mor da descrición estocástica empregada para a formación de pseudópodos.

- Os resultados de migración ameboidal en microcanles e ambientes labirínticos tamén suxiren que acoplar a dinámica do medio extracelular, a membrana, e o citosol é determinante para unha mellor comprensión da quimiotaxe e da mobilidade ameboidal, especialmente no caso de migración en ambientes confinados. Os modelos que pasan por alto este acoplamento bidireccional (citosol-membrana e membrana-medio extracelular) poden ser incapaces de reproducir algunhas características particulares das células móbiles. Neste sentido, os nosos resultados de migración en ambientes confinados suxiren que as células poden aproveitarse do seu microambiente para buscar estratexias migratorias máis efectivas.

- Realizamos simulacións 3D que se corresponden a células movéndose en substratos planos e mallas fibrosas formadas por obstáculos. A incorporación da interacción célula-substrato (ou célula-fibra) supón unha migración tridimensional máis realista en substratos (ou en mallas fibrosas). O exemplo correspondente a migración en substratos planos representa a típica aproximación bidimensional de migración celular, aínda que realizada nun dominio tridimensional. Este exemplo pode ser un punto de referencia importante a medida que o campo da migración celular computacional evolucione de simulacións 2D a simulacións 3D.

D.5 Futuras liñas de traballo

Ao longo desta tese mencionamos posibles ampliacións do modelo e futuras liñas de traballo. A continuación resumimos as principais liñas de investigación abertas durante o traballo realizado nesta tese.

Dinámica da matriz extracelular Na tese consideramos a matriz extracelular como unha malla formada por fibras ríxidas. A matriz extracelular é unha substancia moi complexa con propiedades viscoelásticas e que posúe, entre outros compostos, proteínas fibrosas. Ademais, as células son capaces de degradar e reestruturar a matriz extracelular. Este comportamento debería acoplarse ao noso modelo dunha forma robusta e consistente. Unha posibilidade podería ser incluír un modelo elástico ou viscoelástico para as fibras. Outra posibilidade sería o uso dun método inmerso para modelar a interacción célula-matriz extracelular.

Haptotaxe e durotaxe A haptotaxe é o movemento de células dirixido por un gradiente de puntos de adhesión celular. No caso de durotaxe, a migración celular depende da rixidez do substrato. Nesta tese consideramos substratos (ou fibras) de rixidez infinita e unha densidade uniforme de puntos de adhesión. Para simular ambos os dous tipos de migración, é necesaria unha descrición máis detallada da dinámica das adhesións focais. Un modelo detallado das adhesións focais e a incorporación da densidade de puntos de adhesión podería levar a reproducir a haptotaxe. No caso de durotaxe, ademais do modelo de adhesións focais, deberiamos incluír a elasticidade do substrato (ou fibras).

Migración tipo *bleb* A migración tipo *bleb* é un tipo de migración ameboidal na cal as extensións da membrana (en inglés denominadas *blebs*) non están provocadas pola polimerización dos filamentos de actina. Unha ruptura na conexión do córtex coa membrana xeralmente provoca a orixe dun *bleb*. Cando a presión hidrostática no citoplasma aumenta, a membrana sepárase do córtex na zona de ruptura e o fluído citoplasmático, non a rede de actina, produce o movemento celular. Da mesma forma, a presión intracelular e a conexión membrana-córtex xogan un papel importante. O modelo presentado nesta tese debe ser adaptado á migración tipo *bleb*, aínda que a metodoloxía do campo de fase, a obtención das forzas na membrana, a presenza de proteínas de membrana, e a consideración de que un fluído Newtoniano deforma a membrana seguen sendo aplicables.

Migración mesenquimal 3D en substratos planos Nesta tese, mostramos exemplos de migración 3D correspondentes a mobilidade ameboidal. Porén, sería interesante simular migración 3D de queratocitos (migración mesenquimal) en substratos planos. Este tipo de migración xeralmente modélase usando unha aproximación bidimensional porque o lamelipodio, a estrutura de filamentos de actina que dirixe o movemento, forma unha lámina bidimensional paralela ao substrato. O modelo de migración mesenquimal proposto na tese é incapaz de reproducir a dinámica do lamelipodio en simulacións 3D. Cremos que pequenas modificacións no funcional de enerxía libre de actina, na descrición das forzas, e na dinámica das adhesións focais poden levar a simular a migración de queratocitos en 3D.

Dinámica das moléculas de sinalización nunha célula deformable O marco teórico proposto nesta tese en relación ao campo de fase pode usarse para resolver outros modelos de mobilidade unicelular en xeometrías 3D deformables. En concreto, referímonos a modelos que reproducen as reaccións das moléculas de sinalización que ocorren na zona da membrana. Normalmente, eses modelos resólvense en xeometrías fixas de unha e dúas dimensións. Do mesmo xeito, sería interesante acoplar esas moléculas de sinalización co quimioatraente e cos compostos citosólicos considerados no noso modelo. Así, poderiamos obter simulacións tridimensionais máis realistas porque a descrición estocástica usada para o activador sería substituída por unha teoría determinista.

Bibliography

Alberts, B., Johnson, A., Lewis, J., Raff, M., Roberts, K., and Walter, P. 2007. *Molecular biology of the cell*. Garland science. ISBN 0-8153-3218-1. ↑1 , ↑7 , ↑8 , ↑9 , ↑10 , ↑13

Allen, S.M. and Cahn, J.W. 1979. A microscopic theory for antiphase boundary motion and its application to antiphase domain coarsening. *Acta Metallurgica*, vol. 27(6), pp. 1085–1095. ↑36 , ↑68

Allena, R. and Aubry, D. 2012. 'Run-and-tumble' or 'look-and-run'? a mechanical model to explore the behavior of a migrating amoeboid cell. *Journal of theoretical biology*, vol. 306, pp. 15–31. ↑27 , ↑125

Allena, R., Aubry, D., and Sharpe, J. 2013. On the mechanical interplay between intra-and inter-synchronization during collective cell migration: a numerical investigation. *Bulletin of mathematical biology*, vol. 75(12), pp. 2575–2599. ↑27

Allena, R. and Maini, P. 2014. Reaction–diffusion finite element model of lateral line primordium migration to explore cell leadership. *Bulletin of mathematical biology*, vol. 76(12), pp. 3028–3050. ↑27

Alt, W. and Dembo, M. 1999. Cytoplasm dynamics and cell motion: two-phase flow models. *Mathematical biosciences*, vol. 156(1), pp. 207–228. ↑31

Anderson, D.M., McFadden, G.B., and Wheeler, A.A. 1998. Diffuse-interface methods in fluid mechanics. *Annual review of fluid mechanics*, vol. 30(1), pp. 139–165. ↑34

Arai, Y., Shibata, T., Matsuoka, S., Sato, M.J., Yanagida, T., and Ueda, M. 2010. Self-organization of the phosphatidylinositol lipids signaling system for random cell migration. *Proceedings of the National Academy of Sciences*, vol. 107(27), pp. 12399–12404. ↑28

Aubry, D., Thiam, H., Piel, M., and Allena, R. 2015. A computational mechanics approach to assess the link between cell morphology and forces during confined migration. *Biomechanics and modeling in mechanobiology*, vol. 14(1), pp. 143–157. ↑27

Auricchio, F., Da Veiga, L.B., Hughes, T., Reali, A., and Sangalli, G. 2010. Isogeometric collocation methods. *Mathematical Models and Methods in Applied Sciences*, vol. 20(11), pp. 2075–2107. ↑64

Balay, S., Abhyankar, S., Adams, M.F., Brown, J., Brune, P., Buschelman, K., Dalcin, L., Eijkhout, V., Gropp, W.D., Kaushik, D., Knepley, M.G., McInnes, L.C., Rupp, K., Smith, B.F., Zampini, S., Zhang, H., and Zhang, H. 2016. PETSc Web page. http://www.mcs.anl.gov/petsc. URL http://www.mcs.anl.gov/petsc. ↑6 , ↑71

Barnhart, E.L., Allen, G.M., Jülicher, F., and Theriot, J.A. 2010. Bipedal locomotion in crawling cells. *Biophysical journal*, vol. 98(6), pp. 933–942. ↑81 , ↑82

Barnhart, E.L., Lee, K.C., Keren, K., Mogilner, A., and Theriot, J.A. 2011. An adhesion-dependent switch between mechanisms that determine motile cell shape. *PLoS biology*, vol. 9(5), p. e1001059. ↑20 , ↑27 , ↑29 , ↑30 , ↑51 , ↑77

Bazilevs, Y., Calo, V., Cottrell, J., Hughes, T., Reali, A., and Scovazzi, G. 2007. Variational multiscale residual-based turbulence modeling for large eddy simulation of incompressible flows. *Computer Methods in Applied Mechanics and Engineering*, vol. 197(1), pp. 173–201. ↑42

Bazilevs, Y., Calo, V.M., Cottrell, J.A., Evans, J.A., Hughes, T., Lipton, S., Scott, M.A., and Sederberg, T.W. 2010a. Isogeometric analysis using t-splines. *Computer Methods in Applied Mechanics and Engineering*, vol. 199(5), pp. 229–263. ↑41

Bazilevs, Y., Calo, V.M., Hughes, T.J., and Zhang, Y. 2008. Isogeometric fluid-structure interaction: theory, algorithms, and computations. *Computational mechanics*, vol. 43(1), pp. 3–37. ↑42

Bazilevs, Y., Michler, C., Calo, V., and Hughes, T. 2010b. Isogeometric variational multiscale modeling of wall-bounded turbulent flows with weakly enforced boundary conditions on unstretched meshes. *Computer Methods in Applied Mechanics and Engineering*, vol. 199(13), pp. 780–790. ↑41

Bell, G.I. *et al.* 1978. Models for the specific adhesion of cells to cells. *Science*, vol. 200(4342), pp. 618–627. ↑132

Bergert, M., Chandradoss, S.D., Desai, R.A., and Paluch, E. 2012. Cell mechanics control rapid transitions between blebs and lamellipodia during migration. *Proceedings of the National Academy of Sciences*, vol. 109(36), pp. 14434–14439. ↑26

Biben, T., Kassner, K., and Misbah, C. 2005. Phase-field approach to three-dimensional vesicle dynamics. *Physical Review E*, vol. 72(4), p. 041921. ↑28 , ↑29 , ↑36 , ↑54

Borau, C., Kim, T., Bidone, T., García-Aznar, J.M., and Kamm, R.D. 2012. Dynamic mechanisms of cell rigidity sensing: insights from a computational model of actomyosin networks. *PLoS One*, vol. 7(11), p. e49174. ↑26

Borden, M.J., Verhoosel, C.V., Scott, M.A., Hughes, T.J., and Landis, C.M. 2012. A phase-field description of dynamic brittle fracture. *Computer Methods in Applied Mechanics and Engineering*, vol. 217, pp. 77–95. ↑36

Bosgraaf, L. and Van Haastert, P.J. 2009a. Navigation of chemotactic cells by parallel signaling to pseudopod persistence and orientation. *PloS one*, vol. 4(8), p. e6842. ↑134 , ↑137 , ↑146

Bosgraaf, L. and Van Haastert, P.J. 2009b. The ordered extension of pseudopodia by amoeboid cells in the absence of external cues. *PloS one*, vol. 4(4), p. e5253. ↑32 , ↑86 , ↑89 , ↑90 , ↑104 , ↑105 , ↑107 , ↑134 , ↑136 , ↑147

Bottino, D., Mogilner, A., Roberts, T., Stewart, M., and Oster, G. 2002. How nematode sperm crawl. *Journal of cell science*, vol. 115(2), pp. 367–384. ↑29 , ↑30

Bueno, J., Bazilevs, Y., Juanes, R., and Gomez, H. 2017. Droplet motion driven by tensotaxis. *Extreme Mechanics Letters*, vol. 13, pp. 10–16. ↑21

Bueno, J., Bona-Casas, C., Bazilevs, Y., and Gomez, H. 2015. Interaction of complex fluids and solids: theory, algorithms and application to phase-change-driven implosion. *Computational Mechanics*, vol. 55(6), pp. 1105–1118. ↑42

Bueno, J., Starodumov, I., Gomez, H., Galenko, P., and Alexandrov, D. 2016. Three dimensional structures predicted by the modified phase field crystal equation. *Computational Materials Science*, vol. 111, pp. 310–312. ↑42

Caginalp, G. 1989. Stefan and hele-shaw type models as asymptotic limits of the phase-field equations. *Physical Review A*, vol. 39(11), p. 5887. ↑34 , ↑36

Cahn, J.W. and Hilliard, J.E. 1958. Free energy of a nonuniform system. i. interfacial free energy. *The Journal of chemical physics*, vol. 28(2), pp. 258–267. ↑36

Calabrò, F., Sangalli, G., and Tani, M. 2017. Fast formation of isogeometric galerkin matrices by weighted quadrature. *Computer Methods in Applied Mechanics and Engineering*, vol. 316, pp. 606–622. ↑64

Camley, B.A. and Rappel, W.J. 2017. Physical models of collective cell motility: from cell to tissue. *Journal of Physics D: Applied Physics*, vol. 50(11), p. 113002. ↑26

Camley, B.A., Zhang, Y., Zhao, Y., Li, B., Ben-Jacob, E., Levine, H., and Rappel, W.J. 2014. Polarity mechanisms such as contact inhibition of locomotion regulate persistent rotational motion of mammalian cells on micropatterns. *Proceedings of the National Academy of Sciences*, vol. 111(41), pp. 14770–14775. ↑28 , ↑33

Camley, B.A., Zhao, Y., Li, B., Levine, H., and Rappel, W.J. 2013. Periodic migration in a physical model of cells on micropatterns. *Physical review letters*, vol. 111(15), p. 158102. ↑52 , ↑79

Camley, B.A., Zhao, Y., Li, B., Levine, H., and Rappel, W.J. 2017. Crawling and turning in a minimal reaction-diffusion cell motility model: Coupling cell shape and biochemistry. *Physical Review E*, vol. 95(1), p. 012401. ↑28

Canham, P.B. 1970. The minimum energy of bending as a possible explanation of the biconcave shape of the human red blood cell. *Journal of theoretical biology*, vol. 26(1), pp. 61IN777–76IN881. ↑58

Cardamone, L., Laio, A., Torre, V., Shahapure, R., and DeSimone, A. 2011. Cytoskeletal actin networks in motile cells are critically self-organized systems synchronized by mechanical interactions. *Proceedings of the National Academy of Sciences*, vol. 108(34), pp. 13978–13983. ↑26

Carlsson, A. 2011. Mechanisms of cell propulsion by active stresses. *New journal of physics*, vol. 13(7), p. 073009. ↑29 , ↑30

Casquero, H., Bona-Casas, C., and Gomez, H. 2015. A nurbs-based immersed methodology for fluid–structure interaction. *Computer Methods in Applied Mechanics and Engineering*, vol. 284, pp. 943–970. ↑42

Casquero, H., Bona-Casas, C., and Gomez, H. 2017. Nurbs-based numerical proxies for red blood cells and circulating tumor cells in microscale blood flow. *Computer Methods in Applied Mechanics and Engineering*, vol. 316, pp. 646–667. ↑27

Causin, P. and Facchetti, G. 2009. Autocatalytic loop, amplification and diffusion: a mathematical and computational model of cell polarization in neural chemotaxis. *PLoS computational biology*, vol. 5(8), p. e1000479. ↑28

Ceniceros, H.D., Nós, R.L., and Roma, A.M. 2010. Three-dimensional, fully adaptive simulations of phase-field fluid models. *Journal of computational physics*, vol. 229(17), pp. 6135–6155. ↑36

Chan, C.E. and Odde, D.J. 2008. Traction dynamics of filopodia on compliant substrates. *Science*, vol. 322(5908), pp. 1687–1691. ↑26

Chan, T.F. and Van der Vorst, H.A. 1997. Approximate and incomplete factorizations. In *Parallel numerical algorithms*, pp. 167–202. Springer. ↑66

Chang, C. and Werb, Z. 2001. The many faces of metalloproteases: cell growth, invasion, angiogenesis and metastasis. *Trends in cell biology*, vol. 11, pp. S37–S43. ↑17

Charras, G. and Paluch, E. 2008. Blebs lead the way: how to migrate without lamellipodia. *Nature reviews Molecular cell biology*, vol. 9(9), pp. 730–736. ↑21 , ↑170

Chen, B.C., Legant, W.R., Wang, K., Shao, L., Milkie, D.E., Davidson, M.W., Janetopoulos, C., Wu, X.S., Hammer, J.A., Liu, Z., *et al.* 2014. Lattice light-sheet microscopy: imaging molecules to embryos at high spatiotemporal resolution. *Science*, vol. 346(6208), p. 1257998. ↑26 , ↑125

Chen, L.Q. 2002. Phase-field models for microstructure evolution. *Annual review of materials research*, vol. 32(1), pp. 113–140. ↑34

Choi, C.K., Vicente-Manzanares, M., Zareno, J., Whitmore, L.A., Mogilner, A., and Horwitz, A.R. 2008. Actin and α-actinin orchestrate the assembly and maturation of nascent adhesions in a myosin ii motor-independent manner. *Nature cell biology*, vol. 10(9), p. 1039. ↑26 , ↑52 , ↑131

Chugh, P., Clark, A.G., Smith, M.B., Cassani, D.A., Dierkes, K., Ragab, A., Roux, P.P., Charras, G., Salbreux, G., and Paluch, E.K. 2017. Actin cortex architecture regulates cell surface tension. *Nature Cell Biology*, vol. 19(6), pp. 689–697. ↑16

Chung, J. and Hulbert, G. 1993. A time integration algorithm for structural dynamics with improved numerical dissipation: the generalized-α method. *Journal of applied mechanics*, vol. 60(2), pp. 371–375. ↑64

Clark, E.A., Golub, T.R., Lander, E.S., and Hynes, R.O. 2000. Genomic analysis of metastasis reveals an essential role for rhoc. *Nature*, vol. 406(6795), p. 532. ↑19

Cogan, N. and Guy, R.D. 2010. Multiphase flow models of biogels from crawling cells to bacterial biofilms. *HFSP journal*, vol. 4(1), pp. 11–25. ↑31

Coleman, B.D. and Noll, W. 1963. The thermodynamics of elastic materials with heat conduction and viscosity. *Archive for Rational Mechanics and Analysis*, vol. 13(1), pp. 167–178. ↑35

Collier, N., Dalcin, L., and Calo, V.M. 2013a. PetIGA: High-performance isogeometric analysis. URL `https://bitbucket.org/dalcinl/petiga`. ↑42

Collier, N., Dalcín, L., and Calo, V.M. 2013b. Petiga: high-performance isogeometric analysis. *arXiv preprint arXiv:1305.4452*. ↑71

Cortese, B., Palamà, I.E., D'Amone, S., and Gigli, G. 2014. Influence of electrotaxis on cell behaviour. *Integrative Biology*, vol. 6(9), pp. 817–830. ↑21

Cottrell, J., Hughes, T., and Reali, A. 2007. Studies of refinement and continuity in isogeometric structural analysis. *Computer methods in applied mechanics and engineering*, vol. 196(41), pp. 4160–4183. ↑41

Cottrell, J.A., Hughes, T.J., and Bazilevs, Y. 2009. *Isogeometric analysis: toward integration of CAD and FEA*. John Wiley & Sons. ISBN 978-0-470-74873-2. ↑43 , ↑44 , ↑45 , ↑63

Cottrell, J.A., Reali, A., Bazilevs, Y., and Hughes, T.J. 2006. Isogeometric analysis of structural vibrations. *Computer methods in applied mechanics and engineering*, vol. 195(41), pp. 5257–5296. ↑42

Cox, M.G. 1972. The numerical evaluation of b-splines. *IMA Journal of Applied Mathematics*, vol. 10(2), pp. 134–149. ↑43

Dalcin, L., Collier, N., Vignal, P., Côrtes, A., and Calo, V.M. 2016. Petiga: A framework for high-performance isogeometric analysis. *Computer Methods in Applied Mechanics and Engineering*, vol. 308, pp. 151–181. ↑6 , ↑47 , ↑48

Danuser, G., Allard, J., and Mogilner, A. 2013. Mathematical modeling of eukaryotic cell migration: insights beyond experiments. *Annual review of cell and developmental biology*, vol. 29, pp. 501–528. ↑26 , ↑87

Dawes, A.T. and Edelstein-Keshet, L. 2007. Phosphoinositides and rho proteins spatially regulate actin polymerization to initiate and maintain directed movement in a one-dimensional model of a motile cell. *Biophysical journal*, vol. 92(3), pp. 744–768. ↑19 , ↑20 , ↑124

de Falco, C., Reali, A., and Vázquez, R. 2011. GeoPDEs: A research tool for isogeometric analysis of PDEs. *Advances in Engineering Software*, vol. 42(12), pp. 1020–1034. ↑42

Dedè, L., Borden, M.J., and Hughes, T.J. 2012. Isogeometric analysis for topology optimization with a phase field model. *Archives of Computational Methods in Engineering*, vol. 19(3), pp. 427–465. ↑35

Del Alamo, J.C., Meili, R., Alonso-Latorre, B., Rodríguez-Rodríguez, J., Aliseda, A., Firtel, R.A., and Lasheras, J.C. 2007. Spatio-temporal analysis of eukaryotic cell motility by improved force cytometry. *Proceedings of the National Academy of Sciences*, vol. 104(33), pp. 13343–13348. ↑26 , ↑156 , ↑158

Devreotes, P.N., Bhattacharya, S., Edwards, M., Iglesias, P.A., Lampert, T., and Miao, Y. 2017. Excitable signal transduction networks in directed cell migration. *Annual Review of Cell and Developmental Biology*, vol. 33, pp. 19.1–19.23. ↑31

Dimova, R. 2014. Recent developments in the field of bending rigidity measurements on membranes. *Advances in colloid and interface science*, vol. 208, pp. 225–234. ↑78

Discher, D.E., Janmey, P., and Wang, Y.l. 2005. Tissue cells feel and respond to the stiffness of their substrate. *Science*, vol. 310(5751), pp. 1139–1143. ↑20 , ↑26

Doubrovinski, K. and Kruse, K. 2010. Self-organization in systems of treadmilling filaments. *The European Physical Journal E: Soft Matter and Biological Physics*, vol. 31(1), pp. 95–104. ↑31

Dreher, A., Aranson, I.S., and Kruse, K. 2014. Spiral actin-polymerization waves can generate amoeboidal cell crawling. *New Journal of Physics*, vol. 16(5), p. 055007. ↑28 , ↑31 , ↑87

Driscoll, M.K. and Danuser, G. 2015. Quantifying modes of 3d cell migration. *Trends in cell biology*, vol. 25(12), pp. 749–759. ↑26

Elliott, C.M., Stinner, B., and Venkataraman, C. 2012. Modelling cell motility and chemotaxis with evolving surface finite elements. *Journal of The Royal Society Interface*, vol. 9(76), pp. 3027–3044. ↑27 , ↑32 , ↑33 , ↑87 , ↑96 , ↑125

Elosegui-Artola, A., Oria, R., Chen, Y., Kosmalska, A., Perez-Gonzalez, C., Castro, N., Zhu, C., Trepat, X., and Roca-Cusachs, P. 2016. Mechanical regulation of a molecular clutch defines force transmission and transduction in response to matrix rigidity. *Nature cell biology*, vol. 18(5), pp. 540–566. ↑26

Emmerich, H. 2003. *The diffuse interface approach in materials science: thermodynamic concepts and applications of phase-field models*, vol. 73. Springer Science & Business Media. ISBN 978-3-540-36409-2. ↑34

Fife, P.C. 1988. *Dynamics of internal layers and diffusive interfaces*. SIAM. ↑34

Flanagan, L.A., Chou, J., Falet, H., Neujahr, R., Hartwig, J.H., and Stossel, T.P. 2001. Filamin a, the arp2/3 complex, and the morphology and function of cortical actin filaments in human melanoma cells. *The Journal of cell biology*, vol. 155(4), pp. 511–518. ↑19

Fournier, M.F., Sauser, R., Ambrosi, D., Meister, J.J., and Verkhovsky, A.B. 2010. Force transmission in migrating cells. *The Journal of cell biology*, vol. 188(2), pp. 287–297. ↑51

Fried, E. 2006. On the relationship between supplemental balances in two theories for pure interface motion. *SIAM Journal on Applied Mathematics*, vol. 66(4), pp. 1130–1149. ↑39 , ↑59

Friedl, P. and Wolf, K. 2003. Tumour-cell invasion and migration: diversity and escape mechanisms. *Nature reviews. Cancer*, vol. 3(5), p. 362. ↑7 , ↑17 , ↑18 , ↑22 , ↑26 , ↑51 , ↑124

Friedl, P. and Wolf, K. 2008. Tube travel: the role of proteases in individual and collective cancer cell invasion. *Cancer research*, vol. 68(18), pp. 7247–7249. ↑25

Friedl, P. and Wolf, K. 2009. Plasticity of cell migration: a multiscale tuning model. *The Journal of cell biology*, pp. jcb–200909003. ↑21 , ↑23 , ↑26 , ↑51

Fuller, D., Chen, W., Adler, M., Groisman, A., Levine, H., Rappel, W.J., and Loomis, W.F. 2010. External and internal constraints on eukaryotic chemotaxis. *Proceedings of the National Academy of Sciences*, vol. 107(21), pp. 9656–9659. ↑134 , ↑135 , ↑136 , ↑147

Gabriele, S., Benoliel, A.M., Bongrand, P., and Théodoly, O. 2009. Microfluidic investigation reveals distinct roles for actin cytoskeleton and myosin ii activity in capillary leukocyte trafficking. *Biophysical journal*, vol. 96(10), pp. 4308–4318. ↑95

Gail, M.H. and Boone, C.W. 1970. The locomotion of mouse fibroblasts in tissue culture. *Biophysical journal*, vol. 10(10), pp. 980–993. ↑26 , ↑28 , ↑87 , ↑104

Gamba, A., de Candia, A., Di Talia, S., Coniglio, A., Bussolino, F., and Serini, G. 2005. Diffusion-limited phase separation in eukaryotic chemotaxis. *Proceedings of the National Academy of Sciences of the United States of America*, vol. 102(47), pp. 16927–16932. ↑31 , ↑125

Geiger, B., Spatz, J.P., and Bershadsky, A.D. 2009. Environmental sensing through focal adhesions. *Nature reviews. Molecular cell biology*, vol. 10(1), p. 21. ↑163

Gerbal, F., Chaikin, P., Rabin, Y., and Prost, J. 2000. An elastic analysis of listeria monocytogenes propulsion. *Biophysical journal*, vol. 79(5), pp. 2259–2275. ↑95

Goldstein, R.E. 1996. Traveling-wave chemotaxis. *Physical review letters*, vol. 77(4), p. 775. ↑149

Gómez, H., Calo, V.M., Bazilevs, Y., and Hughes, T.J. 2008. Isogeometric analysis of the cahn–hilliard phase-field model. *Computer methods in applied mechanics and engineering*, vol. 197(49), pp. 4333–4352. ↑35 , ↑42 , ↑64 , ↑66

Gomez, H. and De Lorenzis, L. 2016. The variational collocation method. *Computer Methods in Applied Mechanics and Engineering*, vol. 309, pp. 152–181. ↑47 , ↑64

Gomez, H. and Hughes, T.J. 2011. Provably unconditionally stable, second-order time-accurate, mixed variational methods for phase-field models. *Journal of Computational Physics*, vol. 230(13), pp. 5310–5327. ↑36

Gomez, H., Reali, A., and Sangalli, G. 2014. Accurate, efficient, and (iso) geometrically flexible collocation methods for phase-field models. *Journal of Computational Physics*, vol. 262, pp. 153–171. ↑36

Gomez, H. and van der Zee, K.G. 2017. Computational phase-field modeling. ↑6 , ↑34 , ↑35 , ↑39 , ↑54 , ↑59

Gracheva, M.E. and Othmer, H.G. 2004. A continuum model of motility in ameboid cells. *Bulletin of mathematical biology*, vol. 66(1), pp. 167–193. ↑29

Grimm, H., Verkhovsky, A., Mogilner, A., and Meister, J.J. 2003. Analysis of actin dynamics at the leading edge of crawling cells: implications for the shape of keratocyte lamellipodia. *European Biophysics Journal*, vol. 32(6), pp. 563–577. ↑29

Hanahan, D. and Weinberg, R.A. 2000. The hallmarks of cancer. *cell*, vol. 100(1), pp. 57–70. ↑1

Hanahan, D. and Weinberg, R.A. 2011. Hallmarks of cancer: the next generation. *cell*, vol. 144(5), pp. 646–674. ↑2

Hart, I. 2005. *Introduction to the cellular and molecular biology of cancer*. Oxford university press. ISBN 019852563X. ↑5

Hatzikirou, H. and Deutsch, A. 2008. Cellular automata as microscopic models of cell migration in heterogeneous environments. *Current Topics in Developmental Biology*, vol. 81, pp. 401–434. ↑28

Hawkins, R.J. and Voituriez, R. 2010. Mechanisms of cell motion in confined geometries. *Mathematical Modelling of Natural Phenomena*, vol. 5(1), pp. 84–105. ↑95

Hecht, I., Levine, H., Rappel, W.J., and Ben-Jacob, E. 2011a. "self-assisted" amoeboid navigation in complex environments. *PloS one*, vol. 6(8), p. e21955. ↑53 , ↑96

Hecht, I., Skoge, M.L., Charest, P.G., Ben-Jacob, E., Firtel, R.A., Loomis, W.F., Levine, H., and Rappel, W.J. 2011b. Activated membrane patches guide chemotactic cell motility. *PLoS computational biology*, vol. 7(6), p. e1002044. ↑27 , ↑32 , ↑87 , ↑96 , ↑104 , ↑125

Heck, T., Smeets, B., Vanmaercke, S., Bhattacharya, P., Odenthal, T., Ramon, H., Van Oosterwyck, H., and Van Liedekerke, P. 2017. Modeling extracellular matrix viscoelasticity using smoothed particle hydrodynamics with improved boundary treatment. *Computer Methods in Applied Mechanics and Engineering*, vol. 322, pp. 515–540. ↑32

Helfrich, W. 1973. Elastic properties of lipid bilayers: theory and possible experiments. *Zeitschrift für Naturforschung C*, vol. 28(11-12), pp. 693–703. ↑58

Hillen, T. and Painter, K.J. 2009. A user's guide to pde models for chemotaxis. *Journal of mathematical biology*, vol. 58(1-2), p. 183. ↑28

Holmes, W.R. and Edelstein-Keshet, L. 2012. A comparison of computational models for eukaryotic cell shape and motility. *PLoS computational biology*, vol. 8(12), p. e1002793. ↑26

Hughes, T.J., Cottrell, J.A., and Bazilevs, Y. 2005. Isogeometric analysis: Cad, finite elements, nurbs, exact geometry and mesh refinement. *Computer methods in applied mechanics and engineering*, vol. 194(39), pp. 4135–4195. ↑6 , ↑41 , ↑63

Hughes, T.J., Reali, A., and Sangalli, G. 2010. Efficient quadrature for nurbs-based isogeometric analysis. *Computer methods in applied mechanics and engineering*, vol. 199(5), pp. 301–313. ↑47

Iglesias, P.A. and Devreotes, P.N. 2008. Navigating through models of chemotaxis. *Current opinion in cell biology*, vol. 20(1), pp. 35–40. ↑31

Iglesias, P.A. and Devreotes, P.N. 2012. Biased excitable networks: how cells direct motion in response to gradients. *Current opinion in cell biology*, vol. 24(2), pp. 245–253. ↑31 , ↑33

Insall, R.H. 2010. Understanding eukaryotic chemotaxis: a pseudopod-centred view. *Nature reviews. Molecular cell biology*, vol. 11(6), p. 453. ↑86 , ↑89 , ↑106 , ↑107 , ↑124 , ↑134

Jacobelli, J., Friedman, R.S., Conti, M.A., Lennon-Dumenil, A.M., Piel, M., Sorensen, C.M., Adelstein, R.S., and Krummel, M.F. 2010. Confinement-optimized three-dimensional t cell amoeboid motility is modulated via myosin iia-regulated adhesions. *Nature immunology*, vol. 11(10), pp. 953–961. ↑105 , ↑112 , ↑113

Janetopoulos, C., Ma, L., Devreotes, P.N., and Iglesias, P.A. 2004. Chemoattractant-induced phosphatidylinositol 3, 4, 5-trisphosphate accumulation is spatially amplified and adapts, independent of the actin cytoskeleton. *Proceedings of the National Academy of Sciences of the United States of America*, vol. 101(24), pp. 8951–8956. ↑162

Jansen, K.E., Whiting, C.H., and Hulbert, G.M. 2000. A generalized-α method for integrating the filtered navier–stokes equations with a stabilized finite element method. *Computer methods in applied mechanics and engineering*, vol. 190(3), pp. 305–319. ↑64 , ↑65

Jeong, J.H., Goldenfeld, N., and Dantzig, J.A. 2001. Phase field model for three-dimensional dendritic growth with fluid flow. *Physical Review E*, vol. 64(4), p. 041602. ↑36

Jilkine, A. and Edelstein-Keshet, L. 2011. A comparison of mathematical models for polarization of single eukaryotic cells in response to guided cues. *PLoS computational biology*, vol. 7(4), p. e1001121. ↑26 , ↑28 , ↑32

Jin, C., Krüger, C., and Maass, C.C. 2017. Chemotaxis and autochemotaxis of self-propelling droplet swimmers. *Proceedings of the National Academy of Sciences*, vol. 114(20), pp. 5089–5094. ↑28

Joanny, J.F. and Prost, J. 2009. Active gels as a description of the actin-myosin cytoskeleton. *HFSP journal*, vol. 3(2), pp. 94–104. ↑29

Jurado, C., Haserick, J.R., and Lee, J. 2005. Slipping or gripping? fluorescent speckle microscopy in fish keratocytes reveals two different mechanisms for generating a retrograde flow of actin. *Molecular biology of the cell*, vol. 16(2), pp. 507–518. ↑163

Keller, E.F. and Segel, L.A. 1971. Model for chemotaxis. *Journal of theoretical biology*, vol. 30(2), pp. 225–234. ↑28

Keren, K., Pincus, Z., Allen, G.M., Barnhart, E.L., Marriott, G., Mogilner, A., and Theriot, J.A. 2008. Mechanism of shape determination in motile cells. *Nature*, vol. 453(7194), p. 475. ↑51 , ↑81

Kiendl, J., Ambati, M., De Lorenzis, L., Gomez, H., and Reali, A. 2016. Phase-field description of brittle fracture in plates and shells. *Computer Methods in Applied Mechanics and Engineering*, vol. 312, pp. 374–394. ↑36

Kim, T. 2015. Determinants of contractile forces generated in disorganized acto-myosin bundles. *Biomechanics and modeling in mechanobiology*, vol. 14(2), pp. 345–355. ↑26

Kim, T., Hwang, W., and Kamm, R. 2009a. Computational analysis of a cross-linked actin-like network. *Experimental Mechanics*, vol. 49(1), pp. 91–104. ↑26

Kim, T., Hwang, W., Lee, H., and Kamm, R.D. 2009b. Computational analysis of viscoelastic properties of crosslinked actin networks. *PLoS computational biology*, vol. 5(7), p. e1000439. ↑26

Kim, Y.T., Provatas, N., Goldenfeld, N., and Dantzig, J. 1999. Universal dynamics of phase-field models for dendritic growth. *Physical Review E*, vol. 59(3), p. R2546. ↑36

Kobayashi, R. 1994. A numerical approach to three-dimensional dendritic solidification. *Experimental Mathematics*, vol. 3(1), pp. 59–81. ↑36

Koblinski, J.E., Ahram, M., and Sloane, B.F. 2000. Unraveling the role of proteases in cancer. *Clinica chimica acta*, vol. 291(2), pp. 113–135. ↑19

Kockelkoren, J., Levine, H., and Rappel, W.J. 2003. Computational approach for modeling intra-and extracellular dynamics. *Physical Review E*, vol. 68(3), p. 037702. ↑27

Kuusela, E. and Alt, W. 2009. Continuum model of cell adhesion and migration. *Journal of mathematical biology*, vol. 58(1-2), p. 135. ↑31

Lämmermann, T. and Sixt, M. 2009. Mechanical modes of 'amoeboid'cell migration. *Current opinion in cell biology*, vol. 21(5), pp. 636–644. ↑26 , ↑124

Larripa, K. and Mogilner, A. 2006. Transport of a 1d viscoelastic actin–myosin strip of gel as a model of a crawling cell. *Physica A: Statistical Mechanics and its Applications*, vol. 372(1), pp. 113–123. ↑29

Lecuit, T. and Lenne, P.F. 2007. Cell surface mechanics and the control of cell shape, tissue patterns and morphogenesis. *Nature reviews. Molecular cell biology*, vol. 8(8), p. 633. ↑26

Lee, P. and Wolgemuth, C.W. 2016. Physical mechanisms of cancer in the transition to metastasis. *Biophysical journal*, vol. 111(1), pp. 256–266. ↑33 , ↑34

Lee, Y., Kouvroukoglou, S., McIntire, L.V., and Zygourakis, K. 1995. A cellular automaton model for the proliferation of migrating contact-inhibited cells. *Biophysical journal*, vol. 69(4), pp. 1284–1298. ↑28

Levchenko, A. and Iglesias, P.A. 2002. Models of eukaryotic gradient sensing: application to chemotaxis of amoebae and neutrophils. *Biophysical journal*, vol. 82(1), pp. 50–63. ↑26 , ↑31 , ↑87 , ↑96 , ↑125 , ↑162

Levine, H., Kessler, D.A., and Rappel, W.J. 2006. Directional sensing in eukaryotic chemotaxis: a balanced inactivation model. *Proceedings of the National Academy of Sciences*, vol. 103(26), pp. 9761–9766. ↑28 , ↑133

Li, L., Nørrelykke, S.F., and Cox, E.C. 2008. Persistent cell motion in the absence of external signals: a search strategy for eukaryotic cells. *PLoS one*, vol. 3(5), p. e2093. ↑104 , ↑105

Li, S., Guan, J.L., and Chien, S. 2005. Biochemistry and biomechanics of cell motility. *Annu. Rev. Biomed. Eng.*, vol. 7, pp. 105–150. ↑26

Li, X., Lowengrub, J., Rätz, A., and Voigt, A. 2009. Solving pdes in complex geometries: a diffuse domain approach. *Communications in mathematical sciences*, vol. 7(1), p. 81. ↑41

Liu, J., Gomez, H., Evans, J.A., Hughes, T.J., and Landis, C.M. 2013. Functional entropy variables: a new methodology for deriving thermodynamically consistent algorithms for complex fluids, with particular reference to the isothermal navier–stokes–korteweg equations. *Journal of Computational Physics*, vol. 248, pp. 47–86. ↑36

Liu, W.K., Liu, Y., Farrell, D., Zhang, L., Wang, X.S., Fukui, Y., Patankar, N., Zhang, Y., Bajaj, C., Lee, J., *et al.* 2006. Immersed finite element method and its applications to biological systems. *Computer methods in applied mechanics and engineering*, vol. 195(13), pp. 1722–1749. ↑27

Löber, J., Ziebert, F., and Aranson, I.S. 2014. Modeling crawling cell movement on soft engineered substrates. *Soft matter*, vol. 10(9), pp. 1365–1373. ↑27 , ↑28 , ↑30 , ↑31 , ↑36 , ↑41 , ↑52 , ↑81

Loeb, L.A., Loeb, K.R., and Anderson, J.P. 2003. Multiple mutations and cancer. *Proceedings of the National Academy of Sciences*, vol. 100(3), pp. 776–781. ↑2

Lorenzo, G., Scott, M., Tew, K., Hughes, T., and Gomez, H. 2017. Hierarchically refined and coarsened splines for moving interface problems, with particular application to phase-field models of prostate tumor growth. *Computer Methods in Applied Mechanics and Engineering*, vol. 319, pp. 515–548. ↑35 , ↑42

Lorenzo, G., Scott, M.A., Tew, K., Hughes, T.J., Zhang, Y.J., Liu, L., Vilanova, G., and Gomez, H. 2016. Tissue-scale, personalized modeling and simulation of prostate cancer growth. *Proceedings of the National Academy of Sciences*, p. 201615791. ↑36

Lowengrub, J.S., Rätz, A., and Voigt, A. 2009. Phase-field modeling of the dynamics of multicomponent vesicles: Spinodal decomposition, coarsening, budding, and fission. *Physical Review E*, vol. 79(3), p. 031926. ↑34

MacDonald, G., Mackenzie, J.A., Nolan, M., and Insall, R. 2016. A computational method for the coupled solution of reaction–diffusion equations on evolving domains and manifolds: Application to a model of cell migration and chemotaxis. *Journal of computational physics*, vol. 309, pp. 207–226. ↑27 , ↑125

Mak, M., Spill, F., Kamm, R.D., and Zaman, M.H. 2016. Single-cell migration in complex microenvironments: mechanics and signaling dynamics. *Journal of biomechanical engineering*, vol. 138(2), p. 021004. ↑26

Mallet, D.G. and De Pillis, L.G. 2006. A cellular automata model of tumor–immune system interactions. *Journal of theoretical biology*, vol. 239(3), pp. 334–350. ↑28

Marée, A.F., Grieneisen, V.A., and Edelstein-Keshet, L. 2012. How cells integrate complex stimuli: the effect of feedback from phosphoinositides and cell shape on cell polarization and motility. *PLoS computational biology*, vol. 8(3), p. e1002402. ↑28 , ↑31 , ↑33 , ↑125

Marée, A.F. and Hogeweg, P. 2001. How amoeboids self-organize into a fruiting body: multicellular coordination in dictyostelium discoideum. *Proceedings of the National Academy of Sciences*, vol. 98(7), pp. 3879–3883. ↑27

Marth, W. and Voigt, A. 2014. Signaling networks and cell motility: a computational approach using a phase field description. *Journal of mathematical biology*, vol. 69(1), pp. 91–112. ↑27 , ↑78 , ↑125

Meinhardt, H. 1999. Orientation of chemotactic cells and growth cones: models and mechanisms. *J Cell Sci*, vol. 112(17), pp. 2867–2874. ↑27 , ↑28 , ↑31 , ↑32 , ↑87 , ↑96 , ↑124

Mori, Y., Jilkine, A., and Edelstein-Keshet, L. 2008. Wave-pinning and cell polarity from a bistable reaction-diffusion system. *Biophysical journal*, vol. 94(9), pp. 3684–3697. ↑19 , ↑32 , ↑53 , ↑56 , ↑96

Moure, A. and Gomez, H. 2016. Computational model for amoeboid motion: Coupling membrane and cytosol dynamics. *Physical Review E*, vol. 94(4), p. 042423. ↑27 , ↑28 , ↑36 , ↑74 , ↑103 , ↑125 , ↑145

Moure, A. and Gomez, H. 2017. Phase-field model of cellular migration: Three-dimensional simulations in fibrous networks. *Computer Methods in Applied Mechanics and Engineering*, vol. 320, pp. 162–197. ↑74 , ↑103 , ↑125 , ↑145

Nagel, O., Guven, C., Theves, M., Driscoll, M., Losert, W., and Beta, C. 2014. Geometry-driven polarity in motile amoeboid cells. *PloS one*, vol. 9(12), p. e113382. ↑91 , ↑112 , ↑113 , ↑115

Neilson, M.P., Mackenzie, J.A., Webb, S.D., and Insall, R.H. 2011a. Modeling cell movement and chemotaxis using pseudopod-based feedback. *SIAM Journal on Scientific Computing*, vol. 33(3), pp. 1035–1057. ↑32

Neilson, M.P., Veltman, D.M., van Haastert, P.J., Webb, S.D., Mackenzie, J.A., and Insall, R.H. 2011b. Chemotaxis: a feedback-based computational model robustly predicts multiple aspects of real cell behaviour. *PLoS biology*, vol. 9(5), p. e1000618. ↑27 , ↑32 , ↑33 , ↑96 , ↑104 , ↑125

Novak, I.L., Gao, F., Choi, Y.S., Resasco, D., Schaff, J.C., and Slepchenko, B.M. 2007. Diffusion on a curved surface coupled to diffusion in the volume: Application to cell biology. *Journal of computational physics*, vol. 226(2), pp. 1271–1290. ↑27

Novak, I.L., Slepchenko, B.M., and Mogilner, A. 2008. Quantitative analysis of g-actin transport in motile cells. *Biophysical journal*, vol. 95(4), pp. 1627–1638. ↑130

Novikova, E.A., Raab, M., Discher, D.E., and Storm, C. 2017. Persistence-driven durotaxis: Generic, directed motility in rigidity gradients. *Physical review letters*, vol. 118(7), p. 078103. ↑28

Otsuji, M., Ishihara, S., Kaibuchi, K., Mochizuki, A., Kuroda, S., *et al.* 2007. A mass conserved reaction–diffusion system captures properties of cell polarity. *PLoS computational biology*, vol. 3(6), p. e108. ↑19 , ↑32 , ↑53 , ↑56

Pauletti, M.S., Martinelli, M., Cavallini, N., and Antolin, P. 2015. Igatools: An isogeometric analysis library. *SIAM Journal on Scientific Computing*, vol. 37(4), pp. C465–C496. ↑42

Penrose, O. and Fife, P.C. 1990. Thermodynamically consistent models of phase-field type for the kinetic of phase transitions. *Physica D: Nonlinear Phenomena*, vol. 43(1), pp. 44–62. ↑36

Piegl, L. and Tiller, W. 2012. *The NURBS book*. Springer Science & Business Media. ISBN 9783642973857. ↑41 , ↑47 , ↑63

Potel, M.J. and Mackay, S.A. 1979. Preaggregative cell motion in dictyostelium. *Journal of cell science*, vol. 36(1), pp. 281–309. ↑26 , ↑87 , ↑104 , ↑116

Preira, P., Valignat, M.P., Bico, J., and Théodoly, O. 2013. Single cell rheometry with a microfluidic constriction: quantitative control of friction and fluid leaks between cell and channel walls. *Biomicrofluidics*, vol. 7(2), p. 024111. ↑95

Provatas, N. and Elder, K. 2011. *Phase-field methods in materials science and engineering*. John Wiley & Sons. ISBN 978-3-527-40747-7. ↑34

Rey, R. and Garcia-Aznar, J. 2013. A phenomenological approach to modelling collective cell movement in 2d. *Biomechanics and modeling in mechanobiology*, vol. 12(6), pp. 1089–1100. ↑27

Ribeiro, F., Gómez-Benito, M., Folgado, J., Fernandes, P., and García-Aznar, J. 2017. Computational model of mesenchymal migration in 3d under chemotaxis. *Computer methods in BiomeChaniCs and BiomediCal engineering*, vol. 20(1), pp. 59–74. ↑32 , ↑88 , ↑162

Roussos, E.T., Condeelis, J.S., and Patsialou, A. 2011. Chemotaxis in cancer. *Nature reviews. Cancer*, vol. 11(8), p. 573. ↑26

Rubinstein, B., Fournier, M.F., Jacobson, K., Verkhovsky, A.B., and Mogilner, A. 2009. Actin-myosin viscoelastic flow in the keratocyte lamellipod. *Biophysical journal*, vol. 97(7), pp. 1853–1863. ↑29 , ↑57 , ↑88

Rugar, D. and Hansma, P. 1990. Atomic force microscopy. *Physics today*, vol. 43(10), pp. 23–30. ↑26

Saad, Y. and Schultz, M.H. 1986. Gmres: A generalized minimal residual algorithm for solving nonsymmetric linear systems. *SIAM Journal on scientific and statistical computing*, vol. 7(3), pp. 856–869. ↑66

Schillinger, D., Dede, L., Scott, M.A., Evans, J.A., Borden, M.J., Rank, E., and Hughes, T.J. 2012. An isogeometric design-through-analysis methodology based on adaptive hierarchical refinement of nurbs, immersed boundary methods, and t-spline cad surfaces. *Computer Methods in Applied Mechanics and Engineering*, vol. 249, pp. 116–150. ↑41

Schmidt, R., Wüchner, R., and Bletzinger, K.U. 2012. Isogeometric analysis of trimmed nurbs geometries. *Computer Methods in Applied Mechanics and Engineering*, vol. 241, pp. 93–111. ↑41

Scianna, M., Preziosi, L., and Wolf, K. 2013. A cellular potts model simulating cell migration on and in matrix environments. *Mathematical Biosciences and Engineering*, vol. 10(1), pp. 235–261. ↑28

Scott, M.A., Thomas, D.C., and Evans, E.J. 2014. Isogeometric spline forests. *Computer Methods in Applied Mechanics and Engineering*, vol. 269, pp. 222–264. ↑41

Shao, D., Levine, H., and Rappel, W.J. 2012. Coupling actin flow, adhesion, and morphology in a computational cell motility model. *Proceedings of the National Academy of Sciences*, vol. 109(18), pp. 6851–6856. ↑27 , ↑29 , ↑36 , ↑52 , ↑53 , ↑54 , ↑87 , ↑96

Shao, D., Rappel, W.J., and Levine, H. 2010. Computational model for cell morphodynamics. *Physical review letters*, vol. 105(10), p. 108104. ↑27 , ↑41 , ↑52 , ↑54 , ↑87

Shi, C., Huang, C.H., Devreotes, P.N., and Iglesias, P.A. 2013. Interaction of motility, directional sensing, and polarity modules recreates the behaviors of chemotaxing cells. *PLoS computational biology*, vol. 9(7), p. e1003122. ↑27 , ↑32 , ↑125

Simson, R., Wallraff, E., Faix, J., Niewöhner, J., Gerisch, G., and Sackmann, E. 1998. Membrane bending modulus and adhesion energy of wild-type and mutant cells of dictyostelium lacking talin or cortexillins. *Biophysical journal*, vol. 74(1), pp. 514–522. ↑78

Skoge, M., Yue, H., Erickstad, M., Bae, A., Levine, H., Groisman, A., Loomis, W.F., and Rappel, W.J. 2014. Cellular memory in eukaryotic chemotaxis. *Proceedings of the National Academy of Sciences*, vol. 111(40), pp. 14448–14453. ↑149 , ↑150

Song, L., Nadkarni, S.M., Bödeker, H.U., Beta, C., Bae, A., Franck, C., Rappel, W.J., Loomis, W.F., and Bodenschatz, E. 2006. Dictyostelium discoideum chemotaxis: threshold for directed motion. *European journal of cell biology*, vol. 85(9), pp. 981–989. ↑124 , ↑133 , ↑135 , ↑136 , ↑147

Strychalski, W., Adalsteinsson, D., and Elston, T.C. 2010. Simulating biochemical signaling networks in complex moving geometries. *SIAM Journal on Scientific Computing*, vol. 32(5), pp. 3039–3070. ↑27

Strychalski, W., Copos, C.A., Lewis, O.L., and Guy, R.D. 2015. A poroelastic immersed boundary method with applications to cell biology. *Journal of Computational Physics*, vol. 282, pp. 77–97. ↑27 , ↑31

Strychalski, W. and Guy, R.D. 2012. A computational model of bleb formation. *Mathematical medicine and biology: a journal of the IMA*, vol. 30(2), pp. 115–130. ↑26

Subramanian, K. and Narang, A. 2004. A mechanistic model for eukaryotic gradient sensing: spontaneous and induced phosphoinositide polarization. *Journal of theoretical biology*, vol. 231(1), pp. 49–67. ↑27 , ↑31 , ↑125

Swaney, K.F., Huang, C.H., and Devreotes, P.N. 2010. Eukaryotic chemotaxis: a network of signaling pathways controls motility, directional sensing, and polarity. *Annual review of biophysics*, vol. 39, pp. 265–289. ↑19 , ↑124 , ↑133

Swanson, K.R., Rockne, R.C., Claridge, J., Chaplain, M.A., Alvord, E.C., and Anderson, A.R. 2011. Quantifying the role of angiogenesis in malignant progression of gliomas: in silico modeling integrates imaging and histology. *Cancer research*, vol. 71(24), pp. 7366–7375. ↑176

Talmadge, J.E. and Fidler, I.J. 2010. Aacr centennial series: the biology of cancer metastasis: historical perspective. *Cancer research*, vol. 70(14), pp. 5649–5669. ↑3 , ↑4

Te Boekhorst, V., Preziosi, L., and Friedl, P. 2016. Plasticity of cell migration in vivo and in silico. *Annual review of cell and developmental biology*, vol. 32, pp. 491–526. ↑23 , ↑26

Teigen, K.E., Li, X., Lowengrub, J., Wang, F., and Voigt, A. 2009. A diffuse-interface approach for modeling transport, diffusion and adsorption/desorption of material quantities on a deformable interface. *Communications in mathematical sciences*, vol. 4(7), p. 1009. ↑41 , ↑89 , ↑101

Thiery, J.P. 2002. Epithelial-mesenchymal transitions in tumour progression. *Nature reviews. Cancer*, vol. 2(6), p. 442. ↑23

Tjhung, E., Tiribocchi, A., and Marenduzzo, D. 2015. A minimal physical model captures the shapes of crawling cells. *Nat. Commun.*, vol. 6, p. 5420. ↑29 , ↑41 , ↑125

Torre, L., Siegel, R., and Jemal, A. 2015. Global cancer facts & figures. *Atlanta: American Cancer Society*. ↑2

Tozluoglu, M., Tournier, A.L., Jenkins, R.P., Hooper, S., Bates, P.A., and Sahai, E. 2013. Matrix geometry determines optimal cancer cell migration strategy and modulates response to interventions. *Nature cell biology*, vol. 15(7), p. 751. ↑32 , ↑112

Truesdell, C. and Noll, W. 2004. The non-linear field theories of mechanics. In *The non-linear field theories of mechanics*, pp. 1–579. Springer. ↑35

Tweedy, L., Meier, B., Stephan, J., Heinrich, D., and Endres, R.G. 2013. Distinct cell shapes determine accurate chemotaxis. *Scientific reports*, vol. 3. ↑151

Uhlenbeck, G.E. and Ornstein, L.S. 1930. On the theory of the brownian motion. *Physical review*, vol. 36(5), p. 823. ↑116

Valero, C., Javierre, E., García-Aznar, J., and Gómez-Benito, M. 2013. Numerical modelling of the angiogenesis process in wound contraction. *Biomechanics and modeling in mechanobiology*, pp. 1–12. ↑27

Van Haastert, P.J. 2010. A stochastic model for chemotaxis based on the ordered extension of pseudopods. *Biophysical journal*, vol. 99(10), pp. 3345–3354. ↑28 , ↑32 , ↑134 , ↑135 , ↑136

Van Haastert, P.J. and Devreotes, P.N. 2004. Chemotaxis: signalling the way forward. *Nature reviews. Molecular cell biology*, vol. 5(8), p. 626. ↑19 , ↑20 , ↑86 , ↑88 , ↑107 , ↑124 , ↑125 , ↑149 , ↑162

Vermolen, F. and Gefen, A. 2013. A phenomenological model for chemico-mechanically induced cell shape changes during migration and cell–cell contacts. *Biomechanics and modeling in mechanobiology*, pp. 1–23. ↑27 , ↑33 , ↑125

Vicente-Manzanares, M., Newell-Litwa, K., Bachir, A.I., Whitmore, L.A., and Horwitz, A.R. 2011. Myosin iia/iib restrict adhesive and protrusive signaling to generate front–back polarity in migrating cells. *The Journal of cell biology*, vol. 193(2), pp. 381–396. ↑26

Vignal, P.A., Collier, N., and Calo, V.M. 2013. Phase field modeling using petiga. *Procedia Computer Science*, vol. 18, pp. 1614–1623. ↑71

Vilanova, G., Colominas, I., and Gomez, H. 2013. Capillary networks in tumor angiogenesis: From discrete endothelial cells to phase-field averaged descriptions via isogeometric analysis. *International journal for numerical methods in biomedical engineering*, vol. 29(10), pp. 1015–1037. ↑36

Walcott, S. and Sun, S.X. 2010. A mechanical model of actin stress fiber formation and substrate elasticity sensing in adherent cells. *Proceedings of the National Academy of Sciences*, vol. 107(17), pp. 7757–7762. ↑26

Wessels, D., Brincks, R., Kuhl, S., Stepanovic, V., Daniels, K.J., Weeks, G., Lim, C.J., Spiegelman, G., Fuller, D., Iranfar, N., *et al.* 2004. Rasc plays a role in transduction of temporal gradient information in the cyclic-amp wave of dictyostelium discoideum. *Eukaryotic Cell*, vol. 3(3), pp. 646–662. ↑156

Wilson, K., Lewalle, A., Fritzsche, M., Thorogate, R., Duke, T., and Charras, G. 2013. Mechanisms of leading edge protrusion in interstitial migration. *Nature communications*, vol. 4, p. 2896. ↑95 , ↑112 , ↑113

Wolgemuth, C.W. and Zajac, M. 2010. The moving boundary node method: a level set-based, finite volume algorithm with applications to cell motility. *Journal of computational physics*, vol. 229(19), pp. 7287–7308. ↑27

Wu, X., Zwieten, G., and Zee, K. 2014. Stabilized second-order convex splitting schemes for cahn–hilliard models with application to diffuse-interface tumor-growth models. *International journal for numerical methods in biomedical engineering*, vol. 30(2), pp. 180–203. ↑36

Xu, J., Vilanova, G., and Gomez, H. 2016. A mathematical model coupling tumor growth and angiogenesis. *PloS one*, vol. 11(2), p. e0149422. ↑36

Xu, J., Vilanova, G., and Gomez, H. 2017. Full-scale, three-dimensional simulation of early-stage tumor growth: the onset of malignancy. *Computer Methods in Applied Mechanics and Engineering*, vol. 314, pp. 126–146. ↑27 , ↑36 , ↑42

Zhang, J., Das, S., and Du, Q. 2009. A phase field model for vesicle–substrate adhesion. *Journal of Computational Physics*, vol. 228(20), pp. 7837–7849. ↑53 , ↑96

Ziebert, F. and Aranson, I.S. 2016. Computational approaches to substrate-based cell motility. *npj Computational Materials*, vol. 2, p. 16019. ↑26 , ↑156

Ziebert, F., Swaminathan, S., and Aranson, I.S. 2011. Model for self-polarization and motility of keratocyte fragments. *Journal of The Royal Society Interface*, p. rsif20110433. ↑31